MECHANICAL BEHAVIOR AND IRRADIATION RESPONSE IN NANOSTRUCTURED METALS WITH LOW STACKING FAULT ENERGY

A Dissertation

by

JIN LI

Submitted to the Office of Graduate and Professional Studies of
Texas A&M University
in partial fulfillment of the requirements for the degree of

DOCTOR OF PHILOSOPHY

Chair of Committee,	Xinghang Zhang
Co-Chair of Committee,	Karl T. Hartwig
Committee Members,	Haiyan Wang
	Debjyoti Banerjee
Head of Department,	Ibrahim Karaman

August 2017

Major Subject: Materials Science and Engineering

ABSTRACT

High-energy particles introduce significant damage to nuclear structural materials and eventually lead to the failure of the materials. Austenitic stainless steels, as a widely used structural material in current nuclear reactors, are face-centered cubic (FCC) metals with very low stacking fault energy (SFE) that are known to be very vulnerable to irradiation damage. Therefore, it is critical to understand the damage mechanisms and to improve the irradiation resistance of those materials. To achieve the goal, both mechanical properties and irradiation response of nanostructured Ag and Au, which are typical FCC metals with low SFE, are investigated.

Mechanical properties. Ag/Fe multilayers with individual layer thicknesses (*h*) varying from 1 to 200 nm have been fabricated. The microstructure and mechanical strength of the multilayers have been studied. Comparison of mechanical strength of several Ag based multilayers reveals that this drastic difference may arise from chemical stress due to the difference in stacking fault energy of the layer constituents.

Irradiation response. By using *in situ* irradiation technique in a transmission electron microscope, it has been shown that NT Ag has significantly improved irradiation tolerance comparing with its coarse-grained counterpart. The surprising resilience of TBs in response to radiation has been revealed. Besides, defect distribution shows a clear dependence on twin thickness. Moreover, irradiation tolerance of NT Ag can be further improved by mixing merely 1 at% of Fe solute atoms into Ag matrix. Similar to NT Ag, NP Au also exhibits the improved irradiation tolerance as compared to coarse-grained, fully dense Au. *In situ* studies show that nanopores can absorb and eliminate a large number of irradiation-induced defect clusters. Besides, it has been shown that both defect density and nanopores evolve with radiation temperature. The sink strength of nanopores as a function of temperature is estimated. Moreover, NP Au exhibits significantly enhanced swelling resistance compared to coarse-grained Au. Potential mechanisms for temperature dependent radiation resistance of NP metals are discussed.

This dissertation serves as a fundamental understanding of both mechanical properties and irradiation response in FCC metals with low SFE and assists the design of advanced nanostructured materials with enhanced radiation tolerance.

To my wife, Fei Peng

ACKNOWLEDGMENTS

The most important acknowledgment of gratitude I wish to express is to my advisor and my committee chair, Prof. Xinghang Zhang, who recruited me four years ago and has provided me a great research opportunity. He has the attitude and the wisdom of a great mentor. He continually and convincingly conveyed a spirit of research and scholarship. His encouragement, trust and support become an important part of my Ph.D. study. Otherwise, this dissertation would not have been possible.

I am also grateful to my committee members, Prof. Hartwig (my co-chair), Prof. Haiyan Wang and Prof. Debjyoti Banerjee, for their guidance and precious suggestions that improved the quality of this dissertation.

I express my gratitude to Dr. Youxing Chen at Los Alamos National Laboratory (LANL) and Dr. Kaiyuan Yu at China University of Petroleum-Beijing for their help on my research, as well as Dr. Mark A. Kirk and Dr. Meimei Li, Peter M. Baldo and Edward A. Ryan at Argonne National Lab (ANL) for their collaboration on *in situ* Kr irradiation. Many thanks to Peter M. Baldo and Edward A. Ryan at ANL for their assistance on *in situ* radiation experiments. I greatly appreciate Jules Henry, the Materials Science and Engineering academic advisor at Texas A&M, who offered a lot of help through my graduate studies.

I also would like to acknowledge my colleagues and friends Yue Liu, Miao Song, Steven Rios, Zhe Fan, Sichuang Xue, Qiang Li, Cuncai Fan, Ruizhe Su, Jie Ding, Zhongxia Shang, Yifan Zhang, Jie Jian and Fauzia Khatkhatay, who have helped my experiments and provided useful suggestions.

I am greatly indebted to my parents and wife for their complete, continued, and undoubted support. Without their understanding and support, I would never have the courage to keep going.

CONTRIBUTORS AND FUNDING SOURCES

Contributors

This work was supported by a dissertation committee consisting of Prof. Xinghang Zhang and Prof. Hartwig of the Department of Materials Science and Engineering, Prof. Haiyan Wang of the Department of Electrical and Computer Engineering and Prof. Debjyoti of the Department of Mechanical Engineering.

The *in situ* irradiation experiments in Chapter IV, V, VI, VII and VIII were assisted by Peter M. Baldo and Edward A. Ryan at Argonne National Laboratory. The Nanoporous Au specimens in Chapter VII and VIII were prepared by Qiang Li and Jie Ding at Texas A&M University and Purdue University.

The student completed all other work conducted for this dissertation independently.

Funding Sources

Graduate study was supported by a graduate research assistantship from Texas A&M University. Research was supported by NSF-DMR-Metallic Materials and Nanostructures Program under grant no. 1304101 and 1643915.

TABLE OF CONTENTS

Page

LIST OF FIGURES

LIST OF TABLES

Page

CHAPTER I

INTRODUCTION AND LITERATURE REVIEW

1.1 Challenges in nuclear reactor materials

About 4 trillion Kilowatt-hours of electricity is generated in the United States in 2016, and 65% was generated from fossil fuels, including coal, natural gas, and petroleum [1]. Fossil fuels are non-renewable, and the use of such materials accounts for more than 30% of the carbon entering the atmosphere every year. In comparison, clean and renewable energy sources, such as wind, solar, geothermal and nuclear, cause less environmental concerns, but can only provide a small fraction of the energy consumed at present. Clearly, the development of clean and renewable energy is of great importance. Nuclear energy as a clean power source provides only about 13% of electricity generated worldwide [2] (about 20% in the US in 2016 [1]). To promote the operation of the nuclear plants for more energy, next-generation nuclear reactors demand the improvement of fuel performance underpinned by advanced structural materials that can sustain under extreme irradiation environment [3, 4]. Materials used in the future reactors must survive at a much greater irradiation dose, 400-600 displacements-per-atom (dpa), during a service lifetime of $\geq$ 80 years. Unfortunately, most materials used in the present nuclear reactors have only been studied in a relatively low dose-range, from several to ~ 200 dpa.

Upon irradiation by the high-energy particle, such as electrons, protons, neutrons, and ions, a tremendous number of defects, including point defects and small clusters, are produced in the materials [5]. These defects can migrate and react with other defects and evolve into defect clusters, such as dislocation loops, dislocation networks and voids [6-8]. As a consequence, significant microstructural damages are introduced in the irradiated materials, such as void swelling that may change a material’s dimension (such as swelling), and phase segregation and precipitation. These microstructural damages can significantly degrade both mechanical properties and corrosion resistance of irradiated materials [9-18]. Although extensive studies over the past several decades have shown that the magnitude of microstructural damage varies drastically for various materials, no materials are immune to irradiation damage to date. Therefore, the understanding of the irradiation damage is the key to the design advanced materials for advanced nuclear reactors.

1.2 Irradiation response of metals

The degradation in both mechanical and structural stability of reactor materials is caused by various types of defects. Therefore, to study the mechanisms of irradiation-induced damage, it is important to understand the nature of defects generated during irradiation. Besides, the microstructural evolution of a material under irradiation depends on its crystallographic structure. Most metallic materials used in nuclear reactors have one of three crystallographic structures, including face-centered cubic (FCC) and body-centered cubic (BCC), and hexagonal close packed (HCP) structures. In this section, the fundamentals of ion-solid interaction will be briefly introduced followed by the review of the primary types of irradiation-induced defects based on the crystal structure of irradiated metallic materials.

1.2.1 Fundamentals of ion-solid interaction

Ion-solid interaction has been widely studied since 1911 when Rutherford reported his famous study on the scattering of particles in the matter [19]. Later, the first theoretical concepts that describe the interaction of particles with solids were given by Thomson and Bohr during 1912-1913 [20, 21]. After a century, the field of ion-solid interaction has become more matured [22, 23]. Fig. 1.1 is a schematic that shows some of the possible consequence of ion-solid interactions. When an energetic incident particle penetrates into a material, it will interact with lattice atoms. The kinetic energy, E, transferred from the incident particle to the first lattice atom that encounters the incident particle forces the lattice atom to leave its lattice site, and this first displaced atom is called primary knock-on atom (PKA). If the amount of energy E transferred to a PKA is smaller than the minimum energy that required to create a displacement. i.e. the threshold displacement energy, E_d, the PKA only undergoes vibrations and stays in its original position. However, if E is larger than E_d, the PKA will be displaced and a Frenkel pair, which consists a vacancy and a self-interstitial atom (SIA), will be created [12, 24, 25]. The fundamental properties of vacancies and SIAs are critical to study irradiation-induced damage in materials. Compare to vacancies, SIAs possess high diffusion coefficient and larger relaxation volume. Higher diffusion coefficient leads to a phenomenon of temperature-dependent irradiation damage accumulation, and larger relaxation volume makes SIAs react more readily with other defects, such as grain boundaries, and sometimes results in a supersaturated vacancy concentration, which is the origin of irradiation-induced void swelling.

In addition to the creation of Frankel pairs, a PKA with high energy will continuously bombard other atoms, leading to the formation of secondary or tertiary knock-on atoms. The multiple displacement sequences of knock-on events are generally referred to as displacement cascades as shown in Fig. 1.2. The Kinchin-Pease method, which based on hard-sphere model, is used broadly to estimate the number of displaced atoms, $N_d(E)$, which created from one cascade by a PKA with energy E [26]. The relation between $N_d(E)$ and E can be described by the displacement damage function, as shown in Fig. 1.3 [12, 27-29].

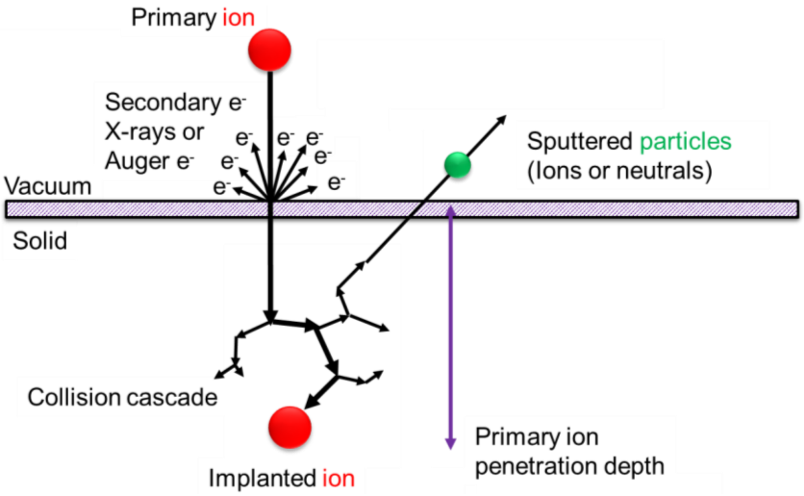

Fig. 1.1. Schematic of ion-solid interactions.

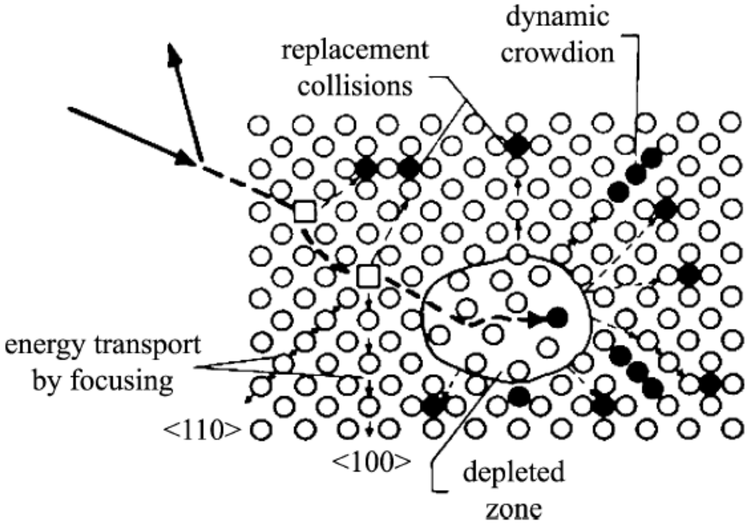

Fig. 1.2. A schematic showing two-dimensional displacement cascade (Reprinted with permission from [12]).

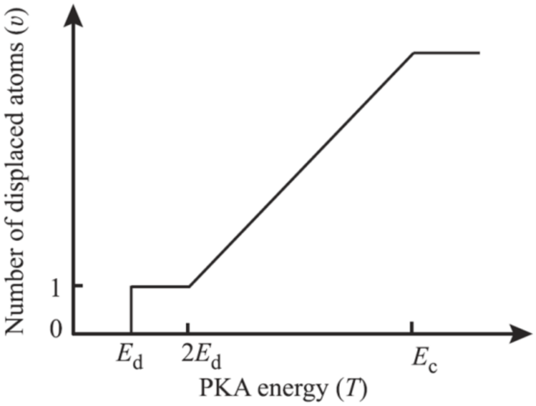

$$\begin{cases} N_d(E) = 0 & (for\, E < E_d) \\ N_d(E) = 1 & (for\, E_d \le E \le 2E_d) \\ N_d(E) = \dfrac{E}{2E_d} & (for\, 2E_d \le E \le E_c) \\ N_d(E) = \dfrac{E_c}{2E_d} & (for\, E > E_c) \end{cases}$$

Fig. 1.3. A graphical representation of the number of displaced atoms in the cascade as a function of PKA energy according to the displacement damage function as shown on the right side E_c is the cut-off energy that can be determined by the mass of target atoms [12, 27-29] (Reprinted with permission from [12]).

The Kinchin-Pease model has been widely applied in SRIM simulations to estimate the damage created during irradiation. However, this model ignores the effect of the electronic stopping as well as the crystal structure. Electronic stopping describes the energy loss caused by retarding force acting on a PKA due to the inelastic collisions between bound electrons in the materials. However, such an effect is minor and negligible when estimating irradiation damage. In comparison, the crystal structure plays a more important role. The energy required to displace an atom depends on the crystallographic directions. For instance, in an FCC structure as shown in Fig. 1.4a, an atom in the lower left-hand corner (the struck atom) has three possible migration paths, which along <100>, <110> and <111>, respectively, after receiving energy from a collision. Fig. 1.4b shows a variation of potential energy along <111> direction. Generally, different crystal direction possesses different displacement energy. Take Cu as an example, Fig. 1.4c shows the dependence of threshold energy (eV) on crystal orientation in Cu [30]. The data indicates that the threshold displacement energy is lower if the struck atom migrates following a line of atoms in the crystal. The minimum threshold energy in Cu is 19 eV, which is along <100> direction.

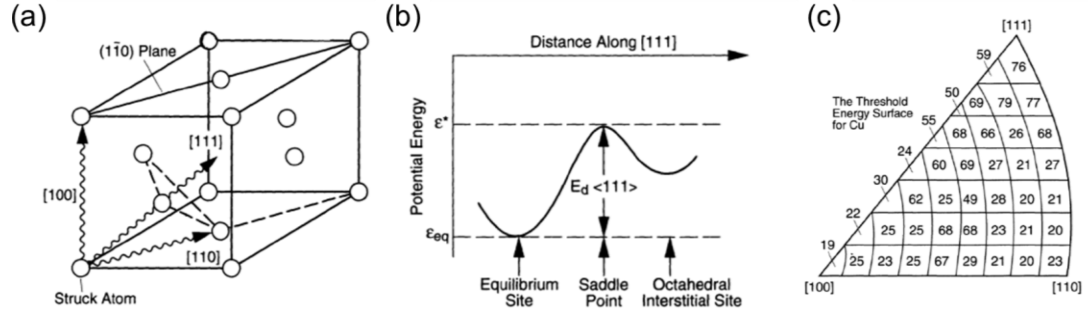

Fig. 1.4. (a) Displacement of a lattice atom recoiling from a collision with an energetic atom; (b) potential energy along the <111> direction [31] (Reprinted from [31] with permission from Elsevier). (c) The dependence of threshold energy (eV) on crystal orientation in Cu (Reprinted form [30]).

When estimating the damage induced by energetic particle bombardment, one has to take the type of energetic particles into consideration. In general, several different particles are used in the present research, including electrons, protons, heavy ions and neutrons. Electrons and protons are light particles that produce isolated Frenkel pairs and small clusters compared to heavy ions and neutrons. Because of this, the morphology of defects, in terms of type, size and density, which induced during collision vary from one type of particles to another. The comparison of the irradiation-induced defects by neutrons, heavy ions and electrons, is reviewed in details in **Chapter 1.2.3**.

Neutron irradiation-induced damage is the major issue in the design of structural materials for nuclear reactors. Therefore, it is necessary to investigate the microstructure evolution of materials under neutron irradiation. However, neutron irradiation study takes a long period due to its low dose-rate, and it is very expensive. From the scientific point of view, using electrons, protons and heavy ions to simulate neutron irradiation is more efficient. However, each type of irradiation has its advantages and disadvantages. A brief description is given below:

(1) Electron irradiation
  - Pros: easy access
  - Cons: beam energy is low; damage profile is not uniform

(2) Proton irradiation
  - Pros: Broadly spaced cascades which close to that under neutron irradiation; deeper penetration depth.
  - Cons: low damage rate

(3) Heavy ion irradiation
  - Pros: high damage rate, relatively low cost
  - Cons: limited penetration depth of ions; significant temperature shifts due to high dose-rate

1.2.2 Role of irradiation temperature and SFE on microstructure evolution

1.2.2.1 Role of irradiation temperature

Microstructure evolution largely depends on irradiation temperature. There are several distinct temperature regimes that are differentiated by the onset migration of point defects. Five major defect recovery stages have been identified by measuring the electrical resistivity as a function of isochronal annealing temperature of materials which irradiated at very low temperature, near the absolute zero degrees [5, 32, 33]. Two models have been proposed to explain such a phenomenon. One is “conversion two interstitial model”, and another is “one interstitial model”. The later one is now widely accepted. Based on one interstitial model, the five stages stand for:

Stage I: onset of long-range SIA migration

Stage II: small SIA clusters and SIA-impurity complexes migration

Stage III: onset of vacancy migration

Stage IV: vacancy-impurity clusters migration

Stage V: thermal dissociation of sessile vacancy clusters

During Stage I, vacancies and mobile SIAs start to recombine. The annihilation of vacancy-SIA leads to the concentration of point defects decreases drastically. At Stage II, the survived SIAs combine together and form SIA clusters. Vacancies start to migrate at Stage III, and interact with SIA clusters. As a result, SIA clusters begin to disappear. During Stage IV, vacancies aggregate together and form vacancy cluster. Finally, at Stage V, vacancy clusters dissociate. Large clusters become individual vacancies. It should be noted that Stage I, III and V generally have a narrower range compared to Stage II and IV in neutron irradiated materials. The reason is that during neutron irradiation, an enormous amount of vacancies is produced during collision cascade. Those vacancies are away from interstitials. Therefore, the recombination between vacancies and SIAs becomes hard. The amount of recovered point defects is limited in Stage I. Instead, the cluster of vacancies and SIAs are easy to form, and Stage II and IV become wider. For electron irradiation, since the major defects created are Frankel pairs, 90% of defects recovered in Stage I. Fig.

1.5 shows the five defect recovery stages in an ideal case (a) and defect recovery of high purity iron with different carbon concentrations (b) [34].

In many cases, Stage I consists of five smaller stages. The first three stages correspond to the close-pair recombination of Frenkel defects created in the same displacement event, and the last two stages are dominated by long-range recombination of defects from different displacement events. In addition, the specific recovery stage depends on the annealing time. Therefore, the onset temperatures for defect migration in neutron irradiation experiments should be adjusted to lower values. The experimental values of each temperature stage for most materials can be found at [35].

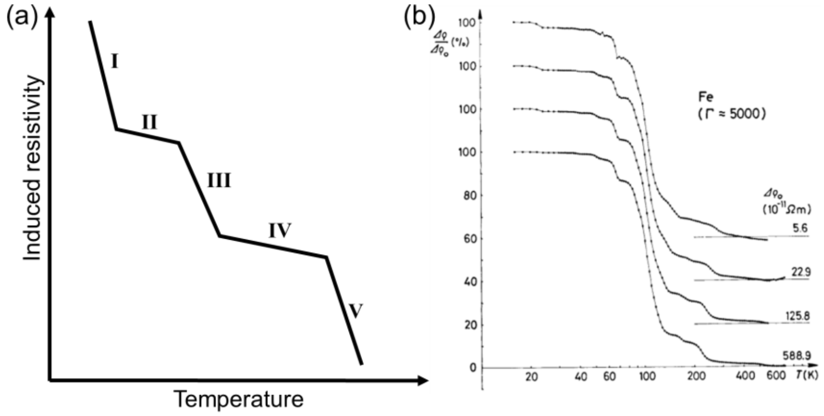

Fig. 1.5. (a) Five defect recovery stages in an ideal case. (b) Defect recovery of high purity iron with different carbon concentrations (Reprinted with permission from [34]).

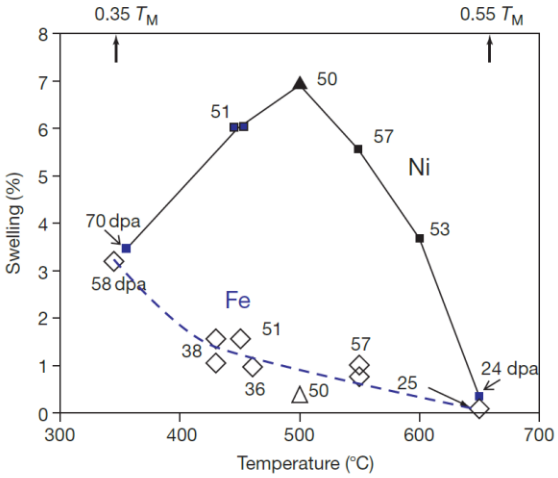

Fig. 1.6. Temperature-dependent void swelling behavior in Fe and Ni (Reprinted from [36] with permission from Elsevier).

Among the five stages, two regimes are of great importance for the study of irradiation damage. In one regime the irradiation temperature T is located between Stage III and Stage V (Stage III < T < Stage V). In this regime, both vacancies and SIAs are mobile, and the evolutions of defect clusters are very complicated. In FCC metals, the predominant features in this regime are dislocation loops (vacancy and interstitial type) and SFTs. Especially, for FCC metals with medium-to-high atomic numbers, most of the vacancies are bundled in sessile vacancy clusters, such as SFTs and loops that are created directly during energetic displacement cascade under neutron or heavy ion irradiation. As a result, most of the dislocation loops formed at this temperature regime are interstitial in nature. Void swelling is strongly suppressed. In BCC metals, since SFTs are difficult to form, the major defects are dislocation loops (vacancy and interstitial type) and voids. Since a cascade in BCC structures creates only small amount of sessile defect cluster, the formation of vacancy loops and void swelling are pronounced. However, void swelling is typically very limited, < 1%, at this temperature regime due to the high probability of interaction between vacancies and SIA clusters [5, 37]. Another decisive temperature regime is T ≥ Stage V. Since sessile vacancy clusters, such as SFTs, are thermally unstable at this regime, the primary defect types are dislocation loops (vacancy and interstitial type), dislocation networks and cavities. The most important difference from lower temperature regimes is the appearance of significant void swelling. For many metallic materials, the peak swelling temperature happens around Stage V. The swelling will be less pronounced if the temperature becomes very high. Fig. 1.6 shows the temperature-dependent void swelling behavior in Fe and Ni [36]. More details for void swelling in FCC, BCC and HCP metals are discussed in the following **Chapter 1.2.3**.

1.2.2.2 Role of SFE

1.2.2.2.1 Overview of SFE

A stacking fault will be created if the normal stacking sequence of atomic planes in a crystal is interrupted. This stacking fault carries a certain energy named the stacking fault energy (SFE), γ, which is a material property. In general, SFE is affected by several major factors, including bonding energy, alloying elements and their concentrations, electron-to-atom ratio (*e/a*), atomic radius, and so on [38]. Generally speaking, the larger the metallic bonding energy, the more difficult the crystal will be to form stacking faults [39]. The alloying element effect and *e/a* ratio effect are briefly discussed below.

Alloying elements. It has long been established that the addition of alloying elements significantly lowers the SFE of most metals. The form of the variation with B-group solutes in all cases follows the pattern established in the earliest studies in that SFE decreases with increasing solute concentration [40, 41]. Liu and Gallagher have expressed the relationships between stacking fault probability (α), SFE (γ), and alloying concentration in binary alloy systems through the following equations [41],

$$\ln^{\alpha} = \ln^{\alpha_0} + K_{\alpha}[C/(1+C)]\ , \qquad (1.1)$$

$$\ln^{\gamma} = \ln^{\gamma_0} + K_{\gamma}[C/(1+C)]^2\ , \qquad (1.2)$$

where α_0 and γ_0 are stacking fault probability and SFE, respectively, for pure metals. K_{α} and K_{γ} are the experimental constants. $C = X/X^*$, where X (at%) is the concentration of the alloying element, and X^* (at%) is the solubility limit at either the peritectic or the eutectic temperature. Note that, if a system that exhibits complete mutual solubility, such as Ag-Au, it cannot be analyzed through the above equations because the solubility limit X^* in such systems cannot be properly established.

K_{α} is usually within the range of 6.2 ± 0.5 for many reported transition elements with cubic structures, such as Al and Sn, when alloying with Ag [40, 41]. K_{α} is normally smaller with the alloying elements exhibit hexagonal close-packed (HCP) structure, such as Mg and Zn. Clearly, adding alloying elements will increase the stacking fault probability α. K_{γ} in general is a negative value for cubic-structure elements. For HCP systems, K_{γ} is larger, and in some cases, becomes positive. Therefore, SFE in Eq. (2) decreases with adding alloying elements. For a brief summary, Eq. (1) and (2) show that the stacking fault probability will be increased and, in many cases, SFE will be decreased by addling alloying elements. As a results, the probability of twinning increases.

Electron-to-atom ratio, e/a. There are many physical properties that are closely related to *e/a* ratio, such as elastic constants, flow stress, activation energy for diffusion, stress corrosion cracking and SFE [42]. In close-packed systems, it is the dissociation of a dislocation into two partials that creates a stacking fault. However, the formation of stacking faults is not simple especially in B-group elements. The competition between energetically comparable structures decides the existence of stacking faults. Generally speaking, the number of d electrons per atom is decisive to the favorable structures, such as stacking faults, compared to s electrons. The SFE is, therefore, expected to be *e/a*-dependent. In an alloy, assume the valences of the solute and solvent atoms are Z_1 and Z_2, respectively, then the *e/a* ratio can be calculated as $e/a = (1 - x)Z_1 + Z_2 = 1 + x\Delta Z$ [40], where x is the solute content in at%. Many previous studies have confirmed that the larger the *e/a* ratio is, the lower the SFE and the higher the stacking fault probability will be. For instance, Gallagher has shown that the SFE value of Ag alloys, such as AgAl, AgZn, and AgSn, decreases with increasing *e/a* ratio [40]. Similar results have been reported by Thornton et al. and other researchers in both Cu-based and Ag-based alloys [38, 42, 43]. It is worth mentioning that *e/a* ratio is used as a normalizing parameter in the study of SFE. If the data of SFE or stacking fault probability is plotted as a function of the concentration of an alloying element, both γ and α will show a large scattering from one alloy species to another.

1.2.2.2.2 The importance of SFE in irradiation study

SFE is an important parameter in the investigation of irradiation damage in metallic materials. During collision cascade, the microstructural evolution is significantly determined by the ratio of glissile SIA clusters created [44-46]. The ratio is typically very high in BCC metals, and the ratio is very low in FCC metals with low SFE because sessile clusters can be stabilized in the form of Frank loops. Therefore, a high-density of Frank loops may be created under irradiation in low SFE metals, and this will increase the number of residual defects [47]. As a result, FCC metals with low SFE appear more irradiation vulnerable.

The stable configuration of defects is also affected by the SFE. For instance, SFTs are frequently observed in FCC metals and alloys with low SFE, such as Ag, Au, Cu and stainless steels [8, 11, 48-52]. The formation mechanisms of SFTs have been widely studied. In the classical Silcox-Hirsch model, SFTs originate from Frank loops by gliding of Shockley partials and form stair-rod dislocation (1/6 <110>). The energy difference between a perfect loop and a faulted loop (Frank loop) is

$$\Delta E = \pi r_L^2 \gamma_{SFE} - \frac{1}{3}\left(\frac{2-\nu}{2(1-\nu)}\right)\mu b^2 r_L \ln\left[\frac{4r_L}{r_c} - 2\right] \qquad (1.3)$$

where ΔE is the energy difference, μ is the shear modulus, b is the burger's vector, r_L is the radius of the faulted area, ν is the passion ratio, r_c is the core size of the dislocation and SFE is indicated by γ_{SFE}. Previous calculations showed that vacancy clusters in FCC metals can be either a stacking fault tetrahedra (SFTs), Frank loops, voids or perfect loops depending on the SFE and other factors [6, 53]. According to the above equation, if $\Delta E <$ 0, faulted loops is more favorable. Therefore, SFTs are very likely to be created during irradiation if SFE is low.

The formation of SFTs during irradiation poses a major challenge on nuclear reactor structural materials because SFTs are very stable, and the removal of them requires high-temperature annealing, annihilation by interstitials or mobile dislocations. Also, the interactions between mobile dislocations and SFTs can modify the mechanical properties, such as strengthening, plastic instability and so on [54-56]. Austenitic stainless steel, as a widely used structural material in current nuclear reactors, has FCC like structure with very low SFE. So, it is critical to clarify the characteristic features of the defect formation process in such as austenitic stainless steel. Clearly, the investigation of the effect of the SFE on damage accumulation during irradiation is nontrivial.

1.2.3 Irradiation damages in metals with different crystal structure

1.2.3.1 Irradiation-induced defects in metals with face-centered cubic (FCC) structures

FCC metals, such as austenitic stainless steels, Ni alloys and Cu, are widely used as structural materials in nuclear reactors, and the related theoretic calculation, experimental as well as computer simulation studies have been extensively performed [2, 36, 57-59]. Materials with monolithic structures, such as Cu, Al, Au, etc., are normally used as model systems to demonstrate the irradiation response in FCC metals. In general, there are two benefits in the investigation of these monolithic metals. First, comparison studies can be carried out for materials with different SFEs. The SFE is an important parameter, as briefly described in the previous chapter, that could be critical for the improvement of irradiation resistance. Second, defect behavior during irradiation is relatively straightforward in those monolithic systems because the effect from chemistry, such as second phases, can be excluded.

1.2.3.1.1 The formation and migration energies of point defects in FCC metals

Upon exposure to high-energy particle bombardments, a tremendous number of defects, including point defects and small clusters, are produced in the materials [12, 36]. Although the defects created by the lower-energy recoils tend to recombine immediately after the displacements cascades, the majority of defects produced by higher-energy recoils remain. Those stable defects will eventually evolve into large defect clusters. Fig. 1.7 shows possible positions of interstitials, including 3 types of dumbbells, a crowdion, a tetrahedral and an octahedral position in FCC metals. Table 1.1 summarizes point defect formation and migration energy as well as the variation of free volume induced by these point defects.

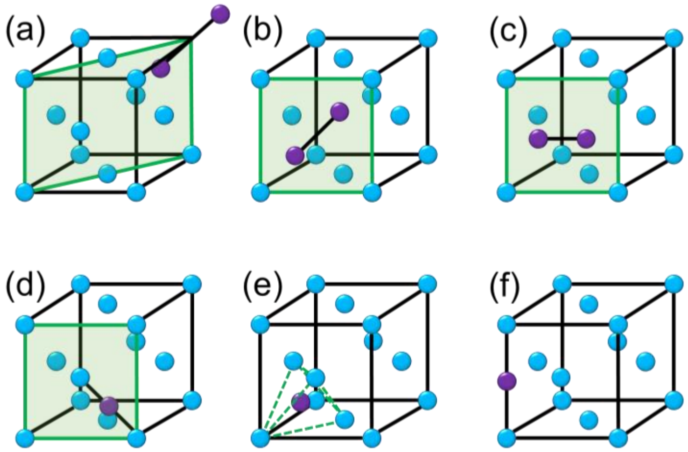

Fig. 1.7. Interstitial sites in FCC metals. (a) <111> dumbbell; (b) <110> dumbbell; (c) <100> dumbbell; (d) crowdion; (e) tetrahedral; and (f) octahedral position.

Table 1.1. The formation and migration energies of vacancies and interstitials.

$\boldsymbol{E_V^F}$- vacancy formation energy; $\boldsymbol{E_I^F}$- interstitial formation energy;
$\boldsymbol{E_V^M}$- vacancy migration energy; $\boldsymbol{E_I^M}$- interstitial migration energy
$\boldsymbol{V_{SIA}^{rel}}$ - relaxation volume for self-interstitials

	E_V^F (eV)	**ref**	**E_V^M (eV)**	**ref**	**E_I^F (eV) - dumbbell (<100>, <110>, <111>)**	**E_I^F (eV) - crow/ tetra/ octa**	**ref**
Cu	1.3 – 1.31	[60]			2.75		[60]
	1.28 – 1.3	[61]	0.72	[61]	2.76		[61]
	1.28	[62]	0.71	[62]			
			1.19	[63]			
			0.67 – 0.72	[64]			
	0.92 – 1.31	[35]	0.67 – 0.76	[35]			
	1.33	[65]					
	1.28	[66]					
	1.28	[67]					
					2.17 – 4.92	2.44 – 4.77	[68]
	1.18 – 1.31	[69]			2.47 – 3.39	3.4 – 5.46	[69]
	1.42	[70]	0.82	[70]	2.61		[70]
	1.38	[71]					
	1.30 – 1.31	[72]					
	1.27	[73]	0.8	[73]	2.2		[73]
Ag	1.1	[60]			2.59		[60]
	0.97 – 1.1	[61]	0.83	[61]	3.92		[61]
	1.13	[62]	0.66	[62]			
			0.65	[63]			
			0.67	[64]			
	1.06 – 1.19	[35]	0.55 – 0.88	[35]			

Table 1.1. Continued

	E_V^F (eV)	**ref**	**E_V^M (eV)**	**ref**	**E_I^F (eV) - dumbbell (<100>, <110>, <111>)**	**E_I^F (eV) - crow/ tetra/ octa**	**ref**	**E_I^M (eV)**	**V_{SIA}^{rel} (Ω)**
Ag	1.24	[65]							
	1.11	[66]							
	1.11	[67]							
					2.10 – 4.50	3.05 – 6.30	[68]		
	1.02 – 1.16	[69]			2.24 – 3.09	3.04 – 4.86	[69]		
	1.37	[70]	0.54	[70]	2.20		[70]		
	1.10	[71]							
	1.10 – 1.16	[72]							
Au	0.86 – 0.9	[60]			2.54		[60]	0.06	1.80
	1.03 – 0.9	[61]	0.71	[61]	2.46		[61]		
	0.95	[62]	0.83	[62]					
			0.59	[63]					
			0.77 – 0.85	[64]					
	0.89 – 1.02	[35]	0.62 – 0.94	[35]					
	0.82	[65]							
	0.89	[66]							
	0.93	[67]			2.24 – 3.72	2.73 – 5.54	[68]		
	0.92 – 0.97	[69]			2.15 – 2.99	2.91 – 4.17	[69]		
	2.75	[70]	0.71	[70]	3.81		[70]		
	0.97	[71]							
	0.94 – 0.97	[72]							

Table 1.1. Continued

	E_V^F (eV)	**ref**	**E_V^M (eV)**	**ref**	**E_I^F (eV) - dumbbell (<100>, <110>, <111>)**	**E_I^F (eV) - crow/ tetra/ octa**	**ref**	**E_I^M (eV)**	**V_{SIA}^{rel} (Ω)**
Ni	1.6 – 1.62	[60]			4.61		[60]	0.14	1.98
	1.6 – 1.63	[61]	1.08	[61]	5.05		[61]		
			1.07	[63]					
			1.04 – 1.25	[64]					
	1.45 – 1.8	[35]	1.03 – 1.3	[35]					
	1.77	[65]							
	1.78	[66]							
	1.79	[67]							
	1.49	[74]	1.32	[74]	4.08		[74]		
	1.72	[71]							
	1.6 – 1.7	[72]							
Pd	1.38 – 1.4	[60]			3.61		[60]	0.08	1.44
	1.4 – 1.44	[61]	0.82	[61]	3.42		[61]		
			1.42	[63]					
			1.21	[64]					
	1.70 – 1.85	[35]	1.03	[35]					
	1.65	[65]							
	1.85	[66]							
Pt	1.48 – 1.5	[60]			4.67		[60]	0.063-0.07	2.05
	1.5 – 1.68	[61]	0.85	[61]	3.51		[61]		
	1.51	[62]	1.43	[62]					
			1.35	[63]					
			1.36 – 1.46	[64]					

Table 1.1. Continued

	E_V^F (eV)	**ref**	**E_V^M (eV)**	**ref**	**E_I^F (eV) - dumbbell (<100>, <110>, <111>)**	**E_I^F (eV) - crow/ tetra/ octa**	**ref**	**E_I^M (eV)**	**V_{SIA}^{rel} (Ω)**
Pt	1.15 – 1.6	[35]	1.13 – 1.48	[35]					
	1.45	[65]							
	1.32	[66]							
	1.35	[67]							
	1.51	[73]	1.43	[73]	3.5		[73]		
Al	0.7	[60]			1.93		[60]	-	2.03
	0.67	[62]	0.62	[62]					
			1.17	[63]					
			0.58 - 062	[64]					
	0.62 – 0.77	[35]	0.55 – 0.65	[35]					
	0.67	[67]							
					1.63 – 4.03	2.44 – 4.77	[68]		
	0.66	[70]	0.41	[70]	2.33		[70]		
	0.65	[71]							
	0.66	[72]							
	0.66	[73]	0.62	[73]	3.2		[73]		

Several important conclusions for FCC metals can be obtained from Table 1.1:

1. Vacancy migration energy varies between 0.41 to 1.48 eV, while interstitial migration energy is significantly smaller, 0.06 - 0.14 eV.
2. Vacancy formation energy varies between 0.62 to 1.85 eV, which is much smaller than interstitial formation energy, 1.63 – 6.30 eV.

3. Migration energy of both vacancies and interstitials is less than their formation energy.

The above conclusions indicate an important fact that interstitials exhibit higher mobility than vacancies. Vacancies are only mobile at elevated temperatures. The consequent result is that defect accumulation is closely related to irradiation temperature. A good example is void swelling in FCC metals. Void swelling is sensitive to irradiation temperature and usually not expected to occur at low temperature because the mobility of vacancies is low, and it is also not expected to happen at very high temperatures due to the strong influence of thermodynamic equilibrium processes [36]. Void swelling will be further discussed in **Chapter 1.4.4**. The volume of a vacancy, V_V^F, is in general less than the volume of an individual atom (Ω) due to the relaxation of atoms. The difference between V_V^F and Ω is then named as the relaxation volume, V_V^{rel}, and is typically ~ 0.25Ω for FCC metals [75]. The relaxation volume, V_V^{rel}, and the activation volume for self-diffusion, V_V^{SD}, of vacancies in FCC metals can be calculated by:

$$V_V^{rel} = \Omega - V_V^F \qquad (1.4)$$

$$V_V^{SD} = V_V^F + V_V^M \qquad (1.5)$$

where V_V^F, V_V^M are respective activation volume for formation and migration of vacancies. As the vacancy migration volume (V_V^M) is typically 0.1 Ω, the activation volume for self-diffusion (V_V^{SD}) of FCC metals is ~ 0.85 Ω.

When an interstitial is inserted in an FCC lattice, the dilatational expansion volume, V_{SIA}^{F},is ~ 1.1 Ω, and the relaxation volume for self-interstitials (V_{SIA}^{rel}) can be estimated by:

$$V_{SIA}^{rel} = V_{SIA}^{F} + \delta V \qquad (1.6)$$

where δV is the volume expansion arising from the non-linear elastic strain. As shown in Table 1.1, V_{SIA}^{rel} is typically ~ 2 Ω.

1.2.3.1.2 Major types of irradiation-induced defects in FCC metals

The formation of defect clusters is due to the agglomeration of point defects. In general, there are four types of microstructures for irradiation-induced vacancies and interstitials, including two 2D structures, faulted and perfect dislocation loops, which occur for both vacancies and interstitials, and two 3D structures, stacking fault tetrahedra (SFTs) and cavities, which occur only for vacancies [36]. For FCC metals with low-to-intermediate SFE, such as Ag, Au and Cu, faulted dislocation loops with Burgers vector (*b*) of a/3 <111> will be created at the beginning of the irradiation process. Those loops are either interstitial-type or vacancy-type in nature, and they are sessile (immobile) loops. During irradiation, faulted loops experience unfaulting process that Shockley partials (*b* = a/6 <112>) sweep across the surface of faulted loops and turn them into perfect loops with *b* = a/2 <110>. After unfaulting, perfect loops may gradually change their habit plane from {111} to {110} through diffusion, and finally, perfect loops become glissile (mobile). Several examples in Fig. 1.8 show the irradiation-induced damage in several FCC metals, Cu, Ni and Al, to a similar dose level by different energetic particles, including Kr heavy ions (1 MeV), neutron (> 0.1 MeV) and electrons (1 MeV) [76-82]. Several distinct phenomena can be observed:

(1) A significant number of small dislocation loops are formed in all cases under heavy ion irradiation at 273 K [77, 78, 83].

(2) Neutron irradiation at a higher temperature, 455K, produces a similar defect morphology but with somewhat lower defect density [79-81].

(3) Cu exhibits greater defect density compared to Al under both heavy ion and neutron irradiation due to the lower SFE.

(4) Electrons introduce significantly large faulted dislocation loops (interstitial-type) on {111} plane [82].

SFTs are only observed in close-packed cubic structures, i.e. FCC structures. SFTs are known to have distinct triangular shapes (complete or truncated) and are considered to be the most energetically favorable configuration compared to faulted and perfect loops when defect cluster size is small [6]. The formation of SFTs relays on three different mechanisms. (1) Directly from the vacancy rich cascade during energetic displacement [36, 84, 85]. (2) The classic Silcox-Hirsch mechanism where SFTs are formed from equilateral triangular vacancy Frank loops by dissociation [86, 87]. However, it is less likely that SFTs are created from equilateral triangular vacancy Frank loops in the real irradiation cascade. Therefore, another mechanism has been proposed that is (3) from the scalene hexagonal vacancy Frank loops [88]. Some examples of SFTs in Ag [89] and Au [78] irradiated by 1 MeV Kr ions after 1 dpa are shown in Fig. 1.9.

1.2.3.2 Irradiation-induced defects in body-centered cubic (BCC) and hexagonal close-packed (HCP) metals

Many of the BCC metals, such as ferritic steels, ferritic-martensitic (F-M) steel and W alloys, are important structural materials that are currently used or proposed as candidates in current and future nuclear reactors [128-131]. Besides, Point defect production is normally different between cubic systems (FCC/BCC) and HCP systems [18, 90-93]. The materials with HCP structures, such as Zr-based alloys, are critical structural materials that used in the present light water nuclear reactors. Therefore, there is a large driving force on the exploration of HCP metals.

1.2.3.2.1 Major types of irradiation-induced defects in BCC metals

Compared to FCC metals, the SFE of BCC metals is generally very high, and therefore, faulted dislocation loops, which have higher energy than perfect loops, are not stable although they have been observed in several studies [82, 92, 94]. Perfect loops in BCC metals may habit on two different planes, {110} with *b* = a/2<111> and {100} with *b* = a<100>, while faulted loops typically only locate on {110} planes with *b* = a/2<110>. Like dislocation loops in FCC metals, perfect loops are mobile (glissile) and faulted loops are immobile (sessile) in BCC metals. Fig. 1.10 shows various types of dislocation loops in BCC Fe, Mo and W irradiated by heavy ions, neutrons and electron [59, 82, 95-102]. It can be seen that the morphology of defects in terms of size and density is similar for heavy ion and neutron irradiated materials, whereas electron bombardment creates much larger dislocation loops. Such phenomena have also been observed in FCC metals as shown in

Fig. 1.8. Moreover, since SFTs are only observed in close-packed cubic structures, they are not expected in BCC metals.

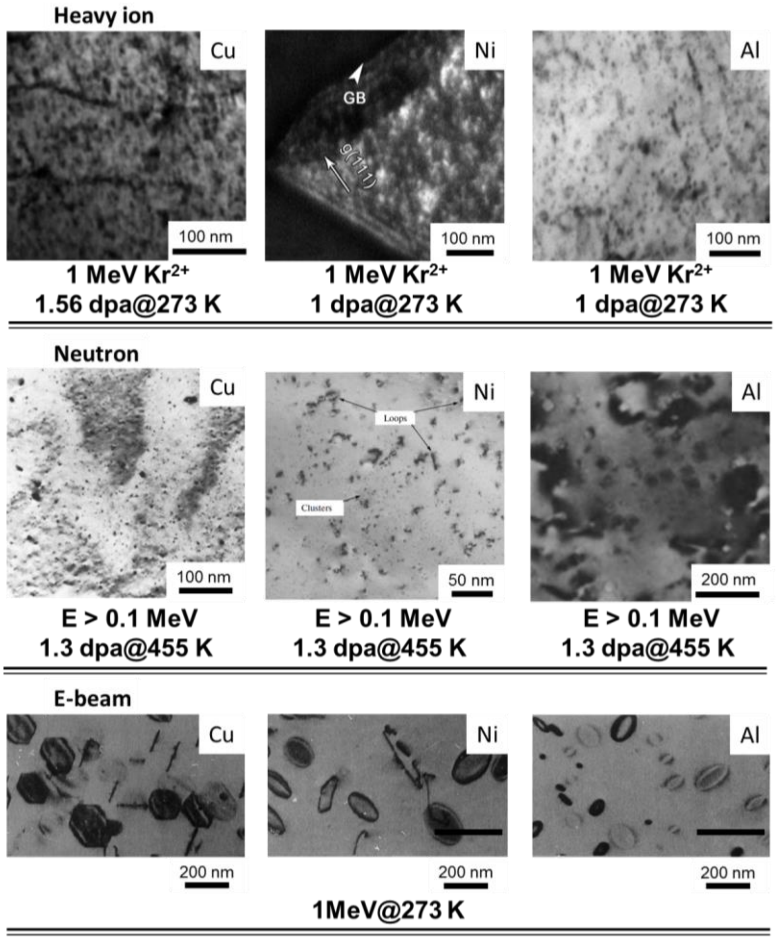

Fig. 1.8. TEM micrographs showing neutron, heavy ion, neutron and electron beam irradiated FCC metals, Cu, Ni and Al. Under heavy Kr ion irradiation at 273 K, a large number of small interstitial dislocation loops are generated in Cu (Reprinted from [83]), Ni (Reprinted from [77] with permission from Springer) and Al. Neutron irradiation at 455 K to a similar level of the dose appears to generate defects with similar morphology (small loops) but with somewhat lower defect density in Cu (Reprinted from [79] with permission from Elsevier), Ni (Reprinted from [80] with permission from Springer) and Al (Reprinted from [81]). Room temperature electron (1 MeV) irradiation introduce large interstitial loops, which are mostly faulted loops on {111} planes (Reprinted from [82] with permission from Elsevier).

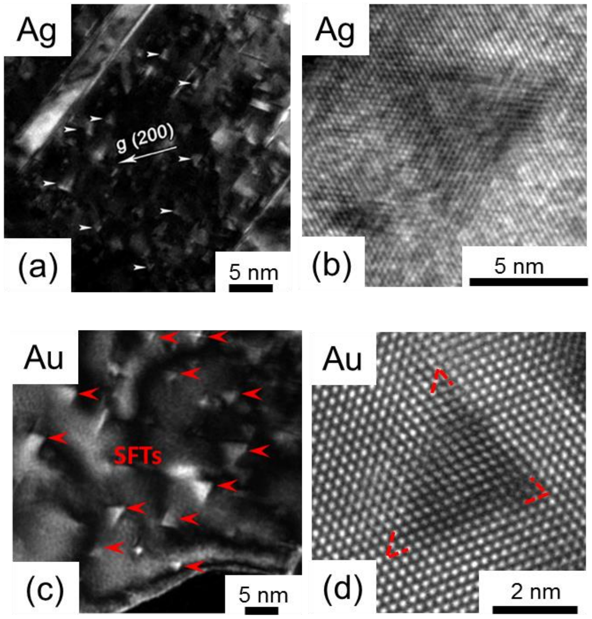

Fig. 1.9. SFTs in irradiated FCC metals. (a-b) Dark field TEM and HRTEM micrographs of SFTs in irradiated Ag films (1 MeV Kr ions/1 dpa/RT) (Reprinted with permission from Macmillan Publishers Ltd [89]). (c-d) Dark field TEM and atomic resolution TEM micrographs of SFTs in irradiated Au films (1 MeV Kr ions/1 dpa/RT) (Reprinted from [78]).

1.2.3.2.2 Major types of irradiation-induced defects in HCP metals

As mentioned above, point defect production is normally different between cubic systems (FCC/BCC) and HCP systems. In the former cases, point defects, such as self-interstitials (SIAs) and vacancies, diffuse isotropically whereas anisotropic diffusion often occurs in the later cases due to their crystallographic anisotropy [103-105]. For instance, it has been shown that the ratio of prism plane to basal plane defects produced by electron irradiation strongly depends on the foil orientation in pure Mg [106]. The major type of irradiation-induced defects in HCP metals are vacancy clusters, including vacancy loops

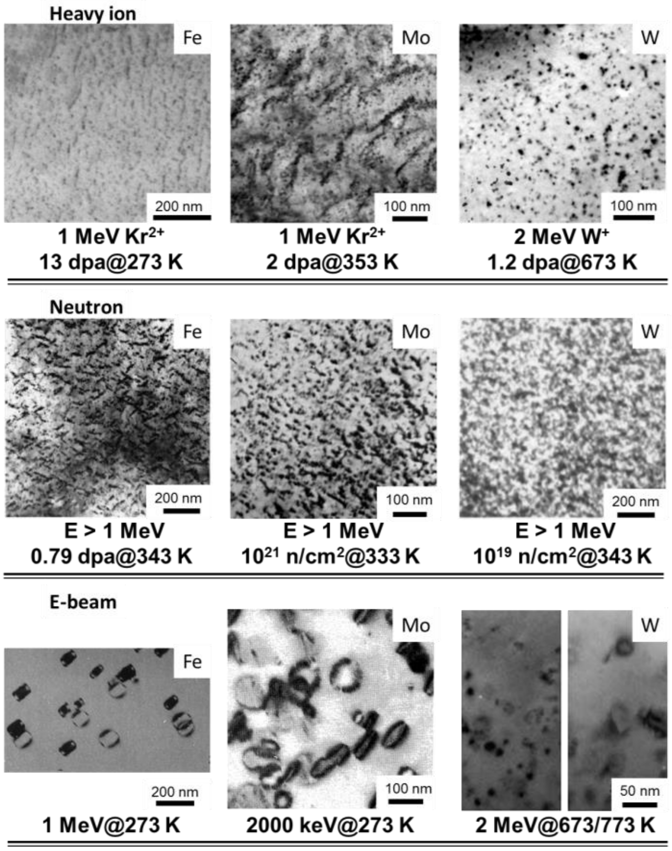

Fig. 1.10. Compilation of TEM micrographs showing irradiation damage in Fe, Mo and W induced by heavy ions, neutrons and electrons. The morphology of defects in terms of size and density is similar for heavy ion and neutron irradiated materials, whereas electron introduces much larger dislocation loops (Heavy ion irradiated Fe, Mo and W are reprinted from [95] with permission from Elsevier, [96] and [97] with permission from Elsevier, respectively. Neutron irradiated Fe, Mo and W are reprinted from [59] with permission from Elsevier, [98] and [100], respectively. E-beam irradiated Fe, Mo and W are reprinted from [82] with permission from Elsevier, [101] and [102] with permission from Elsevier, respectively.).

and voids, and interstitial loops. Perfect interstitial loop habit on $\{10\bar{1}0\}$ plane with b = a/3 $<11\bar{2}0>$, and faulted interstitial loops resides on (0001) plane with b = a/6 $<20\bar{2}3>$ or c/2 [0001]. Perfect vacancy loops are observed on $\{10\bar{1}0\}$ prismatic planes with b = a/3

$<11\bar{2}0>$, and faulted vacancy loops typically locate on (0001) basal planes with b = a/6 $<20\bar{2}3>$ [91, 92, 107].

Furthermore, it is generally adopted that the evolution of irradiation-induced defects has a strong correlation with (1) c/a ratio and (2) impurities [90, 91, 108]. For HCP metals with high purity, nucleation of basal plane loops takes place when c/a ratio is greater than the ideal value (1.633) while prism plane loops form with c/a ratio less than the ideal value. The reason is that basal planes are the most closely packed planes when c/a > 1.633, while prismatic planes become more densely packed when c/a < 1.633. Exceptions have been found in both experiment and simulations. For instance, basal plane loops have been observed in Mg [109], Zr [110, 111], Ti [112] (c/a ratio < 1.633 for these metals). The impurity atoms also play a critical role in determining the most stable configurations as shown in Fig. 1.11. When purity is low, the formation of basal plane loops is dominating even when c/a ratio is less than 1.633, such as Mg and Zr [90, 113-115]. Compared to Zr, Mg is particularly sensitive to impurities due to its c/a ratio (1.623) that is close to the ideal value (1.633) [90]. It remains unclear why the habit planes are dependent on impurities. One possible effect of impurities is the reduction of the SFE resulting in the formation of faulted basal plane dislocations [40]. However, Griffiths has suggested that the SFE may not necessarily important in determining the loop habit planes [90], so the effect of impurities on SFE may not be a major factor in controlling loop habit planes as the impurities may contribute to other factors, such as dislocation bias, lattice strain and anisotropic diffusion, which will in turn affect the loop habit planes. Notice that, in addition to impurities, other reasons, such as stresses in irradiated thin foils [116], also need to be taken into account.

Nonetheless, the damage induced by irradiation in the real world is far complex than that predicted by these rules. The void formation has been observed in most HCP metals, and a more detailed discussion is given in **Chapter 1.4.3**.

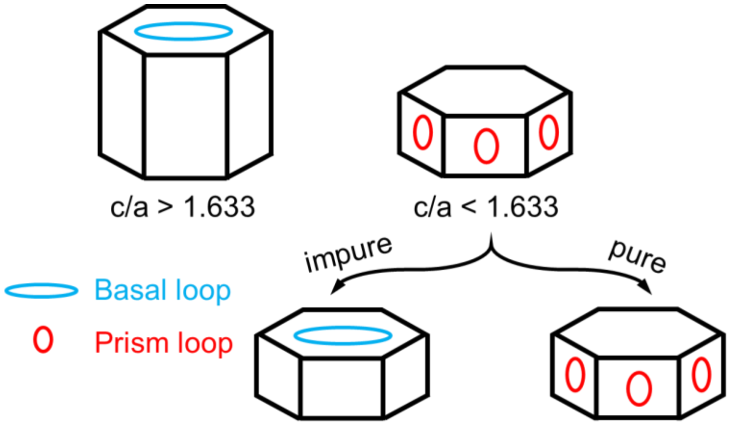

Fig. 1.11. Schematics showing the effects of c/a ratio on loop habit planes for pure HCP metals as well as the purity on loop habit planes for HCP metals with c/a < 1.633.

The majority of studies on HCP metals are on Zr and its alloys. Another relatively well-studied HCP metal is Mg. Fig. 1.12 shows irradiation-induced damage in Zr and Mg induced by heavy ions, neutron and electrons. Heavy ion irradiation induced c-component loops in Zr have been observed [117]. Neutron and electron irradiation induce both a-loops and c-loops in Zr [111]. For Mg under 1 MeV Kr ion irradiation [106], all the basal plane dislocation loops are interstitial in nature with b = a/6 <$20\bar{2}3$>, whereas prism plane dislocation loops can be either interstitial or vacancy in nature with b = a/3 <$11\bar{2}0$>. Neutron-irradiated Mg also exhibits a similar phenomenon compared to heavy ion irradiation as shown in both BCC and FCC metals. Dislocation networks form after neutron irradiation [118]. After electron irradiation, the formation of large loops is obvious. These loops are typically either a-type loops with b = a/3 <$11\bar{2}0$> or c-type loops with b = a/6 <$20\bar{2}3$> [91].

The nature of dislocation loops in FCC, BCC and HCP metals are very different. It is straightforward to imagine that since FCC and BCC are cubic systems, they must exhibit totally different defect types compared to the hexagonal system, HCP structure. However, even between FCC and BCC, since FCC is a close-packed system with well-defined slip systems, while there are no truly close-packed planes in the BCC structures, they also exhibit different types of defects. A summary of defect clusters in all three systems is given in Table 1.2.

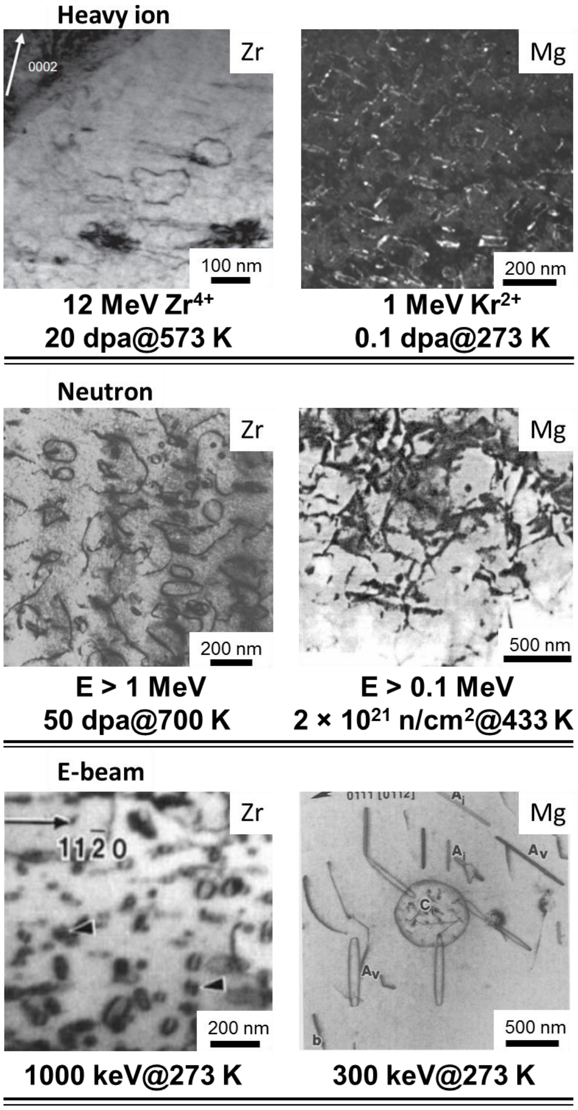

Fig. 1.12. TEM micrographs showing irradiation damage in HCP Zr and Mg irradiated by heavy ions, neutrons and electrons. Self-ion-irradiated Zr exhibits c-component loops (Reprinted from [117] with permission of Elsevier). Neutron-irradiated Zr showing a-loops and c-loops (Reprinted from [111] with permission of Elsevier). Electron irradiation of Zr induces a-loops and c-loops (Reprinted from [111] with permission of Elsevier). Basal Mg foil irradiated by Kr ions showing abundant prism loop with b = a/3 <11$\bar{2}$0> (Reprinted from [106] with permission of Elsevier). Neutron irradiation of Mg induces dislocation networks (Reprinted from [118] with permission of Taylor & Francis). Electron irradiation of Mg produces a-loops with b = a/3 <11$\bar{2}$0>, which are vacancy (A_v) or interstitial (A_i) in nature, and c-type interstitial loop (C_i) with b = a/6 <20$\bar{2}$3> (Reprinted from [91] with permission of Elsevier).

Table 1.2. Type of dislocations loops in FCC, BCC and HCP metals.

	Vacancy loops		**Interstitial loops**	
	Type	***b* and Habit plane**	**Type**	***b* and Habit plane**
FCC	Perfect loop	a/2 <110>{111} or a/2 < 110>{110}	Perfect loop	a/2 <110>{111} or a/2 < 110>{110}
	Faulted (Frank) loop	a/3 <111>{111}	Faulted (Frank) loop	a/3 <111>{111}
	SFT/ Voids			
BCC	Perfect loop	a/2 <111>{110} or a<100>{100}	Perfect loop	a/2 <111>{110} or a<100>{100}
	Faulted loop	a/2 <110>{100}		
HCP	Perfect loop	a/3 <11$\bar{2}$0>{10$\bar{1}$0} or a/3 <11$\bar{2}$3>{10$\bar{1}$1}	Perfect loop	a/3 <11$\bar{2}$0>{10$\bar{1}$0} or a/3 <11$\bar{2}$3>{10$\bar{1}$1}
	Faulted loop	a/6 <20$\bar{2}$3>{0001} or c/2 <0001>{0001}	Faulted loop	a/6 <20$\bar{2}$3>{0001} or c/2 <0001>{0001}
	Voids			

1.2.4 Irradiation-induced property degradation

There are several major property changes that are associated with irradiation-induced microstructure evolution [36]. These property changes are (1) irradiation-induced hardening, (2) irradiation-induced amorphization, (3) irradiation-induced segregation and precipitation, (4) irradiation-induced embrittlement, decrease in (5) thermal and (6) electrical conductivity, and (7) dimensional instabilities. A brief introduction of phenomena (1-5) is given in **Chapter 1.4.3.1**, and (7) in terms of irradiation-induced swelling is discussed separately in **Chapter 1.4.3.2**. Phenomenon (6) is not reviewed because it has less relation to the present studies.

1.2.4.1 Overview of key degradation phenomena in irradiated metals

1.2.4.1.1 Irradiation-induced hardening

Irradiation-induced hardening is largely due to the creation of high-density sessile defect clusters. During irradiation, point defects preferentially migrate to different sinks which results in an unbalanced point defect concentration. Those point defects will form large clusters, and the clustering event is predominately determined by the irradiation temperature. At low temperatures, $\leq 0.3\ T_M$ (T_M is the melting temperature), defect clusters, which originate from the clustering of irradiation-induced point defects, inhibits the movement of dislocation, and therefore, hardening and reduction in ductility and fracture toughness occur. The defect cluster densities decrease rapidly with increasing temperature above recovery Stage V, $> 0.5\ T_M$, and hardening becomes less pronounced. Irradiation-induced hardening can happen at very low doses, ≤ 0.1 dpa when temperatures are low, and tends to reach a plateau at ~ 10 dpa. Fig. 1.13 shows temperature-dependent defect cluster densities in neutron-irradiated Cu, austenitic stainless steel, and V–4Cr–4Ti (Fig. 1.13a) as well as the dose-dependent increase in yield strength for F-M steels (Fig. 1.13b), where the dashed lines are simply the guidance that indicates the tendency. Defect density decreases with the increase of temperature. The yield strength increases rapidly to ~ 10 dpa, and then, reaches to saturation thereafter.

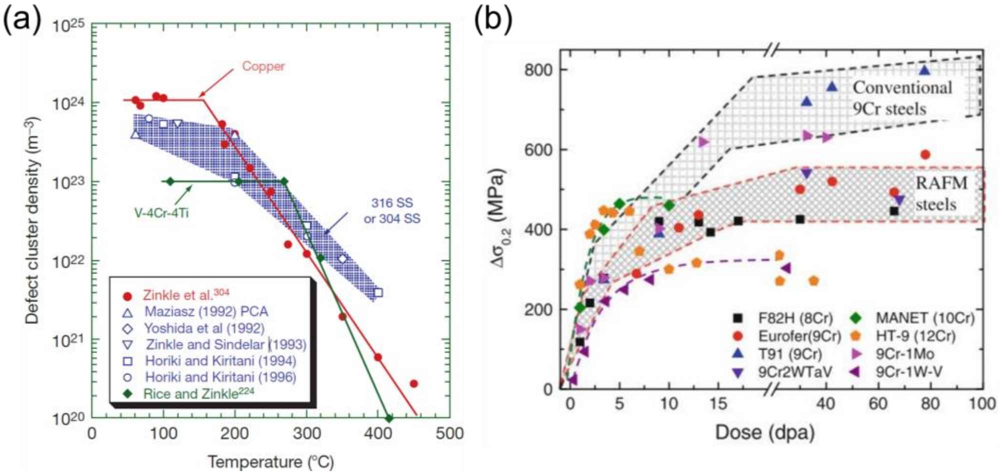

Fig. 1.13. (a) Temperature-dependent defect cluster densities in neutron-irradiated Cu, austenitic stainless steel, and V–4Cr–4Ti (Reprinted from [36] with permission of Elsevier), and (b) Yield strength versus dose at irradiation temperatures between 360 °C to 400 °C (Reprinted from [119] with permission of Springer).

1.2.4.1.2 Irradiation-induced amorphization

Irradiation-induced amorphization happens at very low temperatures, where interstitials and their clusters are immobile, and low dose, ~ 0.1 – 1 dpa. Irradiation-induced swelling is usually accompanied by such a phase transformation. Irradiation-induced amorphization is very sensitive to the temperature. If the irradiation temperature increases to a certain level when long-range migration of interstitial and their clusters occurs, the increase in free energy as interstitials generate will be reduced through the clustering event. The dose required to induce amorphization will increase drastically as the temperature increases. Finally, when the temperature is above a critical value, no amorphization could occur. Such a critical temperature increases with increasing PKA energy. Fig. 1.14 compares the effect of PKA energy on the temperature-dependent dose for complete amorphization in irradiated CuTi and SiC [36]. In both materials, for all types of irradiating particles, the critical dose for amorphization increases rapidly when the irradiation temperature exceeds a critical value.

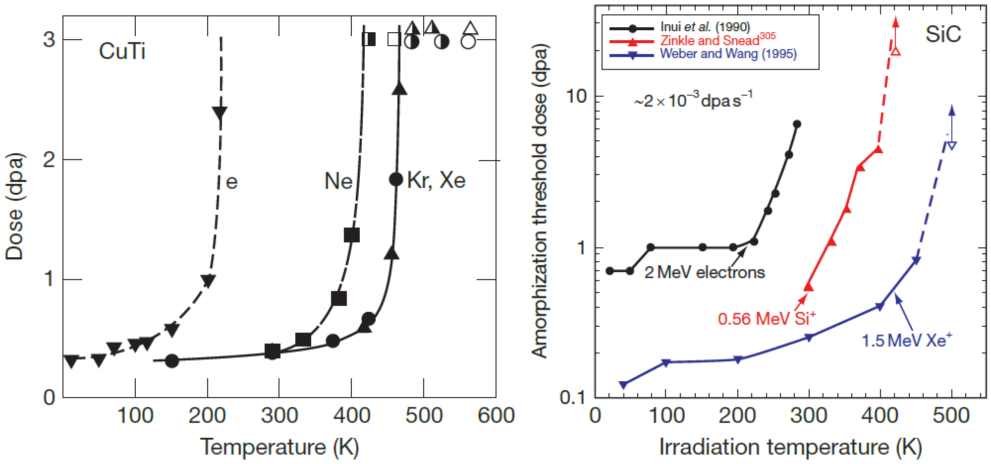

Fig. 1.14. Effect of irradiating particle with different PKA energies on the temperature-dependent dose for amorphization in irradiated CuTi and SiC. Filled symbols in the figures denote complete amorphization and open and half-open symbols denote no amorphization occur (Reprinted from [36] with permission of Elsevier).

1.2.4.1.3 Irradiation-induced segregation and precipitation

Irradiation-induced segregation and precipitation are widely observed in ferritic and austenitic steels after irradiation at elevated temperatures with doses > 10 dpa [120-123]. In reactor pressure vessel steels, the phenomena could happen at very low doses, 0.0001 – 0.01 dpa. The reason that causes the irradiation-induced precipitation is due to the migration of solute atoms to defect sinks at intermediate temperatures. The accumulation of solute atoms leads to the precipitation of new phases due to either the local enrichment or depletion of solute atoms. In general, three types of precipitation associated with segregation during irradiation are widely reported, including (1) irradiation-induced, (2) irradiation-enhanced and (3) irradiation-modified. In addition, irradiation-retarded precipitation has also been observed [36]. The irradiation-induced precipitation phenomenon can drastically modify the microstructures. For instance, the localized corrosion or stress corrosion cracking due to the enhanced susceptibility caused by solute segregation [124-126]. Another example is the swelling behavior of austenitic stainless steels can be either suppressed or enhanced [127, 128]. Fig. 1.15 shows the enlarged void formation in a Ti-modified austenitic steel after neutron irradiation at 500 °C to 11 dpa [123]. Large voids generate next to the irradiation-induced precipitate phase $Mn_6Ni_{16}Si_7$ (G phase), which is the bias sink for interstitials.

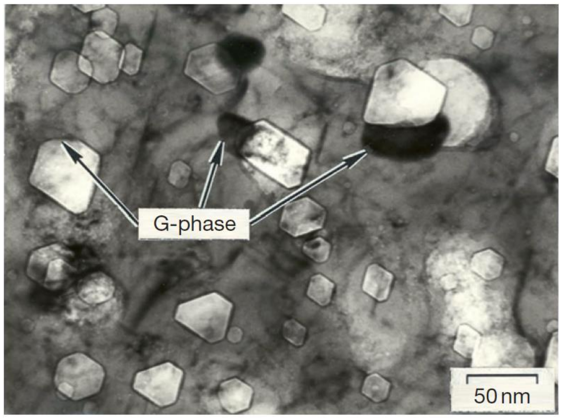

Fig. 1.15. Enlarged void formation in association with G phase ($Mn_6Ni_{16}Si_7$) precipitates in Ti-modified austenitic steel following mixed-spectrum fission reactor irradiation at 500 °C to 11 dpa (Reprinted from [123] with permission of Elsevier).

1.2.4.1.4 Irradiation-induced embrittlement

Irradiation-induced embrittlement usually happens at elevated temperatures, typically > 0.5 T_M, accompanied with He gas that is generated by transmutation reactions during irradiation. He migrates toward grain boundaries and forms large bubbles under the applied tensile stress during irradiation. If He bubbles transform into voids, intergranular fracture may be triggered due to the coalescence of cavities. Therefore, irradiation-induced embrittlement is closely related to void swelling. Fracture may occur when swelling reaches to a threshold which generally at less than 10% of swelling. Fig. 1.16a shows the formation of He bubbles in He ion irradiated FCC (Cu and Al) and BCC (Fe and W) metals [129-132], and Fig. 1.16b shows the tensile properties of Fe-15Cr-25Ni and Fe-15Cr-45Ni after irradiation in EBR-II to 12.5 dpa at 450 °C [133]. Clearly, irradiation leads to a drastic increase in strength and a reduction in ductility which is catastrophic for the safety of reactors.

1.2.4.2 Irradiation-induced dimensional instability – void swelling

Irradiation-induced dimensional instability includes several aspects, such as irradiation-induced creep, anisotropic growth, and void swelling. Void swelling describes a phenomenon that an increase in volume accompanied with the formation of voids within the materials after irradiation. Void swelling is broadly observed in neutron and heavy ion irradiated metals [134-138]. It is very difficult to accommodate a swelling level up to 5% through engineering design. When swelling is larger than 10%, the materials suffer from severe irradiation embrittlement. Clearly, there is a strong need for the design of swelling-resistant structural materials. Void formation occurs due to the preferential absorption of interstitials by biased defect sinks [139], and typically requires two conditions: a supersaturation of vacancies; and agglomeration of vacancies before being annihilated by interstitials or defect sinks. If more vacancies than interstitials arrive at void nuclei, voids will grow continuously.

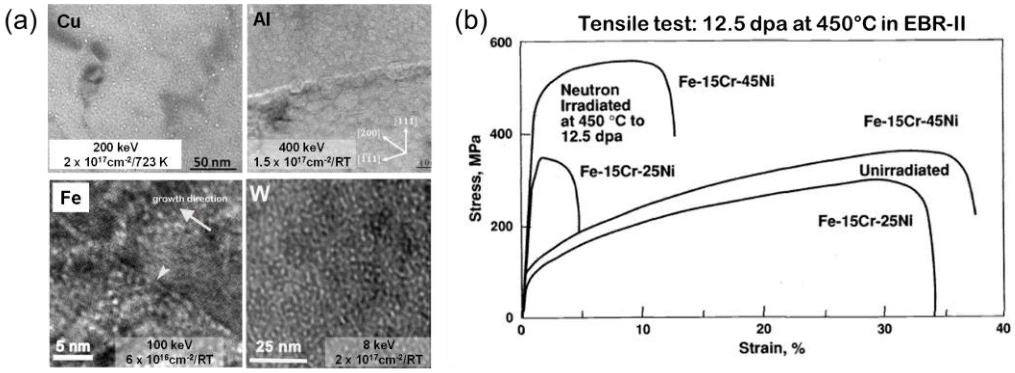

Fig. 1.16. (a) The formation of He bubbles in He ion irradiated metals with FCC (Cu and Al) and BCC (Fe and W) structures (He ion irradiated Cu, Al, Fe and W are Reprinted from [129], [130] with permission from Elsevier, [131] with permission from Elsevier and [132] with permission from Elsevier, respectively.). (b) Tensile properties of Fe-15Cr-25Ni and Fe-15Cr-45Ni before and after irradiation in EBR-II to 12.5 dpa at 450°C (Reprinted from [133] with permission of Elsevier).

Void swelling is sensitive to irradiation temperature, and it generally occurs at two different temperature stages, a very low-temperature stage and a high-temperature stage. Swelling at very low temperatures where point defects and their clusters are immobile generally refers to lattice parameter swelling. It is also called “point defect” or “defect cluster” swelling. At very low temperatures, irradiation-induced defects are frozen inside the materials as they are generated. The accumulation of such immobile defects causes the volumetric swelling. At high temperatures, such as Stage V for FCC and HCP metals, and Stage III for BCC metals, swelling occurs when irradiation-induced vacancy-type defects are mobile enough to combine into large clusters, and finally into voids. Besides, sessile vacancy clusters, such as SFTs, could also dissociate at such temperatures which will also contribute to the onset growth of voids. Void swelling is not expected to happen at low-temperature ranges, such as 0 – 200 °C, because of the poor mobility of point defect, and at very high-temperature ranges, such as > 500 °C, where defect recombination and absorption rather than agglomeration dominates. For most of the metals, void swelling is observed at the temperatures of 0.3 – 0.6 T_M. Fig. 1.17 shows the temperature-dependent void swelling behavior in Cu and Cu–B alloy after neutron irradiation to 1.1 dpa [36]. Swelling occurs between 200 °C to 500 °C in both cases, and Peak swelling happens at ~ 300 °C. Table 1.3 summarizes peak void swelling temperature ($\boldsymbol{T_S^P}$) for various metallic materials with FCC, BCC and HCP crystal structures. Peak swelling temperature in FCC metals is usually between 0.4 T_M to 0.45 T_M, which is higher than that in BCC metals, 0.3 T_M – 0.35 T_M. Peak swelling in HCP Zr happens at ~ 0.35 T_M. However, since the studies of peak swelling temperature in HCP metals remain scarce, no clear conclusion can be drawn for HCP metals.

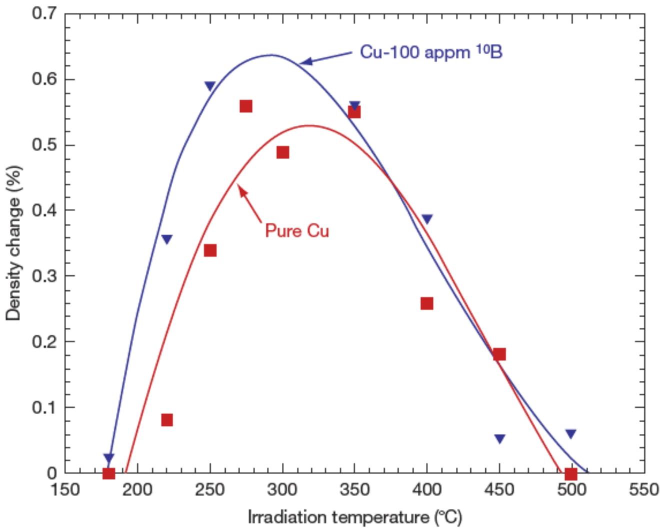

Fig. 1.17. Temperature-dependent void swelling behavior in Cu and Cu–B alloy after neutron irradiation to 1.1 dpa (Reprinted from [36] with permission of Elsevier).

Void swelling casts serious threats to the reactor structural materials [134, 140, 141]. For instance, in neutron irradiated austenitic stainless steels (FCC systems), the swelling rate can reach to 1%/dpa without evidence for saturation [142]. In many FCC metals, volume expansion can be as large as several tens of percent [140, 142, 143]. Fig. 1.18 summarizes the dose-dependent swelling behavior in 20% cold-worked Type 316 SS after neutron irradiation. The amount of void swelling is typically lower in BCC metals. For instance, the void swelling in many F-M steels is limited to 2% after the damage levels of 50 dpa or higher [142]. Fig. 1.19 lists several examples of void swelling in neutron irradiated metals with FCC [58, 144] and BCC [145, 146] crystal structures. Voids are typically spherical, such as He bubbles. Faceted voids with faces corresponding to low-index crystal planes are also observed. It should be noted that heavy ion irradiation typically generates a depth-dependent dose profile, and the size and density of voids, therefore, vary as a function of irradiation depth [147, 148].

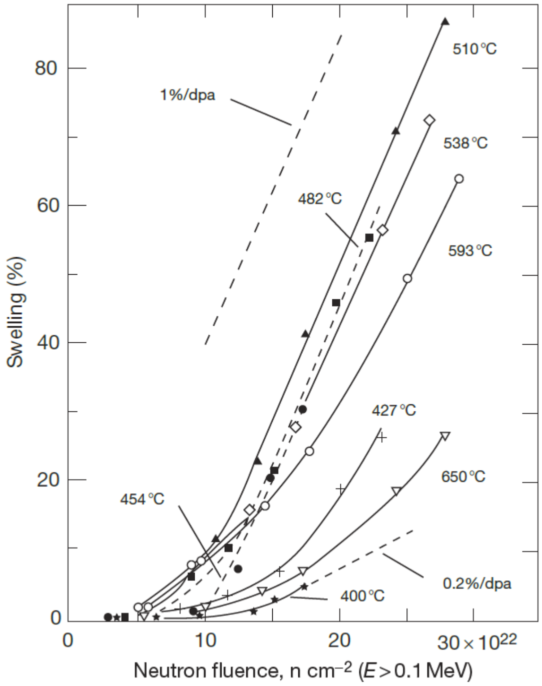

Fig. 1.18. Summary of dose-dependent swelling behavior in 20% cold-worked Type 316 austenitic stainless steel due to fast fission reactor irradiation (Reprinted from [36] with permission of Elsevier).

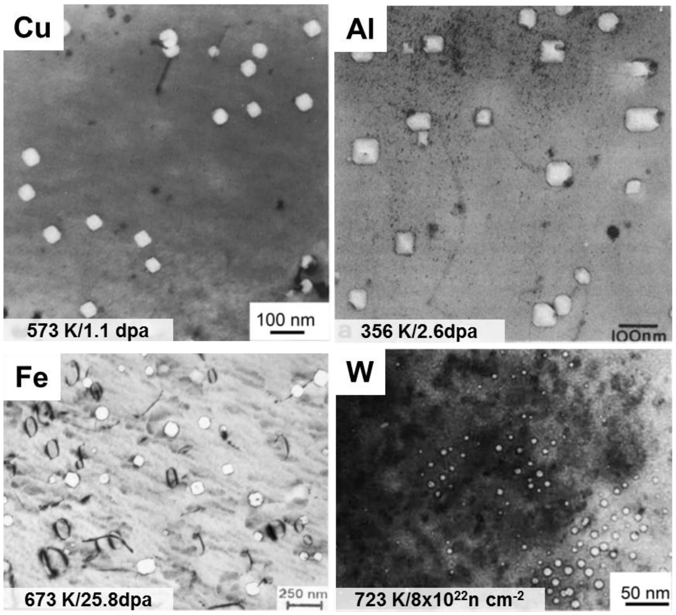

Fig. 1.19. Neutron irradiation induced void swelling in a variety of monolithic metals with FCC (Cu and Al) and BCC (Fe and W) crystal structure. Voids with different geometry, spherical or rectangular, are observed (Neutron irradiated Cu, Al, Fe and Fe are reprinted from [58], [144], [145] and [146], respectively, with permissions from Elsevier).

Void formation has been observed in most HCP metals, such as neutron irradiated Mg [149], both neutron and electron irradiated Zr [150-152], neutron irradiated Ti [149] and Re [153]. Voids in HCP metals are normally faceted along $\{10\bar{1}1\}$ and (0001) planes and often align in layers parallel to the basal plane, and in many cases, voids are reported to be faceted. For instance, voids formed in Marz-grade Zr during neutron irradiation in DFR at temperatures between 725 and 740 K were faceted along basal, prism, and pyramidal planes [90], were mostly near grain boundaries.

Table 1.3. Peak swelling temperature T_S^P in FCC, BCC and HCP metals

FCC	**T_S^P (K)**	**T_M (K)**	**T_S^P/T_M**	**ref**	**Irradiation source**
Al	423	933	0.45	[154]	Al^+ ions (1100 grade Al)
Al	No void	933		[155]	Al^+ ions Pure Al (< 0.1 appm impurities)
Al	300	933	0.32	[155]	Al^+ ions pre-injected with 10 ppm He
Ag	-	1235	-		-
Au	-	1337	-		-
Cu	600	1358	0.44	[58, 156]	Neutron
Ni	780	1728	0.45	[157]	Neutron
	873	1728	0.51	[158]	Ni^+ ions
Pd	-	1828	-		-
Pt	-	2041	-		-
BCC	**T_S^P (K)**	**T_M (K)**	**T_S^P/T_M**	**ref**	**Source**
Fe	630 – 780	1811	0.35 – 0.43	[140, 157]	Neutron
Mo	740 – 870	2896	0.26 – 0.3	[146, 159, 160]	Neutron
Mo	1173	2896	0.41	[161]	Ni^+ ions
Nb	1073 – 1273	2750	0.4 – 0.46	[161, 162]	Ni^+ ions
Ta	900	3290	0.27	[163]	Neutron
Ta	1400	3290	0.43	[164]	Cu^{2+} ions
V	630	2183	0.41	[160]	Neutron
V	973	2183	0.45	[165]	Cu^+ ions
W	1000	3695	0.27	[166]	Neutron
HCP	**T_S^P (K)**	**T_M (K)**	**T_S^P/T_M**	**ref**	**Source**
Zr	750	2128	0.35	[150]	Electron, pre-injected with 100 appm helium
Zr	700 - 740	2128	0.33 – 0.35	[151, 152]	Neutron

The development of swelling-resistant materials is manifested by an extensive investigation of void swelling in metals with FCC, BCC and HCP crystal structures. One method is to introduce a high density of point defect sinks that can suppress the formation and growth of voids. An enlightening thought has been proposed is the development of naturally porous structural materials in nuclear fuels to alleviate the fission gas accumulation with nanophases [167].

1.3 Overview of nanostructured materials

Nanostructured metallic materials (NMMs) are materials contain nanoscale features the characteristic length scale of which is on the order of 100 nm or less [168, 169]. NMMs synthesized by different methods exhibit various nanostructures that contain a significant volume fraction of interfaces, such as grain boundaries, twin boundaries, phase boundaries, etc. [76, 89, 170-179]. Fig. 1.20 shows four different nanostructures, including nanocrystalline (NC), Nanotwinned (NT), Nanoporous (NP) and nanolayers. Many properties, such mechanical, electrical, optical and magnetic, of NMMs are modified due to the existence of high-density interfaces, and therefore, NMMs have various applications. For instance, the strength of metallic nanolayers could approach 1/2 - 1/3 of the theoretical value [180, 181]. Nanotwinned (NT) metals containing high-density growth twins exhibit increased strength and ductility simultaneously [182]. Furthermore, nanoporous (NP) metals with a large surface-to-volume ratio may have superior irradiation tolerance [172, 183, 184].

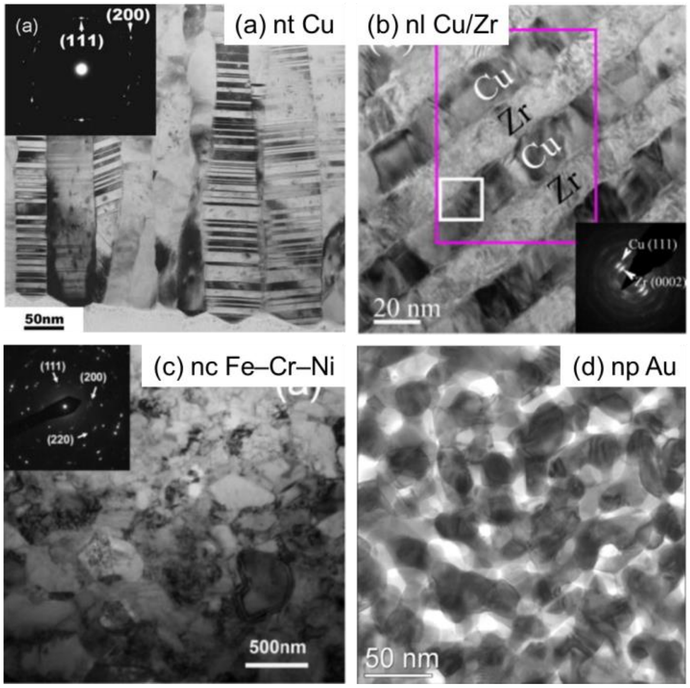

Fig. 1.20. Transmission electron microscopy (TEM) micrographs of (a) nanotwinned (NT) Cu (Reprinted from [185] with permission of AIP Publishing LLC), (b) Cu/Zr multilayers with individual layer thickness of 20 nm (Reprinted from [186] with permission of Elsevier), (c) nanocrystalline (NC) Fe-Cr-Ni alloy (Reprinted from [187] with permission of Elsevier), and (d) nanoporous (NP) Au (Reprinted from [188] with permission of AIP Publishing LLC).

1.4 Brief introduction of microstructure and mechanical properties of several nanostructured metallic materials

1.4.1 Nanolayered metals

Generally, metallic nanolayers (or multilayers) are synthesized by electrodeposition or physical vapor deposition (PVD), such as magnetron sputtering [189-191]. The interfaces between two different components are responsible for their unique properties. This section will introduce the microstructure and mechanical properties of certain metallic nanolayers. The orientation relationship (OR) is generally used to describe the relation between aligned planes and directions in nanolayers between two different components. There are at least four major types of FCC/BCC interfaces in nanolayers, including Kurdjumov-Sachs (K-S) [192], Nishiyama-Wassermann (N-W) [193], Pitsch [194] and Bain [195].

Size-dependent strengthening mechanisms in metallic nanolayers, often reported as the evolution of film hardness with individual layer thickness, h, have been extensively studied [180, 181, 196-204]. Since the establishment of the Hall-Petch (H-P) model in 1950th, it has been widely adopted to explain the grain boundary (GB) induced strengthening mechanism due to dislocation pile-ups [205, 206]. The H-P model also works well for metallic nanolayers when the individual layer thickness h is greater than tens of nanometers (normally when h > 50 nm) [181, 196, 207-212]. At this length scale, the hardness increases linearly with h-1/2, and the H-P slope has been used to estimate the interface barrier strength and predict the peak hardness of nanolayers. When h decreases to below 50 nm, film hardness deviates from the linear prediction of the H-P model, as dislocation pile-ups are less likely at such a small length scale. Instead, the confined layer slip (CLS) model derived from the Orowan bowing of single dislocations may be a more realistic deformation mechanism [202, 213]. When h reduces to several nm (generally 1 ~ 5 nm), the strength of nanolayers typically reaches a plateau and is independent of h. The maximum (or plateau) strength of the nanolayers is determined by various mechanisms, including Koehler stress [214-216], misfit dislocations [208, 215, 217, 218], chemical stress [208, 212, 215, 219], coherency stress [215, 220] and twinning [211, 212, 217, 221, 222]. A hardness plateau is generally observed at smaller *h* in incoherent systems [189, 191, 196, 205, 223], while softening often occurs in coherent systems due to the formation of fully coherent interfaces (also referred to as transparent interfaces, that is the interface is transparent to the transmission of dislocations) [196, 210, 215]. Fig. 1.21 shows schematically the overview of deformation mechanisms of nanolayers at different length scale [180, 181, 202].

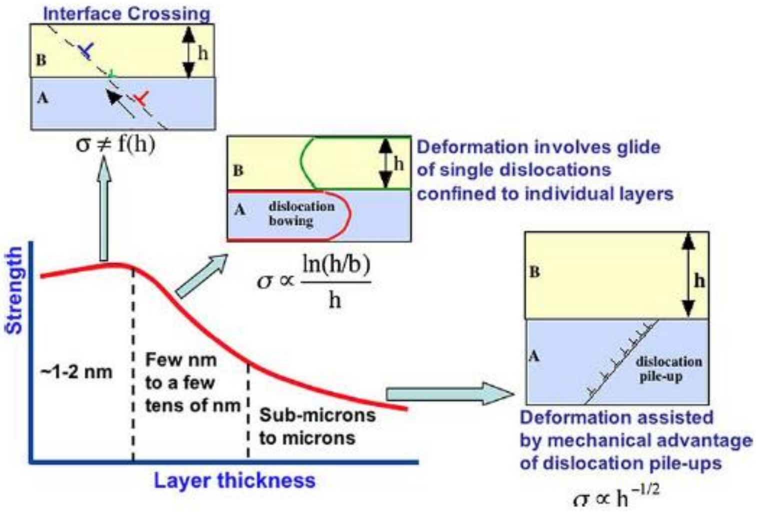

Fig. 1.21. Schematic illustration of the deformation mechanisms of nanolayers at different length scale (Reprinted from [181] with permission of Elsevier).

1.4.2 Nanotwinned metals

Twin boundary (TB) is a special class of grain boundaries (GBs) with mirror symmetry across the twinning plane. Among a variety of TBs, Σ3 (111) coherent twin boundaries (CTBs) and Σ3 (112) incoherent twin boundary (ITB) are of particular interest and are relevant to this proposal. Fig. 1.22 shows some typical twinned structures in FCC metals (Cu and Ag). TB has been extensively reported in FCC metal. For instance, NT Cu exhibits superior strength and ductility simultaneously as shown in Fig. 1.23 [224, 225]. Later, it has been demonstrated that TBs can enhance strength and/or ductility in Cu and several other metallic materials, such as Ag and 330 stainless steel [190, 209, 226]. TBs are strong barriers to dislocation propagation [225, 227-229]. When a dislocation encounters a TB in FCC metals, the perfect dislocation could dissociate and left a sessile dislocation (Frank dislocation) at the TB ($1/2\left[101\right] \rightarrow 1/6[121] + 1/3[111]$) [226, 227]. In addition, since CTBs exhibit much lower interface energy than high angle GBs, they have much better mechanical and thermal stabilities than other types of GBs [229, 230].

It is noteworthy that in general TBs can be easily introduced in metals with low-to-intermediate stacking fault energy (SFE), such as Ag, Cu, and 330 stainless steels [209, 225, 226], but it is very challenging to introduce twins for metals with high SFE. However, recent studies have shown basic criteria for the formation of growth twins in high SFE metals [231], and some examples show successfully fabricated Al with high-density growth twins [232, 233].

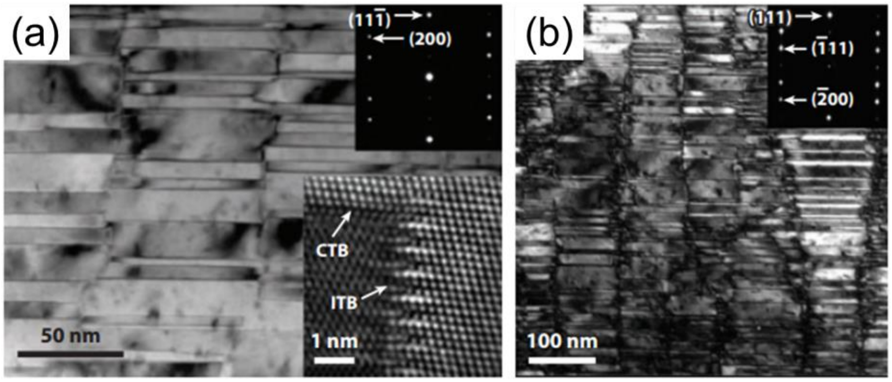

Fig. 1.22 Bright-field transmission electron microscopy (TEM) images of magnetron sputtered (a) epitaxial NT Cu (Reprinted from [234] with permission of AIP Publishing LLC) and (b) epitaxial NT Ag (Reprinted from [226] with permission of Elsevier).

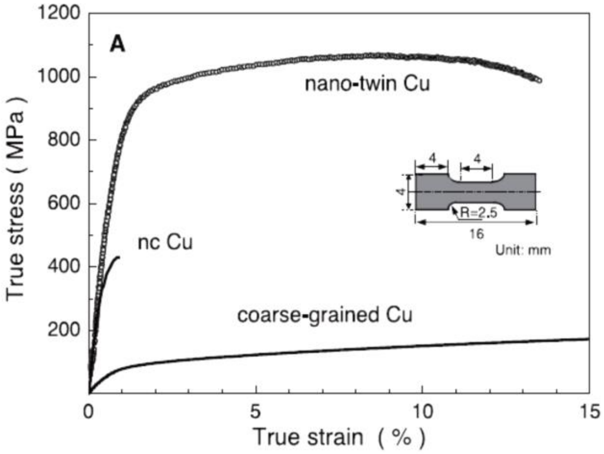

Fig. 1.23. (a) Nanotwinned Cu with twin lamellae thickness of ~15 nm shows improved yield stress and considerable ductility (Reprinted from [225] with permission of The American Association for the Advancement of Science).

1.4.3 Nanoporous metals

The presence of high-density nanopores inside metallic materials significantly remodels the response of materials under high pressure-high strain rate loading conditions.

For instance, nanoporous (np) metals have attracted extensive attention in the absorption of high energy impacts [235, 236]. Besides, many recent studies focused on the mechanical properties of the ligaments (or struts) and revealed the size-dependent strength behaviors of NP metals [172, 237-240].

For example, a recent study has investigated the mechanical properties of NP Au using a combination of nanoindentation, column microcompression, and molecular dynamics (MD) simulations, and observed that the mechanical behavior of NP Au is governed by its ligament dimension [237]. More specifically, with a relative density of 20% and ligament dimensions 10, 25 and 50 nm, the strength of NP Au decreased with increasing ligament diameter. Especially, the yield strength of NP Au with 10nm ligaments and a porosity of 75% is stronger than bulk Au, indicating that NP Au can be strong as its bulk counterpart while maintaining a highly porous structure.

1.5 Defect sinks and general philosophy for alleviation of irradiation damage

Energetic particle (such as ions, neutrons and protons) irradiations induce a large population of vacancies and self-interstitial atoms (SIAs) in metallic materials, and these point defects can combine into clusters, in the form of dislocation loops and networks, voids, bubbles and stacking fault tetrahedra (SFTs) [9-12]. As a result of severe irradiation, the microstructure and mechanical properties of the materials can be significantly degraded as evidenced by void swelling, irradiation hardening, embrittlement and significant loss of ductility [13-17]. The search for irradiation tolerant materials has been a subject of intense research for decades. However, no material is known to be immune to irradiation-induced damage. It remains a major challenge to design materials that have significantly enhanced irradiation tolerance at high temperatures and high doses. Numerous approaches have been adopted to design irradiation-resistant materials. The basic criterion is that certain types of defect sinks may promote the absorption and recombination of interstitials and vacancies and thus enhance the irradiation tolerance of materials. Consequently, various types of defect sinks have been investigated, including grain boundary (GB), twin boundary (TB), phase boundary, etc. [76, 170-176, 241]. For instance, nanocrystalline materials have abundant GBs and may have excellent irradiation resistance because GBs act as defect sinks that can absorb irradiation induced defects, and in some cases may serve as sources to emit interstitials and annihilate vacancies [89, 131, 147, 242, 243]. The irradiation behavior of nanolayered, nanotwinned and Nanoporous metals is briefly reviewed in this section.

1.5.1 Nanolayered metals

Layer interface is an effective defect sink and its influence on irradiation tolerance of materials has been extensively studied [76, 175, 178, 241, 244]. For instance, significant layer thickness-dependent reduction of both helium bubble density and alleviation of irradiation hardening were reported in some of the immiscible systems, such as Cu/Nb [245] and Cu/V [246]. Significant reduction of both helium bubble density was reported, as shown in Fig. 1.24. In addition to Cu/Nb and Cu/V, many other systems, such as Cu/V [52, 246], Ag/V [175, 247], Fe/W [248], Al/Nb [249], Cu/Mo [250] and Cu/W [251], have also been investigated. A common conclusion can be obtained from these studies is that the nucleation and migration of defects will be largely limited when the individual layer thickness is very small, 1~5 nm.

MD simulations of Cu/Nb also indicate that the Cu-Nb interface is a highly efficient sink for the annihilation of irradiation-induced defects [252]. Demkowicz *et al.* showed that two types of interfaces regarding two different Kurdjumov-Sachs (K-S) orientation relationships exist in Cu/Nb nanolayers. One type is the typical K-S relation where {111} FCC || {110} BCC, <110> FCC || <111> BCC). Another type contains a distorted Cu layer (only the first atomic layer) grown on top of Nb layer. The two different interfaces can convert alternatively by absorbing a vacancy or an interstitial and form extended jogs [253]. Such a process makes the Cu/Nb interface an unsaturable defect sink.

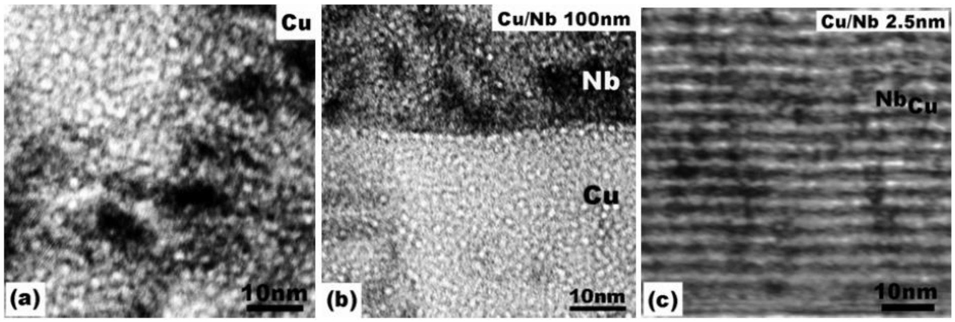

Fig. 1.24. XTEM micrograph of He-ion irradiated Cu/Nb multilayer films. (a) Vacancy clusters and He bubbles, 2-3 nm in diameter, were observed in irradiated Cu films (b) He bubbles aggregated along layer interfaces in irradiated Cu100/Nb 100nm multilayers. (c) No aggregation of point defects into Frank loops or SFTs were detected in Cu2.5/Nb2.5 nm nanolayers (Reproducd from [245] with permission of Elsevier).

1.5.2 Nanotwinned metals

Twin boundaries (TB) are low energy boundaries and are generally anticipated to be less efficient defect sinks. Han *et al.* showed that the width of void denuded zone in non-Σ3 GBs is much greater compared to Σ3 TBs, indicating low sink efficiency of TBs [254]. A recent study on He ion implantation of nanotwinned (NT) Cu at room temperature suggests that TBs are poor sinks because point defects at Σ3 TBs have nearly identical properties to those in pure face-centered-cubic (FCC) Cu [255]. However, Niewczas and Hoagland reported, through MD simulations, that the interaction between Σ3 {111} coherent twin boundaries (CTBs) and stacking fault tetrahedra (SFTs) lead to the destabilization of SFTs [51]. Yu *et al.* validated the MD simulation experimentally by using *in situ* Kr ion irradiation study of NT Ag and showed that the density of SFTs in NT Ag is much lower than that in its bulk counterpart as shown in Fig. 1.25 [89]. The density of SFTs decreases drastically when average twin spacing is smaller than 15 nm. In addition, they also observed the frequent migration of incoherent twin boundaries (ITBs) [256]. Recent *in situ* study on NT Ag provided more evidence that TBs are effective defect sinks [179]. First, TBs may actively engage with defect clusters as shown by the distortion and self-healing of TBs during interaction with different types of defect clusters. Second, TB affected zones (TBAZs) have been identified. Time accumulative defect density and defect diffusivity within TBAZs are substantially distinct from those in twin interior. More specifically, the accumulative defect concentration within a 60 nm-thick twin is significantly higher in the central area than in the areas close to CTBs, and defect clusters form within the regions that are ~5 nm away from CTBs [179].

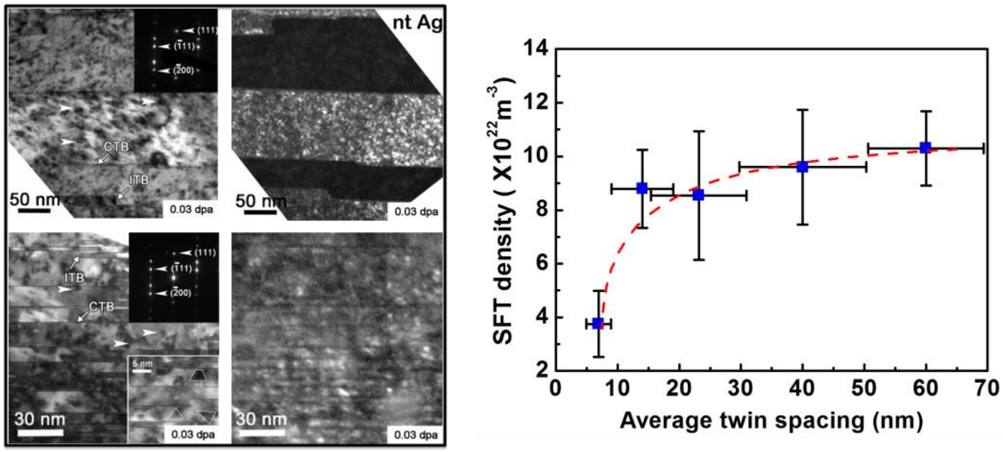

Fig. 1.25. TEM images are showing the overview of defects morphology in NT Ag with different twin densities and the statistics of defect (SFT) density as a function of average twin spacing (Reprinted from [89]).

1.5.3 Nanoporous metals

Free surface is typically considered as an unsaturable defect sinks, and nanoporous (NP) materials with a giant surface-to-volume ratio may have the potential to be irradiation tolerant compared to the fully dense coarse-grained (CG) counterparts.[183, 184, 257] There are extensive studies on mechanical properties of NP metals.[237-240] An enlightening thought has been proposed almost 20 years ago to develop naturally porous structural materials in nuclear fuels to alleviate the fission gas accumulation with nanophases [167]. However, the number of irradiation studies on NP metals remains very limited [78, 172, 183, 184, 188]. Fig. 1.26 shows the window of irradiation resistance proposed by E. M. Bringa et al.. The resistance is described in terms of the diameter of the ligaments and the dose-rate under 45 keV Ne ions irradiation at room temperature [183]. Fu *et al*. performed an *ex situ* study on NP Au under 400keV Ne^{++} ion irradiation and showed that defect accumulation depends on dose rate.[188] More specifically, SFTs formed at high dose rate, while few SFTs were generated at low dose rate. Their MD simulations indicate that low dose rate leaves ample time for SIAs and vacancies to diffuse to the surface or recombine, whereas at higher dose rate, the time interval between cascades is shorter than the time needed for migration of defects to the surface. Consequently, vacancies have enough time to aggregate and form SFTs. Previous *in situ* study on NP Ag showed the removal of various types of defect clusters, including SFTs, small dislocation loops and large segments, by the free surface in NP Ag under 1 MeV Kr^{++} ion irradiation [184]. Furthermore, the *in situ* studies showed that both the global and instantaneous diffusivities in NP Ag are lower than those in CG Ag.

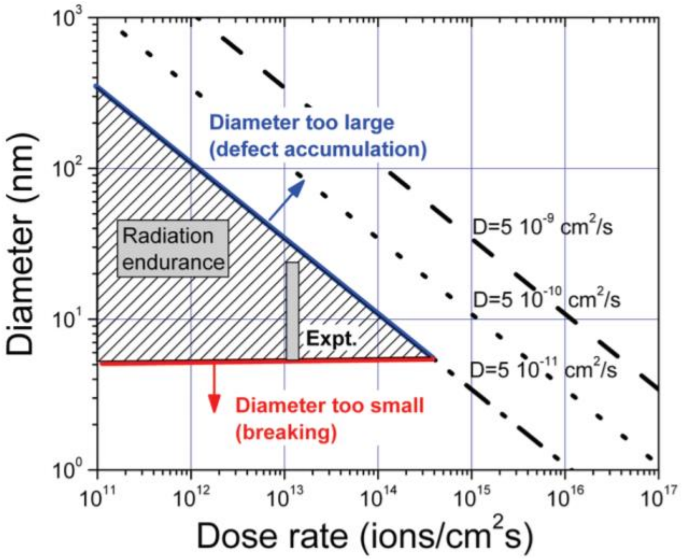

Fig. 1.26. Window of irradiation endurance showing the irradiation resistance (triangular area) in terms of the diameter of the ligaments and the dose-rate under 45 keV Ne ions irradiation at room temperature (Reprinted from [183] with permission from American Chemical Society).

1.6 Motivation and objective

Irradiation involves extensive ion-solid interactions that lead to the degradation of many aspects of mechanical properties, such as irradiation hardening, embrittlement, etc., as well as thermal and electrical properties. For materials used in nuclear reactors, the stability and reliability of these materials are challenged by the accumulated irradiation damage during their service period. Next-generation nuclear reactors ask for the improvement of fuel performance at the cost of increased severity of structural materials under extreme irradiation environment [3, 4]. FCC metals with low SFE, such as stainless steels, are widely used in nuclear reactors. Low values of SFE lead to severe irradiation-induced damage. Besides, Low values of SFE lead to wide dissociation of dislocations in their glide planes into Shockley partial dislocations, which severely affecting the hardening process of the metal. Therefore, the goal of this dissertation is to investigate the practical methods that can enhance the mechanical properties and irradiation tolerance of FCC metals with low SFE. One strategy of imparting desired properties to those FCC metals is to incorporate into them with a high density of defect sinks, such as multilayer interfaces, TBs and free surface.

1.6.1 Ag/Fe nanolayers

Metallic nanolayers have advanced physical properties and have been widely studied for various applications, including magnetic data storage [258, 259], hydrogen storage [219, 260], and irradiation tolerance, etc. [76, 175, 241, 244, 261-263]. In addition, NMMs may have applications as the future micro/nano-electromechanical devices as certain multilayer systems exhibit close to theoretical strength and relatively large deformability [189, 196, 208, 213, 264]. Size-dependent strengthening in NMMs, that is the evolution of film hardness as a function of individual layer thickness *h*, has been extensively studied [180, 196-200, 202-204, 265].

Here, we studied Ag/Fe multilayers for the following reasons. First, the strengthening mechanisms in Ag/Fe with FCC/BCC interfaces are less well understood. Prior studies on Ag/Fe focused on their magnetic properties [266], microstructures and indentation creep behavior [267-269]. Second, when comparing Ag/Fe and Ag/Ni, it is evident that the elastic modulus of Fe and Ni are similar. Thus the Koehler stress due to elastic modulus difference should be similar in both Ag/Fe and Ag/Ni multilayers. Consequently, we anticipate that Ag/Fe and Ag/Ni multilayers should have comparable peak strength. Such a hypothesis will be tested. Third, we will compare the mechanical strength of Ag/Fe to Cu/Fe multilayers. In Cu/Fe multilayers, the grain size of Fe is smaller than h and determines the mechanical strength of system at large h (h > 50 nm). At small h (1 nm or so), Cu and Fe form coherent interfaces as Fe has transformed to FCC phase. Softening has been observed in Cu/Fe with small h due to the formation of coherent (transparent) interfaces. Furthermore, nanotwins with an average twin spacing of ~ 6 nm has been observed in Cu/Fe multilayers. It is unclear if twins can form in Ag/Fe multilayers at this small length scale; and if softening exists in Ag/Fe multilayers.

1.6.2 Nanotwinned Ag

High-density irradiation-induced defect clusters can significantly undermine the mechanical properties of irradiated materials. NMMs have high-density defect sinks that can improve irradiation resistance. Among all NMMs, twin boundaries (TBs) however are low energy boundaries that are generally anticipated to be less effective in alleviation of irradiation damage, comparing to high angle grain boundaries [254, 255]. Interestingly, counter to the prediction, Yu et al reported that the density of SFT in NT Ag strongly depends on average twin spacing as TBs can effectively remove SFTs [89]. Moreover, *ex situ* [170] and *in situ* [89, 256] irradiation studies have revealed frequent TB migration in irradiated NT metals, which is desirable to actively engage and remove irradiation-induced defects.

Despite these prior studies, physics of irradiation damage mechanisms in NT metals remains poorly understood. First, although one would anticipate the existence of twin boundary affected zones, it has been shown that defect density may not vary as a function of distance to TBs [170]. Second, in spite of the study of SFT removal by TBs, it is unclear if TBs can also remove dislocation loops. Third, it remains a challenge to measure defect migration kinetics in irradiated metallic materials [270], and defect migration kinetics in NT metals is largely unknown.

1.6.3 Nanotwinned AgFe (Ag-1at%Fe)

Numerous works have also been done to show that by mixing a small amount of impurity atoms could significantly amend irradiation-induced microstructures in metallic materials. Some of the impurity effects have been attributed to solid solution effect, i.e. point defect trapping at impurity atoms, and others to various aspects of precipitation effect [5, 271-274]. Mansel and Vogl have shown that neutron irradiation-induced interstitials in Al will be trapped at Co substitutional atoms [275]. Detrapping also occurs when vacancies become mobile and migrate to the trapped interstitials. Alexander and

Stanislav also indicated that adding solute atoms may decrease the diffusion rate of interstitial clusters, and therefore, increasing the recombination rate of those clusters with freely migrating vacancies [276].

FCC metals with very low stacking fault energy (SFE), such as Ag and Cu, are in general vulnerable to irradiation [8, 11, 48-51, 229, 277]. Previous reports have shown by introducing high-density defect sinks, such as twin boundaries and nanovoids, the irradiation tolerance of nanostructured Ag and Cu can be greatly enhanced [83, 89, 178, 179]. There may be another approach that can drastically improve irradiation tolerance of Ag, which is by mixing merely 1 at% of Fe solute atoms into Ag matrix. Adding a small amount of Fe impurities leads to the formation of ultra-high-density twins, ~ 2 nm thick, in Ag-1at%Fe (referred to as NT AgFe). Compare to CG Ag, NT AgFe possesses three types of different defect sinks, GBs, TBs, and solutes. As a result, both irradiation-induced defect size and the defect density in NT AgFe have been significantly suppressed compared to coarse-grained pure Ag and NT Ag.

1.6.4 Nanoporous Au

Nanoporous metals exhibit a large surface-to-volume ratio have the potential to be superior irradiation tolerance compared to their coarse-grained (CG) bulk counterparts. There are extensive studies on mechanical properties of NP metals [237-240]. However, there are limited cases on irradiation responses of NP materials [172, 183]. Previous *in situ* study on NP Ag showed the removal of various types of defect clusters, including SFTs, small dislocation loops and large segments, by the free surface in NP Ag under 1 MeV Kr^{++} ion irradiation.[184] Furthermore, the *in situ* studies showed that both the global and instantaneous diffusivities in NP Ag are lower than those in CG Ag. Dose-rate-dependent defect accumulation in NP Au has also been reported [188]. Defect migration kinetics is crucial for the modeling of defect dimension, density and their evolution under irradiation condition. However, such information remains largely unknown [87, 278]. Besides, the influence of dose rate on defect diffusivities is still unclear [10, 183, 279]. The behavior of defect cluster and the stability of nanopores are important factors to understand the enhanced irradiation tolerance of NP materials. Therefore, an *in situ* Kr ion irradiation studies have been carried out to investigate the irradiation resistance of NP metals.

CHAPTER II

EXPERIMENTAL

2.1 Thin film and TEM sample fabrication

2.1.1 Ag/Fe metallic nanolayers

Ag/Fe nanolayer (or multilayer) thin films with identical individual thicknesses, h, varying from 1 to 200 nm and overall thicknesses of 1-4 µm were deposited onto HF acid etched single crystal Si (111) substrates via DC magnetron sputtering, as shown in Fig. 2.1, at room temperature from pure Ag (99.99%) and Fe (99.95%) targets. A base pressure of better than 8×10^{-8} torr was achieved before deposition, and the Ar pressure during deposition was 2~3 mtorr. A 50 nm-thick Ag buffer layer was deposited before the deposition of any Ag/Fe multilayers. Cross-sectional TEM (XTEM) samples were ground and polished mechanically, and further thinned by dimpling. Finally, low energy Ar ion milling (3.0~4.0keV) and ion polishing (2.0 keV) were involved in reducing film thickness to roughly 100 nm.

2.1.2 Nanotwinned Ag

Epitaxial NT Ag films, ~2 µm in thickness, were deposited through DC magnetron sputtering by using 99.99% purity Ag target onto HF-etched single-crystal Si (111) substrates at room temperature. Prior to deposition, the chamber was evacuated to a base pressure of < 8×10^{-8} torr. After deposition, part of Ag films was annealed at 700 ˚C for 0.5 h in order to obtain an average twin thickness of ~70 nm. Otherwise, the average twin thickness of as-deposited Ag films is smaller than 20 nm. Cross-sectional transmission electron microscopy (TEM) specimens were prepared by grinding, polishing and ion milling. Both as-annealed and post-irradiated specimens were investigated using an FEI Tecnai G2 F20 ST microscope. XTEM specimens were prepared by grinding, polishing and low energy ion-milling.

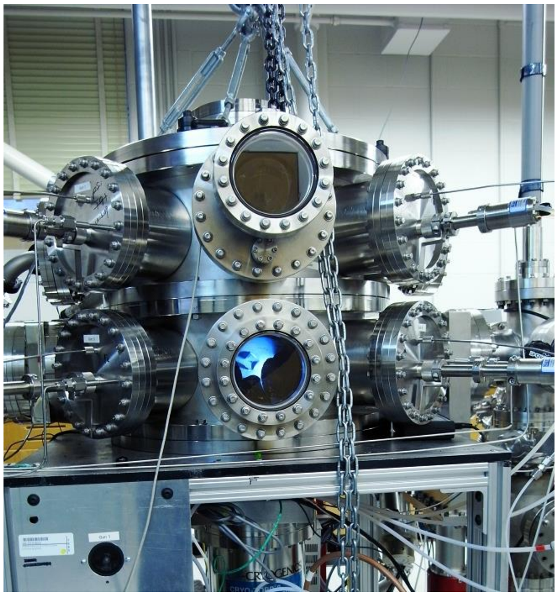

Fig. 2.1. Magnetron sputtering system used for thin film deposition.

2.1.3 Nanotwinned AgFe (Ag-1at%Fe)

NT Ag and S-NT AgFe thin films with the thickness of 1 µm were deposited onto HF acid etched single crystal Si (111) substrates and P-NT AgFe were deposited on SiO_2 substrate (Si (100) substrates with 1µm-thick amorphous oxidized Si on top), respectively, via DC magnetron sputtering at room temperature from pure Ag (99.99%) and Fe (99.95%)

targets. A base pressure of ~ 5 × 10^{-8} torr was achieved before deposition, and the Ar pressure during deposition was ~ 2 mtorr. Both cross-sectional and plan-view transmission electron microscopy specimens were prepared by grinding, polishing and finally, ion milling by a Gatan PIPS II system. CG Ag samples were made from small pieces of Ag target using the same TEM specimen preparation method as aforementioned.

2.1.4 Nanoporous Au

The $Ag_{65}Au_{35}$ (atomic ratio) leaves (procured from New York Central Art Co.) with dimensions 20 mm × 20 mm × 120 nm were sandwiched by two 304 stainless steel plates and then cold rolled up to ~ 20 % strain so as to reduce the foil thickness and achieve electron beam transparent transparency under TEM. The Ag65Au35 foils in a smashed leaf form were chemically de-alloyed in a 70% HNO_3 solution for 4 h at room temperature. The etched leaves were repeatedly rinsed in deionized water to remove residual acid and eventually lifted off by Cu grids (400 mesh) for *in situ* radiation studies.

2.2 Indentation hardness

The indentation hardness was measured using a Fischerscope HM2000XYp micro/nanoindenter with a Vickers indenter tip using instrumented nanoindentation technique. Approximately 15 indents were performed at different locations with different indentation depths. The loading rate was kept at 10 mN/s and each indent will typically penetrate into several bilayers, and the maximum depth was kept to be less than 15% of total film thickness to avoid the substrate effect. Hardness versus indentation depth was plotted, and the plateau value was chosen as the hardness of the measured film.

During indentation, a Vickers indenter is poked into the film with a load F, a deformed area A_c is created. The hardness (H_{IT}) of the material measured by nanoindentation can be calculated by

$$H_{\mathrm{IT}} = F_{\max} / A_c \qquad (2.1)$$

where $F_{\max}$ is the maximum applied force and Ac is the cross-sectional area of the contact between the indenter and the test piece. For a pyramid shaped Vickers indenter, $A_c = 24.5 \cdot h_c^2$, where h_c is the contact depth and can be calculated by

$$h_c = h_{\max} - \varepsilon(h_{\max} - h_i) \qquad (2.2)$$

where $h_{\max}$ is the maximum depth and h_i is the intercept depth [280]. The correction factor ε represents the shape of the indenter tip, which is 0.75 for Berkovich, Vickers and spherical tips, 1 for flat punch tips and 0.73 for conical punch tips [281]. Fig. 2.2 shows a typical load-displacement curve during indentation.

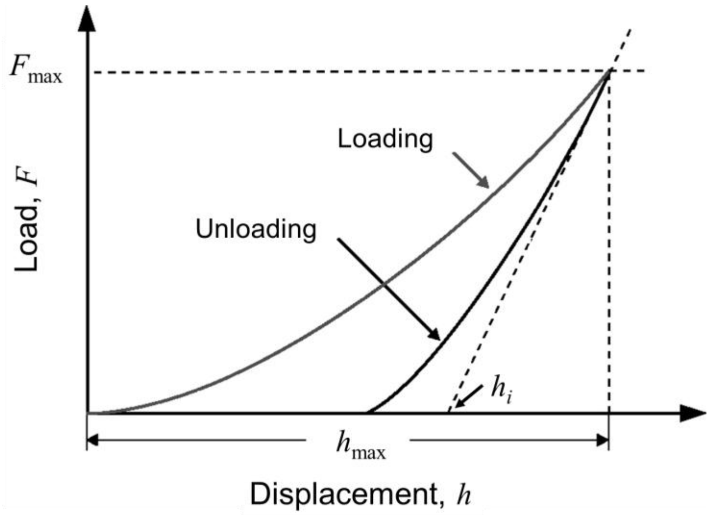

Fig 2.2. A typical load-displacement curve during indentation.

2.3 Structural characterization

2.3.1 X-Ray Diffraction (XRD)

Data analysis for XRD experiment is based on the Bragg's law, $\lambda = 2d \cdot sin\theta$, where λ is the wavelength for the incident x-ray beam, d is the spacing between crystallographic planes, and θ is the angle between incident beam and the crystallographic plane. Information, such as crystal structure, film texture, lattice distortion, etc., can be obtained by analyzing XRD profiles. For instance, crystal structure can be investigated by comparing the peak position with standard PDF (power diffraction file) cards, and film texture is implied by the intensity of certain peaks. For all studies in this dissertation, XRD experiments were performed by using a PANalytical X'Pert PRO Materials Research Diffractometer (Cu Kα radiation) at room temperature.

2.3.2 Profilometer

A Dektak 150 stylus profilometer is used to measure thin film thickness. The resolution in Z axis (height) of the profilometer is ~ 1Å, and the maximum depth can be measured is 65,000 nm. The radius of the stylus is 12.5 μm, and the horizontal resolution is determined by both the scan speed and scan length. Deposition rate can be obtained from film thickness divided by deposition time. Therefore, the total thin film thickness can be control fairly well during deposition.

2.3.3 Transmission Electron Microscopy (TEM)

Transmission electron microscopy (TEM) is a powerful tool for investigating microstructure of nanostructured metals and the induced damage by irradiation [96]. Transmitted electrons through TEM thin films can generate micrographs which results in bright-field (BF) images. If diffracted electrons is selected in the imaging process, then dark-filed (DF) images will be obtained and the DF technique is particularly useful in the characterization of radiation-induced defects [282]. Under weak beam DF (WBDF) mode, it is possible to image the dislocation lines and to determine the Burgers vector via $g \cdot b$ criteria [283], that is, if , $g \cdot b = 0$, the dislocation loop is invisible, otherwise it will be visible [282].

Selected area diffraction (SAD) pattern under TEM is obtained by varying the focal plane of objective lens. The formation mechanism of SAD is also governed by Bragg's law. However, compared to XRD, SAD provides more detailed data about a specific area at a relatively high magnification. This makes it straightforward to identify different crystallographic features, such as phase boundaries, twin boundaries and so on.

TEM studies were carried out on (2) FEI Tecnai F20 Super Twin microscope or (2) JEOL 2010 TEM microscope or (3) a Thermo Fischer Scientific/FEI Talos 200X microscope operated at 200 kV. Cross-sectional TEM (XTEM) samples were ground and polished mechanically, and further thinned by dimpling. Finally, low energy Ar ion milling (3.0~4.0keV) and ion polishing (2.0 keV) were involved in reducing film thickness to roughly 100 nm.

2.4 Irradiation

2.4.1 Estimation of radiation damage

The radiation damage in the metal films was estimated by Kinchin-Pease model in SRIM software [284]. The radiation damage in the term of displacements-per-atom (dpa) is calculated by

$$DPA = D(1/\text{Å}\cdot ion) \times \frac{Dose(ions/cm^2)}{N(atoms/cm^3)} \qquad (2.3)$$

where D is displacement obtained from SRIM calculation and N is atomic density. An example is shown in Fig. 2.3. Most Kr ions (99.99%) penetrate directly through the specimen because the ion energy is as high as 1MeV and the TEM foil is very thin (~ 100 nm). The plateau of DPA profile in Fig. 2.1 reveals that the damage is relatively uniform with respect to the depth of the irradiated specimen. The temperature rise of specimens during *in situ* Kr ion irradiation measured by the thermocouple is typically less than 10^{o}C.

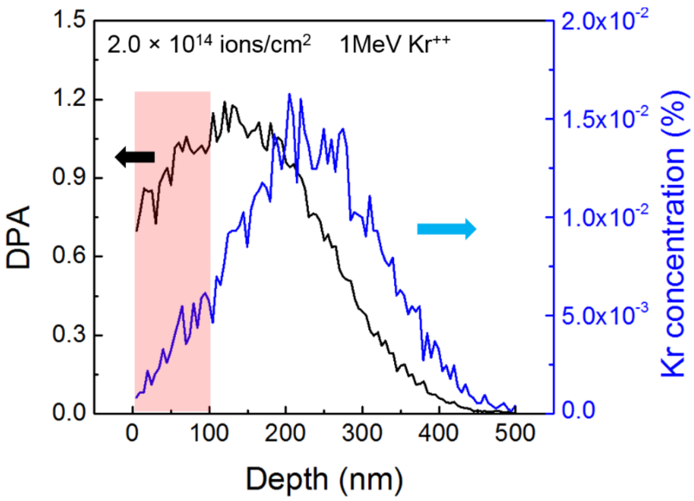

Fig. 2.3. SRIM simulation showing the dpa and Kr concentration profiles along the ion penetration depth for 1 MeV Kr ions. The first 100 nm thick TEM foil was subjected to an average dose of ~ 0.93 dpa (arithmetic mean value) and most Kr^{2+} ions penetrated through the TEM foil, leaving behind radiation damage and insignificant Kr concentration.

2.4.2 *In situ* Kr ion irradiation

In situ irradiation experiment was performed at room temperature at the IVEM-TANDEM facility at Argonne National Laboratory (Fig. 2.4). A HITACHI H-9000NAR microscope, with operation voltage up to 300kV, is equipped with 1 MeV Kr^{2+} ion beam was used for radiation experiments to a maximum fluence of 2×10^{14} ions cm^{-2} (~ 1 dpa). The beam source is not limited to Kr, many different ion sources are available, such as H, He, Fe, Cu and so on. The ion beam diameter at the specimen location is ~ 1.5 mm. The dose rate applied during *in situ* radiation experiments can be varied from a few counts/s to a few hundred counts/s (for Ag and Au, ~ 32000 counts = 1 dpa).

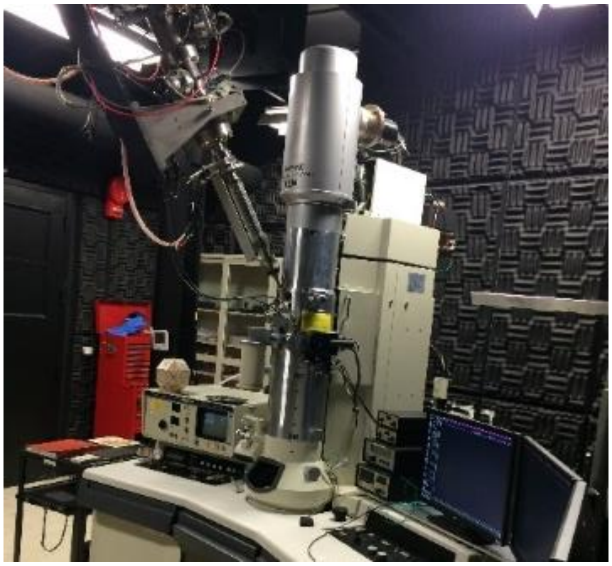

Fig. 2.4. IVEM-TANDEM facility at Argonne National Laboratory

CHAPTER III

COMPARISON OF SIZE DEPENDENT STRENGTHENING MECHANISMS IN AG/FE AND AG/NI MULTILAYERS*

3.1 Overview

Nanostructured metallic multilayers have attracted substantial attention as they often possess high mechanical strength. Here we report on the microstructure and mechanical strength of sputtered Ag/Fe multilayers with individual layer thicknesses (*h*) varying from 1 to 200 nm. Phase transformation of Fe from body-centered-cubic (BCC) to face-centered-cubic (FCC) structure occurred when $h < 5$ nm. Nanotwins formed in fine Ag/Fe multilayers. Although modulus mismatch is similar between Ag/Fe and Ag/Ni multilayers, the peak hardnesses of Ag/Fe multilayers is much lower than that of Ag/Ni system. Comparison of mechanical strength of several Ag based multilayers reveals that this drastic difference may arise from chemical stress due to the difference in stacking fault energy of the layer constituents.

3.2 Introduction

Nanostructured metallic multilayers (NMMs) have advanced physical properties and have been widely studied for various applications, including magnetic data storage

---

*Reprinted from "J. Li, Y. Chen, S. Xue, H. Wang, X. Zhang, Comparison of size dependent strengthening mechanisms in Ag/Fe and Ag/Ni multilayers, Acta Materialia, 114 (2016) 154-163" with permission from Elsevier.

[258, 259], hydrogen storage [219, 260], and radiation tolerance [76, 175, 207, 241, 244, 261-263, 285] etc. In addition, NMMs may have applications as the future micro/nano electromechanical devices as certain multilayer systems exhibit close to theoretical strength and relatively large deformability [189, 196, 208, 213, 264]. Size-dependent strengthening in NMMs, that is the evolution of film hardness as a function of individual layer thickness, h, has been extensively studied [180, 181, 196-202, 204, 265].

Since the establishment of the Hall-Petch (H-P) model in 1950th, it has been widely adopted to explain the grain boundary (GB) induced strengthening mechanism due to dislocation pile-ups [205, 206]. The H-P model also works well for NMMs [76, 181, 191, 196, 208-212, 217, 221] when the individual layer thickness h is greater than tens of nanometers (normally when $h > 50$ nm). At this length scale, the hardness increases linearly with $h^{-1/2}$, and the H-P slope has been used to estimate the interface barrier strength and predict the peak hardness of multilayers. However, if the multilayers contain a significant number of defects, such as nanotwins and nanograins, that have much smaller dimensions than h, the peak hardness predicted from the H-P slope may show a substantial deviation from the measured values [191, 208, 217, 221, 286, 287].

When h decreases to below 50 nm, film hardness deviates from the linear prediction of the H-P model, as dislocation pile-ups are less likely at such a small length scale. Instead, the confined layer slip (CLS) model derived from the Orowan bowing of single dislocations may be a more realistic deformation mechanism [202, 213]. At this length scale, dislocation movement is confined within the layers since the stress required for transmission of dislocations across interfaces is larger than that to bow dislocations in form of hairpins. A refined CLS model has also been developed by taking interface stresses and misfit dislocations into account, and the model describes the size dependent hardness evolution of certain metallic multilayers fairly well [181, 217].

When *h* reduces to several nm (generally 1 ~ 5 nm), the strength of NMMs typically reaches a plateau and is independent of h. The maximum (or plateau) strength of the multilayers is determined by various mechanisms, including Koehler stress [214-216], misfit dislocations [208, 215, 217, 218], chemical stress [208, 212, 215, 219], coherency stress [215, 220] and twinning [211, 212, 217, 221, 222]. A hardness plateau is generally observed at smaller *h* in incoherent systems [189, 191, 196, 205, 223], while softening often occurs in coherent systems due to the formation of fully coherent interfaces (also referred to as transparent interfaces, that is the interface is transparent to the transmission of dislocations) [196, 210, 215].

A substantial number of prior studies have focused on the microstructural evolution and mechanical properties of NMMs with various types of interfaces, including FCC/FCC [208, 209, 212, 221], BCC/BCC [221, 288, 289], HCP/HCP [290], FCC/BCC [189, 196, 217, 265], FCC/HCP [211, 217] and BCC/HCP [291-293] interface (FCC: face-centered cubic; BCC: body-centered cubic; HCP: hexagonal close-packed). Among these systems, FCC/BCC multilayers with opaque and immiscible layer interfaces have attracted considerable attention as such interfaces are strong barriers to the transmission of dislocations because of the discontinuity of slip systems [294, 295]. Cu/Nb, Cu/V and Cu/Fe are some of the typical multilayers with FCC/BCC interfaces [196, 203]. Molecular dynamics (MD) simulations have shown that the interfaces in Cu/Nb multilayer systems exhibit lower elastic modulus than layer constituents and thus the stress field of a glide dislocation can locally shear the interface and lead to dislocation core spreading along “weak” layer interfaces. The reemission of dislocations therefore becomes very difficult [295]. The study on Cu/V showed that weak interface and slip discontinuity may be the key to determining the peak strength in this system [189]. The strengthening mechanism in Cu/Fe system is slightly different, as high strength is observed in multilayers with relative large *h* (50 ~ 100 nm). The high strength over this length scale is ascribed to the confined dislocation propagation within nanoscale columnar grains (in the Fe layers), which are much smaller than h [217]. High-density growth twins have been observed in fully coherent (111) Cu/Fe multilayers when $h = 0.75$ nm and Fe has transformed to FCC structure. Peak hardness was retained because nanotwins are strong barrier to the transmission of dislocations [277, 296]. In Ag/V system, multiple growth orientation relations, including K-S, N-W, Bain as well as other intermediate relations, exist between two layer components, and therefore the habit planes change locally with the curvature of the interfaces [297].

Nanotwins have been extensively observed in some FCC/FCC multilayer systems, such as Cu/Ni [221], (100) textured Cu/Co ((100) Co has FCC phase) [211], Ag/Al [212], Ag/Ni [208], etc., and twin boundaries (TBs) contribute significantly to their peak strength. For instance, in (111) textured Cu/Ni multilayers, nanotwins significantly enhance the mechanical strength compared with their (100) textured counterparts. However, the large difference in peak hardness between (100) Cu/Ni and (100) Cu/Co (Co has transformed to FCC phase) is unexpected as both systems have nearly epitaxial microstructure, similar lattice mismatch (~2.6%) and elastic modulus mismatch. Such a large difference in hardness has led to a hypothesis that the difference in stacking fault energy (SFE) between layer constituents could contribute significantly to the strength of multilayer systems [211].

In this study, we selected Ag/Fe multilayers for the following reasons. First, the strengthening mechanisms in Ag/Fe with FCC/BCC interfaces are less well understood. Prior studies on Ag/Fe focused on their magnetic properties [266], microstructures and indentation creep behavior [267-269]. Second, when comparing Ag/Fe and Ag/Ni, it is evident that the elastic modulus of Fe and Ni are similar. Thus the Koehler stress due to elastic modulus difference should be similar in both Ag/Fe and Ag/Ni multilayers. Consequently, we anticipate that Ag/Fe and Ag/Ni multilayers should have comparable peak strength. Such a hypothesis will be tested. Third, we will compare the mechanical strength of Ag/Fe to Cu/Fe multilayers. In Cu/Fe multilayers, the grain size of Fe is smaller than h and determines the mechanical strength of system at large h (h > 50 nm). At small h (1 nm or so), Cu and Fe form coherent interfaces as Fe has transformed to FCC phase. Softening has been observed in Cu/Fe with small *h* due to the formation of coherent (transparent) interfaces. Furthermore, nanotwins with an average twin spacing of ~ 6 nm has been observed in Cu/Fe multilayers. It is unclear if twins can form in Ag/Fe multilayers at this small length scale; and if softening exists in Ag/Fe multilayers.

In this paper, we provide a comprehensive study on the microstructures of Ag/Fe multilayers by transmission electron microscopy (TEM), and the mechanical properties of Ag/Fe multilayers obtained by nanoindentation. The comparison of size dependent strengthening mechanisms in Ag/Fe to other systems, such as Ag/Ni and Cu/Fe, reveals several surprises, and the conclusion derived from this study may have general implications on size dependent strengthening mechanisms in numerous metallic multilayer systems.

3.3 Experimental

Ag/Fe multilayer thin films with identical individual thicknesses, *h*, varying from 1 to 200 nm and overall thicknesses of 1-4 μm were deposited onto HF acid etched single crystal Si (111) substrates via DC magnetron sputtering at room temperature from pure Ag (99.99%) and Fe (99.95%) targets. A base pressure of better than 8×10^{-8} torr was achieved before deposition, and the Ar pressure during deposition was 2~3 mtorr. A 50 nm-thick Ag buffer layer was deposited before the deposition of any Ag/Fe multilayers. The indentation hardness was measured using a Fischerscope HM2000XYp micro/nanoindentor with a Vickers indenter tip using instrumented nanoindentation technique. Approximately 15 indents were performed at different locations with different indentation depths. Each indent will typically penetrate into several bilayers, and the maximum depth was kept to be less than 15% of total film thickness to avoid the substrate effect. Hardness versus indentation depth was plotted, and the plateau value was chosen as the hardness of the measured film. X-ray diffraction (XRD) experiments were performed by using a PANalytical X'Pert PRO Materials Research Diffractometer (Cu Kα radiation) at room temperature. Transmission electron microscopy (TEM) studies were carried out on both FEI Tecnai F20 Super Twin microscope and JEOL 2010 TEM microscope operated at 200 kV. Cross-sectional TEM (XTEM) samples were ground and polished mechanically, and further thinned by dimpling. Finally, low energy Ar ion milling (3.0~4.0keV) and ion polishing (2.0 keV) were involved in reducing film thickness to roughly 100 nm.

3.4 Results

3.4.1 Microstructure characterization

Fig. 3.1a compiles XRD profiles of as-deposited Ag/Fe multilayers on Si (111) substrates. When $h > 50$ nm, Fe layers had BCC (110) texture, while Ag layers had strong (111) texture. The Fe (110) peak shifted to lower angles when $h < 25$ nm. The magnified XRD patterns for multilayers with h of 1 ~ 10 nm in Fig. 3.1b show a peak with interplanar distance of ½ ($d_{Ag}^{(111)} + d_{Fe}^{(111)}$) and a Ag (111) sueprlattice satellite peak (n = +1) in the Ag 5 nm/Fe 5 nm (referred to as Ag/Fe 5 nm) multilayer. Additionally, FCC Fe (111) peak emerged in Ag/Fe 5 nm and Ag/Fe 2.5 nm multilayers. The Ag/Fe 1 nm multilayer exhibited a single predominant Ag (111) peak, indicating the formation of strong (111) texture.

A bright-field XTEM micrograph and the corresponding selected area diffraction (SAD) patterns of Ag/Fe 200 nm multilayer are shown in Fig. 3.2a and 3.2b respectively. The SAD pattern indicates the formation of polycrystalline film with strong BCC Fe (110) and Ag (111) texture. Furthermore, Fe layers had nanoscale columnar grains with an average grain size of ~ 21 nm, much smaller than that (~ 106 nm) in Ag layers as shown in Fig. 3.2c. The average columnar grain size clearly evolved with *h, as* shown in Fig. 3.2d. When $h > 50$ nm the average columnar grain size of Ag decreased from 106 ± 25 to 28 ± 6 nm, and the grain size of Fe decreased from 21 ± 5 to 9 ± 4nm. When h decreased to below 50 nm the grain size of Ag and Fe did not decrease further.

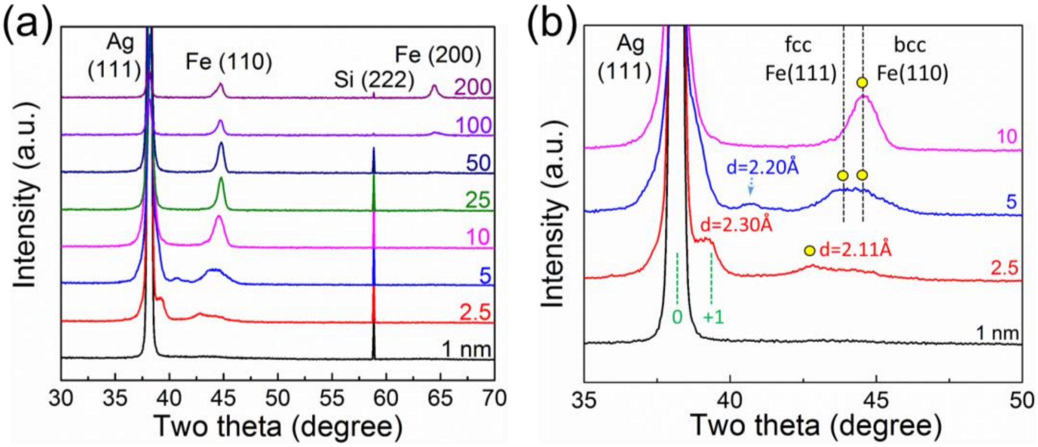

Fig. 3.1. (a) XRD patterns of Ag/Fe multilayers deposited on Si (111) substrates. When *h* > 50 nm, Fe exhibits BCC (110) texture, while Ag has strong (111) texture. When *h* < 25 nm, the BCC Fe (110) peak shifts to lower angles. (b) Magnified XRD patterns for a multilayer with h of 1 ~ 10 nm. When *h* = 5 nm, a superlattice peak with $\frac{1}{2}(d_{Ag}^{(111)} + d_{Fe}^{(111)})$ forms, and both BCC Fe (110) and FCC Fe (111) peaks emerges. A Ag (111) satellite peak (n = +1) appeared when *h* = 2.5 nm. The BCC Fe (110) peak disappears when *h* = 1 nm, and the Ag/Fe 1 nm multilayer exhibits single predominant Ag (111) peak.

Fig. 3.3a shows clear layer interfaces in the Ag/Fe 5 nm multilayers deposited on Si (111) substrates. The SAD pattern of Ag/Fe 5 nm multilayer (in Fig. 3.3c) examined from the Ag <110> zone axis reveals the following orientation relationship: $(111)_{Ag}$ // $(110)_{Fe}$, $[110]_{Ag}$ // $[100]_{Fe}$, that is the typical N-W orientation. Also we have observed twinned orientation among Ag diffraction spots (as shown by the green and blue dotted lines). The SAD pattern of the Ag/Fe 5 nm multilayer examined from an orthogonal direction (along the Ag <112> zone axis) shows that $(111)_{Ag}$ // $(110)_{Fe}$, $[112]_{Ag}$ // $[110]_{Fe}$. Fig. 3.3b shows schematically the orientation relationship between Ag and Fe in the Ag/Fe 5 nm multilayer.

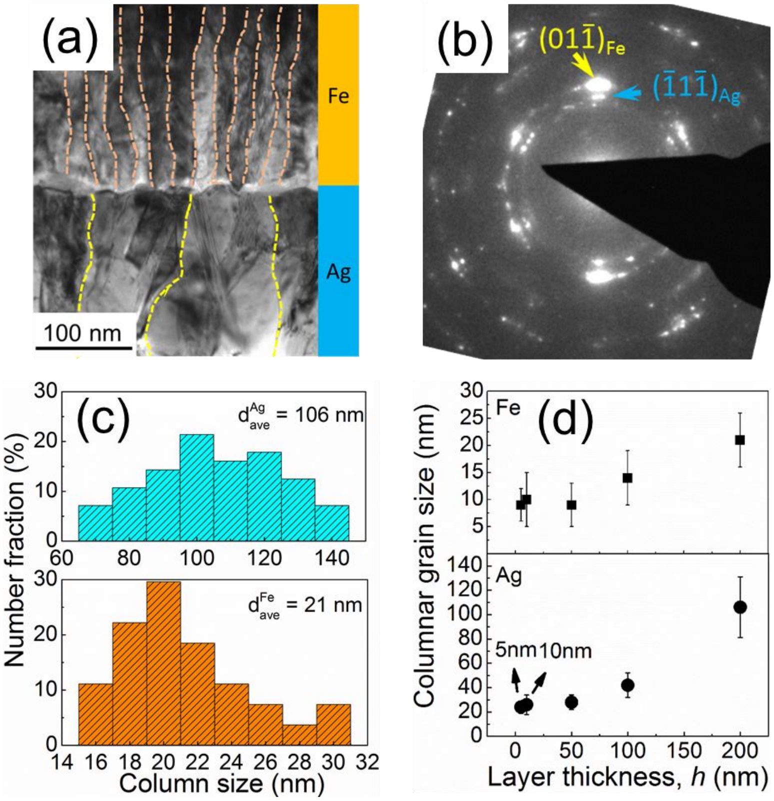

Fig. 3.2. (a) A bright field cross-section TEM (XTEM) micrograph of Ag/Fe 200 nm multilayer showing the formation of nanoscale columnar grains in Fe layers. (b) The corresponding selected area diffraction (SAD) pattern reveals BCC Fe (110) and Ag (111) texture. (c) The statistical studies show that the average columnar grain size is ~106 nm for Ag, and 21 nm for Fe. (d) The evolution of columnar grain size as a function of *h*. When h > 50 nm the average grain size of Ag decreased from 106 ± 25 to 28 ± 6 nm, and the grain size of Fe decreased from 21 ± 5 to 9 ± 4nm. When h decreased to below 50 nm, the average grain size of Ag and Fe did not decrease further.

Fig. 3.4 and Fig. 3.5 show separately, the existence of both incoherent and coherent interfaces in Ag/Fe 5 nm multilayer on Si (111) substrate. High-resolution TEM (HRTEM) micrograph in Fig. 3.4a shows distinct layer interfaces between Ag and Fe. Fast Fourier transform (FFT) and the corresponding inverse FFT (IFFT) in the selected areas in Ag and Fe layer as well as along their interface are shown in Fig. 3.4b1 – b3 respectively. Ag is examined from <110> zone axis, and Fe has BCC phase along <100> zone axis. Fig. 3.4b3 shows a clear incoherent interface between FCC Ag and BCC Fe. In contrast, the HRTEM micrograph in Fig. 3.5a shows the formation of coherent interfaces in the same Ag/Fe 5 nm multilayer specimen. Three interfacial zones (labeled as A, B and C in Fig. 3.5a) are examined in detail. The magnified HRTEM micrograph in Fig. 3.5b2 shows a nearly coherent Ag/Fe interface formed at location B, and Fe had distorted FCC structure. Furthermore, an interesting hetero-twinning relationship is evident between Ag and Fe. As shown in Fig. 3.5b1 and Fig. 3.5b3, TBs formed between the adjacent Ag and FCC Fe layers. The zigzag pattern of these plane traces in the schematic in Fig. 3.5a clearly shows the twin orientation relationships between successive layers.

Interface coherency was further enhanced when $h < 5$ nm. For instance the HRTEM micrographs of Ag/Fe 2.5 nm multilayer in Fig. 3.6a and the magnified TEM micrographs of the box d (Fig. 3.6c and 3.6d) show the formation of nearly coherent Ag/Fe interfaces. Although coherent interfaces are frequently observed in this specimen, the SAD pattern in Fig. 3.6b shows the existence of distorted FCC Fe. In particular the 6 {111} FCC Fe diffraction spots appear to match the diffraction pattern of the Ag <110> zone axis. Similar to Fig. 3.6, several HRTEM micrographs of the Ag/Fe 1 nm film in Fig. 3.7a, 3.7c and 3.7d confirm the formation of semi-coherent interfaces with distorted FCC Fe. The SAD pattern in Fig. 3.7b shows the formation of distorted FCC Fe examined along

<110> zone axis. Furthermore the HRTEM micrograph in Fig. 3.7d shows a stacking fault in Fe and a misfit dislocation at the Ag/Fe layer interface.

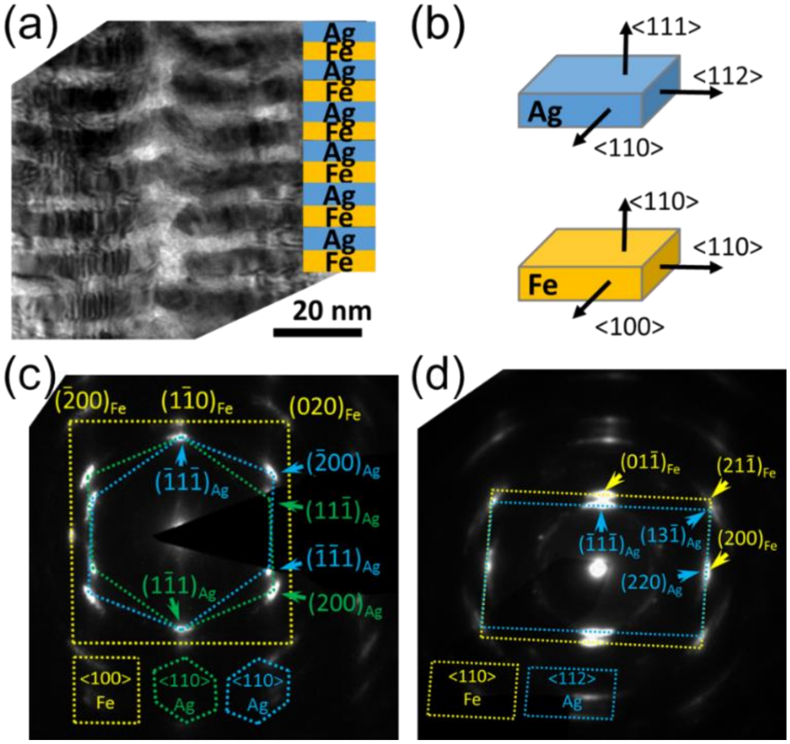

Fig. 3.3. (a) A bright field XTEM micrograph of Ag/Fe 5 nm multilayer on Si (111) substrates. N-W orientation relationship, $(111)_{Ag}$ // $(110)_{Fe}$, $[110]_{Ag}$ // $[100]_{Fe}$, between Ag and Fe was schematically illustrated in (b), and was revealed in SAD pattern in (c) examined along Ag <110> and Fe <100> zone axis. Ag layers have twinned orientations. The N-W orientation relationship was further proved in SAD pattern in (d) where the image was taken from the Ag <112> and Fe <110> zone axis.

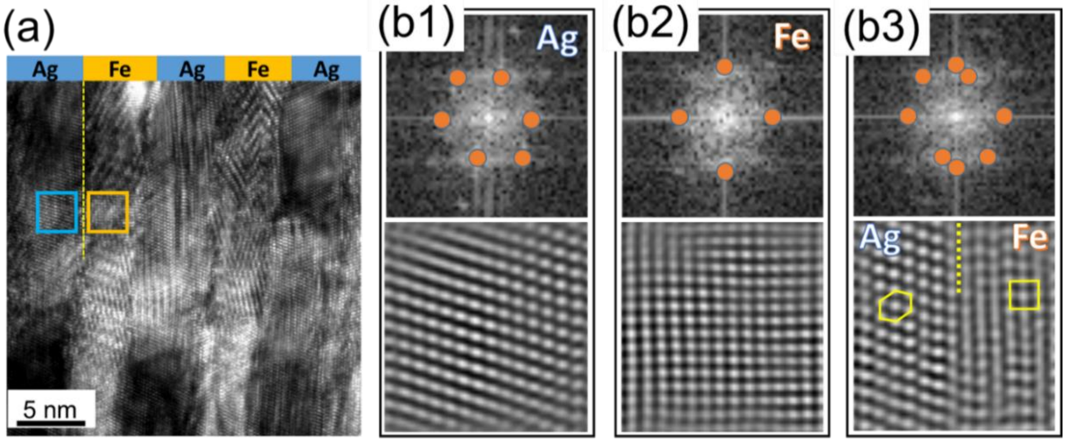

Fig. 3.4. The formation of incoherent interfaces in Ag/Fe 5 nm multilayer film on Si (111) substrate. (a) An HRTEM micrograph shows the clear interface between Ag and Fe. (b1 - b3) Fast Fourier transforms (FFTs) and the corresponding inverse FFTs (IFFTs) in the selected areas in Ag and Fe layer as well as along their interface. Ag is examined from <110> zone axis, whereas Fe has BCC phase as revealed along <100> zone axis. (b3) FFT and IFFT showing the incoherent interface between FCC Ag and BCC Fe.

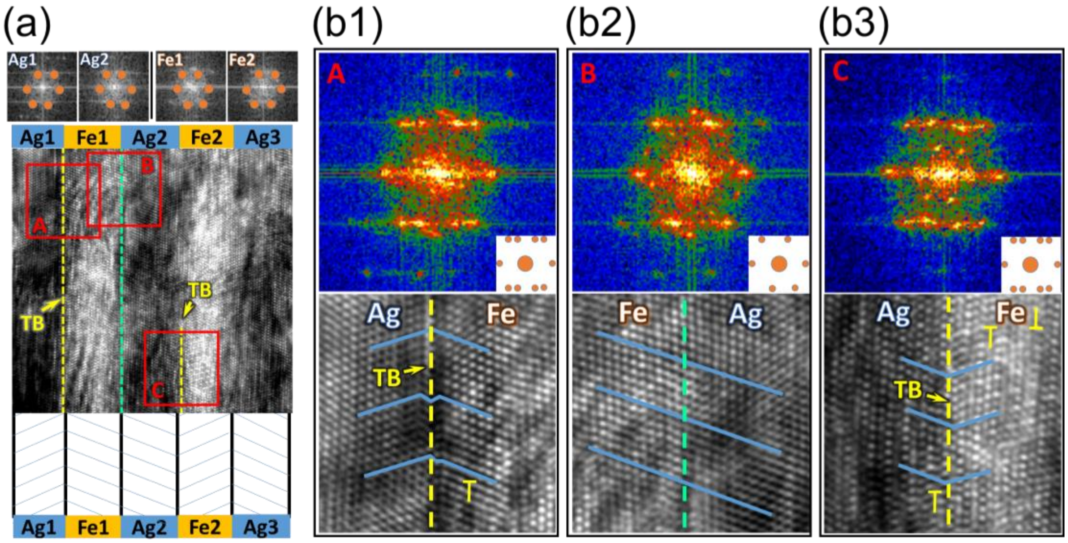

Fig. 3.5. Coherent interface and growth twins in the Ag/Fe 5 nm multilayer film. (a) HRTEM micrograph of the multilayer combined with the FFT of each individual layer and schematics showing the formation of twin boundaries (TBs) in the multilayer. (b1 and b3) HRTEM micrographs and FFTs show the formation of nearly coherent TBs between Ag and Fe in multilayers at two different locations (A and C in Fig. 6a). (b2) A nearly coherent Ag/Fe interface forms in box B and Fe has distorted FCC structure.

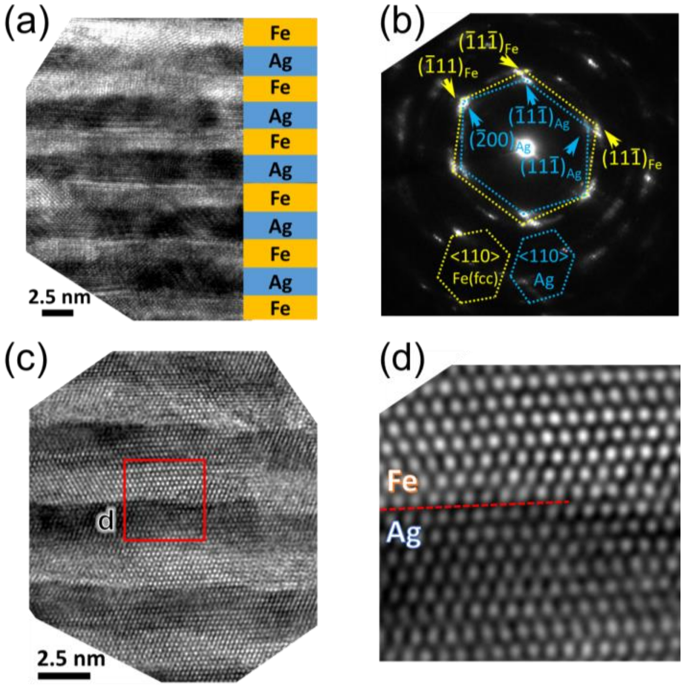

Fig 3.6. (a) A cross-sectional HRTEM micrograph of Ag/Fe 2.5 nm multilayer on Si (111) substrate. (b) The corresponding SAD pattern shows a largely distorted FCC Fe pattern, where the 6 {111} FCC Fe diffraction spots appear to match the diffraction spots from FCC Ag {110} diffraction zone axis. (c-d) For the same specimen at a slightly different location, an HRTEM micrograph and the magnified box d at interface showing the formation of nearly coherent Ag/FCC Fe interface.

3.4.2 Multilayer hardness

The hardnesses of Ag/Fe multilayer films on Si (111) substrate as a function of $h^{-1/2}$ are compared with Cu/Fe (111) [217] and Ag/Ni (111) multilayers [208] in Fig. 3.8. The peak hardness of Ag/Ni is ~ 6 GPa (when $h = 1$ nm), comparing to ~ 4 GPa for the Ag/Fe 5 nm multilayers and ~ 4.5 GPa for the Cu/Fe 1 nm multilayers. Three distinct characteristics are noteworthy in this plot:

(1) When $h \geq 50$ nm, the hardnesses of Cu/Fe and Ag/Fe are larger than Ag/Ni. In addition, the H-P slope is ~4.5 GPa•nm$^{1/2}$ for Ag/Fe multilayers, much smaller compared with that for the Cu/Fe multilayers, ~10.3 GPa•nm$^{1/2}$, and Ag/Ni, ~19.8 GPa•nm$^{1/2}$.

(2) When 50 nm > $h \geq 5$ nm, Ag/Ni multilayers become harder than Ag/Fe, but remain softer than Cu/Fe multilayers.

(3) When $h < 5$ nm, the hardness of Ag/Ni continuously increases and finally becomes larger than that of the Ag/Fe and Cu/Fe films. No softening is observed for the Ag/Ni and Cu/Fe systems while softening occurred in the Ag/Fe multilayers.

3.5 Discussion

3.5.1 Microstructure evolution of Ag/Fe multilayers

3.5.1.1 Coherency and phase transformation of Fe when h ≤ 2.5 nm

Our previous study on Cu/Fe multilayers showed clear h dependence of columnar grain size in both Fe and Cu layers [217]. A similar phenomenon has been observed in this study. When h = 200 nm, the grain size of Ag is ~ 106 nm, which is approximately five times that of Fe (~ 21 nm). The lattice constants of Ag and BCC Fe are 4.085 Å and 2.867 Å, respectively. Thus in general, Ag and Fe should form incoherent interfaces due to the large lattice mismatch, ~ 35%. However, a middle peak and a superlattice peak were observed when h = 5 and 2.5 nm. Furthermore, the Fe (110) peak gradually shifted to smaller 2θ angle and finally diminished at h = 1 nm. These observations indicate that semi-coherent interfaces might have formed when h < 10 nm. More specifically when h = 1 nm, coherent interface may have become dominant as implied by the single predominant Ag

(111) peak in XRD pattern. Meanwhile, Fe might experience a BCC-to-FCC phase transformation (as evidenced by the HRTEM micrographs in Fig. 3.7). The formation of semi-coherent Ag/Fe interfaces with distorted FCC Fe phase is somewhat surprising. Coherent Cu/Fe interfaces have been observed before, where FCC Fe has lattice parameters, ~ 3.585 Å, similar to that of Cu (3.615 Å).

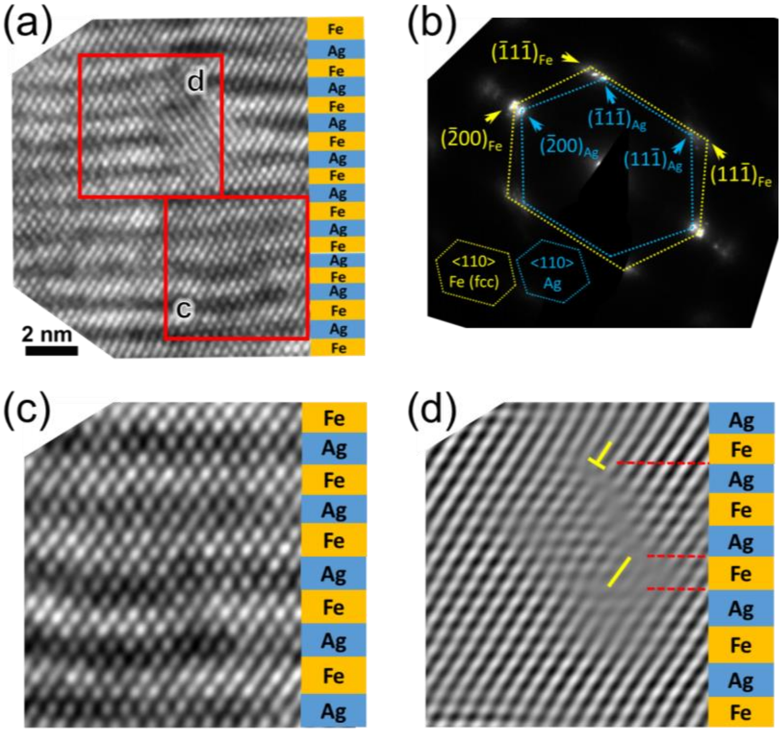

Fig. 3.7. (a) An HRTEM micrograph of Ag/Fe 1 nm film on Si (111) substrate. (b) The corresponding SAD pattern shows the formation of distorted FCC Fe examined along <110> zone axis. (c) The magnified view in box c showing nearly coherent Ag/Fe interfaces. (d) An inverse of FFT of the box d in Fig. 3.7a showing a stacking fault in FCC Fe and a misfit dislocation at the Ag/Fe layer interface.

The critical film thickness to keep coherent interface (free from misfit dislocation) can be estimated by [298],

$$h_c = \frac{b}{8\pi(1+\nu)\varepsilon_m}\left[\ln\left(\frac{h_c}{b}\right) + 1\right] \qquad (3.1),$$

where h_c is often referred to as the critical layer thickness for the formation of misfit dislocations, the magnitude of the Burgers vector b is ~ 0.25 nm, the mismatch strain ε_m between Ag and FCC Fe is 13%, and the Poisson's ratio ν is 0.33. The calculated value for h_c is ~ 0.5 nm. In Ag/Fe multilayers, since Fe is sandwiched by two Ag layers, the maximum thickness for maintaining coherent interface could be $2h_c$ = ~ 1 nm. Thus, it is feasible that Ag/Fe may exhibit semi-coherent interface when h = 1 nm.

When h = 2.5 nm, we also observed coherent Ag/Fe interface (as revealed by TEM micrographs in Fig. 3.6). Additionally, the same multilayer also shows the formation of distorted BCC Fe, as indicated by the SAD pattern in Fig. 3.6b. It appears that 6 FCC Fe {111} diffraction spots tend to match the diffraction spots of FCC Ag (along <110> zone axis). Such an intriguing phenomenon has not been reported before.

3.5.1.2 Hetero-twin formation when h = 5 nm

Although FCC Fe could form in Ag/Fe 1 nm multilayers, the formation of FCC Fe in Ag/Fe 5 nm multilayers is even more surprising. Both semi-coherent Ag/Fe (FCC Fe) and incoherent Ag/Fe (BCC Fe) interfaces were observed in Ag/Fe 5 nm multilayers. Furthermore, we have observed hetero-twins formed between Ag and Fe, that is the Ag/Fe layer interface may also serve as a TB between the two constituents in the Ag/Fe 5 nm multilayer. A somewhat similar observation has been reported in a metal/ceramic system, Al/TiN, where alternating Al layers may have a twin orientation separated by adjacent TiN layers [299]. Nanotwins have been observed in Cu/Fe 0.75 nm multilayers, and the average twin spacing is typically 6 nm [217]. In the current study, however, nanotwins were barely observed in Ag/Fe 1nm multilayers.

3.5.2 Strengthening mechanisms in Ag/Fe multilayers and comparisons to other systems

3.5.2.1 Strengthening at large layer thickness where h = 50 – 200 nm

Previous studies typically show that, when $h > 50$ nm, the hardness of multilayer films scales approximately linearly with $h^{-1/2}$. The maximum hardness can be estimated reasonably well by using a traditional H-P relationship [205, 206, 300]:

$$\mathrm{H_{IT}} = \mathrm{H_0} + \mathrm{k_{HP}} \mathrm{h}^{-0.5}, \qquad (3.2)$$

where H_0 is the hardness when the grain size is infinitely large and it represents the overall resistance of the crystal lattice to dislocation motion. H-P slope, k_{HP}, is a measure of the relative hardening contribution from layer interfaces, and can be expressed via [300]:

$$\mathrm{k_{HP}} = \sqrt{\tau^{*} \mathrm{G} b / [\pi(1-\nu)]} \qquad (3.3),$$

where τ^{*} is the interface barrier strength, G is the shear modulus (30 GPa for Ag), b is 0.289 nm for Ag, and ν is ~ 0.33. From k_{HP} measured from the H_{IT} vs. $h^{-1/2}$ plot, 4.45 GPa·nm$^{1/2}$, we calculate τ^{*} to be 0.073 GPa. The Tabor relation, $H = 2.7\sigma$, can be used to estimate peak hardness [301], where σ is the flow stress and can be calculated by taking into account the Taylor factor so that $\sigma = 3\tau^{*}$. Thereby the peak hardness ($=8.1\tau^{*}$) is estimated to be ~0.6 GPa, which is much lower than the measured value, ~ 4.4 GPa. Thus the measured H-P slope in the current study cannot predict the peak hardness of Ag/Fe multilayer films, different from numerous prior studies [189, 208, 209, 211]. When comparing Ag/Fe to Cu/Fe multilayers, it is evident that the Cu/Fe multilayers have similarly low H-P slope [217]. Furthermore when $h > 50$ nm, the hardnesses of Ag/Fe and Cu/Fe multilayers are much greater than that of Ag/Ni with identical h. This is primarily because the Fe layers have small columnar grain sizes, ~ 20 nm, much smaller than h. In this case, the deterministic dimension for film hardness is no longer h, but columnar grain size. Thus once dislocations (nucleated in Ag layers) propagate through Ag/Fe layer interfaces, they will be confined by the narrow columnar grain boundaries (channels) in Fe. In this case the stress for the propagation of dislocations (via Orowan bowing) in Fe layers may determine the hardness of Ag/Fe multilayers over this length scale (h > 50 nm). In contrast, the columnar grain sizes in Ag/Ni multilayers are comparable to layer thickness, and thus the strength of Ag/Ni multilayers is lower than that of Ag/Fe multilayers.

3.5.2.2 Strengthening mechanisms when h = 25 – 10 nm

At these length scales, the hardness is no longer dominated by columnar grain boundaries because their dimension is comparable or greater than individual layer thickness (refer to Fig. 3.2d). Consequently, dislocation pile-ups become less effective, and the movement of single dislocations is confined within the layers and the strengthening mechanism is described by the CLS model based on Orowan bowing mechanism. The critical resolved shear stress τ_{CLS} needed to initiate dislocation movement can be calculated as [202, 213]:

$$\tau_{\text{CLS}} = \frac{\text{G}b}{8\pi h'}\left(\frac{4-\nu}{1-\nu}\right)\left(\ln\frac{h'}{b}\right) \qquad (3.4),$$

where h' is the effective layer thickness - the distance along the slip plane between adjacent interfaces. Other variables carry the same meaning as defined previously. Using G_{Ag} = 30 GPa, b_{Ag} = 0.289 nm, ν = 0.33 and $h' = \sqrt{2}h$ = 14 nm (corresponding to h = 10 nm), the τ_{CLS} is calculated to be ~ 0.52 GPa, corresponding to a hardness value of ~ 4.2 GPa. This is in agreement with the measured hardness value of ~ 4.0 GPa. The size dependent strengthening in Ag/Ni multilayers in this regime has similar trend comparing to Ag/Fe. Furthermore, the hardnesses of the two systems over this length scale are very close at the same h.

3.5.2.3 Peak hardness when h = 5 nm

The hardness of Ag/Ni multilayers reaches a maximum value of ~ 4.4 GPa when h = 5 nm. At such a length scale, the maximum strength is determined by the intrinsic resistance of the Ag/Fe interface to the transmission of dislocations. In general, the interface barrier strength, $\tau_{barrier}$ can be estimated by [302]:

$$\tau_{barrier} = \tau_k + \tau_d + \tau_{ch} \qquad (3.5),$$

The first term τ_k is the Koehler stress due to the difference in elastic modulus of the layer constituents. The maximum τ_k can be estimated by [214]:

$$\tau_k = \text{RG}_{\text{Ag}} \sin\theta\,/8\pi \qquad (3.6),$$

where R = $(\mathrm{G_{Fe}} - \mathrm{G_{Ag}})/(\mathrm{G_{Fe}} + \mathrm{G_{Ag}})$, $\mathrm{G_{Fe}}$ and $\mathrm{G_{Ag}}$ are the shear moduli of Fe and Ag separately. θ is the angle between the slip plane and the interface. Assuming θ = 54.74°, the Koehler stress τ_k is calculated to be ~0.44 GPa, corresponding to a hardness of ~ 3.6 GPa.

The second term τ_d arises from misfit dislocations, and the third term τ_{ch} originates from the difference in SFE of each layer constituent. Since FCC Ag and BCC Fe have incoherent interface, the contribution of misfit dislocations to hardness is negligible. Therefore, the maximum hardness in Ag/Fe system is mainly dominated by Koehler stress. Hardness of the Ag/Fe multilayers at such length scale could also be related to hetero-twinned structure between adjacent Ag and Fe layers. TBs form at the Ag/Fe interfaces. It has been shown previously by both experiments and molecular dynamics simulations that TBs are strong barriers for the transmission of dislocations[296, 303]

3.5.2.4 Softening when h = 2.5 – 1 nm

When individual layers become extremely thin (1-2.5 nm in thickness), the hardness decreases with decreasing *h* due to the increase of interface coherency. Coherent and semi-coherent interfaces have lower resistance than incoherent interfaces to the transmission of dislocations. Hence such interfaces are sometimes referred to as more “transparent” interfaces to dislocations than incoherent (also called “opaque”) interfaces [294, 295]. The softening in coherent and semi-coherent multilayers at small h is also related to the decreasing Koehler stress as the dislocation core radius is comparable to layer thickness [215]. A similar result has been observed in Cu/Fe (100) [217] and Cu/Ni

(100) multilayers [221]. However, no or little softening occurs in the coherent (111) Cu/Fe 1nm and (111) Cu/Ni 2.5 nm multilayers due to the formation of high-density growth twins.

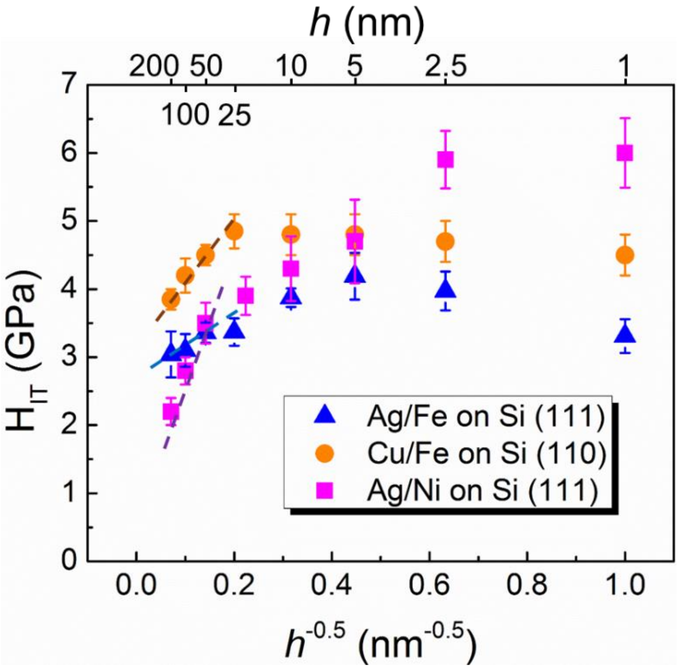

Fig. 3.8. Comparison of size dependent hardnesses among Ag/Fe, Cu/Fe and Ag/Ni multilayers. No softening was observed in Ag/Ni, while both Ag/Fe and Cu/Fe show softening at small h. The peak hardness of Ag/Ni is ~ 6 GPa (when h = 1 nm), comparing to the peak hardness of ~ 4 GPa in Ag/Fe and ~ 4.5 GPa for the Cu/Fe multilayers (when h = 5 nm).

3.5.3 The role of stacking fault energy in the determination of peak hardness

The interface barrier strength, in general, determines the maximum strength of multilayers. Some factors, such as τ_k, τ_d and chemical stress τ_{ch} are taken into account to estimate the total interface strength. Among these factors, τ_k and τ_d have been widely investigated. In contrast, the contribution from chemical stress τ_{ch} are less well understood. To better understand the role of SFE in the determination of multilayer peak hardness, all three terms (τ_k, τ_d and τ_{ch}) for several systems, Ag/Fe, Ag/Ni, Cu/Fe and Ag/Al are compared in Table 3.2, and Table 3.1 lists the shear modulus, SFE and lattice type and constant for these systems.

Table 3.1. Comparison of modulus, SFE, ΔSFE (SFE difference between two components) and crystal structure for several multilayer systems.

	Ag/Fe	**Ag/Ni**	**Cu/Fe**	**Ag/Al**
Shear modulus, G (GPa)	30/80	30/76	48/80	30/26
SFE (mJ m^{-2})	10/20	10/110	55/20	10/180
ΔSFE (mJ m^{-2})	10	100	35	170
Crystal structure	FCC/FCC	FCC/FCC	FCC/FCC	FCC/FCC
Lattice constant (Å)	4.09/3.59	4.09/3.52	3.62/3.59	4.09/4.05

(Note: In Cu/Fe and Ag/Fe multilayers, Fe has become FCC phase when h is ~ 1-5 nm)

Table 3.2. Comparison of Koehler stress (τ_k), misfit dislocation induced barrier stress τ_d, chemical stress (τ_{ch}), calculated peak hardness (H_{cal}^{peak}) and experimentally measured peak hardness (H_{exp}^{peak}) for several multilayer systems.

	τ_k (GPa)	τ_d (GPa)	τ_{ch} (GPa)	τ_{total}	H_{cal}^{peak}	H_{exp}^{peak}
Ag/Fe	0.44	0.09	-	0.53	4.3	4.3
Ag/Ni	0.44	-	0.31	0.75	6.1	6.0
Cu/Fe	0.37	0.25	-	0.62	5.0	4.8
Ag/Al	0.05	-	0.5	0.65*	5.3	5.5

Note: ($\tau_{total} = \tau_k + \tau_d + \tau_{ch}$; $H_{cal}^{peak} = 8.1\tau_{total}$)

* τ_{total} in Ag/Al also comes from ω interaction.

It is not surprising to see that Ag/Fe and Cu/Fe have the similar peak hardness since in both systems, τ_k is the primary term and similar for Ag/Fe and Cu/Fe multilayers. Whereas it is unexpected that Ag/Ni is ~ 2 GPa harder than Ag/Fe because Koehler stress is exactly the same for these two systems. Such a big difference in peak hardness can be explained in terms of the chemical stress, τ_{ch}, which can be estimated by [214, 215]

$$\tau_{ch} = \frac{\gamma_{Ag} - \gamma_{Fe}}{b} \qquad (3.7),$$

where τ_{ch} is chemical stress, γ_{Ag} and γ_{Fe} are respective SFE of Ag and Ni, and b is Burgers vector of Ag. In Ag/Ni, the SFE difference between Ag (10 mJ/m^2) and Ni (110 mJ/m^2) is very large, resulting in a large chemical stress term, ~ 0.3 GPa in Ag/Ni; while the chemical stress is negligible in Ag/FCC Fe (as FCC Fe also has very low SFE, ~20 mJ/m^2

[304]). Another interesting comparison is made between Ag/Fe and Ag/Al multilayers, where Ag/Al is more than 1 GPa harder than Ag/Fe multilayers. The Koehler stress in Ag/Al, is roughly an order of magnitude smaller than Ag/Fe (0.05 GPa vs. 0.44 GPa), but the chemical stress τ_{ch} for Ag/Al is significant, ~ 0.5 GPa, due to the giant SFE difference between Ag and Al (10 mJ/m^2 vs. 180 mJ/m^2). Consequently the Ag/Al multilayers have higher peak hardness than Ag/Fe multilayers [212].

The difference in SFE may determine the peak hardness of multilayers with FCC/FCC interfaces to a greater extent. Our recent studies show that the peak hardness of (100) textured Cu/FCC Co is much smaller than that of (100) Cu/Ni multilayers [211]. When Co transforms to FCC phase (in (100) Cu/Co multilayers), the chemical stress is very low as both Cu and FCC Co have low SFE. Consequently, the partial dislocations nucleated in FCC Cu may transmit across the Cu/FCC Co interface with low resistance. In contrast, the Cu/Ni system has a large SFE mismatch so that partials in Cu may have to constrict to perfect dislocations before they can transmit across the Cu/Ni interfaces (as Ni has a much greater SFE than Cu).

Comparison of normalized peak hardness (H_{peak}/G_{ave}) as a function of SFE difference $\Delta\gamma_{SFE}$ between two components in different Ag and Cu based multilayer systems (with FCC/FCC interfaces) is shown in Fig. 3.9. The dashed line shows a simple linear fit to the literature data. A clear trend is identified, that is H_{peak}/G_{ave} increases with increasing $\Delta\gamma_{SFE}$, indicating that chemical stress may play a major role in determining the peak strength of a variety of Ag and Cu based multilayer systems. Such an observation may provide a fresh perspective for the design of high strength metallic multilayers.

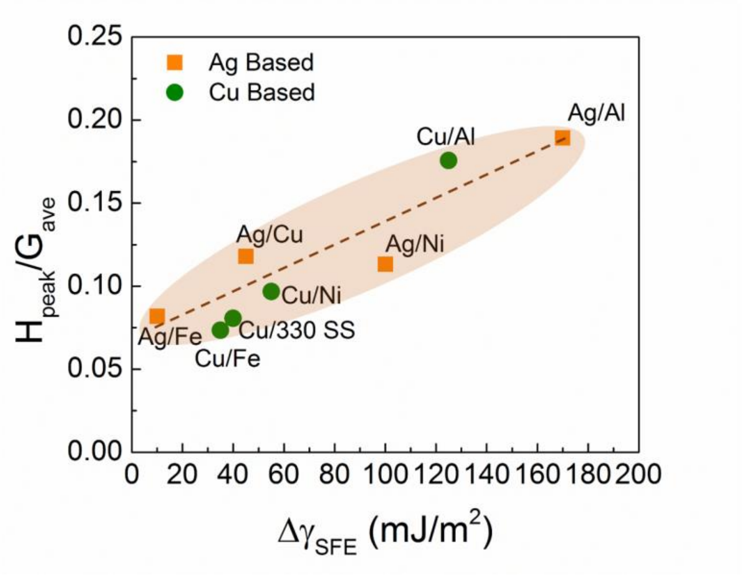

Fig. 3.9. Comparison of normalized peak hardness (H_{peak}/G_{ave}) as a function of stacking fault energy difference $\Delta\gamma_{SFE}$ between two components in different Ag and Cu based FCC/FCC multilayer systems. The dashed line shows a simple linear fit of the literature data. The values of H_{peak}/G_{ave} appear to increase with increasing $\Delta\gamma_{SFE}$, indicating that chemical stress due to stacking fault energy difference plays a significant role in determining the peak strength of these multilayers.

3.6 Conclusions

Ag/Fe multilayers with various individual layer thicknesses were deposited on Si (111) substrate by magnetron sputtering. The coherency between Ag and Fe increases with decreasing *h*. Nearly coherent interfaces form in Ag/Fe 1 nm multilayers. Phase transformation from BCC to FCC Fe occurred when h < 5 nm. Hetero-twinned interfaces were observed between adjacent Ag and Fe when *h* = 5 nm. Comparisons of hardness between Ag/Fe, Ag/Ni, Cu/Fe and Ag/Al reveal the significance of stacking fault energy of layer constituents in the determination of peak hardness of multilayers with FCC/FCC interfaces.

3.7 Acknowledgement

We acknowledge financial support by NSF-DMR-Metallic Materials and Nanostructures Program under grant no. 1304101. YC is supported financially by NSF-CMMI 1161978. S. Xue is supported by DoE-OBES under grant no. DE-SC0010482. We also acknowledge the use of microscopes at the Microscopy and Imaging Center at Texas A&M University and the DoE Center for Integrated Nanotechnologies managed by Los Alamos National Laboratory.

CHAPTER IV

IN SITU STUDY OF DEFECT MIGRATION KINETICS AND SELF-HEALING OF TWIN BOUNDARIES IN HEAVY ION IRRADIATED NANOTWINNED METALS*

4.1 Overview

High energy particles can introduce severe radiation damage in metallic materials especially those with low stacking fault energy. Twin boundary (TB) has recently been shown to enable the reduction of defect density in heavy ion irradiated nanotwinned Ag. However, the defect-twin boundary interaction mechanisms in nanotwinned metals remain poorly understood. Here we report on the study of TB affected zone wherein time accumulative defect density and defect diffusivity are substantially different from those in twin interior. *In situ* studies also reveal surprising resilience of TBs in response to radiation: TBs continue to change their geometry to facilitate the capture, transportation and removal of defect clusters and can recover by absorbing opposite type of defects. This study provides further support for the implementation of TBs as effective defect sinks for the design of radiation tolerant nanostructured metallic materials.

---

*Reprinted from "J. Li, K.Y. Yu, Y. Chen, M. Song, H. Wang, M.A. Kirk, M. Li, X. Zhang, In situ study of defect migration kinetics and self-healing of twin boundaries in heavy ion irradiated nanotwinned metals, Nano Lett, 15 (2015) 2922-2927" with permission from American Chemical Society.

4.2 Introduction

High-density irradiation induced defect clusters, such as dislocation loops and networks, voids, bubbles and stacking fault tetrahedra (SFT), can significantly undermine the mechanical properties of irradiated materials in form of radiation hardening, embrittlement, etc., [2, 9-12, 14, 17, 94, 305, 306]. Next generation nuclear reactors call for exploration of advanced structural materials that can sustain extreme radiation up to several hundred displacements-per-atom (dpa) [3, 4]. Nanostructured materials, such as nanocrystalline, nanolayered, nanoporous and nanotwinned (nt) materials, have high-density defect sinks that can alleviate radiation damage. Fine grained materials have shown significantly reduced defect density and radiation induced hardening [77, 131, 147, 242]. Grain boundary affected zones have been observed in various nanomaterials where defect clusters migrate toward grain boundaries swiftly before being absorbed. As a result, there are apparently fewer dislocation loops or He bubbles within grain boundary affected zones, a phenomenon also frequently referred to as the “grain boundary denuded zone” in the literature [243, 254, 307, 308]. Size dependence of radiation damage has been reported in He irradiated nanolayers where He bubble density and radiation induced hardening decrease drastically with the decrease of individual layer thickness [175, 241, 244, 246, 309]. More recently, NP metals have shown drastic impact on defect population [183] and migration dynamics [184] in single crystal and NP Ag. The local and global diffusivities of defect clusters has been measured to be quite different. In addition, NP Au showed enhanced radiation tolerance as long as the ligament size is within an optimum range [183]. Twin boundaries (TBs) are low energy boundaries that are generally anticipated to be less effective in alleviation of radiation damage, comparing to high angle GBs. However, Yu *et al* [89] reported that density of SFT in NT Ag strongly depends on average twin spacing as TBs can effectively remove SFTs. Moreover, *ex situ* [310] and *in situ* [89, 256] radiation studies have revealed frequent TB migration in irradiated NT metals. Beyond aforementioned nanostructured materials, other interesting structures and materials, such as nanopillars [170] and metallic glasses, have also been studied under radiation. For instance, the study on helium ion irradiated $Ni_{73}P_{27}$ indicated that metallic glasses exhibit an impressive resistance to high fluence of He ion irradiation, and could be a potential candidate for nuclear radiation applications [171].

Despite these prior studies, physics of radiation damage mechanisms in NT metals remains poorly understood. First, although one would anticipate the existence of twin boundary affected zones (TBAZs similar to GBAZs), it has been shown that defect density may not vary as a function of distance to TBs [310]. Second, in spite of the study of SFT removal by TBs, it is unclear if TBs can also remove dislocation loops. Third, it remains a challenge to measure defect migration kinetics in irradiated metallic materials [311], and defect migration kinetics in NT metals is largely unknown.

Here we provide evidence for the existence of twin boundary affected zones in NT metals, and compare the global and instantaneous diffusivity of defect clusters at different separation distance from TBs in NT Ag. *In situ* radiation studies revealed dislocation loop induced distortion of coherent twin boundaries (CTBs) and self-healing of TBs after absorbing opposite type of defect clusters. The outstanding self-healing capability of TBs has important implication for the design of materials under extreme radiation environment.

4.3 Experimental

Epitaxial NT Ag films, ~2 μm in thickness, were deposited through DC magnetron sputtering by using 99.99% purity Ag target onto HF-etched single-crystal Si (111) substrates at room temperature. Prior to deposition, the chamber was evacuated to a base pressure of ~1 × 10^{-5} Pa. Ag films were annealed at 700 ˚C for 0.5 h after deposition and an average twin thickness of ~70 nm was obtained. Cross-sectional transmission electron microscopy (TEM) specimens were prepared by grinding, polishing and ion-milling. Both as-annealed and post-irradiated specimens were investigated using an FEI Tecnai G2 F20 ST microscope. *In situ* irradiation experiment was performed at room temperature at the IVEM-TANDEM facility at Argonne National Laboratory. 1 MeV Kr^{2+} ion beam was used for radiation experiments to a maximum fluence of 2 × 10^{14} ions cm^{-2} (~ 1 dpa). The dose rate and beam current applied during *in situ* radiation expeirments are 1.25 × 10^{-3} dpa/s and ~250 nA, respectively. The radiation damage profile in unit of displacements-per-atom (DPA) has been calculated by using SRIM (Kinchin-Pease method). Most Kr ions (99.99%) penetrated directly through the specimen because the ion energy was as high as 1MeV and the TEM foil was very thin (~ 100 nm). The plateau of DPA profile in Fig. 4.S1 reveals that the damage was relatively uniform with respect to the depth of the irradiated specimen. The temperature rise of specimen during *in situ* Kr ion irradiation is typically less than 50^{o}C.

4.4 Results

As-deposited Ag has high-density growth twins with predominantly {111} CTBs. Before radiation, the TEM specimen was tilted to <110> zone Axis, nearly parallel to the direction of Kr ion flux as shown in Fig. 4.1a. Frequent migration of irradiation induced defect clusters was observed during *in situ* radiation experiment and an example is shown in Fig. 4.1 (b1-b6). These defect clusters are primarily interstitial loops and SFTs as reported in our previous study [89], and the average size of the defect clusters was calculated to be 6 ± 2 nm, nearly independent on their relative distance to the TBs. Abundant SFTs were observed in irradiated NT Ag. During radiation processes at room temperature, the interstitial loops are typically mobile, while vacancy loops and SFTs are immobile clusters [312]. A defect cluster generated in Zone A, which is in the center of a 60 nm thick twin in NT Ag, is labeled in Fig. 4.1b1. After a dwell time of 0.8 s, the defect cluster migrated over ~ 20 nm to position 1 within ~ 0.1 s (Fig. 4.1b2). The same defect cluster marched a few more times in Zone A by 14, 10 and 6 nm sequentially during subsequent irradiation (Fig. 4.1b3 - b5), until it was eventually removed (Fig. 4.1b6). Diffusion length and time were measured accordingly and the accumulative diffusion distance (*L*) as a function of accumulative time (*t*) is shown in Fig. 4.1c. Similar strategy was used to quantify defect migration kinetics in Zone B.

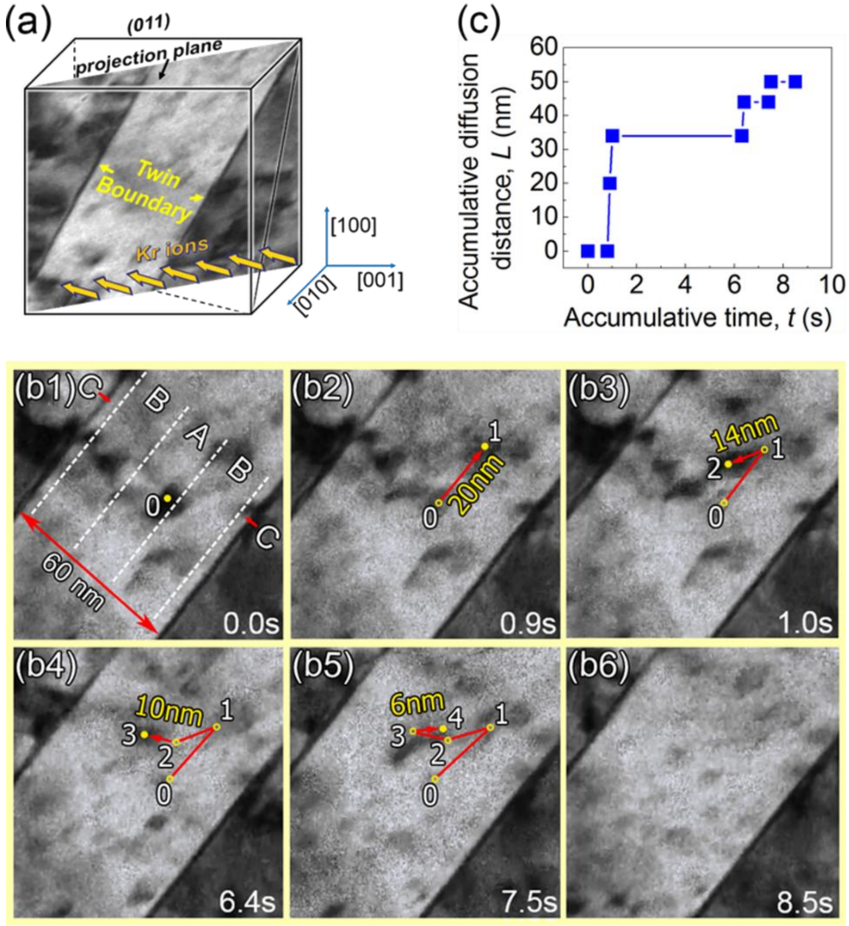

Fig. 4.1. Defect migration in Kr ion irradiated nanotwinned (nt) Ag. (a) Schematics showing the (011) zone Axis of NT Ag is nearly parallel to the direction of Kr ion flux. (b1-b6) *In situ* Video snapshots capturing defect migration kinetics in Zone A in the center of NT Ag. A defect cluster generated in Zone A at 0 s (b1) stayed static for 0.8 s, then migrated to position 1 over a distance of 20 nm within ~ 0.1 s (b2). The same defect cluster moved a few more times in Zone A during irradiation (b3-b5), until it was eventually removed (b6). (c) the plot of accumulative defect migration distance (L) versus accumulative time (t).

To investigate the impact of TBs on the evolution of defect density in irradiated NT Ag, the accumulative defect concentration in various zones was evaluated using a 4 min-long Video (0.6 - 1 dpa). As shown in Fig. 4.2a, the accumulative defect concentration in Zone A (central) is greater than those in Zone B (closer to TBs) and significantly higher than those in Zone C (closest to TBs). Zone C was determined by overlapping numerous Video frames. As shown in Fig. 4.2b, a majority of defects in Zone C were “born” at ~ 5 nm away from TBs. The yellow dash lines, which indicate the average distance from the edge of these defect clusters to TBs, demarcate the boundary of Zone C. Very few defect clusters were detected in Zone C because most of them were eventually removed by TBs. The history of defects in Zone A and B are intentionally not shown in Fig. 4.2b for clarity.

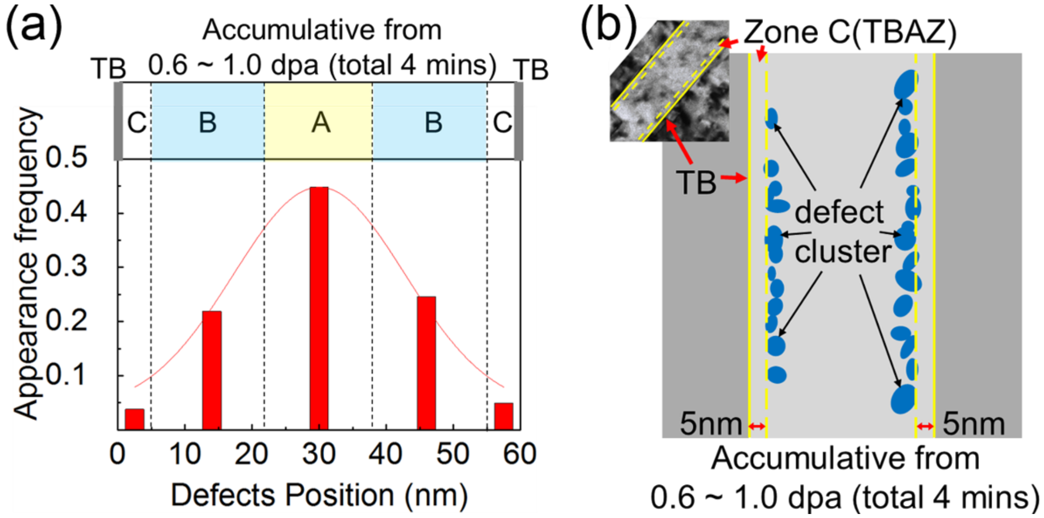

Fig. 4.2. The existence of twin boundary affected zone. (a) The accumulative defect concentration (0.6-1.0 dpa over 4 min) in Zone A (shown as appearance frequency) is significantly higher than those in Zone Bs. Zone Cs (closest to TBs) possess the lowest accumulative defect concentration. (b) Determination of Zone Cs by overlapping numerous frames captured during radiation. Abundant defects appeared to “park” at the boundaries of Zone Cs. The history of defects in Zone A and Bs are intentionally not shown for clarity.

Defect diffusivity was measured by tracking the migration of numerous individual defect clusters in the Video. The global diffusivity D^{Global} is determined by averaging accumulative diffusion distance $\boldsymbol{L}$ over defect's life time t (accumulative time), which includes both migration and dwell time; whereas instantaneous diffusivity, $D^{\mathrm{Inst.}}$, is measured by only considering the migration time (without dwell time). Several hundred mobile defect clusters were tracked through the analyses of the *in situ* radiation video. Among such a large number of defect clusters, ~ 50 defect clusters have distinguishable multiple migration events, permitting a reliable determination of of D^{Global} ($D^{\mathrm{Global}} = L^2/4t$). Fig. 4.3a shows a comparative plot of L^2 versus defect life time for numerous defect clusters in Zone A and B. Linear fit shows that the D^{Global} in Zone A ($D_{\mathrm{A}}{}^{\mathrm{Global}}$) is 40 ± 7 nm^2/s, which is ~ three times of that in Zone B ($D_{\mathrm{B}}{}^{\mathrm{Global}} = 13 \pm 2\ \mathrm{nm}^2/\mathrm{s}$). In comparison, $D^{\mathrm{Inst.}}$ exhibits little size dependence in both Zone B and C and is at least an order of magnitude greater than the respective D^{Global} (Fig. 4.3b). However, $D^{\mathrm{Inst.}}$ in Zone A is 1500 ± 150 nm^2/s, twice of that in Zone B (750 ± 100 nm^2/s).

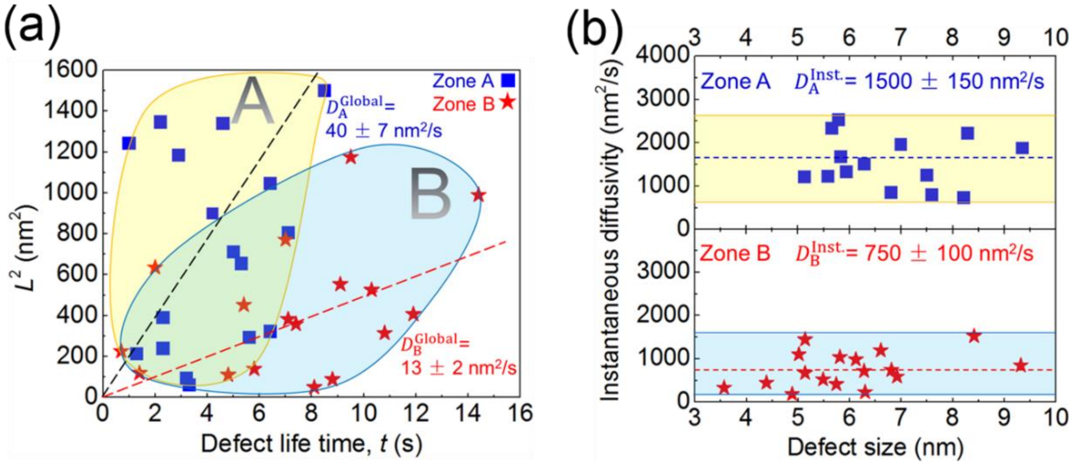

Fig. 4.3. Different defect migration kinetics in Zone A and B in irradiated NT Ag. (a) The global diffusivity, derived by fitting the the plot of L^2 as a function of defect life time (t) as indicated by the dash lines is 40 ± 7 nm^2/s for defect clusters in Zone A, ~ three times larger than that in Zone B, 13±2 nm^2/s. (b) Instantaneous diffusivities of defect clusters in Zone A is 1500 ± 150 nm^2/s, twice greater than that in Zone B, 750 ± 100 nm^2/s. The instantaneous diffusivities exhibit little size dependence in both zones.

4.5 Discussion

4.5.1 The evidence of twin boundary affected zones in irradiated NT metals

Previous *ex situ* study shows a lack of twin boundary affected zones in NT metals [310]. Here we show that by using accumulative defect statistics over a period of time obtained from *in situ* studies, there are apparent twin boundary affected zones next to TBs in NT Ag as evidenced by their lowest accumulative defect concentration. TBs are thus effective defect sinks for adjacent defect clusters. In addition to the prominent reduction of defect density in twin boundary affected zones, TBs also impose great influence on the defect migration kinetics in NT Ag.

4.5.2 Defect migration kinetics in NT Ag

Defect migration kinetics is crucial for the modeling of defect density, dimension and their evolution with radiation dose (time). However, the determination of defect migration kinetics (such as diffusivity) is non-trivial. In general, one has to track the migration of defect clusters continuously (dynamically) during radiation.

In this study, we calculated both global and instantaneous diffusivities of defect clusters and noticed a counterintuitive trend: the closer the separation distance to TBs, the lower the diffusivities of defect clusters. The influence of TBs on migration kinetics of defects is illustrated schematically for Zone A and B in Supporting Fig. 4.S5. Zone A (further away from TBs) contains higher defect density than Zone B, and consequently small interstitial loops interact frequently with the preexisting loops. Frequent migration of defect clusters in Zone A reduces dwell time and thus increases their global diffusivity. In contrast, defect clusters in Zone B are more sparsely distributed from one another (due to a lower defect density), and therefore their frequency of interactions become diminished, resulting in their lower diffusivities in Zone B. Recently Sun *et al* compared radiation tolerance between NP Ag and coarse grained (cg) Ag, and reported lower value of D^{Inst} for NP Ag, ~ 350 nm^2/s, comparing to 1200 nm^2/s in CG Ag. The value of D^{Global} for NP Ag is 12 nm^2/s, very close to that of NT Ag measured in the current study [184].

If TBs affect diffusivity of defect clusters, it is natural to speculate that the diffusivity of defect clusters may depend on twin spacing (or twin thickness). To validate such a hypothesis, we examined twins with different twin thickness in irradiated NT Ag. For a 40-nm-thick twin, the global diffusivity of defect clusters, is ~23 ± 5 nm^2/s in the center area (Zone A), and ~ 11 ± 4 nm^2/s in the area near TBs (Zone B). Clearly, the global diffusivity of defect clusters in Zone A of the 40-nm-thick twin is lower than that in the Zone A of the 60-nm-thick twin (40 ± 7 nm^2/s). Compared to the 60-nm-thick twin, more point defects (mainly interstitials) in the 40-nm-thick twin were absorbed due to a shorter migration distance to the TBs. The concentration of defect clusters in zone A of the thinner twin was therefore lower than that in the 60-nm-thick twin. Hence, the reduced interactions among sparsely spaced defect clusters may lead to longer dwell time, manifested as lower measured global diffusivity in the 40-nm-thick twin. The global diffusivity of defect clusters in Zone Bs (adjacent to TBs) in both cases is similar (11 ± 4 nm^2/s vs. 13 ± 2 nm^2/s). Reliable determinations of the diffusivity of defect clusters in twins with an average twin spacing of 13 nm or less become very difficult, primarily because there was a lack of mobile defect clusters in these fine nanotwins. This phenomenon is probably due to the overlap of the twin boundary affected zones on each side of the TBs in these fine nanotwins.

4.5.3 Dislocation loop-TB interactions: loop induced distortion of TBs and self-healing of TBs

Our previous studies [256, 313] have shown frequent migration of incoherent twin boundaries (ITBs) during radiation and CTBs can destruct SFTs. However, the interaction mechanisms between dislocation loops and CTBs remain unclear. In what follows we show a significant and representative event: CTBs can change their geometry to capture defect clusters.

Frequent distortions of CTBs during their capturing of different types of defect clusters were observed. A typical example is shown in Fig. 4.4 a1 – a4. At 0 s (Fig. 4.4a1), a CTB appeared straight. At 11 s, when a mobile interstitial loop emerged next to the CTB (Fig. 4.4a2), the CTB was distorted by forming a concavity (referred to as a puddle). Later the dislocation loop was partially captured by the curved CTB at 13 s (Fig. 4.4a3), and nearly completely absorbed by the CTB by 16 s (Fig. 4.4a4), leaving the puddle at position P1 along the CTB.

The next few snap shots show that such a distorted CTB can self-heal by absorbing opposite type of defect clusters. The puddle on the CTB remained at P1 at 16 s (Fig. 4.4a4), until a moment later, it was replaced by two neighboring undulations, labeled as P2 and P3 at 18 s in Fig. 4.4a5, adjacent to two SFTs (vacancy clusters). The two SFTs were then gradually absorbed by the hitherto deformed CTB (Fig. 4a6), and the CTB nearly recovered (self-healed) by 25 s (Fig. 4.4a7) as implied by the return of its straight appearance.

Schematics in Fig. 4.4b depict the distortion and self-healing of CTBs. A small interstitial loop was generated by radiation near a CTB (Fig. 4.4b1). As the interstitial loop grows, its stress field may be large enough to deform the adjacent CTB (Fig. 4.4b2), forcing it to bend rightwards. Meanwhile, the atoms at CTBs rearrange themselves to accommodate the shape variation. The absorption of interstitial loop by the CTB creates an interstitial-rich puddle locally. The newly captured interstitials on the CTB could be highly mobile. As shown in Fig. 4.4b4, the formation of two SFTs (vacancy clusters) near the CTB prompts the interstitials to rapidly redistribute themselves along the CTB into two smaller puddles right next to each SFT. The annihilation of interstitials with SFTs leads to the gradual self-healing of the CTB (Fig. 4.4b5-4b6).

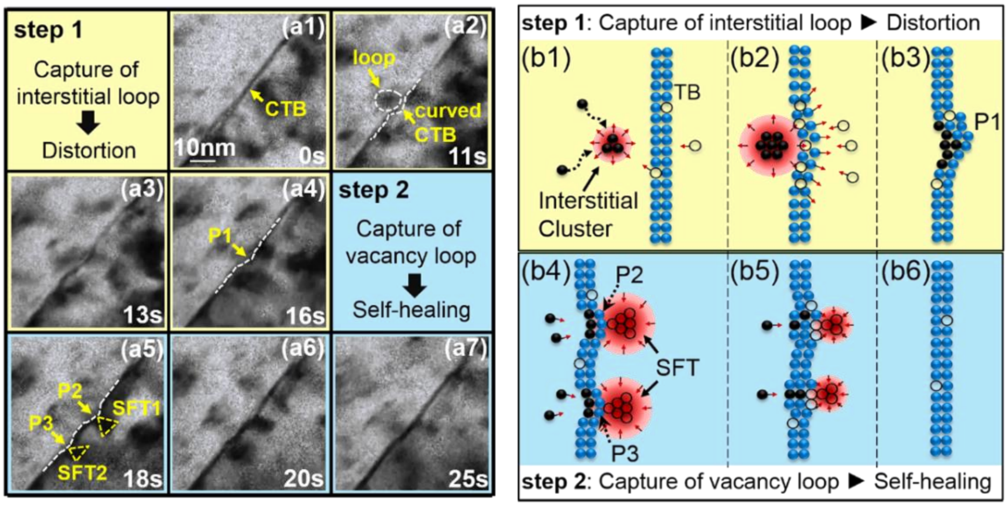

Fig. 4.4. Distortion and self-healing of CTBs. (a1-a4) Distortion of CTB and capture of an interstitial loop. An initially straight CTB (a1) formed a curved puddle upon its encountering of a mobile interstitial loop (a2). (a3-a4) The dislocation loop was eventually captured by the CTB, leaving the puddle at position P1. (a5-a7) The self-healing of CTB via absorption of SFTs (vacancy loops). The puddle on CTB at P1 (a4) was replaced by two undulations, labeled as P2 and P3 (a5). Two SFTs adjacent to each puddle were gradually absorbed by the CTB (a6). By 25 s (a7), the CTB was nearly recovered (self-healed). (b1-b6) Schematics illustrate the capturing of defect clusters by CTBs and their self-healing mechanism. The stress field of interstitial loops creates curvature in adjacent CTB (b1-b2). (b3) The atoms at CTBs rearrange themselves to accommodate the shape variation. (b4) The formation of SFTs prompts the interstitials stored in the puddle to quickly redistribute into two smaller puddles right next to each SFT. (b5-b6) The annihilation of interstitials with SFTs leads to the self-healing of the CTB.

Foregoing discussions provide natural yet significant insight on one type of defect cluster-CTB interaction mechanisms, highlighted by distortion and recovering of the CTB. A fundamental hypothesis emerges: the stress field surrounding a dislocation loop could distort the CTB, forming curved puddles, which could also be considered as a combination of discrete ITB and CTB steps. Next we attempt to estimate the stress field induced by a dislocation loop and compare such a value to the stress necessary to deform CTBs.

Khraishi et al., calculated the stress field, without losing generality, of a circular Volterra dislocation loop with a Burgers vector normal to the plane of the loop numerically [314]. Using a similar method, the stress field components relevant for the distortion of TB, including σ_{xx}, σ_{yy} and σ_{xy} can be calculated. For instance, σ_{xx} is calculated under global coordinate system $(x\,y\,z)$ by:

$$\sigma_{xx} = \frac{x^2}{\rho^2}\sigma_{x'x'} + \frac{y^2}{\rho^2}\sigma_{y'y'} \tag{4.1}$$

where $\sigma_{x'x'}$ and $\sigma_{y'y'}$ are stress components under local coordinate system $(x'y'z')$, and can be calculated by:

$$\begin{aligned}\sigma_{x'x'} &= -\frac{Gb_z^{'}}{\pi}[C_1\mathbf{E}(k)+C_2\mathbf{K}(k)] - \frac{Gb_z^{'}}{2\pi(1-\nu)}[C_3\mathbf{E}(k)+C_4\mathbf{K}(k)]\,,\\ \sigma_{y'y'} &= -\frac{Gb_z^{'}}{\pi}[C_5\mathbf{E}(k)+C_6\mathbf{K}(k)] - \frac{Gb_z^{'}}{2\pi(1-\nu)}[C_7\mathbf{E}(k)+C_8\mathbf{K}(k)]\end{aligned} \tag{4.2}$$

where *G* is the shear modulus, and *v* is Poisson's ratio, which are 30 GPa and 0.37 respectively for Ag in this study. **K**(*k*) and **E**(*k*) in equation (4.2) are complete elliptic integrals of the first and second kinds respectively, where *k* is the modulus of these integrals or functions. $b_z^{'}(=b_z=0.289\,\text{nm})$ is Burgers vector of loop along z-axis. Coefficients C_1 -C_8 are given in Supporting Information. For the dislocation loop with radius of 4 nm (Fig. 4.4a3), the stresses σ_{xx}, σ_{yy} and σ_{xy} on adjacent CTB are calculated to be ~ 110, 110 and 80 MPa, respectively.

A recent *in situ* nanoindentation study on NT Cu [315] showed that the stress to induce migration of ITB or Shockley partials is as low as 100 MPa, similar to the prediction from molecular dynamics simulations [316]. Although there is no theoretical calculation on the shear stress needed for migration of ITB in Ag, given Ag has a lower elastic modulus than Cu, we suspect that the stress for ITB migration in Ag should be similar to or smaller than that in Cu. Thus the stress generated by the dislocation loop may be sufficient to provide both climb and glide force for Shockley partials to migrate perpendicular to and along CTB. Consequently a curved TB consisting of many discrete ITB and CTB steps emerges.

4.6 Conclusions

Nanotwinned epitaxial Ag was *in situ* irradiated using Kr ions at room temperature to explore mechanisms of dislocation loop - TB interactions. TBs are effective defect sinks that drastically reduce defect population within twin boundary affected zones. The stress field of loops can induce geometry change for TBs so that they can actively engage and remove defect clusters. Furthermore, TBs accelerate recombination of unlike defects by rapid transportation of interstitials along TBs to regions with high vacancy concentration, greatly increasing the odds for annihilation of opposite types of loops and consequently TBs self-heal. The impressive capture-recovering capability makes TBs attractive defect sinks for the design of radiation tolerant metallic materials.

4.7 Acknowledgement

We acknowledge financial support by NSF-DMR-Metallic Materials and Nanostructures Program under grant no. 1304101. YC is supported financially by NSF-CMMI 1161978. KY Yu and the work on fabrication of nanotwinned metal are supported by DOE-OBES under grant no. DE-SC0010482. We also thank Peter M. Baldo and Edward A. Ryan at Argonne National Laboratory for their help during *in situ* irradiation experiments. The IVEM facility at Argonne National Laboratory is supported by DOE-Office of Nuclear Energy. Access to the DOE - Center for Integrated Nanotechnologies (CINT) at Los Alamos and Sandia National Laboratories and Microscopy and Imaging Center at Texas A&M University is equally acknowledged.

CHAPTER V

IN SITU STUDIES ON TWIN THICKNESS DEPENDENT DISTRIBUTION OF DEFECT CLUSTERS IN HEAVY ION IRRADIATED NANOTWINNED AG*

5.1 Overview

Recent studies have shown that twin boundaries are effective defect sinks in heavy ion irradiated nanotwinned (nt) metals. Prior *in situ* radiation studies on NT Ag at room temperature indicate that the accumulative defect concentration is higher in center areas in the 60 nm-thick twins, and twin boundaries are distorted and self-healed during the absorption of different types of defect clusters. In this follow-up study, we show that the spacial distribution of accumulative defect concentrations in NT metals has a clear dependence on twin thickness, and in certain cases, the trend of spatial distribution is reversed. Potential mechanisms for the counterintuitive findings are discussed.

5.2 Introduction

Heavy ion irradiations can introduce a significant amount of defect clusters in metallic materials including dislocation loops, vacancy clusters, precipitates and voids [6-8]. Consequently, the mechanical properties of irradiated metallic materials can be

---

*Reprinted from "J. Li, Y. Chen, H. Wang, X. Zhang, In situ studies on twin-thickness-dependent distribution of defect clusters in heavy ion-irradiated nanotwinned Ag, Metallurgical and Materials Transactions A, 48 (2017) 1466-1473" with permission from Springer.

severely undermined in terms of irradiation hardening, embrittlement, irradiation-induced void swelling, etc [13-17]. Numerous types of high-energy boundaries, such as grain boundaries (GBs), phase boundaries and free surfaces, have proven to be effective defect sinks that can alleviate irradiation damage in materials [76, 77, 83, 89, 131, 147, 172, 174, 178, 183, 184, 257, 317]. For instance, MD simulations show that GBs can act as efficient defect sinks by absorbing irradiation-induced interstitials or serve as sources to emit interstitials to annihilate vacancies [243]. Grain boundary affected zones (GBAZs, or grain boundary denuded zones (GBDZs)) have been reported in several previous studies, where the concentration of defect clusters, such as dislocation loops or He bubbles, is drastically reduced near GBs [254, 307, 308]. In metallic multilayers certain types of layer interfaces can act as efficient defect sinks, and size-dependent enhancement of radiation tolerance was observed in various multilayer systems [241, 244, 245, 262, 317]. In addition, free surface may have infinite sink capacity, and nanoporous (np) materials with a large surface-to-volume ratio may have superior irradiation resistance [183, 188, 257].

Comparing to aforementioned high-energy defect sinks, twin boundaries (TB) are low energy boundaries and are generally anticipated to be less efficient defect sinks. Han *et al.* showed that the width of void denuded zone in non-Σ3 GBs is much greater compared to Σ3 TBs, indicating low sink efficiency of TBs [254]. A recent study on He ion implantation of nanotwinned (nt) Cu at room temperature suggests that TBs are poor sinks because point defects at Σ3 TBs have nearly identical properties to those in pure face-centered-cubic (FCC) Cu [255]. However, Niewczas and Hoagland reported, through MD simulations, that the interaction between Σ3 {111} coherent twin boundaries (CTBs) and stacking fault tetrahedra (SFTs) lead to the destabilization of SFTs [51]. Yu *et al.* validated the MD simulation experimentally by using *in situ* Kr ion irradiation study of NT Ag and showed that the density of SFTs in NT Ag is much lower than that in its bulk counterpart [89]. They also observed the frequent migration of incoherent twin boundaries (ITBs) [256]. Recent *in situ* study on NT Ag provided more evidence that TBs are effective defect sinks [179]. First, TBs may actively engage with defect clusters as evidenced by the distortion and self-healing of TBs during interaction with different types of defect clusters. Second, TB affected zones (TBAZs) have been identified. Time accumulative defect density and defect diffusivity within TBAZs are substantially distinct from those in twin interior. More specifically, the accumulative defect concentration within a 60 nm-thick twin is significantly higher in the central area than in the areas close to CTBs, and defect clusters form within the regions that are ~5 nm away from CTBs [179].

If TBs affect the distribution of defects during irradiation, it is natural to conjecture that the defect concentration profile may depend on twin thickness, *t*. To validate such a hypothesis, we performed *in situ* radiation studies on NT Ag at 473K (200^{o}C), with *t* varing from 10 to 120 nm. The *in situ* studies show that the accumulative concentration of irradiation-induced defects indeed exhibits twin-thickness dependence. In the thicker twins, more defect clusters were detected in central areas than that close to TBs. However, an opposite trend has been observed in 20 nm-thin twins, where the central area exhibits slightly lower accumulative defect concentration than the areas close to TBs. Potential mechanisms that lead to twin thickness dependent distribution of defect concentration are discussed.

5.3 Experimental

Epitaxial 1μm-thick NT Ag films were deposited onto HF-etched single-crystal Si (111) substrates at room temperature by the magnetron sputtering technique. X-ray diffraction (XRD) experiments were performed on a PANalytical X'Pert PRO Materials Research Diffractometer (Cu Kα radiation) at room temperature. Cross-sectional transmission electron microscopy (XTEM) specimens were prepared for *in situ* irradiation studies. Detailed specimen preparation method can be found elsewhere [226]. *In situ* irradiation experiment was performed at the IVEM-TANDEM facility at Argonne National Laboratory. Before irradiation, specimens were annealed inside microscope at 473K (200^{o}C) for about 15 min to remove some pre-existing defects. Specimens were then irradiated under 1 MeV Kr^{2+} ion beam up to a maximum fluence of 2×10^{14} ions cm^{-2} (~1 dpa) at 473K (200^{o}C). The radiation damage profile in unit of displacements-per-atom (dpa) has been calculated by using the SRIM (Stopping and Range of Ions in Matter) with Kinchin-Pease method [179]. Most Kr ions (99.99%) penetrated directly through the specimen because the TEM foil was very thin (~100 nm). The temperature rise of specimens during *in situ* Kr ion irradiation is typically less than 10 °C. Post radiation analysis was performed on an FEI T20 transmission electron microscope operated at 200 keV.

5.4 Results

The XRD profile of the as-deposited films in Fig. 5.1a shows predominant Ag (111) and (222) peaks, indicating the epitaxial growth of films on Si (111) substrates. The bright-field XTEM micrograph in Fig. 5.1b shows high-density growth twins with TBs parallel to the substrate surface. The inserted selected area diffraction (SAD) pattern reveals the epitaxial growth of NT Ag. The average twin spacing of as-deposited films is ~ 11 nm. During irradiation, a number of defects, consisting primarily of interstitial loops and SFTs, are generated, and Fig. 5.1c shows the typical microstructure of NT Ag that has been irradiated to 0.5 dpa.

TEM snapshots taken from *in situ* video are adopted to systematically investigate the number and dimension of radiation-induced defects. As shown in Fig. 5.2a, the average defect size after radiation to 0.025 dpa increases with t and reaches a constant of ~ 8 nm when t ≥ 30 nm (defect size is measured along the longest dimension and the error bar represents standard deviation). Statistical analysis performed after radiation to 0.025 dpa shows nearly identical results. Accumulative defect density (within 0.025 dpa shown in Fig. 5.2b) increases with increasing t, and appears to reach a saturation when t ≥ 50 nm. The defect density in thicker twins (t ≥ 50 nm) is twice as large as that in thinner twins (t ≤ 20 nm).

For most ex situ studies, to estimate the concentration of irradiation-induced defects, data are typically derived for a particular dose. The calculated concentration at a particular dose is therefore referred to as instantaneous defect concentration. In situ studies provide an opportunity to track the evolution of defects with time and dose during radiation. In this in situ study, a different method was used to probe the evolution of defect concentration during radiation to obtain accumulative defect concentration. Fig. 5.3 shows the difference between instantaneous and accumulative defect concentrations with respect to their positions in an 80 nm-thick twin in NT Ag. A TEM snapshot in Fig. 5.3a demonstrates the twin of interest that appeared relatively clean before irradiation. Fig. 5.3b and 3e are the same TEM snapshot captured at the dose of 0.005 dpa via in situ video. Two methods were adopted to calculate defect concentration. For method ①, red circles

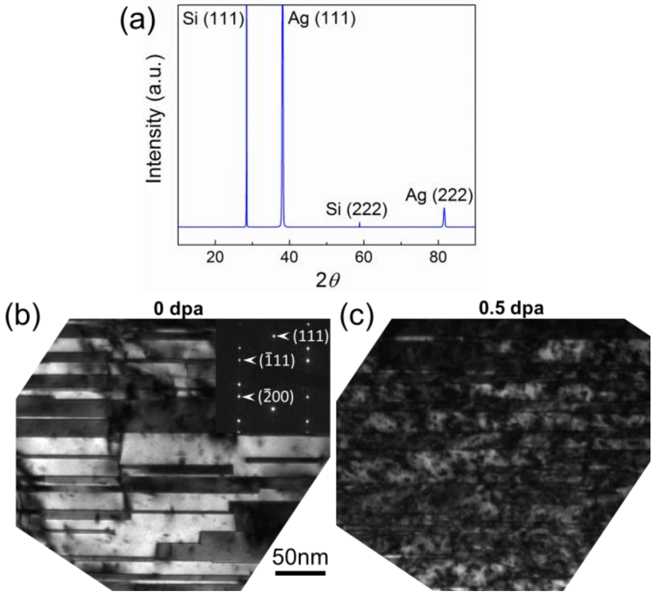

Fig. 5.1. (a) The XRD profile shows predominant Ag (111) and (222) peaks. (b) A bright field cross-section TEM (XTEM) micrograph showing the high density growth twins in as-deposited NT Ag film. The inserted selected area diffraction (SAD) pattern reveals single-crystal-like structure. (c) The influence of radiation damage on the microstructure of NT Ag after radiation (the TEM micrograph was taken in an area close to (b), but not exactly the same).

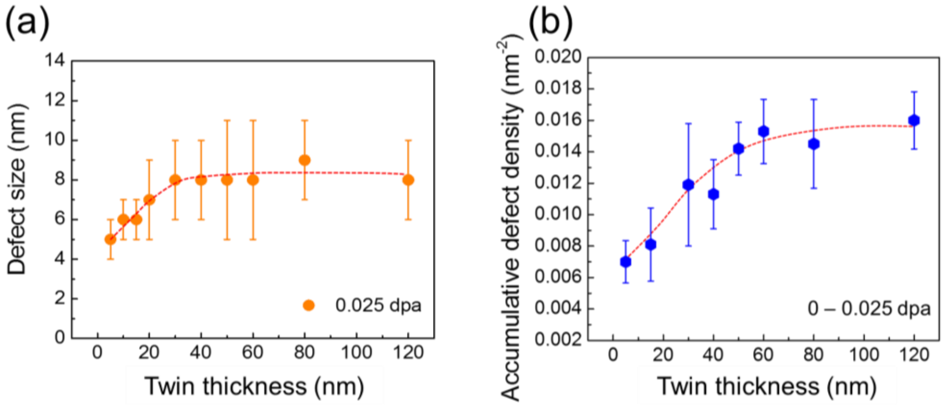

Fig. 5.2. (a) Statistics of defect size at 0.005 and 0.025 dpa versus twin thicknesses (t). The average defect size increases with twin thickness t and reaches a constant of ~ 8 nm when t ≥ 30 nm. (b) Accumulative defect density (within 0.025 dpa) increases with increasing t, and the defect density in thicker twins (t > 40 nm) is twice as large as that in thinner twins (t < 30 nm).

indicate the positions of defect clusters appeared on the single snap shot taken at 0.005 dpa, and the distribution of these defects within the twin is plotted in Fig. 5.3c. On the x-axis, zero represents the center of the twin, and ± 40 nm corresponds to the location of the TBs for an 80 nm thick twin. Fig. 5.3c shows a uniform distribution of defects derived from the single snap shot in Fig. 5.3b. In contrast, method ② considers defects observed (generated) both during irradiation up to 0.0042 dpa (indicated by blue circles) and at 0.005 dpa, that is Fig. 5.3b + Fig. 5.3d = Fig. 5.3e), and correspondingly there appear to be more labeled defects in Fig. 5.3e. The distribution of all defects, labeled as red and blue in Fig. 5.3e, with respect to their position is shown in Fig. 5.3f. The center areas exhibit evidently higher concentration of defects (when blue circles are taken into account).

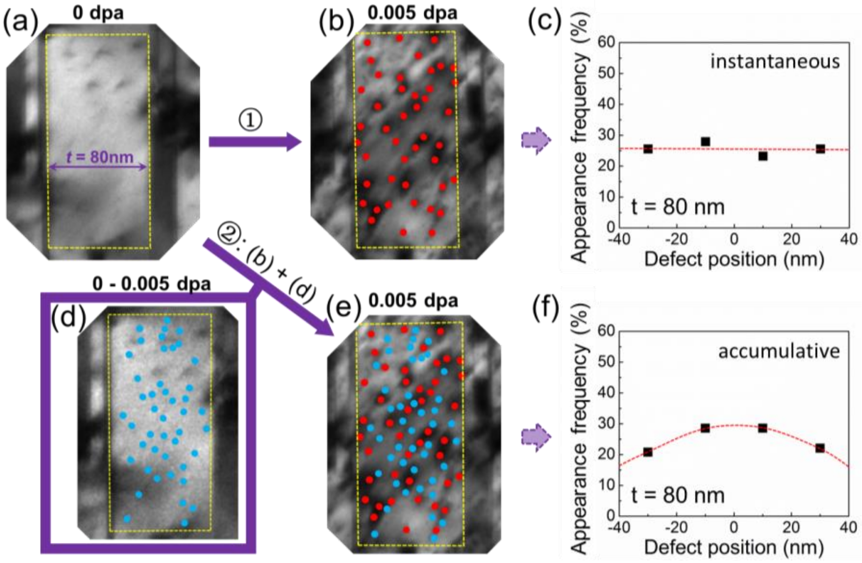

Fig. 5.3. The difference between instantaneous and accumulative defect concentrations with respect to their positions in an 80nm-thick twin in NT Ag. A TEM snapshot shows a twin matrix appeared relatively clean at 0 dpa (a). (b) and (e) are the same TEM snapshot at 0.005 dpa. ① and ② are different methods when calculating defect concentration. For method ①, red circles indicate the positions of those defect clusters appeared on the single snap shot was taken at 0.005 dpa. (c) The distribution of defects (outlined in red circles in Fig. 3b). A uniform distribution indicates that defects distributed evenly at a single snap shot. In contrast, method ②considered the blue circles accumulated during 0.005 dpa and defects captured at 0.005 dpa ((b) + (d) = (e)). (f) shows the distribution of all circles, both red and blue, in (e) with respect to their position. The center areas exhibit higher concentration when blue circles are taken into account.

By using the method ② as described in Fig. 5.3, the distributions of accumulative defect concentrations during irradiation up to 0.025 dpa in twins with various twins thicknesses are shown in Fig. 5.4 a. The position of x = 0 is defined as the center of the twinned crystals, whereas the left and right Y axis represent the locations of two TBs. The minimum bin width of investigated regions is 5 nm. When t = 10 nm, defect clusters distributed nearly uniformly as shown in Fig. 5.4b, while more defects appear close to TBs when t = 20 nm (Fig. 5.4c). When t = 40 nm, defects tend to distribute relatively uniformly within the twins (Fig. 5.4d). When t ≥ 60 nm, the accumulative frequency of defect concentration in the center areas is higher than that near the TBs as shown in Fig. 5.4e-f.

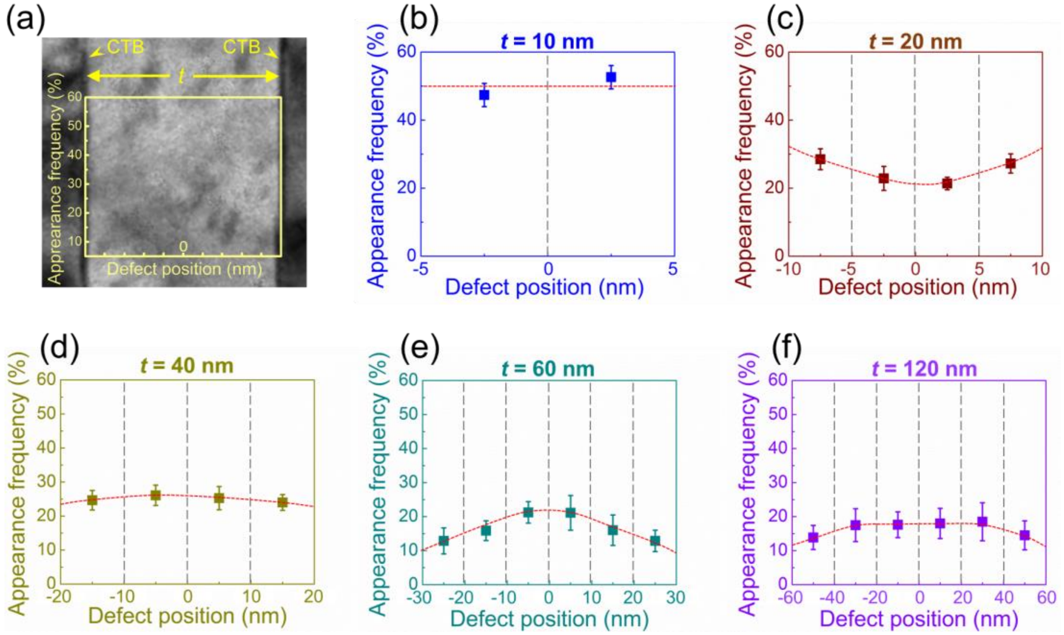

Fig. 5.4. Accumulative appearance frequency of defect clusters during 0.025 dpa in NT Ag with respect to defect position for twins with different thicknesses. (a) The position of 0 (center axis) is defined as the center of the twinned crystals. The left and right Y axis represent the two twin boundaries. The minimum width of sampled regions is 5 nm. (b) When t = 10 nm, defect clusters distributed nearly uniformly. (c) When t = 20 nm, more defects appeared close to twin boundaries. (d) When t = 40 nm, defects tend to distribute relatively uniformly through the twins. (e-f) When t ≥ 60 nm, the accumulative frequency of defect concentration in the center areas is higher than near the twin boundaries.

5.5 Discussion

To alleviate radiation-induced damage in metallic materials, various types of defect sinks have been investigated over the years. Recent studies show nanostructured metallic materials, such as nanoporous (np), nanocrystalline (nc) and nanolayered metallic materials may have outstanding radiation tolerance compared to their bulk counterparts as evidenced by smaller or less irradiation-induced defects. Most of these defect sinks, such as free surface, high angle GBs or phase boundaries are high energy defect sinks. And thus the general perception has been that high-energy defect sinks may have a greater impact on the alleviation of radiation damage than low energy defect sinks, such as TBs. However, there are increasing evidence that shows TBs in NT metals may significantly reduce radiation damage. For instance, it has been reported that the density of SFTs and dislocation loops formed during heavy ion irradiation decreased sharply in NT metals with small twin thickness as compared to that in thicker twins [89]. In our *in situ* study of heavy ion irradiation of NT Ag at 473K (200^{o}C), the average defect size decreases from 8 nm (when $t \geq 30$ nm) to 5 nm (when t = 10 nm) as shown in Fig. 5.2a.

For NT Ag irradiated at room temperature, the major types of defects are interstitial loops (mobile) and SFTs (immobile). In the present study, although the radiation temperature is higher, the defects are somewhat similar, consisting of SFTs, vacancy and interstitial loops. The present study was performed at the temperature range between Stage III and Stage V. At such temperature regime, both interstitials and vacancies are mobile. The predominant visible features for irradiated FCC metals in this temperature regime are vacancy and interstitial loops and SFTs [36]. For FCC metals with medium- to high-atomic number, such as Ag, exposed under energetic cascades (heavy ion irradiation in this case), most vacancies are bundled in sessile vacancy clusters (such as SFTs). As a result, the major type of observed dislocation loops in FCC metals in this temperature regime are of interstitial type. Void nucleation and growth are largely suppressed.

The accumulative defect density is also less in fine twins than that in thicker twins, indicating that the formation of defect clusters becomes increasingly difficult when twin thickness is smaller. The concentration of interstitials can be expressed by a chemical rate equation [318]

$$\frac{\partial C_i}{\partial \tau} = R - R_{iv}C_iC_v - R_{is}C_iC_s \qquad (5.1)$$

where τ is time, R is the atomic displacement rate and C_i, C_v and C_s are respective concentration of interstitials, vacancies and defect sinks (TBs in this case). R_{iv} is recombination rate of interstitial and vacancy and R_{is} is the absorption rate of interstitials. Before the steady state concentrations of interstitials and vacancies are attained (In this regime, sinks contribute to interstitial annihilation ,C_i, can be calculated as [318]

$$C_i = \left(\frac{R}{R_{iv}R_{is}C_s\tau}\right)^{1/2} \qquad (5.2)$$

In equation (5.2), R, R_{iv} and R_{is} are all constant and $C_s \propto 1/t$ (t is twin thickness), therefore, C_i is proportional to $t^{1/2}$, that is $C_i \propto t^{1/2}$. This simple analysis suggests that interstitial concentration can be effectively reduced in fine twins, in qualitative agreement with our experimental observations.

GBAZs (or GBDZs) have been observed in various metallic materials [254, 307, 308] while TBAZs are rarely reported [179]. In this study, we show that *in situ* technique provides an opportunity to reveal the existence of TBAZs. For most *ex situ* studies, in general, a single or a couple of TEM micrographs are used to study defect density in irradiated materials. In a dynamic process during irradiation, defects are continuously generated and they frequently recombine or annihilate during irradiation, and therefore the instantaneous defect concentration (obtained in a single snapshot) and accumulative defect concentrations (accrued within a period of time) could be very different. This hypothesis has been illustrated in Fig. 5.3, which shows the prominent difference between instantaneous and accumulative defect concentrations in an 80 nm-thick twin. More specifically the accumulative defect analysis reveals the existence of TBAZs. An analogy of such a statistical analysis is the methodology to compare the traffic flow during weekdays vs. weekends. In that case, enough statistics must be accrued during all 5 weekdays and 2 weekends over a period of months or years, rather than comparing the statistics of one weekday vs. one weekend. The width of TBAZs in NT Ag irradiated at 473K (200^{o}C), is ~ 5-15 nm, comparable to the width of TBAZ observed in NT Ag irradiated at room temperature, ~ 5 nm [179].

Our previous studies show in a 60 nm-thick twin in NT Ag irradiated at room temperature up to 0.6-1.0 dpa, the accumulative defect concentration is higher in the center of twins, similar to the observation reported in this study (when $t \geq$ 40 nm). However, the opposite concentration profile has been observed in this study when t = ~ 20nm, that is the concentration of defects is lower in the center of twins. This observation is quite surprising and requires further discussion. One should also note that the previous study on spacial distribution of defect in NT Ag was derived when a steady state defect concentration has been reached. In this case, thermodynamics works better and can predicts that defect density should be lower near defect sinks. Whereas the current study of NT Ag at 473K (200^{o}C) focus on an ultra-low dose regime (<0.025 dpa), where a steady state defect concentration has not been established, and the chance for recombination or growth defect clusters is insignificant. Hence the discussion on interpretation of spacial distribution of defect density in this case should eye more on kinetics (migration of defects and their clusters).

For a defect cluster to be absorbed (annihilated) by TBs, the defect cluster normally experiences two stages, migration and absorption. As reported in our previous study in NT Ag irradiated at room temperature [179], when a defect cluster approaches to a TB, it will interact with the TB before being absorbed. And this interaction-absorption process in general takes a few seconds according to our *in situ* observations. The time for a TB to absorb adjacent defect clusters, τ_a, is mainly affected by defect size when dose rate is constant. In contrast, the time for a defect cluster to travel (migrate) to TBs (defect sinks), τ_t, not only depends on defect size but also the travel distance. A longer travel distance (as TB is further away from the defect cluster) normally leads to a greater τ_t. Fig. 5.5 illustrates two different scenarios during the competition between τ_t and τ_a. The first scenario (Case I), describes the defect accumulation in fine twins, where $\tau_t < \tau_a$. At the beginning of radiation (Fig. 5.5a), irradiation-induced defect clusters are randomly distributed within a twin, where several defect clusters close to a TB are labeled as “1”s, and some defect clusters are located in the central area (labeled as “2”s). After a time period of τ_t, most of the group 2 defects (in the center) come closer to the TBs due to the existence of defect sinks (or TBAZs) (Fig. 5.5b). However, as $\tau_t < \tau_a$, that is the absorption of group 1 defect

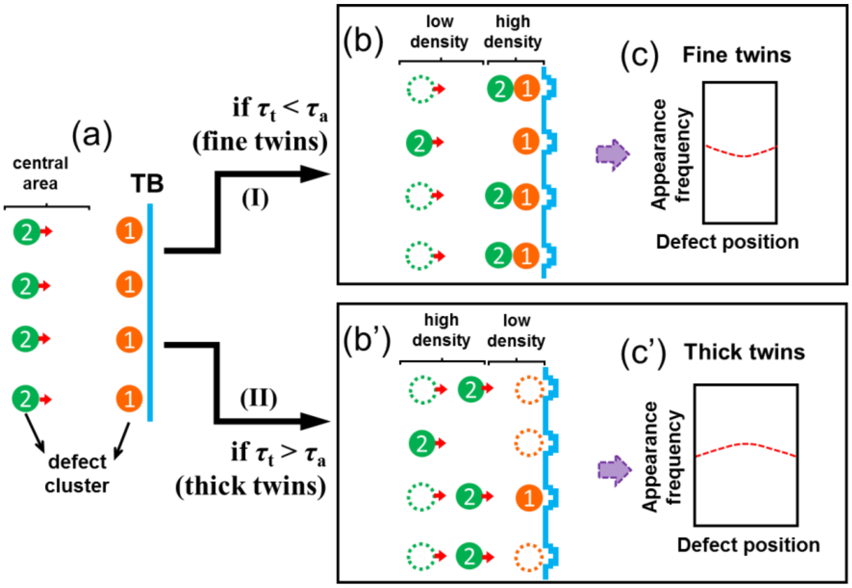

Fig. 5.5. Schematics illustrating the opposite types of defect distribution in twinned metals. Case I: $\tau_t < \tau_a$ (a-b-c); and case II: $\tau_t > \tau_a$ (a-b'-c'). τ_t is the time for a defect cluster to travel (migrate) to twin boundaries (defect sinks), and τ_a is the time it takes for a twin boundary to absorb adjacent defect clusters. (b) In case I (a-b-c), when twins are very fine, as $\tau_t < \tau_a$, defects (labeled as "2"s) arrive at twin boundary before predecessors (marked as "1"s) can be absorbed, and thus defect clusters pile-up near the TBs, and consequently leads to higher defect density near the TBs (c). Note that the TBs are distorted while attempting to absorb adjacent defect clusters. Case II: The scenario becomes the opposite for thick twins, it is likely that $\tau_t > \tau_a$, that is the arrival of group 2 defect clusters takes longer time than the absorption of defect clusters (group 1 adjacent to TBs). (c') Thus the central area exhibits higher defect density.

clusters has not been completed before the arrival of newcomers, defect clusters will build up near the TB. Consequently, the central area has fewer defect clusters than near the TBs (Fig. 5.5c). In the second scenario (Case II) for thicker twins, we assume that $\tau_t > \tau_a$. In this case, it is likely that the absorption of group 1 defect clusters is faster than the migration of group 2 defect clusters, that is defect clusters adjacent to TBs can be absorbed before the arrival of incoming dislocation loops (due to the longer migration distance in thicker twins (Fig. 5.5b'). Consequently, the density of defect clusters generated in the central area will exceed that in the area close to the TB (Fig. 5.5c'), which is a classical example for the evidence of TBAZs.

If the foregoing hypothesis is correct, then it is natural to speculate that the accumulative defect concentration is equal everywhere within the twins when $\tau_\mathrm{t} = \tau_\mathrm{a}$. To verify the hypothesis, the absorption time τ_a for defect cluster is estimated. The global diffusivity, D_g, of the defect clusters close to TBs is measured to be ~ 13 nm^2/s for NT Ag irradiated at room temperature [179]. Thus, τ_t can be calculated from $L = 2 \cdot \sqrt{D_\mathrm{g}\tau_\mathrm{t}}$, where L is travel distance. In this study, a nearly uniform defect distribution is observed when t = 40 nm as shown in Fig. 5.3d. For a defect cluster formed in the center of the 40 nm thick twin, L is 20 nm (= t/2). Therefore τ_a (= τ_t) is calculated to be ~ 8 s. Our previous study on *in situ* study of radiation damage in NT Ag at room temperature shows that the absorption time of dislocation loops by CTBs is typically ~ 5 s [179]. Notice that D_g used in the aforementioned estimation is obtained at room temperature. The irradiation temperature used in this study is 473K (200$^\mathrm{o}$C), thus D_g may be larger at this temperature, and thus the estimated τ_a could be shorter than that obtained at room temperature.

Nonetheless, the forgoing discussion provides an opportunity to probe defect migration/annihilation kinetics in irradiated materials in close proximity to defect sinks. When a flat distribution profile of defect clusters is measured (an indication of $\tau_\mathrm{a} = \tau_\mathrm{t}$), one can estimate defect absorption time (by defect sinks), if the global diffusivity of defect clusters can be determined and vice versa.

5.6 Conclusion

In situ heavy ion irradiation studies were performed on nanotwinned Ag at 473K (200^{o}C). Our studies show that the accumulative concentration of irradiation-induced defects exhibits twin-thickness dependence that is more defect clusters were detected in central areas than that close to TBs in thicker twins ($t > 40$ nm), and an opposite trend has been observed in fine twins ($t = 20$ nm). Such twin-thickness-dependent distribution of defect concentration is considered as a result of the competition between defect travel time τ_t and defect absorption time τ_a. The number of defect clusters generated in the central area will be greater than that in the area close to the TB if $\tau_t > \tau_a$ (for thicker twins) due to the longer migration distance. However, if $\tau_t < \tau_{a,}$(in the case of thin twins), then the central area has fewer defect clusters than near the TBs.

5.7 Acknowledgement

We acknowledge financial support by NSF-DMR-Metallic Materials and Nanostructures Program under grant no. 1643915. We also acknowledge the access of microscopes at the Microscopy and Imaging Center at Texas A&M University and the DoE Center for Integrated Nanotechnologies managed by Los Alamos National Laboratory. The IVEM facility at Argonne National Laboratory is supported by DOE-Office of Nuclear Energy.

CHAPTER VI

ENHANCED RADIATION TOLERANCE AND RADIATION STABILITY OF NANOTWINS IN AG-1AT.%FE ALLOY

6.1 Abstract

Face-centered cubic metals with low stacking fault energy, such as Ag and Cu, are in general vulnerable to high-energy ion irradiation. Our previous studies have shown by introducing high-density defect sinks, such as twin boundaries, the irradiation tolerance of nanostructured monolithic Ag and Cu can be greatly enhanced. However nanotwins in monolithic metals may detwin during radiation. In this study, we report a follow-up study that shows drastically improved irradiation stability of twin boundaries in Ag. By adding merely 1 at.% of Fe solute atoms into Ag matrix, ultra-high-density twins with an average twin thickness of ~ 3 nm form in Ag. In situ Kr ion irradiation studies show that defect size and density in AgFe have been significantly reduced comparing with monolithic coarse-grained Ag and nanotwinned Ag. Furthermore, these extremely fine twins survived the heavy ion irradiation. The mechanisms that lead to enhanced radiation tolerance are discussed.

6.2 Introduction

Irradiation of metallic materials by energetic particles, such as neutrons and heavy ions, introduces a large population of point defects and small defect clusters in the displacement cascades. These defects can interact with each other and form larger defect clusters, such as dislocation networks, stacking fault tetrahedrons (SFTs) and voids, etc..

These significant microstructure damage can degrade a material's mechanical properties in terms of irradiation-induced hardening and embrittlement [3, 15, 16, 119, 120], results in degradation of thermal and electrical conductivity [3, 36], and lead to dimensional changes, such as void swelling [14, 17, 36, 134-136, 317]. Significant research has been performed to design irradiation-tolerant materials. A basic premise is that the introduction of certain types of defect sinks that can enhance the recombination of irradiation-induce defects. Different types of defect sinks have been investigated, such as grain boundaries (GBs) [131, 147, 173, 254, 319, 320], twin boundaries (TBs) [89, 178, 179, 321], free surface [78, 183, 257], and phase boundaries [76, 174-176].

Grain boundaries (GBs) are effective defect sinks that can eliminate irradiation-induced defects [131, 147, 242, 243, 322]. For instance, prior studies show grain-size effect on alleviation of irradiation-induced defects in neutron irradiated alloys [3, 305, 323]. An interesting simulation study showed that GBs can also act as sources that emit interstitials into the grain interior to annihilate vacancies [243]. There are increasing evidence showing that nanocrystalline (NC) metals exhibit lower helium bubble density than their coarse-grained counterparts [131, 324]. TBs are a special type of GBs and they are normally considered to be ineffective defect sink because the energy of TBs is very low [254, 255]. For instance, Han *et al.* showed that the width of void denuded zone in non-Σ3 GBs is much greater than Σ3 coherent TBs (CTBs), indicating CTBs have low efficiency in eliminating defects [254]. Interestingly, several recent studies have shown that TBs can effectively remove irradiation-induced defects, such as stacking fault tetrahedrons (SFTs), which is a major type of vacancy clusters formed in face-centered cubic (FCC) metals, and interstitial clusters [51, 89, 170, 178, 179]. The twin boundary affected zone (TBAZ) has also been observed in NT Ag and the accumulative concentration of irradiation-induced defects exhibits twin-thickness dependence [177, 179]. More defect clusters were identified in central areas than that close to TBs in the thicker twins, whereas the opposite phenomenon has been found in fine twins.

Numerous works have shown that a small amount of impurity atoms can significantly amend irradiation-induced microstructures in metallic materials. Some of the impurity effects have been attributed to solid solution effect, i.e. point defect trapping at impurity atoms, and others to various aspects of precipitation effect [5, 271-274]. Mansel and Vogl have shown that neutron irradiation-induced interstitials in Al will be trapped at Co substitutional atoms [275]. Detrapping also occurs when vacancies become mobile and migrate to the trapped interstitials. Alexander and Stanislav have indicated that adding solute atoms may decrease the diffusion rate of interstitial clusters, and therefore, increasing the recombination rate of those clusters with freely migrating vacancies [276].

FCC metals with very low stacking fault energy (SFE), such as Ag and Cu, are in general vulnerable to irradiation [8, 11, 48-51, 229, 277]. Previous studies have shown by introducing high-density defect sinks, such as TBs and nanopores, the irradiation tolerance of nanostructured Ag and Cu can be greatly enhanced [83, 89, 178, 179]. In this study, we report another approach that can drastically improve irradiation tolerance of Ag. Adding a small amount of Fe impurities leads to the formation of ultra-high-density twins, ~ 2 nm thick, in Ag-1at%Fe (referred to as NT AgFe hereafter). NT AgFe possesses a powerful TB-solute network that significantly improve radiation tolerance of NT alloys.

6.3 Experimental

NT Ag and S-NT AgFe thin films with thickness of 1 μm were deposited onto HF etched Si (111) substrates, and P-NT AgFe were deposited on SiO_2 substrate (Si (100) substrates with 1μm-thick amorphous SiO_2), respectively, via DC magnetron sputtering at room temperature from pure Ag (99.99%) and Fe (99.95%) targets. A base pressure of ~ 5×10^{-8} torr was achieved in the main chamber before deposition, and the Ar pressure during deposition was ~ 2 mtorr. X-ray diffraction (XRD) experiments were performed on a PANalytical Empyrean system (Cu Kα radiation) at room temperature. Both cross-sectional and plan-view transmission electron microscopy (TEM) specimens were prepared by grinding, polishing and ion milling by a Gatan PIPS II system. CG Ag samples were made from small pieces of Ag target using the same TEM specimen preparation method. All TEM specimens were examined by using a Thermo Fischer Scientific/FEI Talos 200X microscope with Super X EDX detectors (4 detectors) before and after irradiation. *In situ* irradiation experiment was performed at room temperature at the IVEM-TANDEM facility at Argonne National Laboratory. 1 MeV Kr^{++} ion beam was used for radiation experiments to a maximum fluence of 2×10^{14} ions cm^{-2} (∼1 dpa). The dose rate applied during *in situ* radiation experiments was kept at ~ 2.5×10^{-3} dpa/s. The Stopping and Range of Ions in Matter (SRIM) (Kinchin-Pease method) simulation was used to estimate the displacement damage profile (in the unit of displacements-per-atom (DPA)) and Kr ion distribution. Most Kr ions (99.99%) penetrated directly through the TEM specimen and the residual Kr ion concentration in the TEM thin foil is ~ 0.01at.%.

More details can be found elsewhere [179]. During *in situ* Kr ion irradiation, the temperature rise of specimens is less than 10 °C.

Table 6.1. Summary of irradiation experiments in this study. Four different types of samples have been studied, including coarse-grained (CG) Ag, nanotwinned (NT) Ag, Single crystal-NT (S-NT) AgFe and polycrystalline NT (P-NT) AgFe. All specimens have been irradiated from their plan-view direction. NT-Ag and S-NT AgFe have also been irradiated from cross-section direction.

Irrad. direction	**CG Ag**	**NT Ag**	**S-NT AgFe**	**P-NT AgFe**
Plan-view	✓	✓	✓	✓
Cross-section	-	✓	✓	-

CG: coarse-grained
NT: Nanotwinned
S-: Single-crystal
P-: Poly-crystal

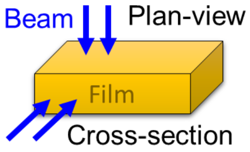

6.4 Results

A summary of irradiation experiments reported in this study is shown in Table 6.1. Four types of specimens have been studied, including coarse-grained (CG) Ag, nanotwinned (NT) Ag, single crystal-NT (S-NT) AgFe and polycrystalline NT (P-NT) AgFe. All specimens have been irradiated from their plan-view direction. NT-Ag and S-NT AgFe have also been irradiated from cross-section direction. The X-Ray diffraction (XRD) profile in Fig. 1a shows highly {111} textured NT Ag and Ag-1at.%Fe (referred to as AgFe hereafter) grown on Si (111) substrates. In comparison, NT AgFe on SiO_2

substrates shows polycrystalline nature with (111) texture and a weak Ag (311) peak. Plan-view scanning TEM (STEM) image (Fig. 1b) of polycrystalline nanotwinned (P-NT) AgFe shows nanograins with clear grain boundaries. The corresponding EDX composition maps of Ag (98.8 at.%) and Fe (1.2 at.%) are shown in Fig. 1c-d, respectively. It can be seen from the EDX Fe composition map (Fig. 1d) that the Fe solute is uniformly distributed throughout the film.

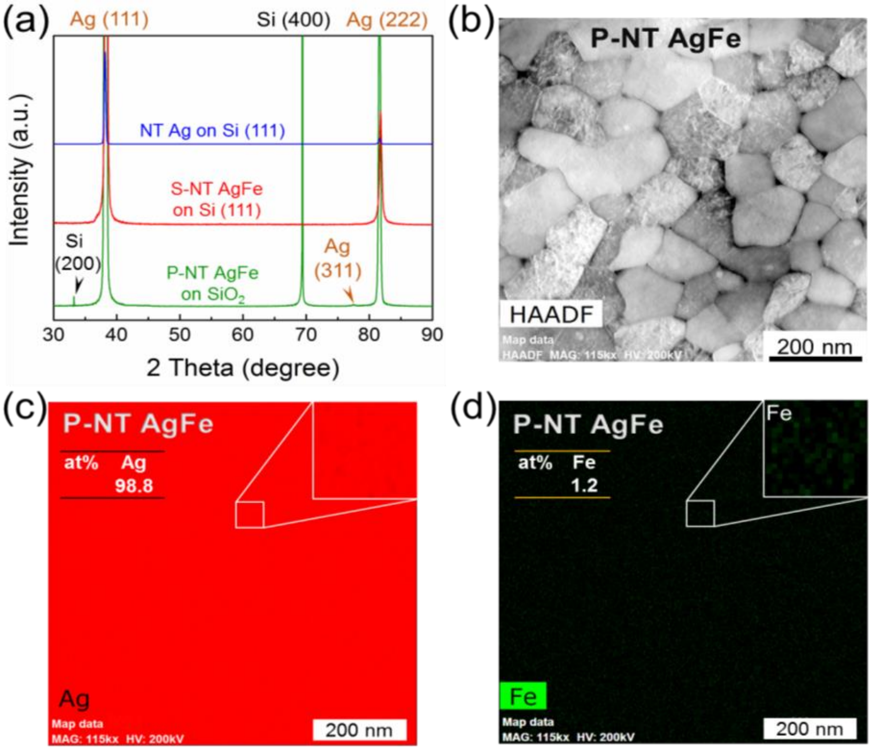

Fig. 6.1. (a) The XRD profile shows highly {111} textured nanotwinned (NT) Ag and NT Ag-1at.%Fe (referred to as AgFe hereafter) grown on Si (111) substrate. In comparison, AgFe on SiO_2 substrates shows polycrystalline nature with (111) texture. However, the predominant peaks are still Ag (111) and (222). Ag (311) is identified but with a very low intensity. (b) A scanning TEM (STEM) plan-view image of polycrystalline nanotwinned (P-NT) AgFe, and (c-d) the corresponding EDX composition maps of Ag (98.77 at.%) and Fe (1.23 at%). Fe is uniformly distributed throughout the film.

The plan-view and cross-sectional TEM micrographs of the NT Ag, S-NT AgFe and P-NT AgFe films are compared in Fig 2a-c and 2d-e, respectively. The average columnar grain size is 120 ± 20 nm for NT Ag, 100 ± 30 nm for S-NT AgFe, and 100 ± 40 nm for P-NT AgFe. The inserted selected area diffraction (SAD) patterns examined along Ag <111> zone axis embedded in Fig. 2a and 2b indicate NT Ag and S-NT AgFe exhibit single-crystal-like pattern. In contrast, the SAD pattern of P-NT AgFe in Fig. 2c shows polycrystalline nature with a strong Ag (111) and a weak (311) diffraction ring, consistent with the XRD results in Fig. 1a. Cross-section TEM (XTEM) micrographs in Fig. 2d-e show the formation of high-density twin boundaries (TBs) in NT Ag and ultra-high-density TBs in S-NT AgFe and P-NT AgFe. The average twin spacing is 13 ± 7, 3 ± 2 and 3 ±2 nm for NT Ag, S-NT AgFe and P-NT AgFe, respectively. The inserted SAD patterns in the three figures indicate the formation of classical twinned structures. TBs are parallel to the substrate surfaces in the NT Ag and S-NT AgFe films, whereas TBs are frequently misaligned in neighboring grains in P-NT AgFe. The columnar boundaries in NT Ag and S-NT AgFe are primarily incoherent twin boundaries (ITBs). As shown in Fig. 2e, ITBs in S-NT AgFe align either on the same line (blue arrows), or appear diffused (yellow arrows). Therefore, the columnar boundaries shown in Fig. 2b are either narrow (depicted by blue dotted lines) or wide (sandwiched by yellow dotted lines). In P-NT AgFe (Fig. 2f), the columnar boundaries are mostly conventional high-angle grain boundaries (HAGBs) rather than ITBs. High-resolution TEM (HRTEM) images in Fig. 3 show that the coherent twin boundaries (CTBs) separating ultra-fine twins in S-NT AgFe are decorated with stacking faults (SFs).

Since Fe solute is a key parameter that affects both the twin morphology and irradiation response in NT AgFe, it is critical to identify the distribution of Fe atoms in NT AgFe films before and after irradiation. EDX composition maps of Ag and Fe in S-NT AgFe film before irradiation from both cross-section (Fig. 4b) and plan-view (Fig. 4d) TEM analysis show that Fe solutes are uniformly distributed. After *in situ* Kr ion irradiation of S-NT AgFe to 1.5 dpa, Fe solutes remain distributed homogeneously throughout the films as shown in Fig. 4f and 4h. The XTEM image (Fig. 4e) of the irradiated film shows the retention of high-density nanotwins, and the plan-view TEM micrograph (Fig. 4g) reveals the formation of high-density defects in irradiated film, but the columnar boundaries are no longer visible. Similar results are obtained in irradiated P-NT AgFe films (see Suppl. Fig. 1).

During irradiation, all films accumulate irradiation-induced damages, but to a very different level. *In situ* video snapshots compare the microstructures of different specimens irradiated to the same dose levels. The scale bar in Fig. 5a applys to all images. The CG Ag film accumulates a large number of defects after merely 0.025 dpa, and is significantly damaged by 0.2 dpa (Fig. 5a-c). In irradiated NT Ag, a moderate number defects are generated within the grains, and the columnar boundaries become blurry by 0.025 dpa. At 0.2 dpa, defect density appears to increase further, and the columnar boundaries become invisible (Fig. 5d-f). In S-NT AgFe, fewer defects are generated at 0.025 dpa compared to NT Ag, and most of the columnar boundaries are still visible at this dose level. The columnar boundaries become indistinguishable at 0.2 dpa. However, the film appears to have smaller and fewer defects compared to NT Ag (Fig. 5g-i). Similar to S-NT AgFe, the

P-NT AgFe film experiences moderate damage, but a large fraction of the grain boundaries in P-NT AgFe remains visible even after 2 dpa (Fig. 5j-o). It is worth mentioning that given the polycrystalline nature of P-NT AgFe, not all grains appear to contain the similar number of irradiation-indued defects due to different imaging conditions. Thus defect analysis for P-NT AgFe was performed by carefully examining grains oriented to the correct imaging conditions.

The XTEM images of NT Ag and S-NT AgFe before and after irradiation to 1.5 dpa are compared in Fig. 6. Both specimens have well defined TBs before irradiation (Fig. 6a and 6c). After irradiation to 1.5 dpa, numerous TBs in NT Ag disappeared, and the average twin spacing increased from 13 ± 7 to 22 ± 15 nm. Additionally, most ITBs at the original columnar boundaries are no longer visible after radiation (Fig. 6b). In comparison, the TBs in irradiated S-NT AgFe are much more stable (Fig. 6d). After irradiation to 1.5 dpa, few TBs were removed and the average twin spacing increased slightly from 3 ± 2 to 5 ± 3 nm. The sharp ITBs became diffused and less distinguishable after irradiation. Also, the sharp edges of CTBs became blurred due to the formation of stacking faults along CTBs.

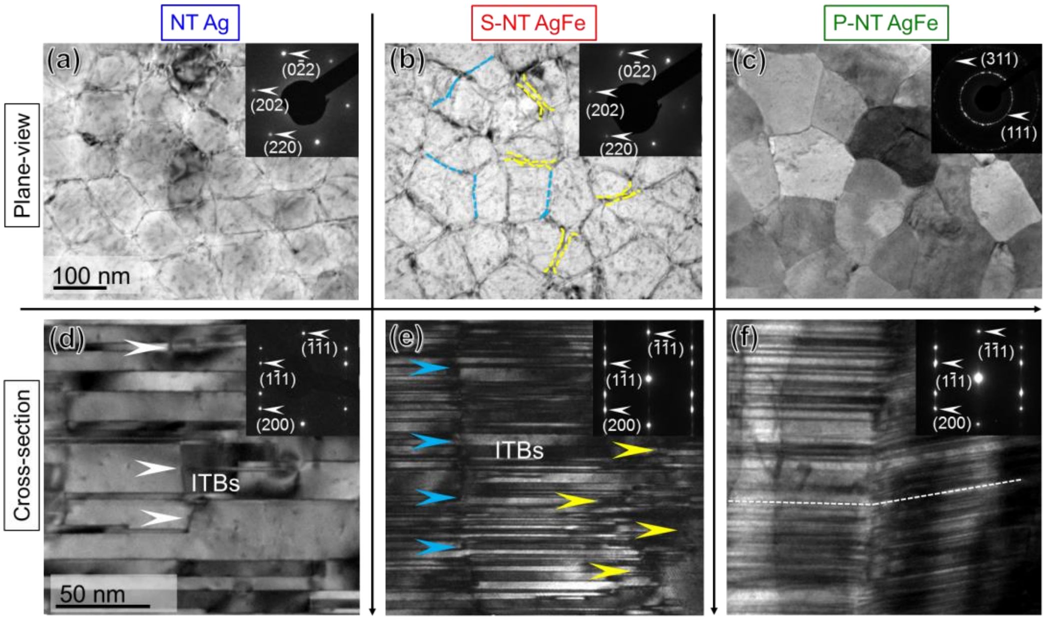

Fig. 6.2. (a-c) Plan-view TEM images are showing the surface morphology of the NT Ag, S-NT AgFe and P-NT AgFe films. The inserted selected area diffraction (SAD) patterns examined along Ag <111> zone axis embedded in (a) and (b) indicate NT Ag and S-NT AgFe exhibit single-crystal-like pattern. In contrast, the SAD pattern of P-NT AgFe shows polycrystalline with predominating Ag (111) and a weak (311) diffraction ring, consistent with the XRD results in Fig. 6.1. (d-f) Cross-section TEM (XTEM) micrographs showing the formation of high-density twin boundaries (TBs) in NT Ag and ultra-high-density TBs in S-NT AgFe and P-NT AgFe. The SAD patterns in the three figures indicate the formation of classical twinned structures. TBs are parallel to the substrate surfaces in the NT Ag and S-NT AgFe films, whereas TBs are frequently misaligned in neighboring grains in P-NT AgFe. The columnar boundaries in NT Ag and S-NT AgFe are predominantly incoherent twin boundaries (ITBs), and S-NT AgFe has a higher density of TBs than NT Ag. As shown in (e), ITBs in S-NT AgFe align either on the same line (blue arrows), or diffused in a wide range (yellow arrows). Therefore, the columnar boundaries as shown in (b) are either narrow and sharp (depicted by blue dotted lines) or wide and blur (sandwiched by yellow dotted lines). In P-NT AgFe (f), the columnar boundaries are mostly conventional high-angle grain boundaries (GBs) rather than ITBs.

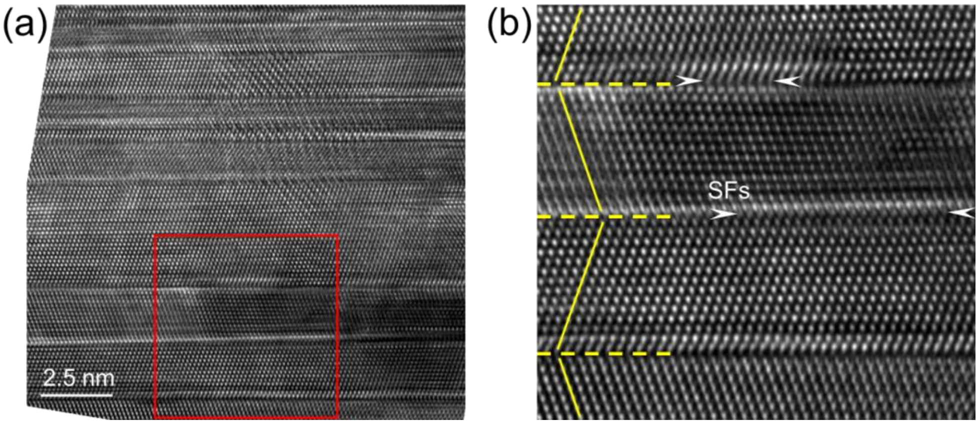

Fig. 6.3. (a) High-resolution TEM images showing the microstructure of ultra-fine twins in S-NT AgFe. (b) The magnified view of box in (a) shows clear (111) TBs are decorated with SFs.

The evolution of defect density as a function of irradiation dose is different for four types of specimens. As shown in Fig. 7, the defect density in CG Ag reaches saturation ~ 21.5 × $10^{22}/m^3$ at ~ 0.05 dpa, while defect densities in NT Ag, S-NT AgFe and P-NT AgFe gradually increase until 0.2 dpa, and level off thereafter. In comparison NT Ag has only half of the defect density, ~ 10.8 × $10^{22}/m^3$. The saturation defect density in both S-NT AgFe and P-NT AgFe reduces further by another 50% to ~ 5.1 and 4.9 × $10^{22}/m^3$, respectively. Note that defect density analysis reflects a lower bound estimation since not all defects can be resolved under *in situ* TEM observation.

A summary of average grain size, twin spacing (before and after irradiation), defect size and density in CG Ag, NT Ag S-NT AgFe and P-NT AgFe are given in Table 6.2. CG Ag has the largest average defect size, ~ 12 nm. NT Ag has a much smaller average defect size, ~ 7 nm, followed by 5 nm in both types of AgFe specimens. In addition, the average defect size in NT AgFe is comparable to their average twin spacing.

6.5 Discussion

It has been shown previously that NT Ag exhibits prominently enhanced irradiation tolerance compared to CG Ag due to high-density TBs. It is, however, surprising to see that the radiation resistance can be further improved by adding merely ~1 at.% Fe solutes. The Fe solute effects on both the microstructure and irradiation response of NT AgFe are considered from three aspects. First, Fe solutes promote the nucleation of growth twins and lead to higher density of growth twins than that in monolithic Ag. Second, the Fe solutes significantly improve the radiation stability of all TBs (CTBs and ITBs) presumably due to the solute drag effect. Third, the uniformly distributed Fe atoms are effective defect sinks that accelerate the recombination of interstitials and vacancy through trapping and detrapping processes. The following discussions are based on the three aspects.

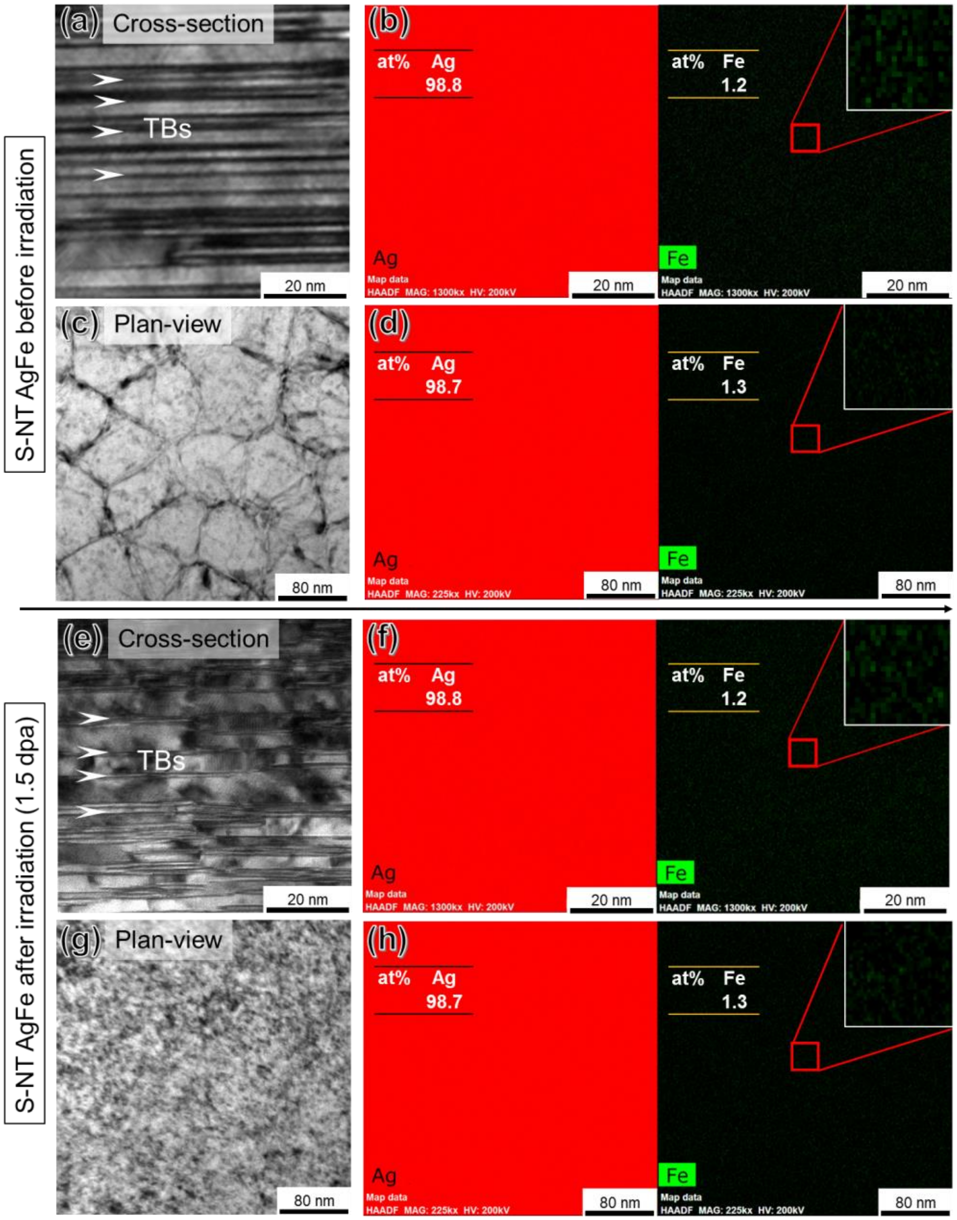

Fig. 6.4. TEM images and EDX maps of S-NT AgFe before (a-d) and after (e-h) Kr ion irradiation. (a) XTEM, (c) plan-view TEM images and (b,d) the corresponding EDX composition maps of Ag and Fe before irradiation. (e) The XTEM image of the irradiated film showing the retention of high- density nanotwins. (g) The plan-view TEM micrograph demonstrates the formation of defects in irradiated film and the columnar boundaries are not visible. (f,h) The corresponding EDX composition maps of irradiated films show that both Ag and Fe are distributed uniformly. The EDX composition maps for P-NT AgFe before and after irradiation are shown in Suppl. Fig. 6.1.

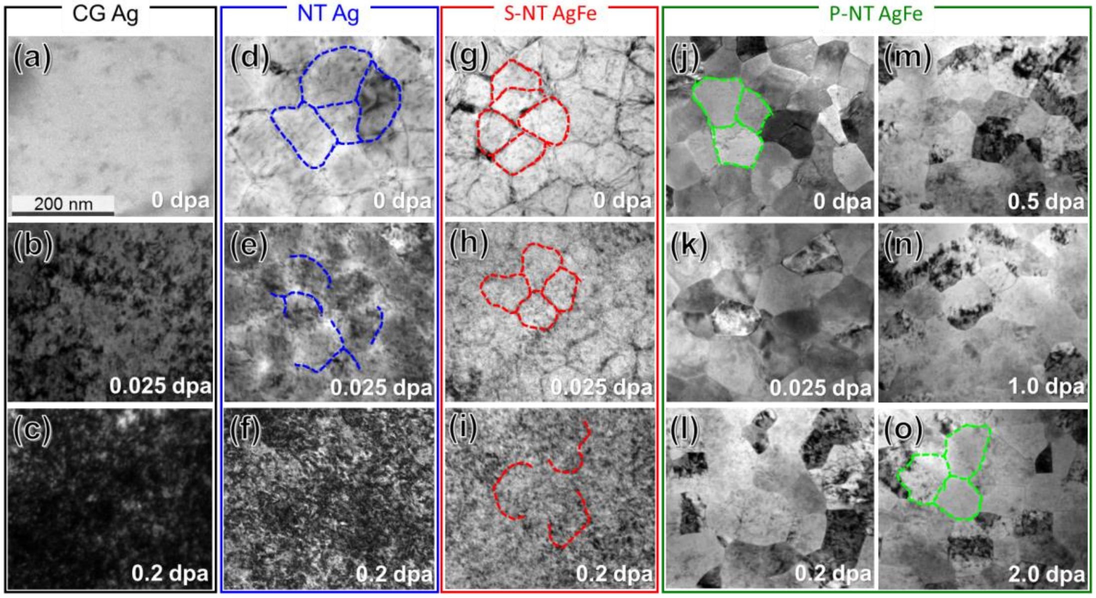

Fig. 6.5. *In situ* video snapshots recorded during Kr ion irradiation at room temperature compare the irradiation response among CG Ag, NT Ag, S-NT AgFe and P-NT AgFe at the same dose levels. The scale bar in (a) applys to all images. (a-c) CG Ag accumulates a large number of defects after 0.025 dpa, and is significantly damaged by 0.2 dpa. (d-f) In irradiated NT Ag, a moderate number defects are generated within the grains, and the columnar boundaries become blurry by 0.025 dpa. At 0.2 dpa, defect density appears to increase further, and the columnar boundaries become invisible. (g-i) In S-NT AgFe, fewer defects are generated at 0.025 dpa compared to NT Ag, and most of the columnar boundaries are still clear at this dose level. The columnar boundaries become indistinguishable at 0.2 dpa. However, the film appears to have smaller and fewer defects compared to NT Ag. (j-o) Similar to S-NT AgFe, the P-NT AgFe film experiences moderate damage. A large fraction of the grain boundaries in P-NT AgFe remains visible after 2 dpa.

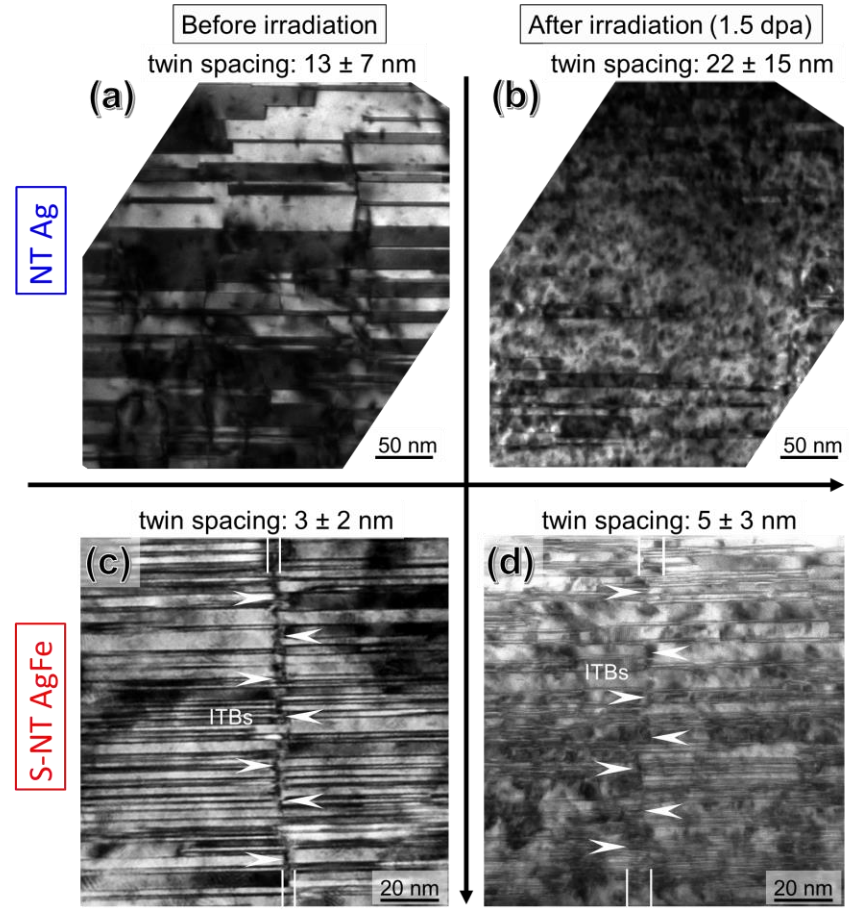

Fig. 6.6. XTEM images of NT Ag and S-NT AgFe before and after irradiation to 1.5 dpa. (a-b) After irradiation to 1.5 dpa, numerous TBs disappeared, and the average twin spacing increased from 13 ± 7 to 22 ± 15 nm, and most ITBs at the original columnar boundaries are no longer visible after radiation. (c-d) In comparison, the TBs in irradiated S-NT AgFe are much more stable. After 1.5 dpa, few TBs were removed and the average twin spacing increased slightly from 2 ± 2 to 4 ± 3 nm. The sharp ITBs became diffused and less distinguishable after irradiation. Also, the edges of CTBs became blurred due to the formation of stacking faults along CTBs.

Table 6.2. Summary of average grain size, twin spacing (before and after irradiation), defect size and density in CG Ag, NT Ag S-NT AgFe and P-NT AgFe.

	CG Ag	**NT Ag**	**S-NT AgFe**	**P-NT AgFe**
Grain size (nm)	~ 5 μm	120 ± 20	100 ± 30	100 ± 40
Twin spacing (nm) Before irradiation	-	13 ± 7	2 ± 2	2 ± 2
Twin spacing (nm) After irradiation	-	22 ± 15	4 ± 3	-
Defect size (nm)	12 ± 5	7 ± 2	5 ± 2	5 ± 1
Defect density (10^{22} m^{-3})	21.5 ± 0.5	10.8 ± 0.5	5.1 ± 0.3	4.9 ± 0.6

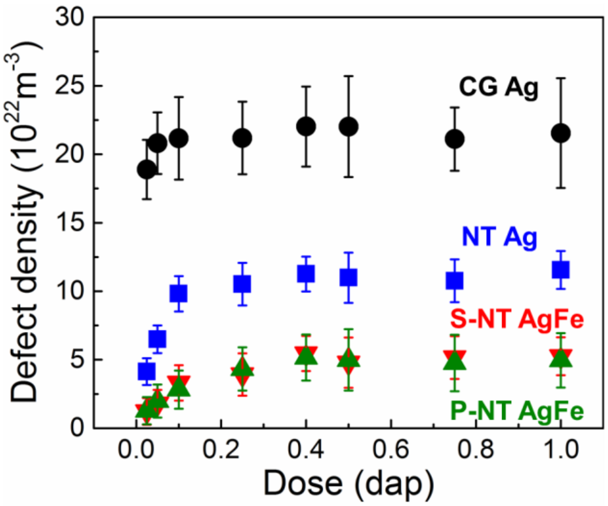

Fig. 6.7. The defect density evolution as a function of irradiation dose for four types of samples. The defect density in CG Ag reaches saturation at ~ 0.05 dpa, while defect densities in NT Ag, S-NT AgFe and P-NT AgFe gradually increase until 0.2 dpa, and then leveled off thereafter. The defect density in CG Ag reaches ~ 21.5 × $10^{22}/m^3$, and is significantly higher than NT Ag, ~ 9.2 × $10^{22}/m^3$. Both S-NT AgFe and P-NT AgFe exhibit very low density, ~ 5.1 and 4.9 × $10^{22}/m^3$, respectively.

6.5.1 Formation of ultra-high-density twins in NT AgFe

Nanoscale growth twins have been observed in numerous monolithic metals, such as Ag [226], Cu [178, 325], Ni [326], Pd [327] and Al [232, 328], and their alloys [296, 329]. The influence of impurity on formation of twins has been a subject under debate [329-331]. Lu and Hellawell have proposed an "impurity-induced twinning" mechanism in their study of twin formation in Al-Si alloys [329]. Their study shows that the adsorption of impurity atoms at monolayer steps may contribute to an alteration of the stacking sequence of {111} planes in Si, and thus to the formation of twins. In this hypothesis, growth twins are created at the interface when the atomic radius of the impurities relative to Si exceeds 1.65. That is to say, a specific radius of impurity atoms is required to trigger twinning. Shahani et al. have studied the twinning in Al-Si-Cu alloys, but they found neither Al nor Cu satisfies the geometrical consideration [331]. Moreover, Timpel et al reported that the chemistry of co-segregated species rather than size effect plays a major role on formation of twins [330]. Clearly, impurity-induced twinning is a phenomenon requiring further investigation.

In general, Fe exhibits body-centered cubic (BCC) structure, but it is plausible to expect that the minute Fe solutes have FCC structure in this study. Our previous study on Ag/Fe multilayers also observed phase transformation of Fe (BCC→FCC) when the individual layer thickness is very small, ≤ 5 nm [332]. For the FCC Ag-1 at.% Fe alloy, the average separate distance between Fe atoms is ~ 2 nm, which matches the average twin spacing measured in both S-NT AgFe and P-NT AgFe, 3 ± 2 nm. This simple estimation indicates that the Fe solutes may have close correlation with the average twin spacing in AgFe films.

6.5.2 Significantly enhanced irradiation stability of twin boundaries in NT AgFe

Prior studies have shown that TBs are mobile under stress (deformation) and radiation. ITB segments consist of 1/6<112> Shockley partial dislocations on consecutive {111} planes. Wang et al. show, by means of in situ nanoindentation inside a TEM and molecular dynamics simulations, ITBs can be highly mobile during deformation, a phenomenon often referred to as detwinning [67]. The driving force for detwinning is the reduction in TB energy. Detwinning has also been reported in irradiate NT Cu [67, 68] and NT Ag [69]. In general, CTBs can actively engage in defect clusters and form a series of tiny ITBs steps. These ITBs are highly mobile and thus promote detwinning. Hence it is critical to enhance radiation stability of TBs in order to design advance radiation tolerant NT metals.

The columnar boundaries in NT Ag and S-NT AgFe are ITBs [56]. After irradiation to 1.5 dpa, TBs in NT Ag detwin significantly and the average twin spacing increases from 13 ± 7 to 22 ± 15 nm. In comparison, the ITBs in S-NT AgFe are highly stable, and after radiation to 1.5 dpa, the average twin spacing only increases slightly. In P-NT AgFe, the GBs remain visible even after irradiation to 2 dpa, indicating TBs are highly stable against radiation as well. The significantly enhanced stability of ITBs in NT AgFe can be interpreted from several perspectives.

First, the solute drag effect may dominate the radiation stability of ITBs. Solute drag effect on GB stability has been extensively investigated [70-75].Lücke and Detert [70] proposed that GB mobility M can be expressed as [76],

$$M = \frac{D}{kT}\frac{1}{nCe^{-E/kT}} \quad , \qquad (6.1)$$

where D is the diffusivity of solute atoms, n is the number of solute atoms per unit area of the boundary, C is the average concentration of solute atoms, and E is the boundary–solute interaction energy, i.e., the heat of segregation. Clearly, the mobility of GB is proportional to the diffusivity of solute atoms and inversely proportional to the concentration of solute atoms. Interestingly, this suggests that there will be no effect in the case when solute atoms are immobile. However, as studied later by Mendelev and Srolovitz using kinetic Monte Carlo (KMC) simulation, it is still possible that solute drag effect exists in the real grains even when solute atoms are immobile [72].

Using a similar strategy, Borovikov et al. have studied the drag effect of Ag solutes in Cu on TB stability by MD simulations [76]. Their modeling suggest that the presence of Ag solutes, 0.2-0.5 at.%, significantly resist the migration of ITBs. The migration rate of ITBs is found to be twin-thickness-dependent, and the ITBs migrate a lot faster, 14 times large, in pure Cu than that in Cu with Ag impurities. ITBs migrate smoothly in the pure Cu, whereas the motion becomes jerky in the presence of Ag solutes. Zhang et al., have also pointed out the importance of solute drag effect in the enhanced high-temperature stability of TBs in NT Cu contains 0.5 at% Fe precipitates at GBs [20]. MD simulations on Cu-Ag solid solution suggests that the mechanism of solute drag effect on the TB migration has little relation with the solute segregation to the ITB. Instead, it is related to variation of the ITB shape or position to accommodate more solute atoms [76]. In the present study, we anticipate that Fe atoms may also impede the migration of ITBs through a similar solute drag effect.

Second, Fe has an atomic radius of 1.56 Å, smaller than Ag, 1.65 Å. It is well known that small solute atoms introduce tensile stress field, and thus may trap dislocations, such as mobile Shockley partials. Such an interaction may slow down the migration of Shockley partial dislocations on the ITBs, and thus prohibit the migration of ITBs. Additionally, it has been shown that the interaction of dislocation loops with Shockley partials (on ITB) may lead to sessile Frank partials. The interaction of perfect dislocation loops with Frank partials may lead to mobile Shockley partials again [77]. It is likely that the Fe solutes may stabilize Frank partials, making them difficult to evolve and thus stabilize ITBs.

Third, the stability of ITBs may be related the influence of solute atoms on SFE of Ag. A recent study shows that the addition of Fe solute to Al increases the stable stacking fault energy slightly, but the unstable stacking fault energy increases significantly. Consequently, trailing partials is difficult to migrate and thus stabilize TBs. We hypothesize that Fe atoms may have a similar impact on the variation of unstable SFE of Ag, and thus may stabilize TBs in Ag.

6.5.3 The integration of Fe solutes to TB networks to enhance radiation tolerance

Here we will discuss the influence of CTB-ITB networks and Fe solutes on the radiation tolerance of NT AgFe.

6.5.3.1 Role of CTBs on irradiation tolerance

It has been known that NT metals have enhanced radiation tolerance compared to their bulk counterparts. The current study confirmed that NT Ag and AgFe indeed have significantly improved radiation tolerance than CG Ag. Although there are studies that show CTBs maybe ineffective defect sinks comparing to HAGBs [254, 255], there are increasing evidence that show CTBs can actively engage in defect capture and annihilation during irradiation. For instance both MD simulations and in situ radiation studies show that CTBs interact with and destruct SFTs [51, 89, 170, 178, 179]. CTBs also change their geometry to accommodate dislocation loops and facilitate the transportation of interstitials along CTBs to locations where vacancy concentration is high and thus promote vacancy-interstitial recombination [179]. Recent studies on NT Ag have also shown the defect-CTB interactions lead to the existence of twin boundary affected zone (TBAZ), where the time accumulative defect concentration is low near CTBs [179]. In addition, the distribution of defects has been revealed to be twin-thickness (spacing between CTBs) dependent [177]. These studies confirm that CTBs are indeed effective sinks in irradiated metals.

The current study shows that NT Ag and NT AgFe have similar columnar grain size, 100-120 nm, but NT AgFe has a much smaller twin spacing, 3 ± 2 nm, comparing to that of NT Ag, ~13 ± 7 nm. Irradiated AgFe has 50% less defects than that in NT Ag, as well as a smaller average defect size. Such a drastic reduction of defect density and a moderate decrease in defect dimension is clearly related to the much smaller average twin thickness in NT AgFe, lending further evidence on the role of CTBs on alleviation of radiation damage. The dislocation loop size in NT AgFe is comparable to their average twin spacing, indicating that nanotwins may significantly suppress the growth of defect clusters during radiation.

6.5.3.2 Grain boundary and ITBs as defect sinks in irradiated NT metals

NT Ag and NT AgFe have abundant grain boundaries. *In situ* TEM snapshots (Fig. 8) show representative defect capture events by grain boundary in P-NT AgFe over ~ 0.15 dpa (~ 69 s) (see Supplementary Video 1). The boundary of a grain is indicated by yellow dotted line (Fig. 8a). After 5s, two defect clusters near GB appeared as indicated by red arrows (Fig. 8b). After 1 s (at 6 s) they combined into a large cluster that grew further (Fig. 8c-d) and remained in contact with the GB. The large defect cluster was gradually absorbed by the GB at 24 s and continuously shrank (Fig. 8e-g). Finally, the defect cluster was removed by the GB at 69 s (Fig. 8h). The corresponding schematic diagrams of the defect-GB interaction events are shown in Fig. 8a'-h'. Such a defect cluster could be a vacancy loop as it appears less mobile, and the absorption of a large vacancy loop by GB is a sluggish process as it involves significant diffusion of atoms along GBs. There are also prior evidence that shows ITBs are effective defect sinks [310, 333]. And it has been shown that ITBs can sometime recover after interaction with dislocation loops [256]. ITBs not only capture large defect clusters, but they can also effectively transport point defects. Prior studies on Kr ion irradiated NT Cu with nanovoids show that Shockley partials ITB steps can effectively transport interstitials to grain boundaries where they can be annihilated by nanovoids [83].

6.5.3.3 Role of Fe solute atoms in irradiation tolerance

Classical solute drag effect assume that solute atoms migrate together with GBs or dislocations. However, EDS maps did not reveal segregation of Fe solutes near TBs in irradiated NT AgFe, indicating that solute atoms did not travel along with ITBs or Shockley partials. The significance of Fe solutes on radiation tolerance of NT AgFe can be interpreted from several perspectives. First, Fe solutes may facilitate the recombination of opposite types of point defects, a phenomena that has been reported previously [5, 271-274]. Fe has smaller atomic radius than Ag, and thus a tensile stress field may arise around substitutional Fe atoms, making Fe solutes preferential sites to attract interstitials. Although Fe solute may not eliminate interstitials due to limited excess free volume, they increase an interstitial's dwelling time, promoting the interstitial to recombine with nearby vacancies. The average separation distance among these Fe solutes is ~ several nm, making them effective to prohibit preferential segregation of vacancy and interstitials clusters.

Second, it is worth mentioning that although Fe solutes may slow down the migration of interstitials and promote the recombination of Frenkel pairs, solutes alone are not effective defect sinks, as they do not have the necessary excess free volumes to accommodate point defects, such as interstitials. Schematics in Fig. 9 illustrate the significance of solute-TB networks on radiation tolerance of NT AgFe alloys. Before irradiation (0 dpa, Fig. 9a), a 10nm-thick twin in NT Ag is nearly free of defects. After 0.1

dpa, numerous defects form within the twin. A portion of the point defects are removed by TBs, and the rest combine to form defect clusters. The frequent defect-TB interactions lead to detwinning in NT Ag (Fig. 9b). At 0.3 dpa, both defect size and defect density are further increased and they tend to reach saturation. Moreover, detwinning happens more frequently (Fig. 9c). After 1 dpa, the defect morphology does not change significantly further. However, a large portion of the twins has been removed (Fig. 9d). However, NT AgFe has abundant ITB and CTB networks. Thus Fe solutes are nicely integrated into the TB networks to facilitate the point defect-TB interactions. As shown in Fig. 9e, S-NT AgFe possesses ultra-high-density twins, with an average twin spacing of 3 nm, and contain uniformly distributed Fe solutes (Fe solutes can either locate on TBs or within twin matrices as shown in the figure). At 0.1 dpa, point defects are absorbed by TBs. Furthermore, the presence of Fe solutes provides extra defect sinks in S-NT AgFe (Fig. 9f). As irradiation processes, both defect size and defect density are moderately increased, and detwinning proceeds at a slow rate as Fe solute stabilize TBs during radiation (Fig. 9g-h).

Atomistic simulation on the interplay of solute-TB networks with radiation induced point defects and defect clusters may provide further insight on the fundamental mechanisms of solute enhanced radiation tolerance and stability of TBs in NT metals. The integration of Fe solutes into TB networks may prove to be an effective approach to significantly enhance the radiation tolerance and stability of NT metals and alloys.

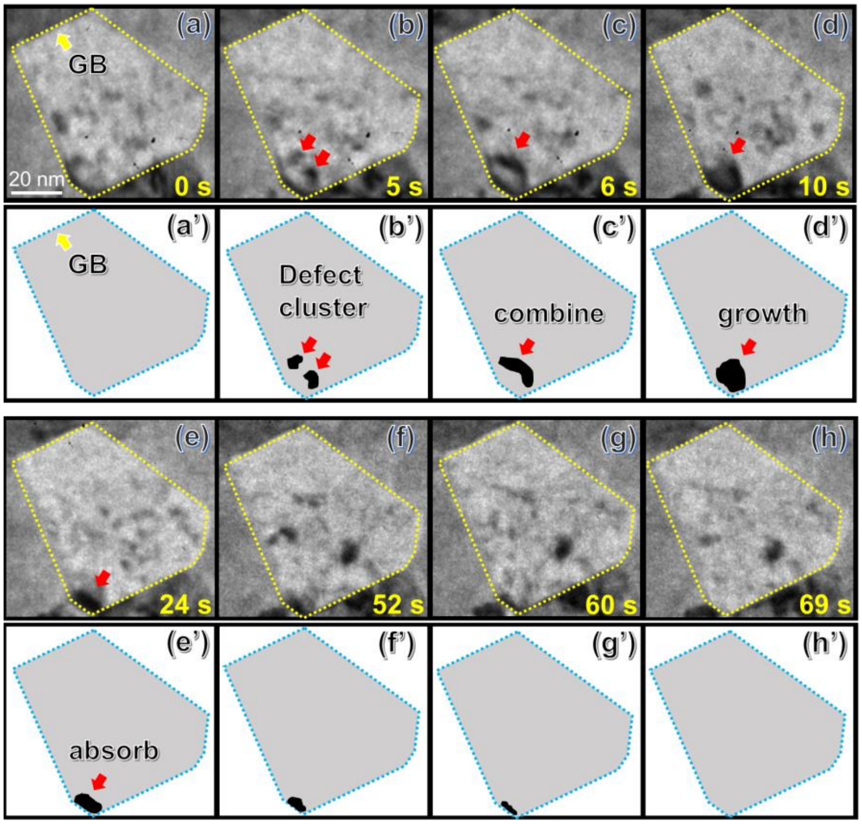

Fig. 6.8. *In situ* TEM video snapshots (a-h) showing representative defect capture events by a grain boundary (GB) in P-NT AgFe over ~ 0.15 dpa (~ 69 s) (see Supplementary Video 1). (a) The boundary of a grain is indicated by yellow dotted line. (b) Two defect clusters appeared at 5 s as indicated by red arrow. (c) They combined into a large cluster at 6 s. (d) The defect grew further into a large defect cluster. (e) The large defect cluster was gradually absorbed by the GB at 24 s and became smaller (f-g). (h) Finally, the defect cluster was removed by the GB. The corresponding schematic diagrams of the defect-GB interaction events described in (a-h) are shown in (a'-h').

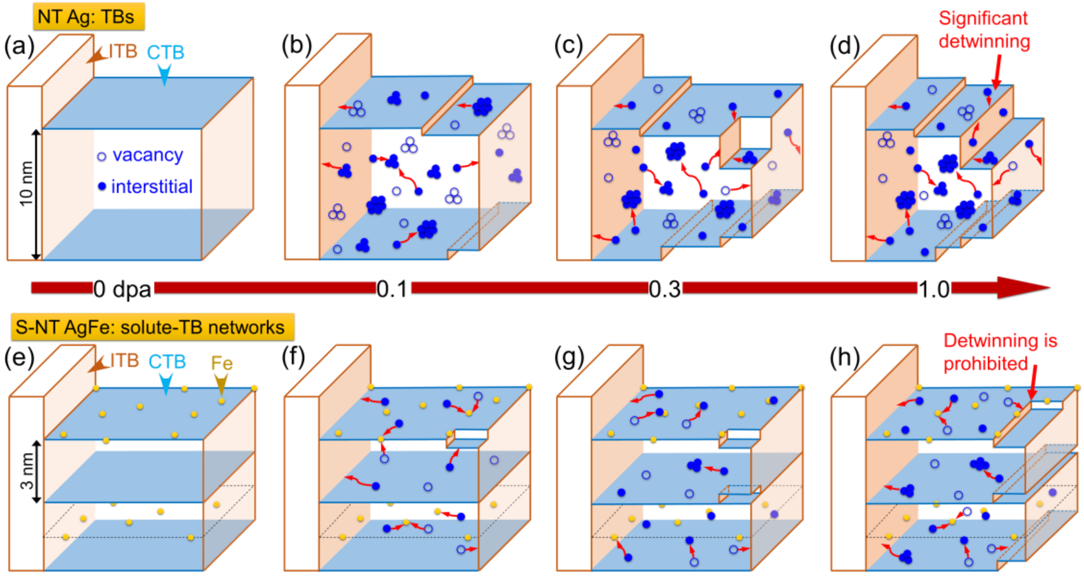

Fig. 6.9. Schematics illustrate the different irradiation responses between NT Ag (a-d) and S-NT AgFe (e-h). (a) Before irradiation (0 dpa), a 10nm-thick twin in NT Ag is nearly free of defects. (b) After 0.1 dpa, numerous defects form within the twin. A portion of the point defects are removed by TBs, and the rest combine together to form defect clusters. The frequent defect-TB interactions lead to detwinning. (c) At 0.3 dpa, both defect size and defect density are further increased and they tend to reach saturation. Moreover, detwinning happens more frequently. (d) After 1 dpa, the defect morphology does not change significantly further. However, a large portion of the twins has been removed. In comparison, S-NT AgFe exhibit significantly improved irradiation resistance. (e) S-NT AgFe possesses ultra-high-density twins, with an average twin spacing of 2 nm, and contain uniformly distributed Fe solutes. (f) At 0.1 dpa, Point defects are absorbed by TBs. Furthermore, the presence of Fe solutes provides extra defect sinks in S-NT AgFe. (g-h) Both defect size and defect density are moderately increased, and detwinning proceeds at a slow rate as Fe solute stabilize TBs during radiation.

6.6 Conclusion

In this study, we report on drastically improved irradiation stability of twin boundaries in NT Ag. By adding merely ~1 at.% of Fe solute atoms into Ag matrix, ultra-high-density twins with an average twin thickness of ~ 3 nm form in NT AgFe. The extremely fine twins in NT AgFe have outstanding stability against heavy ion irradiation compared to that in NT Ag. Moreover, NT AgFe has much smaller defect size and lower defect density than NT Ag. The uniformly distributed Fe atoms incorporate nicely into CTB-ITB networks to capture and promote recombination of opposite point defects and stabilize ITBs. This study provides an important solution to the design of NT metals with improved irradiation tolerance and stability.

6.7 Acknowledgement

We acknowledge financial support by NSF-DMR-Metallic Materials and Nanostructures Program under grant no. 1643915. HW acknowledges the support from the U.S. Office of Naval Research (N00014-16-1-2778). We also acknowledge the use of microscopes at the Microscopy and Imaging Center at Texas A&M University and the DoE Center for Integrated Nanotechnologies managed by Los Alamos National Laboratory. The IVEM facility at Argonne National Laboratory is supported by DOE-Office of Nuclear Energy.

CHAPTER VII

IN SITU HEAVY ION IRRADIATION STUDIES OF NANOPORE SHRINKAGE AND ENHANCED RADIATION TOLERANCE OF NANOPOROUS AU*

7.1 Overview

High energy particle radiation induces severe microstructural damage in metallic materials. Nanoporous materials with a giant surface-to-volume ratio may alleviate radiation damage in irradiated metallic materials as free surface are defect sinks. Here we show, by using *in situ* Kr ion irradiation in a transmission electron microscope at room temperature, that nanoporous Au indeed has significantly improved radiation tolerance comparing with coarse-grained, fully dense Au. *In situ* studies show that nanopores can absorb and eliminate a large number of radiation-induced defect clusters. Meanwhile, nanopores in nanoporous Au shrink (self-heal) during radiation, and their shrinkage rate is pore size dependent. Furthermore, the *in situ* studies show dose-rate-dependent diffusivity of defect clusters. This study sheds light on the design of radiation-tolerant nanoporous metallic materials for advanced nuclear reactor applications.

---

*Reprinted from "J. Li, C. Fan, J. Ding, S. Xue, Y. Chen, Q. Li, H. Wang, X. Zhang, In situ heavy ion irradiation studies of nanopore shrinkage and enhanced radiation tolerance of nanoporous Au, Scientific Report, 7 (2017) 39484" with permission from Nature Publishing Group.

7.2 Introduction

Energetic particle (such as ions, neutrons and protons) radiations induce a large population of vacancies and self-interstitial atoms (SIAs) in metallic materials, and these voids, bubbles and stacking fault tetrahedra (SFTs).[9-12] As a result of severe radiation, the microstructure and mechanical properties of the materials can be significantly degraded as evidenced by void swelling, radiation hardening, embrittlement and significant loss of ductility.[13-17] The search for radiation tolerant materials has been a subject of intense research for decades. Numerous approaches have been adopted to design radiation-resistant materials. The central premise is that certain types of defect sinks may promote the absorption and recombination of interstitials and vacancies and thus enhance the radiation tolerance of materials. Consequently, various types of defect sinks have been investigated, including grain boundary (GB), twin boundary (TB), phase boundary, etc.[76, 170-176, 241] Nanocrystalline materials have abundant GBs and may have extraordinary radiation resistance because GBs act as defect sinks that can absorb irradiation induced defects, and in some cases may serve as sources to emit interstitials and annihilate vacancies.[89, 131, 147, 242, 243] TBs are low energy boundaries and are generally considered to be weak defect sinks. However, recent studies reported that TBs in nanotwinned (nt) metals can capture defect clusters, remove irradiation-induced defects (including SFTs) effectively, form a TB affected zone within which the accumulative defect cluster density is lower than in crystal interior, and thus NT metals may have remarkable radiation resistance.[76, 89, 178] Layer interface is another effective defect sink and its influence on radiation tolerance of materials has been extensively studied.[76, 175, 241, 244] For instance, significant layer thickness-dependent reduction of both helium bubble density and alleviation of radiation hardening were reported in some of the immiscible systems, such as Cu/Nb[245] and Cu/V.[246] MD simulations of Cu/Nb also indicate that the Cu-Nb interface is a highly efficient sink for the annihilation of irradiation-induced defects.[252]

Free surface is typically considered as an unsaturable defect sinks, and nanoporous (np) materials with a giant surface-to-volume ratio may have the potential to be radiation tolerant compared to the fully dense coarse-grained (cg) counterparts.[183, 184, 257] There are extensive studies on mechanical properties of NP metals.[237-240] However, there are limited cases on irradiation responses of NP materials.[172, 183] Fu *et al*. performed an *ex situ* study on NP Au under 400keV Ne^{++} ion irradiation and showed that defect accumulation depends on dose rate.[188] More specifically, SFTs formed at high dose rate, while few SFTs were generated at low dose rate. Their MD simulations indicate that low dose rate leaves ample time for SIAs and vacancies to diffuse to the surface or recombine, whereas at higher dose rate, the time interval between cascades is shorter than the time needed for migration of defects to the surface. Consequently, vacancies have enough time to aggregate and form SFTs. Previous *in situ* study on NP Ag showed the removal of various types of defect clusters, including SFTs, small dislocation loops and large segments, by the free surface in NP Ag under 1 MeV Kr^{++} ion irradiation.[184] Furthermore, the *in situ* studies showed that both the global and instantaneous diffusivities in NP Ag are lower than those in CG Ag.

Despite these previous studies, the number of *in situ* studies on irradiation response of NP metals remains scarce. In addition, defect migration kinetics, which is crucial for the modeling of defect evolution in irradiated metals, remains largely unknown.[87, 278] The influence of dose rate on defect diffusivities is still unclear.[10, 183, 279]

Here we present *in situ* Kr ion irradiation studies on CG and NP Au. The migration of defect clusters and their elimination by free surfaces were captured by *in situ* video. Compared to our previous study on NP Ag[32], we have confirmed that NP Ag also has significantly better radiation tolerance than coarse-grained Au in terms of reduced size and density of radiation-induced defect clusters. Furthermore, we discovered the dose-rate-dependent defect global and instantaneous diffusivities in NP Au, which has not been studied in NP Ag previously. In addition, we observed void shrinkage due to the absorption of defect clusters by nanovoids during irradiation in NP Au, and their shrinkage rate depends on pore size. The outstanding irradiation tolerance of NP Au has important implications for the design of advanced NP materials under extreme radiation environment.

7.3 Experimental

The $Ag_{65}Au_{35}$ (atomic ratio) leaves (procured from New York Central Art Co.) with dimensions 20 mm × 20 mm × 120 nm were sandwiched by two 304 stainless steel plates and then cold rolled up to ~ 20 % strain so as to reduce the foil thickness and achieve electron beam transparent specimens. The rolled $Ag_{65}Au_{35}$ leaves were then chemically de-alloyed in a 70% HNO_3 solution for 4 h at room temperature. The etched leaves were repeatedly rinsed in deionized water to remove residual acid and eventually lifted off by Cu grids (400 mesh) for *in situ* radiation studies. All specimens were investigated using an FEI Tecnai G2 F20 ST microscope before and after irradiation. *In situ* irradiation experiment was performed at room temperature at the IVEM-TANDEM facility at Argonne National Laboratory. An 1 MeV Kr^{++} ion beam was used for radiation experiments to a maximum fluence of 2×10^{14} ions cm^{-2} (~1 dpa). The dose rate applied during *in situ* radiation experiments varied from 3.2×10^{-3} to 5×10^{-4} dpa/s. SRIM (Kinchin-Pease method) simulation was used to estimate the displacement damage profile (in the unit of displacements-per-atom (DPA)) and Kr ion distribution. Most Kr ions (99.99%) penetrated directly through the specimen and the residual Kr ion concentration in the TEM thin foil is ~ 0.01at.%. The temperature rise of specimens during *in situ* Kr ion irradiation measured by thermocouple is less than 10 °C.

7.4 Results

As-prepared CG Au and NP Au were both transparent to the electron beam. The diameter of nanovoids varies from ~10 to 100 nm, and the selected area diffraction (SAD) pattern suggests the film was highly textured. Fig. 7.1 compares the microstructural evolution in CG and NP Au under 1 MeV Kr^{++} ion irradiation at room temperature. Before irradiation, both NP Au and CG Au appeared relatively clean with little preexisting defects (Fig. 7.1a–a’). Radiation leads to a gradual and

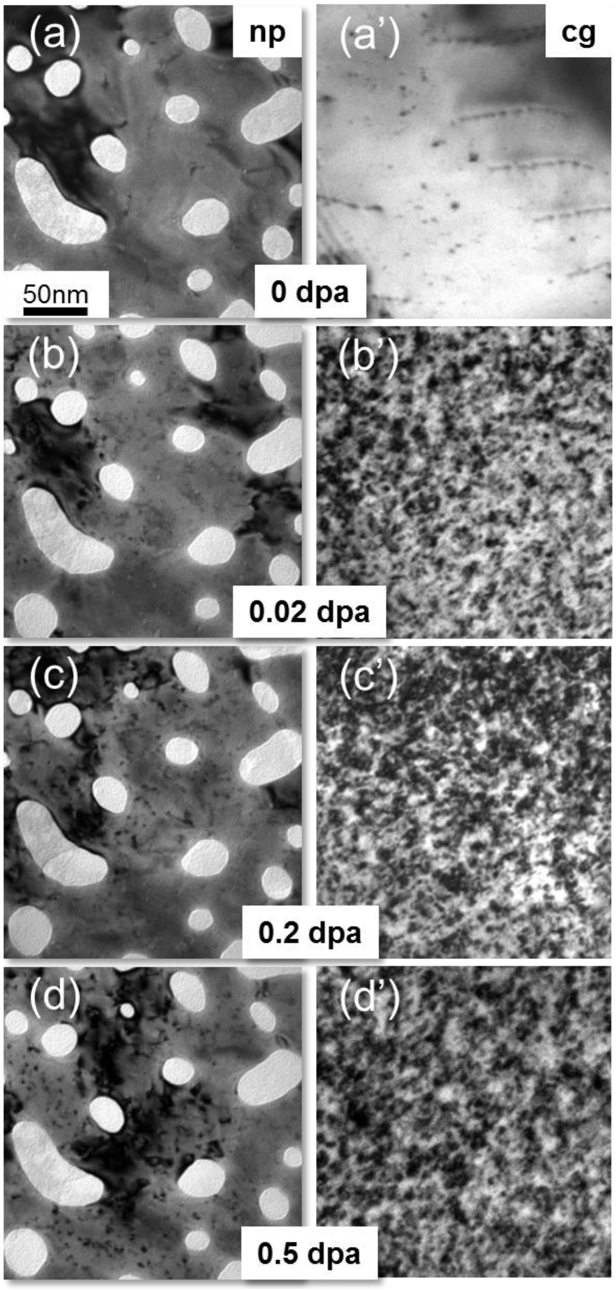

Fig. 7.1. Transmission electron microscopy (TEM) snap shots obtained from *in situ* radiation video revealed drastically different irradiation response between nanoporous (NP) and coarse grained (CG) Au subjected to *in situ* Kr ion irradiation at room temperature. (a-a') Before irradiation, both NP Au and CG Au appeared relatively clean with little preexisting defects. (b-d) TEM snap shots show gradual and moderate increase of defect density in irradiated NP Au, up to 0.5 dpa. (b'-d) In contrast, CG Au has accumulated much more defects rapidly by 0.5 dpa.

moderate increase of defect density in NP Au, up to 0.5 dpa (Fig. 7.1b-d). In contrast, CG Au has accumulated much more defects rapidly by 0.5 dpa (Fig. 7.1b'-d'). Bright field and weak beam dark field (WBDF) TEM images show that a majority of defect clusters are dislocation loops and SFTs. TEM snapshots from *in situ* videos compare CG and NP Au irradiated to several doses. From 0 to 0.02 dpa (Fi. 1b and 1b'), few defect clusters formed in NP Au, whereas defect density in CG Au increased rapidly. By 0.2 dpa, both the diameter and density of defect clusters in CG Au increased significantly (Fig. 7.1c'), while only a few defect clusters were generated in NP Au. By 0.5 dpa (Fig. 7.1d and 1d'), the average diameter of defect clusters in NP Au appeared much smaller than that in CG Au. Fig. 7.2 shows statistics of the diameter and density of defect clusters in NP Au and CG Au. The average defect size is ~ 10 and 4 nm for CG and NP Au, respectively (Fig. 7.2a). The defect density in both CG and NP Au reached saturation at similar dose, ~0.1 dpa (Fig. 7.2b).

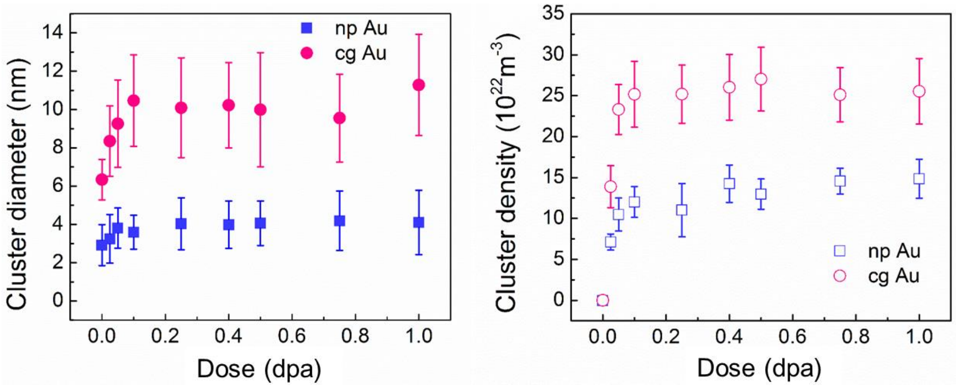

Fig. 7.2. Statistics of defect cluster diameter and density in NP Au and CG Au. (a) The average defect diameter is ~ 10 and 4 nm for CG and NP Au, respectively. (b) The defect density in both CG and NP Au reached saturation at similar dose level, ~0.1 dpa.

The migration of a large number of defect clusters in NP Au has also been examined to estimate their global and instantaneous diffusivities. The global diffusivity, D^{Global}, of a defect cluster is determined by using the square of overall defect migration distance (L^2) over the accumulative defect lifetime, which includes the migration time and dwelling time. Most defects migrate in a 'stick-slip' manner that is a defect cluster migrates instantaneously within a fraction of a second, and then stays for a while (dwelling time) before its next movement. Thus D^{Global} is correlated qualitatively to the average migration speed of a defect cluster over its entire lifetime. Meanwhile, we have also determined the instantaneous diffusivity, $D^{Inst.}$, of a defect cluster by only considering the diffusion distance over its migration time (excluding dwelling time). Thus $D^{Inst.}$ appears much greater (by an order of magnitude) than D^{Global}. The detailed methods to determine diffusivity have been shown previously [76]. Fig. 7.3a shows D^{Global} of defect clusters in NP Au at a higher dose rate of 3.2×10^{-3} is ~ 23 ± 5 nm^2/s (D_H^{Global}), significantly greater than ~ 4 ± 2 nm^2/s at a lower dose rate of 5×10^{-4} dpa/s (D_L^{Global}). Meanwhile, Fig. 7.3b shows the $D^{Inst.}$ of defect clusters of irradiated NP Au varies from 200 to 800 nm^2/s, and due to a large scattering, the average value of $D^{Inst.}$ shows little dependence on dose rate.

Typical examples of the evolution and interaction of defect clusters with nanovoids are demonstrated by *in situ* video snapshots over 0.02 – 0.04 dpa in Fig. 7.4. Two small isolated loops were identified at 0 s, one of them (outlined by red dots) was several nm away from the nanovoid, and the other one was adjacent to the void (marked in green) (Fig. 7.4a). After 2.8 s, two other loops (indicated by the yellow dotted lines) and an SFT (blue marker) emerged near the void (Fig. 7.4b). Fig. 7.4c-4e show the individual loops combined into a dislocation segment. Meanwhile, the SFT interacted with the void surface and was destructed. In Fig. 7.4f-4h, the same video also shows a small dislocation loop (marked by the red dotted line) migrated towards the void and was captured by 15.9 s. The dislocation segment combined more defects and then interacted with an adjacent SFT, leading to their mutual destruction (Fig. 7.4i-4l). Later a cluster of small SFTs emerged at 25.7s during irradiation (Fig. 7.4l).

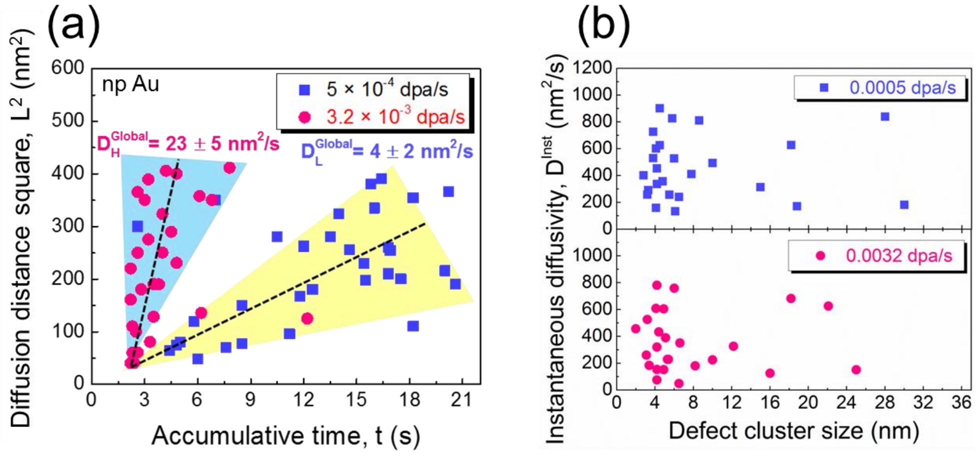

Fig. 7.3. The global and instantaneous diffusivities of defects under different dose rate in NP Au. (a) The global diffusivity of defects in NP Au is significantly reduced (by six times) when the dose rate decreased from 3.2×10^{-3} to 5×10^{-4} dpa/s. (b) The instantaneous diffusivity of defect clusters in irradiated NP Au varies from 200 to 800 nm^2/s, and the average value of instantaneous diffusivity shows little dependence on dose rate and cluster diameter.

Another phenomenon is the universal shrinkage of numerous nanopores during *in situ* radiation of NP Au and an example is shown in Fig. 7.5. Three pores with diameters of 15, 12 and 11 nm were tracked during radiation over 2 dpa (~ 1600s). During irradiation, a significant number of defect clusters migrated to these pores (defect absorption), and the dimension of pores decreased continuously (Fig. 7.5a-5e). For instance, by 1.25 dpa (Fig. 7.5f), the diameter of the pore (marked by red arrows) decreased substantially from 12 to merely 3 nm, and eventually disappeared by 1.5 dpa (Fig. 7.5g). The diameter of the other two nanopores changed from 15 to 8 nm, and 11 to 8 nm, respectively over 2 dpa. Statistical data in Fig. 7.6a show that nanopores shrink much faster at higher dose rate, 0.0032 dpa/s, compared to lower dose rate, 0.0005 dpa/s. Furthermore, the normalized shrinkage of pores, $\Delta d/d$, decreases rapidly with increasing pore size (Fig. 7.6b), indicating smaller pores shrink faster during irradiation.

7.5 Discussion

Free surfaces are perfect sinks for defects, so it is natural to speculate that NP Au with high surface-to-volume ratio would be more radiation tolerant compared to its CG counterpart. Indeed, our *in situ* studies show NP Au has excellent radiation resistance as evidenced by its substantially lower defect dimension and density than those in CG Au. During irradiation, although the defect density in both CG and NP Au reached saturation at similar dose level, the continuous migration of point defects and their clusters towards nanovoids leads to significant reduction of defect concentration, manifested by an overall decrease in defect size and density. Although it appears that there is only a moderate reduction of defect cluster density (a factor of 2) and cluster size (a factor of ~2.5) for NP Au compared to CG Au, the point defect concentration difference can be substantial. Assuming all defect clusters are spherical, the point defect concentration amounts to $(2.5)^3$

× 2 ≈ 30. Furthermore, many of the defect clusters in CG Au are much greater than the average defect diameter, whereas the defect clusters in NP Au has a much narrower size distribution. *In situ* studies captured evidence that shows the capturing of numerous types of defect clusters (including SFTs, individual dislocation loop, and dislocation segments) by nanovoids. The removal of various types of defect clusters by free surface has been reported previously during *in situ* radiation study of NP Ag [184].

Another significant observation revealed by *in situ* radiation study is the shrinkage of nanovoids in NP Au at room temperature. During radiation of NP Au at room temperature, most of the vacancies are bound in the form of sessile defect clusters, and thus there may be insufficient vacancies to support void growth. Meanwhile, there is a continuously biased flock of interstitials and their clusters to nanovoids during irradiation. As void shrinkage in the current study is caused by the absorption of irradiation-induced defects, these deliberately introduced nanovoids are excellent defect sinks, providing NP Au much better radiation tolerance than their CG counterparts. Furthermore, it is natural to speculate that the void shrinkage rate could be determined by the defect capture (absorption) rate or the frequency of interactions between nanovoids and defects. Fig. 7.6a confirms this hypothesis by tracking the evolution of diameters for a number of nanovoids. When the dose rate is increased by ~ six times, the void area, *A*, decreased much faster. Void shrinkage rate (indicated by the slope of the plots) in the high dose rate area (shaded by yellow color) is ~ six-times larger than the slope of the data in low dose rate area (highlighted in blue color), indicating the void shrinkage rate scales with dose rate.

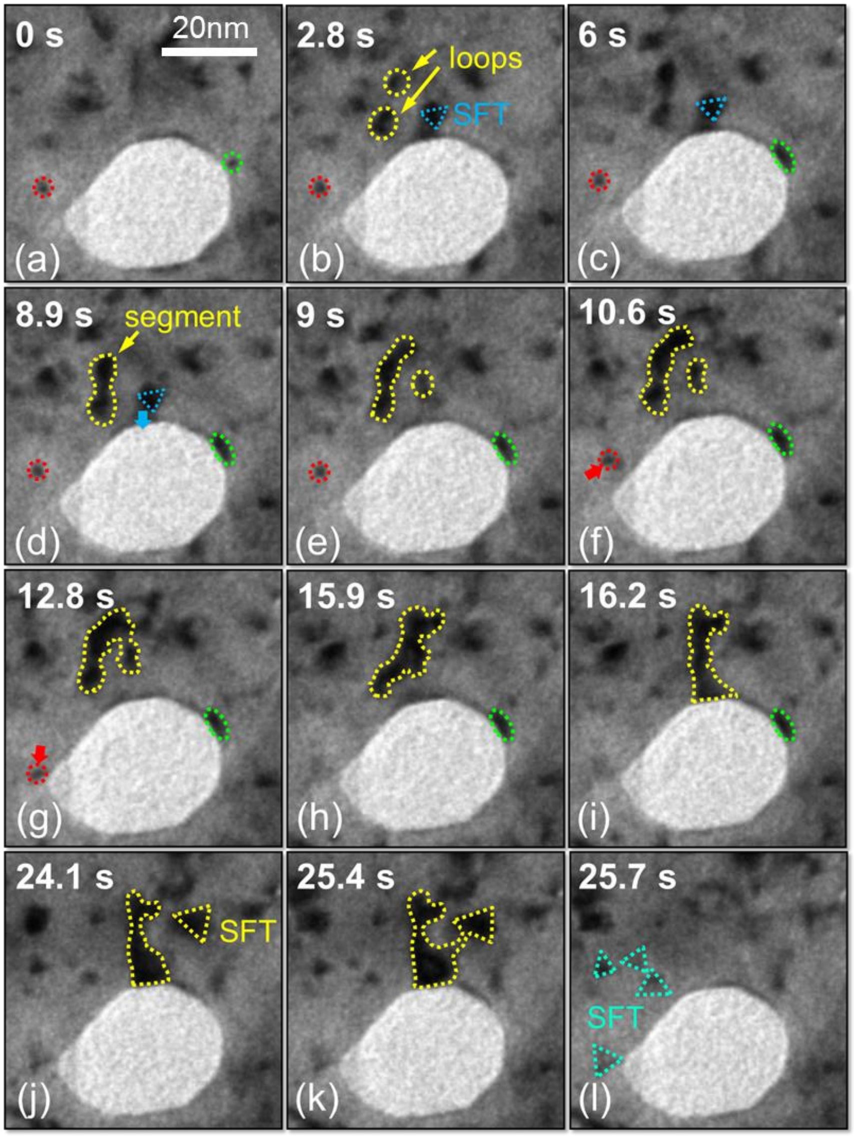

Fig. 7.4. *In situ* video snapshots showing several representative defect capture events by an individual nanovoid over 0.02-0.04 dpa (~ 26 s). (a) Two small isolated loops were observed, one of them (outlined by red dots) was several nm away from the nanovoid, and the other one was adjacent to the void (green marker). (b) After 2.8 s, two more loops (indicated by the yellow markers) and a SFT (blue marker) emerged near the void. (c-e) The individual loops combined into a short dislocation segment. Meanwhile, the SFT interacted with the void surface and was destructed. (f-h) A small dislocation loop (marked by the red dotted line) migrated towards the void and was captured by the void at 15.9 s. (i-l) The dislocation segment and a SFT interacted with each other and were eventually eliminated by the adjacent void.

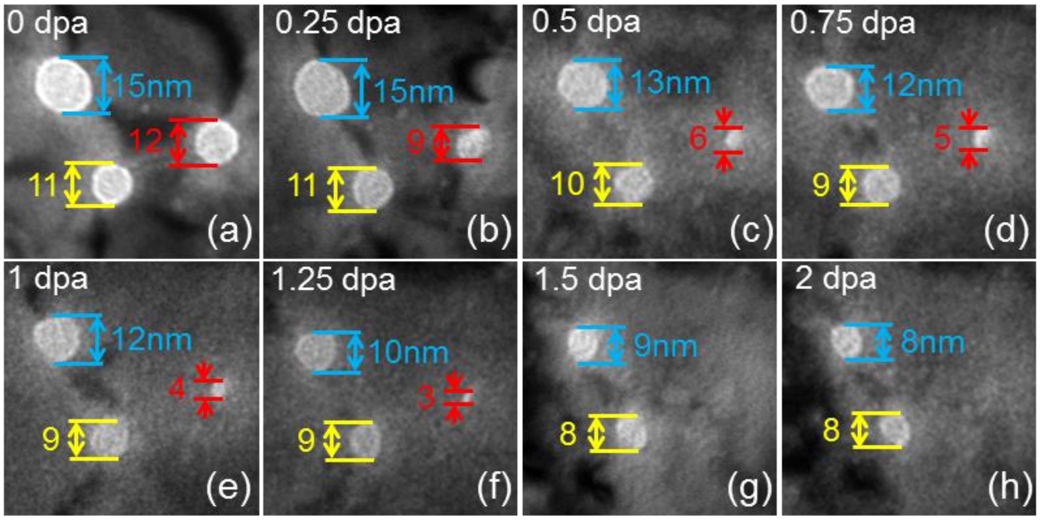

Fig. 7.5. *In situ* video snapshots showing the shrinkage of nanopores during irradiation (0-2 dpa). (a) Three pores with diameter of 15, 12 and 11 nm were observed before irradiation (0 dpa). (b-e) During irradiation, a large number of defects migrated to the pores (defect absorption), and the dimension of pores continuously decreased. (f) By 1.25 dpa, the diameter of the void (marked by red arrows) decreased substantially from 12 to merely 3 nm, and finally disappeared by 1.5 dpa (g). (h) The diameter of the other two nanopores changed from 15 to 8 nm and from 11 to 8 nm, separately.

Besides the direct observation of defect absorption events, another benefit of *in situ* study is that it allows us to estimate global and instantaneous diffusivities of defect clusters by carefully analyzing the videos and tracking the migration of defect clusters continuously during irradiation. More details on the methods to estimate diffusivity can be found in previous studies.[76, 178, 184] The global diffusivity for defect clusters in NP Au is calculated to be 4 ± 2 nm^2/s when dose rate is 5×10^{-4} dpa/s, and 23 ± 5 nm^2/s at a higher dose rate of 3.2×10^{-3} dpa/s. Clearly, the global diffusivity is significantly reduced (by six times) when the dose rate decreases. However, the instantaneous diffusivity in NP

Au varies from 200 to 800 nm^2/s and shows little dependence on dose rate. Such intriguing phenomena clearly warrant further discussions.

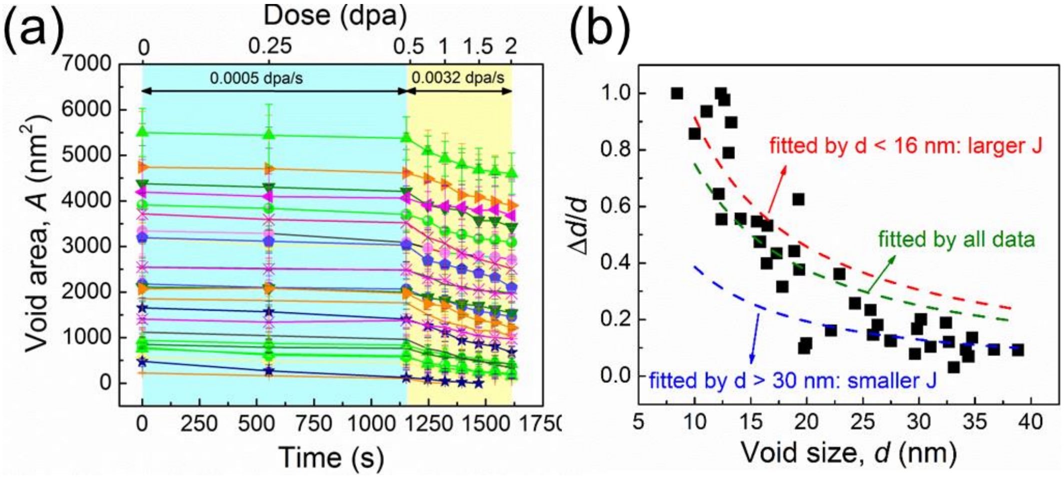

Fig. 7.6. Statistic data revealing the shrinkage of nanopores during irradiation (0-2 dpa). (a) Statistic data showing the evolution of pore diameter vs radiation dose. Nanopores shrank much faster at higher dose rate, 0.0032 dpa/s, compared to lower dose rate, 0.0005 dpa/s. (b) The normalized diameter reduction, $\Delta d/d$, as a function of pore size. The olive dashed line is the result of fitting for all data, and the red dashed line and blue dashed line are fitting results by choosing the data in the range of d < 16 nm and d > 30 nm, respectively. A significant deviation between three fitting results indicates that J is greater (smaller) for smaller (larger) voids.

Both global and instantaneous diffusivities are determined by two factors: diffusion distance and a defect's lifetime. In this study, the diffusivities of defect clusters were estimated when defect density reached saturation. The saturated defect cluster density in NP Au is ~ 15×10^{22} m^{-3} as shown in Fig. 7.2b, and therefore, the distance between two defect clusters can be simply estimated to be 15 ~ 21 nm (these values considered (1) average defect diameter, 4 nm, and (2) the length between two defect clusters can be either side length or diagonal length in a square). Although dose rate has been changed, the defect density has reached a plateau (independent of dose rate from ~0.1 - 2.0 dpa). It follows that the average diffusion distance (limited by defect separation distance) for both high and low dose rate is nearly the same, ~ 18 nm (see Fig. 7.3a). Thus the global diffusivity of defects may be largely determined by defects' lifetime.

A defect's lifetime includes two components, defect migration time (hopping time) and dwell time (rest time). To estimate the global diffusivity, both migration and dwell time were taken into account. As a defect migrate very rapidly, the migration time of a defect is very short, and the lifetime of a defect is dominated by its dwell time. Compared to low dose rate, both defect generation rate and recombination rate increased prominently at higher dose rate. As a consequence, a defect cluster cannot stand still for a long time. Instead, it will frequently migrate toward the free surface, or combine with other clusters. Thus the defect's dwell time significantly decreases at higher dose rate. Since diffusion lengths are similar in both cases (low vs. high dose rate), the global diffusivity at high dose rate is larger than that at low dose rate.

In contrast to global diffusivity, only a defect's migration time is considered to determine the instantaneous diffusivity. Nearly all defects migrated within a single frame, and therefore, a defect's migration time is assumed to be 66 ms for a single migration event (limited by the camera's capture speed of 15 frames/s). Notice that such an assumption may overestimate a defect's migration time. There is a large scattering of instantaneous diffusivity. Consequently, the instantaneous diffusivity appears to have an insignificant dependence on dose rate and defect dimension.

We now examine the shrinkage of nanovoids in NP Au. Void swelling is frequently observed in many neutron and heavy ion irradiated metals at elevated temperatures,[134-138] while void shrinkage is commonly observed at room temperature or at the temperature much below the material's melting point.[146, 334-336] It is known that vacancies will be bundled in thermally stable defect clusters, such as vacancy loops and SFTs, during energetic displacement cascade under heavy ion irradiation, and interstitials are mobile near room temperature.[36, 337, 338] Therefore, void shrinkage is anticipated in the current study. However, a question remains to be addressed is: Does defect absorption efficiency dependents on void size in NP materials? Fig. 7.6b may provide some clues to this question.

Assuming the incoming flux of defect into a single void is a constant J (unit: volume/area·second), and these defects will fill in the voids (leading the reduction of void diameter), then J can be simply estimated by (assuming that most nanovoids are through thickness nanopores with cylindrical shape):

$$\Delta V = \Delta R \cdot 2\pi R \cdot h = J \cdot \Delta t \cdot 2\pi R \cdot h \qquad (7.1)$$

where V is the volume of voids, R (= d/2) is the radius of voids, h is the film thickness. ΔR is the reduction of void radius over a period of Δt. It is readily seen that $\Delta R = J\Delta t$, i.e., $\Delta d = 2J\Delta t$. Consequently the relation between normalized void shrinkage, $\Delta d/d$, and void size d can be expressed as:

$$\Delta d / d = 2(J \cdot \Delta t)/d \qquad (7.2)$$

Thus, the normalized void shrinkage is inversely proportional to the initial defect diameter. This is very close to what has been captured experimentally (Fig. 7.6b). Furthermore, the attempt to use a constant J to fit all data point (Olive dash line) seems to underestimate (overestimate) $\Delta d/d$ for smaller (larger) voids. Such systematic deviation suggests that J is greater for smaller voids and less for larger voids. In other words, defects may interact more frequently with smaller voids than the larger ones during irradiation, and therefore, defect absorption efficiency is higher for smaller voids than larger voids. In a recent study on nanovoid-nanotwinned Cu (with an average void diameter of ~ 10 nm), significant loop-void interactions were observed. Analytical calculations show the existence of significant tensile stress surrounding voids.[83] When a loop comes closer to a void, its migration rate increases drastically due to the substantial reduction of formation and migration energies of the loop under tensile stress. Compared to larger voids, smaller voids generate higher stress field near void surfaces and therefore, smaller voids capture more defects during irradiation.

It may appear that the irradiation resistance of NP metals will degrade over the long term if most of the nanovoids are completely filled with radiation induced defect clusters. Such concern can be eased for the following reasons. First, bulk (fully dense) Au is extremely vulnerable to radiation damage as shown by severe radiation damage at merely 0.02 dpa. It is clear that nanovoids significantly delay damage accumulation in Au by more than an order of magnitude, rending NP Au more resistant to heavy ion irradiations to a much greater dose (1 dpa). Furthermore, the foregoing studies show that the concentration of point defects (such as self-interstitial atoms) could also be an order of magnitude lower in NP Au than in CG Au. Such a concept derived from the current study indicates that the safe service period (lifetime) of nuclear reactor steels, if engineered with nanoporous structures, could also be significantly extended. Second, Au is a model system that is known to be vulnerable to radiation damage than many other alloys, such as austenitic stainless steels. One can envision that for a practical reactor steel, the incorporation of nanovoids/nanopores could achieve even greater radiation tolerance than what has been demonstrated in the current model system. Third, although nanovoids may be eliminated during radiation, modeling tool (such as phase field models), may reliably predict the correlation between the service lifetime and desirable combination of different diameter and density nanovoids for design purposes. As Fig. 6(b) suggested, smaller voids shrink faster than the larger ones. Therefore, by deliberately introducing nanovoids with different diameters and density, the radiation stability of reactor steels may be significantly prolonged. Of course, further improvements in nanopore stability might also be beneficial before this concept transfers into a practical option for future reactor steels.

7.6 Conclusion

In situ heavy ion irradiation studies were performed on nanoporous Au at room temperature. Dose-rate-dependent defect migration diffusivities were examined, and the global diffusivity is significantly reduced when the dose rate decreases, while the instantaneous diffusivity shows little dependence on dose rate. Nanovoids are effective defect sinks where various types of defect clusters can be absorbed during irradiation. The absorption of defect clusters leads to the shrinkage of nanovoids, and the shrinkage rate, or defect absorption efficiency, is size-dependent. Comparing to larger voids, smaller voids exhibit higher defect absorption efficiency capture more defects during irradiation. This study provides significant insight into the design of radiation-tolerant nanoporous metallic materials.

7.7 Acknowledgement

We acknowledge financial support by NSF-DMR-Metallic Materials and Nanostructures Program under grant no. 1643915. JD is supported financially by Petroleum Research Foundation # 53741 -ND10. S. Xue is supported by DoE-OBES under grant no. DE-SC0010482. We also acknowledge the use of microscopes at the Microscopy and Imaging Center at Texas A&M University and the DoE Center for Integrated Nanotechnologies managed by Los Alamos National Laboratory. The IVEM facility at Argonne National Laboratory is supported by DOE-Office of Nuclear Energy.

CHAPTER VIII

IN SITU STUDIES ON RADIATION RESISTANCE OF NANOPOROUS AU THROUGH TEMPERATURE-JUMP TESTS

8.1 Overview

Nanoporous (NP) materials have great potentials to alleviate irradiation-induced damage due to their giant surface-to-volume ratio. Previous *in situ* irradiation study on NP Au at room temperature has shown the shrinkage of nanopores due to the absorption of irradiation-induced defects, and the shrinkage rate is pore-size-dependent. In this follow-up temperature-dependent study, we show that both defect density and nanopores evolve with radiation temperature. Higher temperature results in lower defect density and reduced shrinkage rate of nanopores. The sink strength of nanopores as a function of temperature is estimated. Moreover, NP Au exhibits significantly enhanced swelling resistance compared to coarse-grained Au. Potential mechanisms for temperature dependent radiation resistance of NP metals are discussed.

8.2 Introduction

Radiation responses of metallic materials subjected to high-energy particle (electron, neutron, and heavy ions) irradiation have been intensively investigated over the past few decades [4, 12, 36, 339]. Next-generation nuclear reactors demand significant improvement of fuel performance as well as superior structural materials that can sustain extreme radiation environment over a much longer period of service lifetime than those materials in conventional reactors [3, 4]. Upon exposure to high-energy particle (neutron or heavy ions) bombardments, a significant number of point defects are produced in the irradiated materials [12, 36]. Furthermore, these point defects can migrate, interact with other defects and evolve into much greater defect clusters, such as dislocation loops, dislocation networks and voids [6-8]. The microstructural damage can dramatically impact the properties and stability of irradiated materials in the form of radiation-induced hardening and loss of ductility, change in material dimension (such as swelling), loss of electrical and thermal conductivities, and radiation-induced phase segregation and precipitation, and degradation of corrosion resistance [9-18].

Among various types of radiation-induced microstructural damage, volumetric swelling caused by the accumulation of voids is a severe problem [3, 16, 36, 340-347]. Void swelling occurs in most irradiated metals and alloys [139, 348]. It is very difficult to accommodate a swelling level up to 5% through engineering design. When swelling is larger than 10%, the materials suffer from servere radiation embrittlement. Clearly, there is a strong need for the design of swelling-resistant structural materials. Void formation occurs due to the preferential absorption of interstitials by biased defect sinks [139], and typically requires two conditions: a supersaturation of vacancies; and agglomeration of vacancies before being annihilated by interstitials or defect sinks. If more vacancies than interstitials arrive at void nuclei, voids will grow continuously. One method to disrupt the formation and growth of voids is to introduce a high density of point defect sinks that can reduce the supersaturation and aggregation of vacancies.

To enhance radiation resistance of materials, various types of defect sinks have been investigated, such as grain boundaries (GBs), twin boundaries (TBs), phase boundaries, etc. [76, 89, 170-179, 317]. Nanoporous (NP) metals are expected to exhibit enhanced swelling resistance compared to their fully dense coarse-grained (CG) counterparts because of their large free surface area per unit volume [183, 184, 257]. An enlightening thought has been proposed almost 20 years ago to develop naturally porous structural materials in nuclear fuels to alleviate the fission gas accumulation with nanophases [167]. However, the number of radiation studies on NP metals remains very limited [78, 184, 188]. The potential of NP metals to alleviate void swelling has not been systematically testified yet. In our previous *in situ* irradiation study on NP Au, nanopore shrinkage has been observed instead of void swelling when irradiated at room temperature [78]. Nanopores shrink during irradiation by absorption of interstitials and their clusters, and their shrinkage rate is pore-size-dependent, i.e. smaller pores shrink faster because of higher efficiency to absorb radiation-induced defects [78, 83]. However, the radiation response and swelling resistance of NP metals have not been investigated at elevated temperatures.

Defect sink strength is a parameter used to quantify the efficiency of a defect sink in annihilating radiation-induced defects (or the affinity of a sink for defects), and it is one of the central parameters in the reaction-rate theory [12, 308]. However, it remains challenging to obtain sink strength from experimental studies [349, 350]. One method frequently used to study the sink strength of different GBs is to compare the width of the defect-denuded zone [254, 307, 308, 351]. In parallel, computer simulations, such as molecular statics and molecular dynamics (MD) simulations are widely used to describe sink strength [254, 320, 349, 352-355]. Most prior studies on sink strength focus on GBs, TBs or layer interfaces [241, 254, 320, 356, 357], while research on sink strength of free surface in NP metals remains limited.

Here we present a systematic study on *in situ* Kr ion irradiation on NP Au and CG Au at various temperatures. Temperature-dependent defect evolutions of defect size, density and diffusivities in both NP Au and CG Au have been investigated. Surprisingly, nanopore shrinkage in NP Au has been observed even close to peak swelling temperature, and void swelling in NP Au is largely suppressed as compared to CG Au. The hypothetical mechanisms that lead to the suppression of void growth in NP Au are discussed. In addition, the sink strength of nanopores is calculated from experimental studies of NP Au.

8.3 Experimental

$Ag_{65}Au_{35}$ (atomic ratio) leaves (procured from New York Central Art Co.) with dimensions 20 mm × 20 mm × 120 nm were sandwiched by two 304 stainless steel plates, and then cold rolled up to ~ 20 % strain so as to reduce the foil thickness and achieve electron beam transparent specimens. More information on TEM specimen preparation can be found elsewhere [78]. All specimens were investigated using a Thermo Fischer Scientific/FEI Talos 200X and an FEI Tecnai G2 F20 ST microscopes before and after irradiation. *In situ* irradiation experiment was performed at room temperature at the IVEM-TANDEM facility at Argonne National Laboratory. An 1 MeV Kr^{++} ion beam was used for radiation experiments to a maximum fluence of 2×10^{14} ions cm^{-2} (∼1 dpa). The dose rate applied during *in situ* radiation experiments varied from 3.2×10^{-3} to 5×10^{-3} dpa/s. SRIM (Kinchin-Pease method) simulation was used to estimate the displacement damage profile (in the unit of displacements-per-atom (DPA)) and Kr ion distribution.

Most Kr ions (99.99%) penetrated directly through the specimen and the residual Kr ion concentration in the TEM thin foil is ~ 0.01at.%. The temperature rise of specimens during *in situ* Kr ion irradiation measured by thermocouple is less than 10 °C.

8.4 Results

A bright-field TEM image in Fig. 8.1a showing the overview microstructure of NP Au before irradiation. NP Au exhibits (110) texture as inferred from the inserted selected area diffraction (SAD) pattern. In this study, three series of *in situ* irradiation experiments are summarized in Fig. 8.1b.

Series I: temperature-jump tests (400→300→200→100 °C, ~ 1 dpa at each temperature) for NP Au and CG Au;

Series II: *in situ* radiation of NP Au at constant temperature, 200 °C; and

Series III: *in situ* radiation of NP Au and CG Au at room temperature (RT).

During irradiation, both NP Au and CG Au exhibit different responses at different temperatures. Fig. 8.2 compares irradiation responses of NP Au and CG Au at various temperatures through a series of transmission electron microscopy (TEM) snapshots obtained from *in situ* videos. Before irradiation, both CG Au and NP Au have little defects (Fig. 8.2a1- e1). During radiation of CG Au at RT (Fig. 8.2a2-a4), defects accumulate rapidly with increasing dose to 1 dpa. At 400^{o}C, radiation of CG Au induces much fewer defects (Fig. 8.2b2-b4). In comparison to radiation of CG Au, during radiation of NP Au at the same temperature (RT and 400^{o}C shown in Fig. 8.2c2-c4 and e2-e4), the number of defects increases gradually and moderately with dose up to 1 dpa. Furthermore, comparison of radiation damage in NP Au at different temperatures (Fig 2c-e) shows that defect density decreases with increasing radiation temperature in NP Au.

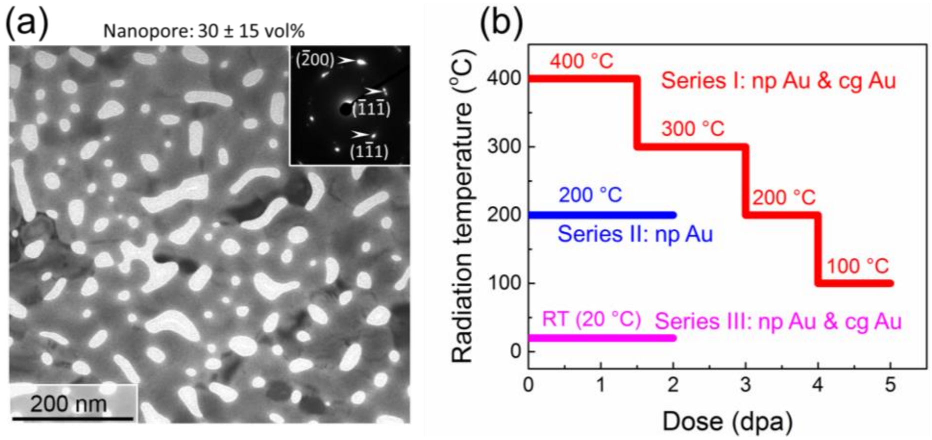

Fig. 8.1. (a) A bright-field TEM image showing the overview microstructure of NP Au before irradiation. The inserted SAD pattern shows NP Au exhibits (110) texture. (b) The summary of *in situ* irradiation experiments reported in this study. Series I: temperature-jump tests (400→300→200→100 °C) for NP Au and CG Au; Series II: *in situ* radiation of NP Au at constant 200 °C and Series III: *in situ* radiation of NP Au and CG Au at room temperature (RT).

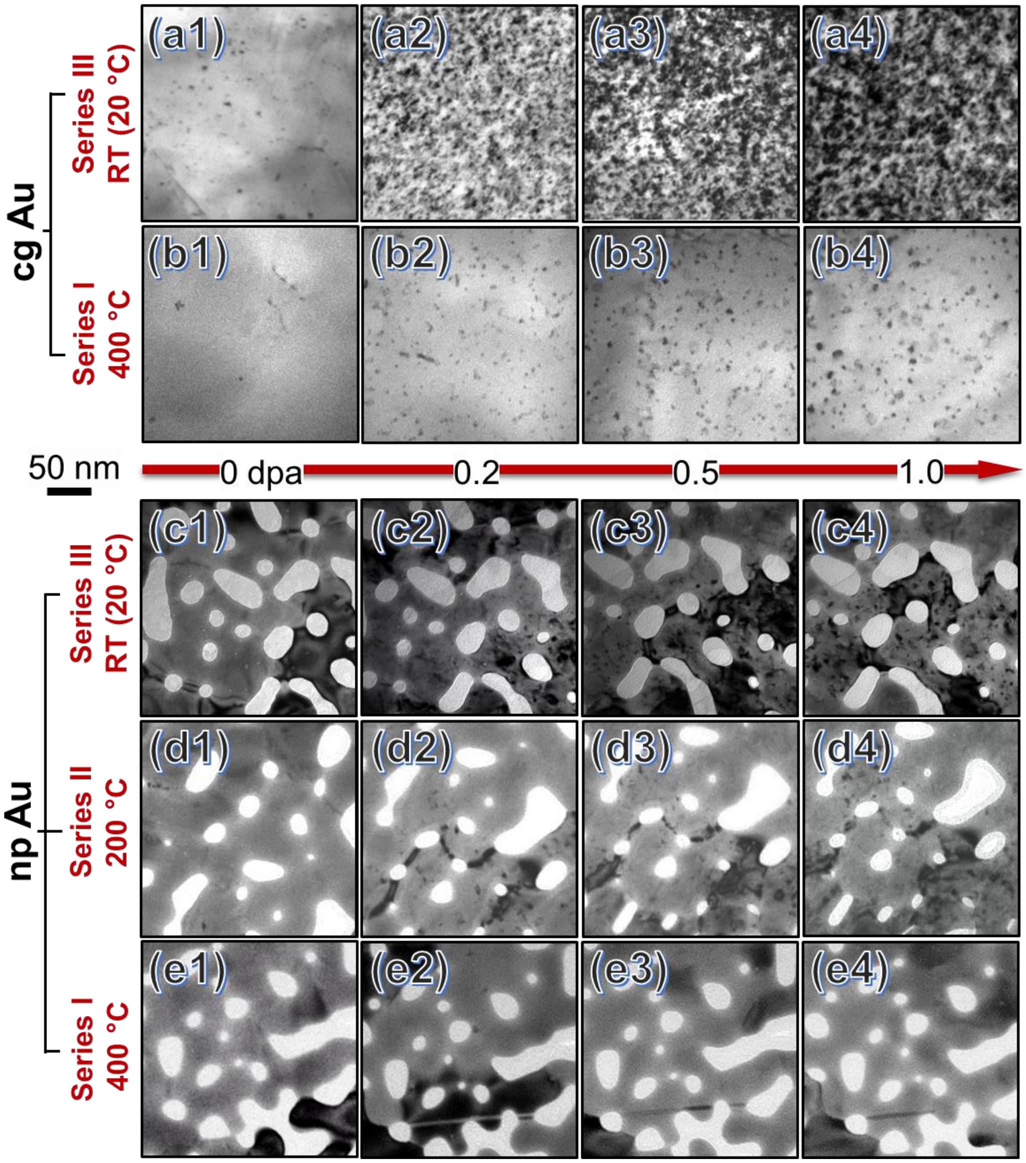

Fig. 8.2. Transmission electron microscopy (TEM) snapshots obtained from *in situ* Kr ion irradiation videos compare irradiation response between NP Au and CG Au at various radiation temperatures. Before irradiation, both CG and NP Au have little defects (a1, b1, c1, d1, e1). (a2-a4) During radiation, defects accumulate rapidly in CG Au at RT (b2-b4). At 400^{o}C, radiation induces much fewer defects in CG Au (c2-c4, d2-d4, e2-e4). In contrast, during radiation of NP Au, the number of defects increases gradually and moderately with dose up to 1 dpa. Furthermore, defect density decreases with increasing radiation temperature.

SFTs are the major type of defect clusters introduced during irradiation. Bright-field TEM images in Fig. 8.3 (a-c) shows that after temperature-jump irradiation tests of NP Au, 400→100 °C (to 5 dpa), many truncated SFTs are observed as confirmed by atomic resolution TEM. Radiation of NP Au at constant temperature, 200 °C to 2 dpa, (Fig. 8.3d-f) also leads to abundant SFTs. The statistics of defect size (cluster diameter) and density evolution as a function of dose and radiation temperature in NP Au and CG Au are shown in Fig. 8.4. The colored background in (a-d) is used to distinguish different temperature stages for Series I specimens (irradiated at 400→100 °C). The average defect size is ~ 4 nm after 0.1 dpa of radiation of NP Au (Fig. 8.4a) regardless of radiation temperature. In CG Au irradiated via temperature-jump tests, however, defect size increases from ~ 4 nm (irradiated at 400^{o}C) to 10 nm (at 100^{o}C) (Fig 4b). At RT, the defect size in CG Au increases drastically before 0.1 dpa and then reaches a plateau, ~ 10 nm. During temperature-jump irradiation tests of NP Au, the defect density in Fig. 8.4c increases stepwise when radiation temperature decreases from 400 to 100^{o}C. For isothermal radiation of NP Au at 200^{o}C, defect density increases rapidly and reach a saturation level comparable to that at 200^{o}C in the temperature-jump test. For radiation performed at RT, the defect density increases much more rapidly to a greater level than that irradiated at 200^{o}C. The stepwise increase of defect density in CG Au shown in Fig. 8.4d is also observed during temperature-jump irradiation studies. Also the defect density in CG Au is 2-3 times larger than that in NP Au irradiated at the same condition. The saturation defect size in NP Au (Fig. 8.4e) is ~ 4 nm and has little temperature-dependence. In contrast in irradiated CG Au, saturation defect size is ~ 10 nm at RT, and decreases monotonically to ~ 4 nm with increasing temperature to 400^{o}C. Fig. 8.4f shows that saturation defect density in both NP Au and CG Au decreases gradually with increasing radiation temperature. Defect cluster diffusivities as a function of radiation temperature for Kr ion irradiated NP Au are also estimated. The global diffusivity of defect clusters, shown in Fig. 8.5a, increases significantly from 23 ± 5 to 48 ± 30 nm^2/s when radiation temperature increases from RT to 400 °C. The instantaneous diffusivity of defect clusters in Fig. 8.5b however, shows little temperature dependence as compared to the global diffusivity.

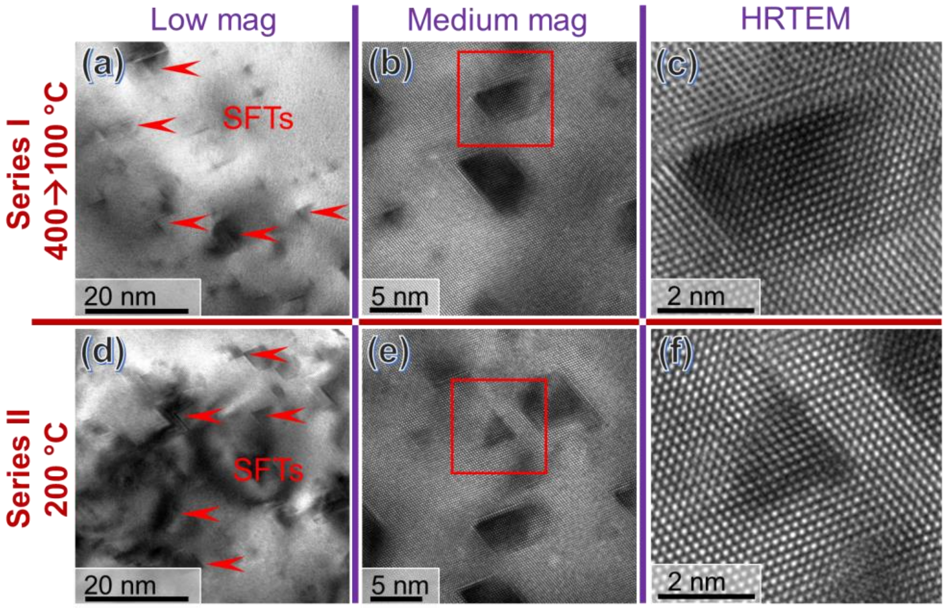

Fig. 8.3. Bright-field TEM images are showing the formation of SFTs in irradiated NP Au. (a-c) After temperature-jump irradiation, 400→100 °C (5 dpa), SFTs (many of them are truncated) are observed as confirmed by their triangular shape and atomic resolution TEM. (d-f) Radiation at 200 °C (2 dpa) also leads to abundant SFTs.

The shrinkage of nanopores in NP Au has been observed at all radiation temperatures explored in this study. At 100 °C, three nanopores in Fig. 8.6 (a) with areas of 150, 380 and 290 nm^2 decreases to 120, 310 and 230 nm^2, respectively after radiation to 1 dpa (Fig. 8.6 (d)) corresponding to 20%, 18.4% and 20.7% reduction in volume. In comparison, three nanopores in Fig. 8.6 (e) irradiated at 400 °C shrink by 2.5%, 6.3 % and 1.3%, respectively. The statistics data monitoring a series of nanopores shrinkage process in NP Au irradiated at 100 and 400^oC temperatures are shown in Fig. 8.7a. The color-dashed lines are the representative linear fitting results showing the reduction of pore areas. As shown in Fig. 8.7b, the average pore shrinkage rate (%/dpa) decreases monotonically with increasing radiation temperature, from ~21%/dpa at RT [78] to1.6%/dpa at 400 °C.

The shrinkage of nanopores is a consequence of the continuous migration of irradiation-induced defects towards nanopores. Representative defect capture events by an individual nanopore are shown in Fig. 8.8 for *in situ* irradiated NP Au at 200 °C over ~ 0.17 dpa (~ 53 s) (see Supplementary Video 1). A nanopore with an area of $430nm^2$ is monitored during radiation (Fig. 8.8a). As the nanopore does not have perfect circular shape, its area rather than diameter is used for analysis. By 7.1 s, a defect cluster (outlined by olive dots) formed next to the nanopore (Fig. 8.8b). The defect cluster was then gradually absorbed by the nanopore (Fig. 8.8c-d). Two defect clusters outlined by blue dots were observed near the pore at 24.2 s (Fig. 8.8e). During irradiation, the smaller cluster gradually migrated towards the nanopore, and combined with the large cluster (Fig. 8.8f-i), and the combined defect cluster was largely absorbed by the nanopore (Fig. 8.8j).

A stacking fault tetrahedron (SFT) formed at 43.3 s (Fig. 8.8k). After 5.7 s, the SFT was destructed and partially removed, and then annihilated at 51.9 s (Fig. 8.8l-n). Fig. 8.8o-p show, by 53 s, a large defect cluster emerged adjacent to the nanopore and was instantly eliminated within 0.2 s. During the interaction of these defect clusters with the nanopore, the area of the nanopore reduced from 430 to 420 nm^2.

Void swelling is, in general, expected in FCC metals under irradiation near peak swelling temperature, ~ 250 °C for Au. The comparison of void swelling behavior between NP Au and CG Au in Series I study (temperature-jump test) after irradiation to 5 dpa is shown in Fig. 8.9. In CG Au as shown in Fig. 8.9a, nanovoids form with a density of 9.6 ± 2.2 (× 10^{21}/m^3). In comparison, in irradiated NP Au (Fig. 8.9b), the radiation-induced nanovoids have a lower density of 1.1 ± 0.5 (× 10^{21}/m^3). The statistic distributions in Fig. 8.9c and 9d show that the average void size in irradiated CG and NP Au is 5 ± 3 nm, and 2 ± 1 nm, respectively. The irradiated CG Au has a maximum void size of 12 nm, comparing to 4 nm in irradiated NP Au.

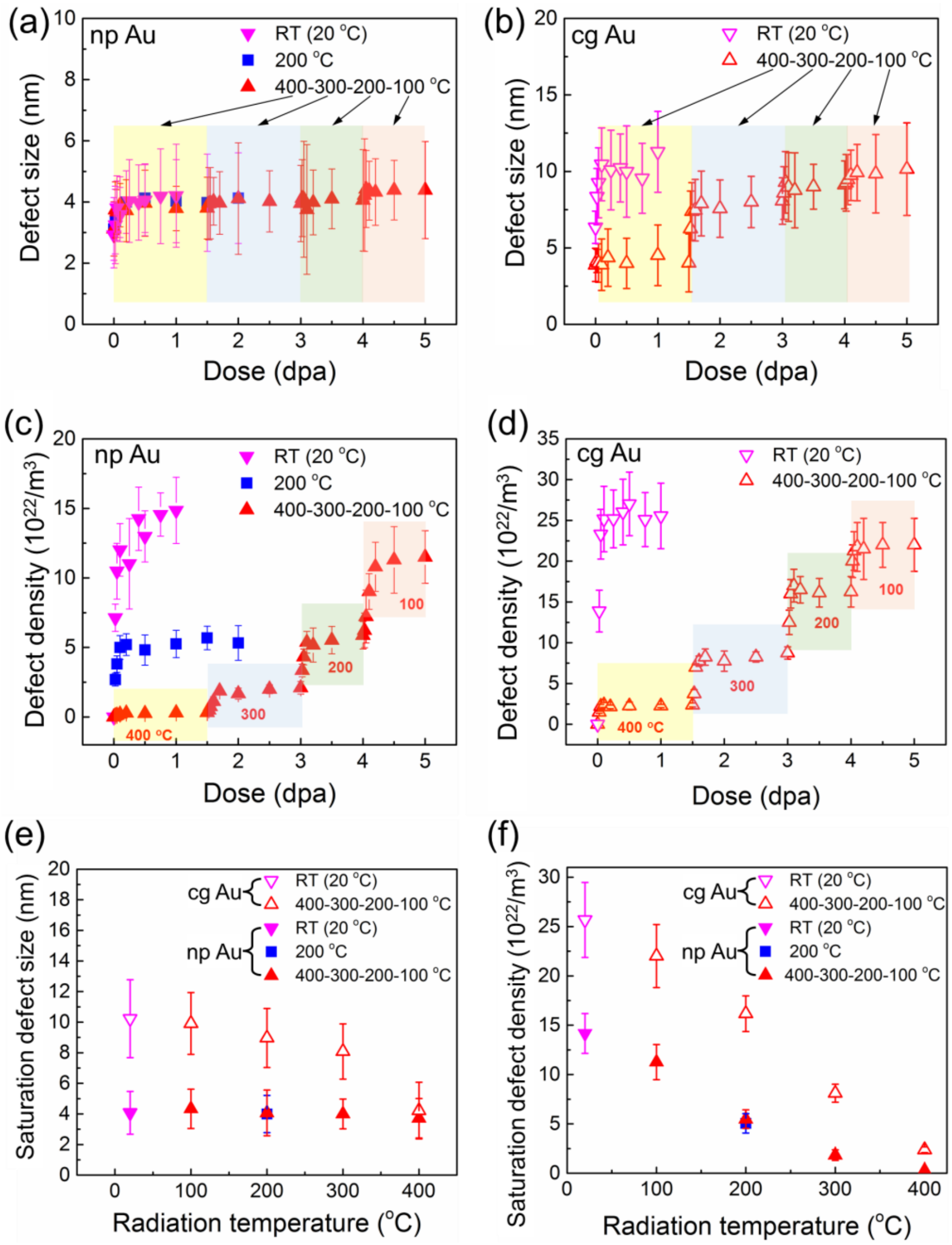

Fig. 8.4. Statistics of defect size (cluster diameter) and density evolution as a function of dose (a-d) and radiation temperature (e-f) in NP Au and CG Au. The colored background in (a-d) is used to distinguish different temperature stages for Series I specimens (irradiated at 400→100 °C).

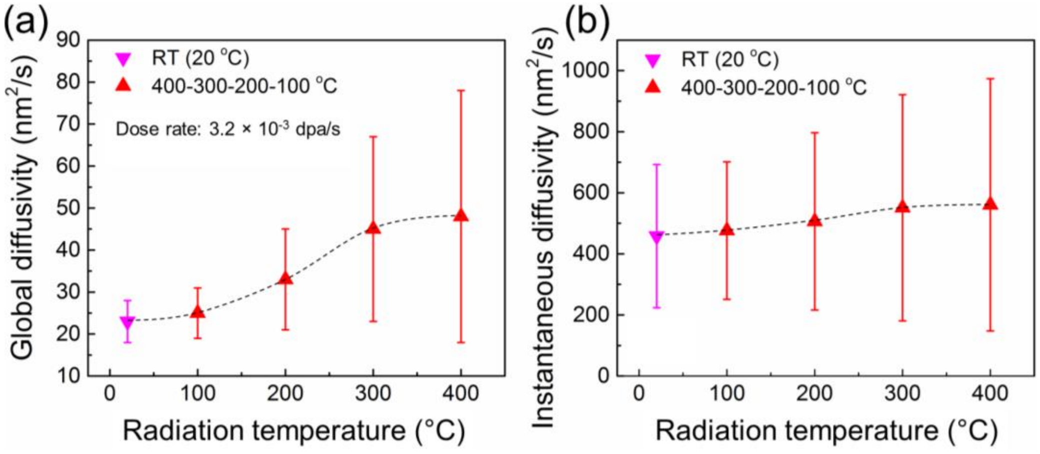

Fig. 8.5. Defect cluster diffusivities as a function of radiation temperature for Kr ion irradiated NP Au. (a) The global diffusivity of defect clusters increases significantly from 23 ± 5 to 48 ± 30 nm^2/s when radiation temperature increases from RT to 400 °C. (b) The instantaneous diffusivity of defect clusters shows little temperature dependence as compared to the global diffusivity.

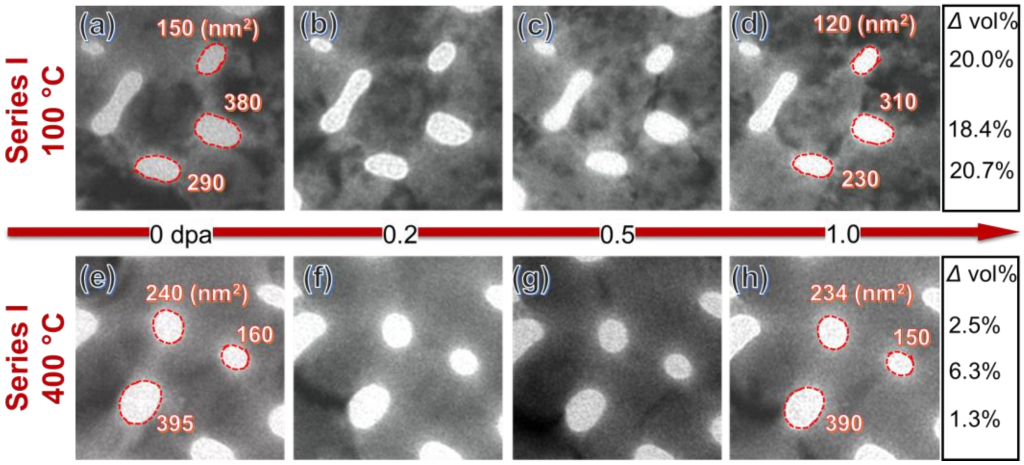

Fig. 8.6. *In situ* video snapshots showing the comparison of pore shrinkage of NP Au at two different temperatures. (a-d) At 100 °C, three nanopores with areas of 150, 380 and 290 nm^2 decreases to 120, 310 and 230 nm^2, respectively after radiation to 1 dpa, corresponding to 20%, 18.4% and 20.7% reduction in volume. (e-h) In comparison, three nanopores barely shrink at 400 °C, by 2.5%, 6.3 % and 1.3%.

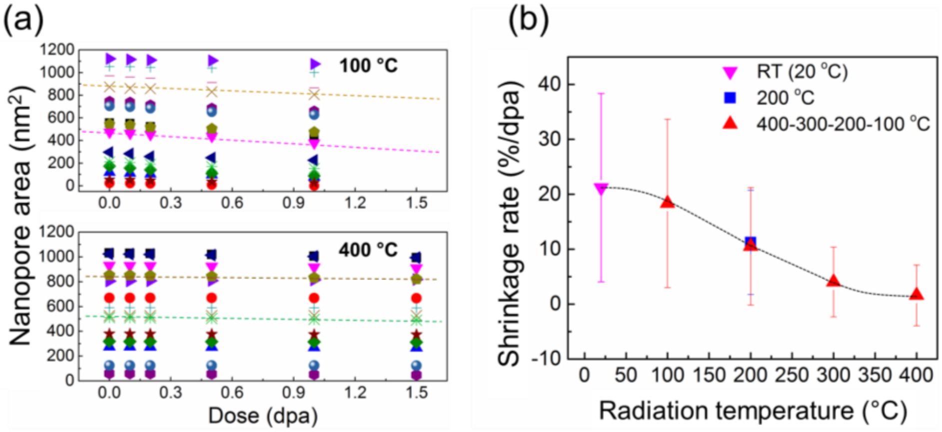

Fig. 8.7. Statistic data reveal the temperature-dependent shrinkage of nanopores during irradiation of NP Au. (a) Two examples of NP Au irradiated at 100 and 400 °C showing the evolution of pore area versus radiation dose. The color-dashed lines are the representative linear fitting results. (b) Average pore shrinkage rate (%/dpa) decreases with increasing radiation temperature, from ~ 21%/dpa at RT [46] to 1.6%/dpa at 400 °C.

Defect sink strength is an important parameter used to quantify the efficiency of a defect sink in annihilating radiation-induced defects. Fig 10a shows the number of defects being absorbed by the free surface of nanopores ($\rho_{\text{absorb}}^{\text{NP}}$) as a function of radiation temperature. The results are deduced from Fig. 8.4f by subtracting the defect density in NP Au from the defect density in CG Au irradiated at the same temperature. Below 200 °C, $\rho_{\text{absorb}}^{\text{NP}}$ decreases slightly (from 11.5 to 10.5 × 10^{22}/m^3) with increasing temperature. However, when T > 200$^{\mathrm{o}}$C, $\rho_{\text{absorb}}^{\text{NP}}$ decreases sharply. The calculated nanopore sink strength as a function of radiation temperature is shown in Fig. 8.10b. The shadow area represents the deviation by considering the variation of nanopore size. Clearly, two distinct regions can be identified. Below 200 °C (Region I), sink strength shows little temperature dependence, whilst above 200 °C (Region II), sink strength is inversely proportional to the irradiation temperature.

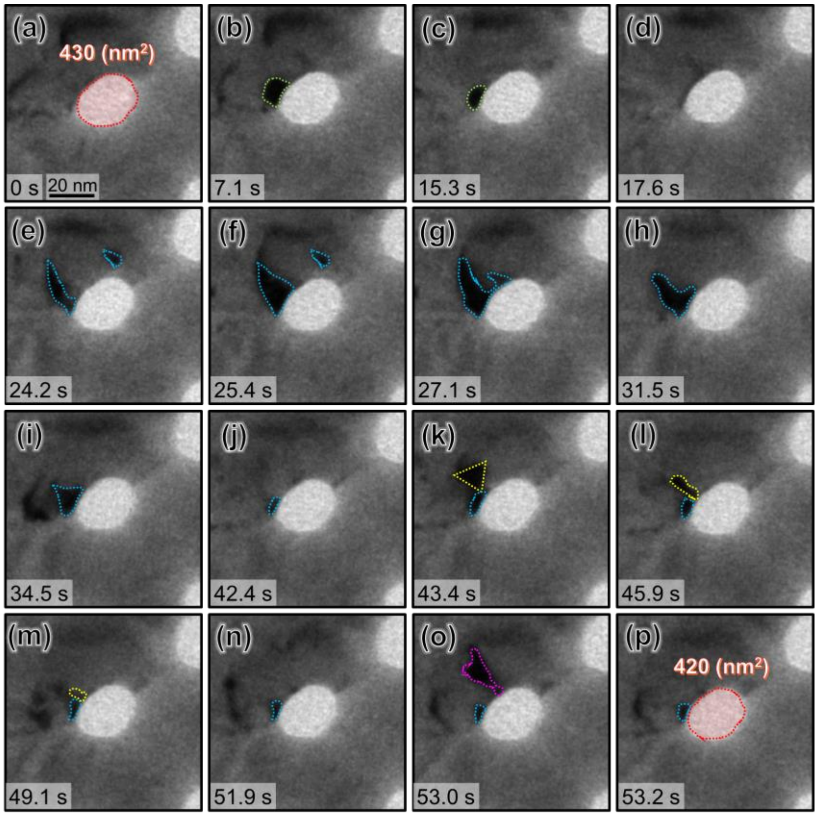

Fig. 8.8. *In situ* video snapshots showing representative defect capture events by an individual nanovoid over ~ 0.17 dpa (~ 53 s) in ng Au irradiated at 200 °C (see Supplementary Video 1). (a) A nanopore with an area of 430nm^2 is monitored during radiation. (b) A defect cluster (outlined by olive dots) formed next to the nanopore after 7.1 s. (c-d) The defect cluster was gradually absorbed by the nanopore. (e-j) Two defect clusters outlined by blue dots were observed at 24.2 s. During irradiation, the smaller cluster gradually migrated towards the nanopore, and the larger cluster continuously grew. Finally, the two clusters combined and were mostly absorbed by the nanopore. (k) A stacking fault tetrahedron (SFT) formed at 43.3 s. (l-n) After 5.7 s, the SFT was destructed and partially removed, and then annihilated at 51.9 s. (o-p) By 53 s, a large defect cluster emerged adjacent to the nanopore and was suddenly eliminated within 0.2 s. Due to the absorption of defect clusters during irradiation, the area of the nanopore reduced from 430 to 420 nm^2.

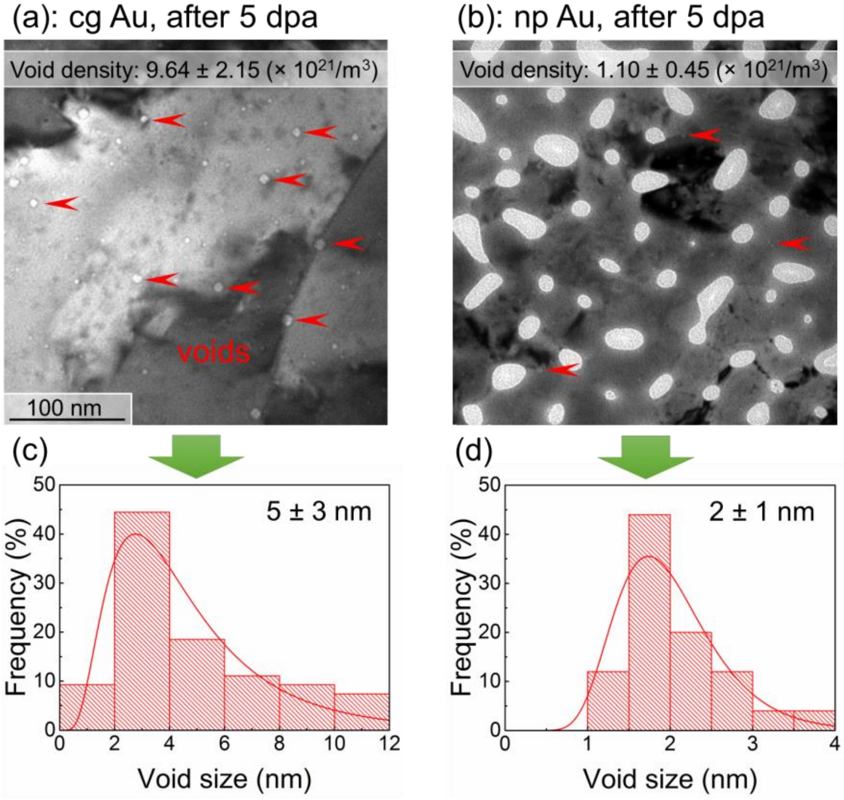

Fig. 8.9. Comparison of void swelling between NP Au and CG Au in Series I study (temperature-jump test) after irradiation to 5 dpa. (a) In CG Au, nanovoids form with a density of 9.6 ± 2.2 (× $10^{21}/\mathrm{m}^3$). (b) In comparison, in irradiated NP Au, the radiation-induced nanovoids have a density of 1.1 ± 0.5 (× $10^{21}/\mathrm{m}^3$). (c) The statistics distribution shows that the average void size is 5 ± 3 nm. (d) The average void size in irradiated NP Au is 2 ± 1 nm. The irradiated CG Au has a maximum void size of 12 nm, comparing to 4 nm in irradiated NP Au.

8.5 Discussion

8.5.1 Defects in irradiated NP Au

In NP Au irradiated at different temperatures, a large number of SFTs are observed. SFTs are known to have distinct triangular shapes (complete or truncated as can be seen from the atomic-resolution TEM images in Fig. 8.3) and are considered to be the most energetically favorable configuration compared to faulted and perfect loops when defect cluster size is small [6]. The formation of SFTs relies on three different mechanisms. (1) Directly from the vacancy rich cascade during energetic displacement [36, 84, 85]. (2) The classic Silcox-Hirsch mechanism where SFTs are formed from equilateral triangular vacancy Frank loops by dissociation [86, 87]. However, it is less likely that SFTs are created from equilateral triangular vacancy Frank loops in the real radiation cascade. Therefore, another mechanism has been proposed that is (3) from the scalene hexagonal vacancy Frank loops [88].

Besides SFTs, a large number of interstitial clusters form during radiation. These perfect interstitial loops typically have Burgers vector of a/2 <110> on either {110} or {111} planes and are usually mobile, while faulted interstitial loops (a/6<112>{111}) and vacancy clusters (vacancy loops and SFTs) are immobile [312]. A majority of the glissile defect clusters in Au are perfect interstitial loops.

In addition, since radiation has been performed from RT to 400 °C in this study, temperature (T) effect should also be considered when discussing the nature of radiation-induced defects. Based on the one-interstitial model [358], Stage III temperature, RT for Au, corresponds to the onset of vacancy motion. Stage V temperature, ~ 250 °C, is correlated to the thermal dissociation of vacancy clusters [36, 338]. Therefore, the current radiation experiments can be divided into two groups. The first group refers to radiation from RT to 200 °C. At this temperature range, because most of the vacancies are tied up in sessile vacancy clusters, the majority of observed mobile dislocation loops in Au are of the interstitial type, SFTs are dominant vacancy type of defects, and void nucleation and growth is strongly suppressed. Hashimoto *et al.* have shown that approximately 90% of irradiation-induced defects near 80 °C are SFTs in Cu [359], and other FCC systems [305, 360, 361]. For the second group (T > Stage V, greater than 200^{o}C), since SFTs are thermally unstable, the predominant visible features are interstitial loops and the coexistence of SFTs and voids, voids become dominating defects as the dose increases [362].

8.5.2 Defect evolution (size/density) as a function of dose and temperature

Defect net concentration is a result of the balance between defect production (dose-rate dependent), absorption (sink dominated) and recombination (radiation temperature dominated). When NP Au and CG Au are irradiated at the same temperature and dose-rate, the generation and recombination of defects are nearly identical in the two cases. However, since NP Au has a much higher density of defect sinks (nanopores), the net concentration of defects is much lower in NP Au compared to CG Au irradiated at the same condition.

Statistical data in Fig. 8.4 present more details on the defect size and density evolutions as a function of dose and temperature. Limited by 2D images, the longest dimension of each defect was measured. Thus, the measured defect size represents an upper bound. In comparison, defect density analysis reflects the lower bound since not all defects can be resolved under *in situ* TEM observation. Several remarkable phenomena are worth mentioning.

1. Defect size and density are smaller in NP Au than those in CG Au at almost all radiation conditions.
2. Defect size in NP Au reaches a plateau quickly after ~ 0.3 dpa regardless of radiation temperature, while in CG Au, defect size is drastically decreased at higher radiation temperatures.
3. Defect density decreases with increasing temperature in both NP Au and CG Au.
4. The NP Au irradiated at 200 °C (Series II) exhibits nearly identical saturation defect size and density compared to the NP Au irradiated during 200 °C stage in temperature jump test (Series I).

Due to the existence of high-density nanopores, NP Au typically have both smaller defect size and lower defect density than those in CG Au. However, there is an interesting exception: defect size in NP Au and CG Au irradiated at 400 °C is similar, ~ 4 nm. One possible reason for such an exception is that at 400^{o}C, the growth of defect clusters becomes very difficult due to an active thermal recombination process. During radiation at RT, the defect size in CG Au grows to 10 nm, whereas defect size in NP Au irradiated at the same condition remains 4 nm. The nanopore free surface in NP Au clearly inhibits the growth of defects in NP Au by absorbing both vacancies and interstitials.

As mentioned above (point 4), defect size and density obtained via temperature-jump radiation tests are similar to those irradiated at different temperatures separately. Therefore, temperature-jump tests may provide an efficient way to investigate defect evolution comparing with a series of stand-alone single-temperature radiation experiments. It should be noticed that temperature-jump tests performed in decremented temperature steps may be more appropriate to investigate temperature dependent studies. As defect generation is an instantaneous event, but defect annihilation requires much longer time. Therefore, if the temperature-jump experiment is carried out in an opposite way (incremental temperature steps), the defects formed at a lower temperature stage may survive radiation at the following stages, compromising the quantification of defect accumulations at higher radiation temperatures.

8.5.3 Temperature-dependent diffusivities of defect clusters

Defect migration kinetics, which is crucial for the modeling of defect evolution in irradiated metals, remains largely unknown [311]. Our previous study has reported the influence of dose-rate on global and instantaneous diffusivities of defect clusters in Kr ion irradiated NP Au at RT [78]. It is found that the global diffusivity of defect clusters (at RT) is significantly reduced when the dose rate decreases, while the instantaneous diffusivity shows little dependence on dose rate. The potential mechanisms are interpreted from the aspects of defect diffusion distance and defect lifetime. In the current study, temperature-dependent global and instantaneous diffusivities of defect clusters for only NP Au are investigated. The estimation of diffusivities is very difficult for CG Au because the film was damaged by ion beam very rapidly. Thus, the migration of single defect clusters can be barely traced. For NP Au, The global diffusivity of defect clusters in NP Au increases prominently from 23 ± 5 to 48 ± 30 nm^2/s, when radiation temperature increases from RT to 400 °C. The rapid increase of global diffusivity is due to the decrease in defect density at higher radiation temperature, which in turn affects the migration distance of defect clusters. In general, a lower defect density leads to longer migration distance, hence greater diffusivity. The error bar of global diffusivity also increases with increasing temperature. This can also be ascribed to defect density. Since the number of defects is very low at high temperature, a defect cluster can migrate over a long distance without being arrested. However, because the existence of high-density nanopores, the defect migration distance is largely determined by the defect-to-pore distance (or defect-sink distance). If a defect is close to a nanopore, then it can only migrate a short distance before being annihilated, and vice versa. Therefore, the calculated global diffusivity varies in a wide range depends on the defect-to-pore distance.

It is intriguing to observe that the instantaneous diffusivity of defect clusters in NP Au shows very limited temperature dependence, 476 ± 225 nm^2/s at RT vs. 560 ± 412 nm^2/s at 400^oC. Although the fundamental mechanisms behind such a phenomenon remain unclear, we hypothesize that the such a weak temperature dependence may be related to the defect-sink separation distance. The instantaneous diffusivity of a defect cluster is largely determined by the distance of a single "jump" between two defect clusters or between defect and sink (nanopores). At 200 °C, the distance between two defects is ~ 25 nm, and such a distance increases to 70 nm at 400 °C due to reduced defect density. The average pore-to-pore separation distance in NP Au is ~ 50 nm. Assume a defect cluster is located between two nanopores, then the defect-to-pore distance is ~ 25 nm, which is equal to the defect-defect separation distance at 200 °C.

8.5.4 Calculation of free surface (nanopores in NP Au) sink strength

Defect sink strength (with a unit of cm^{-2}) is a key parameter in the reaction-rate theory used to quantify the efficiency in annihilating radiation-induced defects. The defect sink strength is in general calculated computationally. Experimentally, the estimation of sink strength can be obtained from the comparison studies between nanostructured materials and their CG counterparts. In this case, Series I NP Au and CG Au are both irradiated at the same conditions with different temperatures. The total number of defects, ρ_{total}, that is estimated from experimental observations can be written as:

$$\rho_{\mathrm{total}}^{\mathrm{NP\ Au}} = \rho_{\mathrm{gen}} - \rho_{\mathrm{recom}} - \rho_{\mathrm{absorb}}^{\mathrm{Sur}} - \rho_{\mathrm{absorb}}^{\mathrm{NP}} \tag{8.1}$$

$$\rho_{\mathrm{total}}^{\mathrm{CG\ Au}} = \rho_{\mathrm{gen}} - \rho_{\mathrm{recom}} - \rho_{\mathrm{absorb}}^{\mathrm{Sur}} \tag{8.2}$$

where ρ_{gen} is the number of defects that generated under irradiation and ρ_{recom} is the number of defects annihilated through recombination. $\rho_{\mathrm{absorb}}^{\mathrm{Sur}}$ and $\rho_{\mathrm{absorb}}^{\mathrm{NP}}$ are the number of defect absorbed by film upper/lower surfaces and nanopores, respectively. Since the radiation conditions are kept the same and TEM specimens have the identical thickness for NP Au and CG Au, ρ_{gen}, ρ_{recom}, and $\rho_{\mathrm{absorb}}^{\mathrm{Sur}}$ are nearly same in the two equations. In addition, since the average grain size in both NP Au and CG Au are both very large (on the order of micronmeters), defect absorption through GBs is negligible. Comparing Eq. (8.1) and (8.2), the only different term is the number of defects annihilated by nanopores, $\rho_{\mathrm{absorb}}^{\mathrm{NP}}$. Fig. 8.10a shows the calculated $\rho_{\mathrm{absorb}}^{\mathrm{NP}}$ as a function of temperature. Below 200 °C, $\rho_{\mathrm{absorb}}^{\mathrm{NP}}$ varies very little from 10.5 to 11.5 ($\times 10^{22}/\mathrm{m}^3$). However, a turning point exist at ~ 200oC, after which $\rho_{\mathrm{absorb}}^{\mathrm{NP}}$ decreases quickly. Note that, this temperature is similar to the thermal dissociation temperature for sessile vacancy clusters (Stage V temperature of defect recovery) in Au [36, 338]. After dissociation, vacancies continuously recombine with interstitials, and the number of defect clusters that migrate (absorb) to nanopores decreases. Therefore, it is reconcilable to see $\rho_{\mathrm{absorb}}^{\mathrm{NP}}$ decreases more rapidly at higher temperatures.

$\rho_{\mathrm{absorb}}^{\mathrm{NP}}$ obtained above provides an important parameter in calculating sink strength for nanopores in NP Au. Assume the nanopore density is ρ_{v} (cm^{-2}), film thickness is h and nanopores exhibit cylindrical shape with the volume-equivalent radius of R. At a given area, A, a measure of the sink strength of nanopores, K_{NP}, the total number of defects absorbed by the inner surface (free surface) of nanopores (per cm^2), can be calculated as:

$$K_{\mathrm{NP}} = \frac{A \cdot h \cdot \rho_{\mathrm{absorb}}^{\mathrm{NP}}}{2\pi R \cdot h \cdot \rho_{\mathrm{v}} \cdot A} = \frac{\rho_{\mathrm{absorb}}^{\mathrm{NP}}}{2\pi R \cdot \rho_{\mathrm{v}}} \qquad (8.3).$$

The value of $\rho_{\mathrm{absorb}}^{\mathrm{NP}}$ is shown in Fig. 8.10a, and the volume-equivalent radius, R, and density, ρ_{v}, are estimated to be 11 ± 5 nm and 3.1×10^{10} cm^{-2}, respectively. The calculated sink strength of nanopores, K_{NP}, as a function of temperature is shown in Fig. 8.10b. The shadowed area represents the deviation by considering the size distribution of nanopores. Two distinct regions can be identified in the plot. When temperature is below 200 °C, which is Region I, sink strength shows little temperature dependence. In this case, defect sinks play a dominating role in eliminating radiation-induced defects compared to thermal recombination, because temperature is not high enough to trigger massive defect recombination. In Region II (T > 200 °C), however, the calculated sink strength decreases rapidly. The effect of defect sinks in this case is less pronounced because of the much greater thermal recombination rate. It is worth mentioning that the result does not necessarily indicate that sink strength decreases at elevated temperature.

The strategy discussed previously makes the the quantification of sink strength possible in nanostructured materials. However, several factors shall be considered. First, the sink strength calculated here considers mostly defect clusters rather than point defects that are captured by sinks. Thus, we may have underestimated sink strength of nanopores. Second the results indicate that sink strength may not depend on the dose level, but it may depend on dose-rate. More defects can be produced at higher dose-rates, and therefore, sink strength increases as more defects may be captured by sinks. Malerba et al. pointed out that the sink strength not only depends on the type, shape, and size of the sinks, but also depends on the dimensionality of the motion of the affected migrating species [353]. Nevertheless, it is not clear from the present study that whether sink strength saturates upon a certain dose-rate. Further studies are necessary to answer this question. The method provided in this study offers an opportunity to compare sink strength for different types of defect sinks under the same radiation condition.

8.5.5 Nanopore shrinkage and suppressed void swelling in NP Au.

As mentioned earlier, our previous studies on NP Au have shown that nanopore shrinkage occurs at room temperature without void swelling. In the current study, nanopore shrinkage has been identified again in NP Au at all radiation temperatures, incorporating the peak swelling temperature for Au. The shrinkage rate of nanopores decreases with increasing radiation temperature (Fig. 8.7b). As nanopore shrinkage is the consequence of defect absorption, it is natural to see that defect density absorbed by nanopores also decreases at elevated temperature (Fig. 8.7(b)).

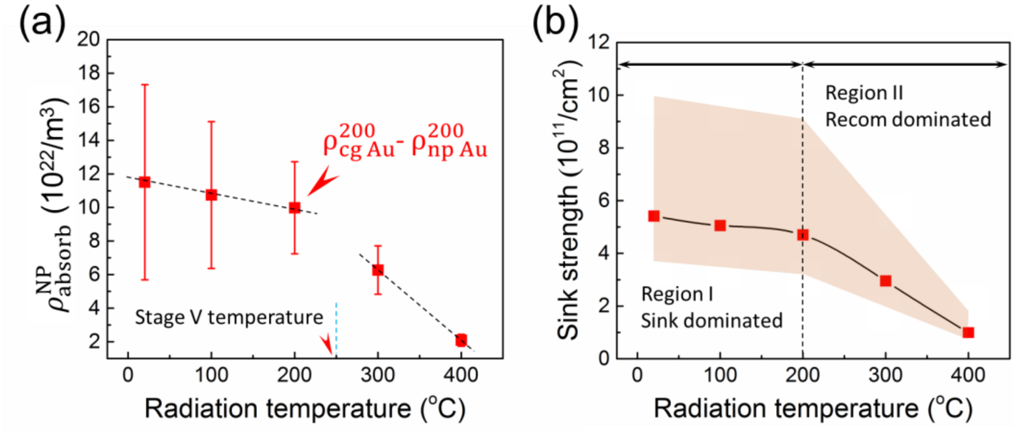

Fig. 8.10. (a) The number of defects being absorbed by the free surface of nanopores ($\rho_{\text{absorb}}^{\text{NP}}$) as a function of radiation temperature. The results are deduced from Fig. 8.4(f) by subtracting the defect density in NP Au from the defect density in CG Au irradiated at the same temperature. Below 200 °C, $\rho_{\text{absorb}}^{\text{NP}}$ decreases slightly (from 11.5 to 10.5 × 10^{22}/m^3) with increasing temperature. However, when T > 200oC, $\rho_{\text{absorb}}^{\text{NP}}$ decreases sharply. (b) Calculated nanopore sink strength as a function of radiation temperature. The shadowed area represents the deviation by considering the variation of nanopore size. Clearly, two distinct regions can be identified. Below 200 °C (Region I), sink strength shows little temperature dependence, whilst above 200 °C (Region II), sink strength is inversely proportional to radiation temperature.

In addition to nanopore shrinkage, void swelling is observed in Series I CG Au after radiation with 5 dpa, while swelling is remarkably reduced in both void size and density in NP Au (Fig. 8.9). Many voids in CG are larger than 4 nm and the maximum size is 12 nm, while most of the voids in NP Au are smaller than 3 nm and the maximum size is 4 nm. Overall, the void size is more than two times smaller, and the void density is reduced by almost an order magnitude in NP Au. Hence the magnitude of void swelling in NP Au is nearly two orders of magnitude lower than that in CG Au.

Schematics in Fig. 8.11 illustrate the hypothetical mechanisms of void formation and nanopore shrinkage in NP Au and CG Au at different temperatures during irradiation. Same amount of interstitials and vacancies are created in a given volume in both NP Au and CG Au during irradiation. However, in CG Au (Fig. 8.11a), interstitials continuously migrate towards film upper and lower surfaces (GBs contribution is not considered because of the giant grain size compared to film thickness), and most of the vacancies are left behind. Therefore, interstitials have medium concentration, and vacancies exhibit high concentration. At high temperature, vacancies become mobile and agglomerate to form large clusters, and finally, transform into voids. Because of high supersaturated vacancy concentration, voids grow rapidly in terms of both size and density. In contrast in NP Au irradiated at high temperatures (Fig. 8.11b), due to the existence of nanopores, both interstitials and vacancies will be trapped by nanopores. Consequently, interstitials exhibit low concentration, and vacancies have medium concentration compared to that in CG Au. In this case, only small vacancy clusters can form, and those clusters eventually evolve into small voids. Compare to radiation of NP Au at low temperatures (Fig. 8.11c), nanopores shrink a lot slower at high temperature due to two major reasons: (1) accelerated thermal recombination at high temperature, and (2) increased the mobility of vacancies at high temperature. Consequently fewer interstitial-type defects could reach to nanopores before being annihilated by vacancy-type defects, and the preferential absorption of interstitial-type defects by nanopores is interrupted because vacancy-type defects could also reach to nanopores. Therefore, nanopore shrinkage rate decreases at high temperature. Since void nucleation and growth are largely suppressed at low temperature, little void swelling occurs in (c). Noted that three other factors related to interstitials are intentionally not shown in the schematics for clarity: (1) interstitial annihilation due to pre-existing defects, such as dislocations; (2) the migration of interstitial to film surface; and (3) the recombination of interstitials and vacancies.

One may speculate that the shrinkage of nanopores could be caused by the surface diffusion of Au atoms at elevated temperatures. However, we have performed the annealing studies on NP Au at 400 °C, and no swelling of nanopores is found. In addition, irradiation resistance of NP metals may degrade over long-term radiation if most of the nanopores are completely filled by radiation-induced defect clusters. Therefore, the stability of nanopores should also be considered if NP materials are adopted to design radiation-resistant materials in nuclear reactors. First, nanopores in Au appear to shrink at a fast speed at lower temperatures, for instance ~ 10%/dpa at 200 °C. However, Au is a model system that is known to be vulnerable to radiation damage than many other alloys. Thus, one can envision that if practical reactor steels are engineered into nanoporous structures, the safe service period (lifetime) of the steels could be significantly extended. Second, the stability of nanopores increases at high temperatures. For instance, the nanopores shrinkage rate at 400 °C decreases to less than 2%/dpa. This is a benefit for NP metals because the nuclear reactors are usually operated at temperatures above 400 °C. Third, the stability can also be increased by increasing the size of nanopores. As discussed previously [78], the shrinking rate of nanopores is size-dependent, i.e., nanopore shrinkage is inversely proportional to the initial pore diameter. Clearly, by deliberately introducing nanopores with desired dimensions, the radiation stability of NP metals can be significantly sustained.

In addition to the radiation stability of nanopores, further investigations on other properties, such as mechanical properties, resistance to corrosion, are beneficial in order to transfer this concept into a practical option for advanced reactor materials.

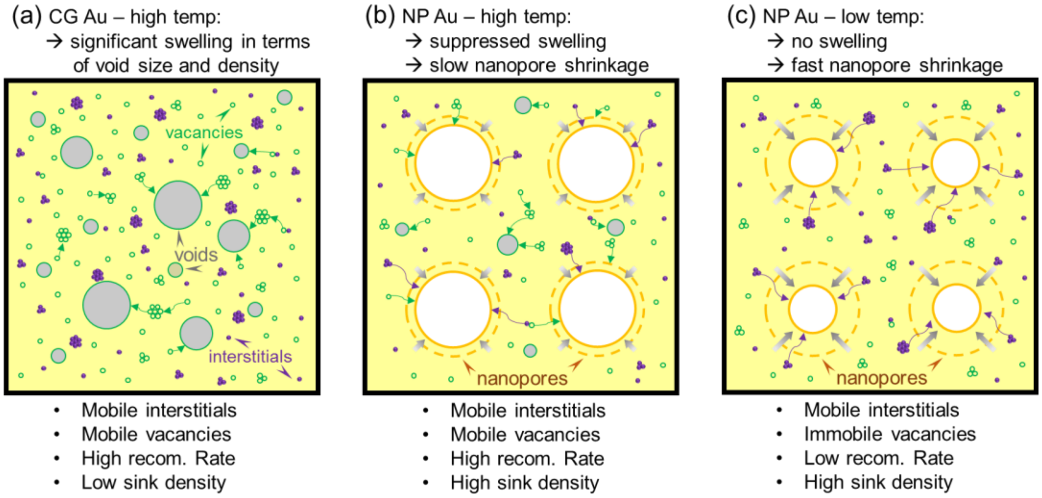

Fig. 8.11. Schematics illustrate the potential mechanisms of void formation in NP Au and CG Au at high temperature as well as pore shrinkage in NP Au at different temperatures after irradiation. As radiation condition is identical, the defect generation rate is assumed to be identical between CG and NP Au. (a) In CG Au irradiated at high temperature, due to a lack of internal defect sinks, interstitials rapidly migrate away, leaving vacancies behind. The supersaturation of vacancies leads to the formation of voids. (b) In contrast in NP Au irradiated at high temperature, both interstitials and vacancies are trapped by nanopores. As the migration rate and territory of interstitials are curtailed by nanopores, the recombination probability of vacancies and interstitials may also increase. Consequently, only small vacancy clusters can form, and the magnitude of void swelling significantly decreases. (c) Comparing to CG Au irradiated at high temperature, nanopores shrinkage rates increases at lower irradiation temperature presumably because (1) less thermal recombination of vacancies and interstitials at low temperature, and (2) absorption of interstitials by nanopores.

8.6 Conclusion

Nanoporous (NP) materials possess a great potential in the alleviation of the irradiation-induced damage due to the giant surface-to-volume ratio. In this study, we show that both defect size and density evolve with radiation temperature, i.e., high-temperature results in reduced defect size and density. Compared to CG Au, defect size and density have been markedly reduced in NP Au. In addition, nanopore shrinkage has been identified at all temperatures, and shrinkage rate becomes less at high temperatures, which are beneficial to the stability of nanopores during radiation. The sink strength of the free surface (nanopores) in NP Au is estimated. The method used in this study not only offer an opportunity for quantitatively analyzing sink strength but more importantly, it provides a new strategy to make crosswise comparisons of sink strength between different defect sinks. The significantly enhanced swelling resistance of NP metals empowers them as promising candidates as structural materials for advanced nuclear reactors.

8.7 Acknowledgement

We acknowledge financial support by NSF-DMR-Metallic Materials and Nanostructures Program under grant no. 1643915. HW acknowledges the support from the U.S. Office of Naval Research (N00014-16-1-2778). We also acknowledge the use of microscopes at the Microscopy and Imaging Center at Texas A&M University and the DoE Center for Integrated Nanotechnologies managed by Los Alamos National Laboratory. The IVEM facility at Argonne National Laboratory is supported by DOE-Office of Nuclear Energy.

CHAPTER IX

CONCLUSIONS AND FUTURE WORK

9.1 Conclusions

9.1.1 Comparison of size dependent strengthening mechanisms in Ag/Fe and Ag/Ni multilayers

Ag/Fe multilayers with various individual layer thicknesses were deposited on Si (111) substrate by magnetron sputtering. The coherency between Ag and Fe increases with decreasing *h*. Nearly coherent interfaces form in Ag/Fe 1 nm multilayers. Phase transformation from BCC to FCC Fe occurred when h < 5 nm. Hetero-twinned interfaces were observed between adjacent Ag and Fe when *h* = 5 nm. Comparisons of hardness between Ag/Fe, Ag/Ni, Cu/Fe and Ag/Al reveal the significance of stacking fault energy of layer constituents in the determination of peak hardness of multilayers with FCC/FCC interfaces.

9.1.2 In situ Study of Defect Migration Kinetics and Self-Healing of Twin Boundaries in Heavy Ion Irradiated Nanotwinned Metals

Nanotwinned epitaxial Ag was *in situ* irradiated using Kr ions at room temperature to explore mechanisms of dislocation loop - TB interactions. TBs are effective defect sinks that drastically reduce defect population within twin boundary affected zones. The stress field of loops can induce geometry change for TBs so that they can actively engage and remove defect clusters. Furthermore, TBs accelerate recombination of unlike defects by rapid transportation of interstitials along TBs to regions with high vacancy concentration, greatly increasing the odds for annihilation of opposite types of loops and consequently TBs self-heal. The impressive capture-recovering capability makes TBs attractive defect sinks for the design of radiation tolerant metallic materials.

9.1.3 In situ studies on twin thickness dependent distribution of defect clusters in heavy ion irradiated nanotwinned Ag

In situ heavy ion irradiation studies were performed on nanotwinned Ag at 473K (200^{o}C). Our studies show that the accumulative concentration of irradiation-induced defects exhibits twin-thickness dependence that is more defect clusters were detected in central areas than that close to TBs in thicker twins ($t > 40$ nm), and an opposite trend has been observed in fine twins ($t = 20$ nm). Such twin-thickness-dependent distribution of defect concentration is considered as a result of the competition between defect travel time τ_t and defect absorption time τ_a. The number of defect clusters generated in the central area will be greater than that in the area close to the TB if $\tau_t > \tau_a$ (for thicker twins) due to the longer migration distance. However, if $\tau_t < \tau_{a,}$(in the case of thin twins), then the central area has fewer defect clusters than near the TBs.

9.1.4 Enhanced radiation tolerance and radiation stability of nanotwins in Ag-1at.%Fe alloy

In this study, we report a drastically improved irradiation stability of twin boundaries in Ag. By adding merely 1 at% of Fe solute atoms into Ag matrix, ultra-high-density twins with an average twin thickness of ~ 2 nm form in Ag due to the solute effect that Fe atoms promote the nucleation and retard detwinning of twins during film growth. The extremely fine twins in NT AgFe are more stable under heavy ion irradiation compared to that in NT Ag. The enhanced stability of TBs is strengthened by Fe solutes due to the solute drag effect. Moreover, both size and density of irradiation-induced defects in both two types of NT AgFe have been significantly reduced compared with monolithic CG Ag and NT Ag. The uniformly distributed Fe atoms are effective sinks that can decrease the diffusion rate of interstitials and accelerate the recombination of interstitials and vacancy through trapping and detrapping processes. This study provides a vision in the design of nanotwinned metals with improved irradiation tolerance and stability.

9.1.5 In situ heavy ion irradiation studies of nanopore shrinkage and enhanced radiation tolerance of nanoporous Au

In situ heavy ion irradiation studies were performed on nanoporous Au at room temperature. Dose-rate-dependent defect migration diffusivities were examined, and the global diffusivity is significantly reduced when the dose rate decreases, while the instantaneous diffusivity shows little dependence on dose rate. Nanovoids are effective defect sinks where various types of defect clusters can be absorbed during irradiation. The absorption of defect clusters leads to the shrinkage of nanovoids, and the shrinkage rate, or defect absorption efficiency, is size-dependent. Comparing to larger voids, smaller voids exhibit higher defect absorption efficiency capture more defects during irradiation. This study provides significant insight into the design of radiation-tolerant nanoporous metallic materials.

9.1.6 In situ studies on radiation resistance of nanoporous Au through temperature-jump tests

Nanoporous (NP) materials possess a great potential in the alleviation of the irradiation-induced damage due to the giant surface-to-volume ratio. In this study, we show that both defect size and density evolve with radiation temperature, i.e., high-temperature results in reduced defect size and density. Compared to CG Au, defect size and density have been markedly reduced in NP Au. In addition, nanopore shrinkage has been identified at all temperatures, and shrinkage rate becomes less at high temperatures, which are beneficial to the stability of nanopores during radiation. The sink strength of the free surface (nanopores) in NP Au is estimated. The method used in this study not only offer an opportunity for quantitatively analyzing sink strength but more importantly, it provides a new strategy to make crosswise comparisons of sink strength between different defect sinks. The significantly enhanced swelling resistance of NP metals empowers them as promising candidates as structural materials for advanced nuclear reactors.

9.2 Future work

The mechanical properties and radiation response of Ag and Au based nanostructured metallic materials, including Ag/Fe nanolayers, nanotwinned Ag, and nanoporous Au, have been covered in this dissertation. The future work will hopefully involve with many other NMMs and different types of techniques. Some of the prospective studies are briefly described below.

9.2.1 Mechanical properties of nanometallic materials

- Shock-loading tests on NT metals. NT metals, such as NT Cu and NT Ag, have been carefully studied in our group. *In situ* nanoindentation has been performed in NT Cu and TB migration under stress loading has been observed. However, we have not done any shock-loading study on NT metals so far. Therefore, the behavior of TBs under ultrafast deformation is unclear.
- *In situ* and ex-situ pillar compression tests on nanostructured metallic materials, such as Ag/Fe, NT Ag, NP Au, etc., before and after irradiation. Our previous studies have done many hardness tests by using nanoindenter. However, the nanopillar compression test is a new technique, and it can be a powerful tool to help the better investigation of the mechanical properties of metallic materials with different nanostructures. It is also provide a great opportunity to study the mechanical properties of materials after irradiation.
- Strengthening mechanisms of other Ag based multilayer systems, such as Ag/Cu nanolayers. The present study showed an interesting twin-interface relation in Ag/Cu nanolayers. The hardness of Ag/Cu could be unexpected high due to the special relation. The growth mechanisms of the relation are also worthwhile to find out.

9.2.2 Radiation properties of nanometallic materials

- Heavy ion radiation and He implantation on Ag/Fe nanolayers. The strengthening mechanisms were studied previously, and interesting heterotwinning relation was found in 5nm-thick nanolayers. Such twinning relationship could be effective defect sink that will mitigate irradiation-induced damage. The study will be hopefully performed at (i) Argonne National lab by *in situ* radiation facility and (ii) Prof. Shao Lin's group at Texas A&M University by *ex situ* He implanter.

- *In situ* study of various NP metals. We have done some studies on Au but the ultimate goal of such research is provide the fundamentals to the future study of more reactor-related materials, such as NP Zr and NP steels. Of course, the fabrication of such materials is also a challenge that requires careful investigations.
- *In situ* study on AgFe co-sputtered alloy. Ultra-high-density twins were found in AgFe co-sputtered alloy, and the preliminary results of radiation studies showed that NT AgFe exhibit extremely high radiation tolerance and TBs are very stable as compared to NT Ag. The mechanisms behind need further studies to be unrevealed.

REFERENCE

[1] U.S. Energy information administration website (https://www.Eia.Gov/tools/faqs/faq.Php?Id=427).

[2] S.J. Zinkle, G.S. Was, Materials challenges in nuclear energy, Acta Materialia, 61 (2013) 735-758.

[3] S.J. Zinkle, Materials issues for generation iv systems, in, Springer Netherlands, 2008, pp. 227-244.

[4] J.L. Boutard, S. Dudarev, E. Diegele, Materials issues for generation iv systems, Springer Netherlands, 481-500.

[5] Fundamental aspects of radiation damage in metals. Proceedings of an international conference, gatlinburg, tennessee, october 6--10, 1975, Oak Ridge, Tenn. : distributed by the Office of Scientific and Technical Information, U.S. Dept. of Energy, Oak Ridge, Tenn., 1975.

[6] S.J. Zinkle, L.E. Seitzman, W.G. Wolfer, I. Energy calculations for pure metals, Philosophical Magazine A, 55 (1987) 111-125.

[7] B.N. Singh, S.J. Zinkle, Defect accumulation in pure fcc metals in the transient regime: A review, Journal of Nuclear Materials, 206 (1993) 212-229.

[8] B.N. Singh, S.I. Golubov, H. Trinkaus, D.J. Edwards, M. Eldrup, Review: Evolution of stacking fault tetrahedra and its role in defect accumulation under cascade damage conditions, Journal of Nuclear Materials, 328 (2004) 77-87.

[9] D.J. Bacon, T.D. Delarubia, Molecular-dynamics computer-simulations of displacement cascades in metals, Journal of Nuclear Materials, 216 (1994) 275-290.

[10] C.-C. Fu, J.D. Torre, F. Willaime, J.-L. Bocquet, A. Barbu, Multiscale modelling of defect kinetics in irradiated iron, Nature Materials, 4 (2005) 68-74.

[11] B.P. Uberuaga, R.G. Hoagland, A.F. Voter, S.M. Valone, Direct transformation of vacancy voids to stacking fault tetrahedra, Physical Review Letters, 99 (2007).

[12] G.S. Was, Fundamentals of radiation materials science: Metals and alloys, 2007.

[13] R.E. Stoller, G.R. Odette, B.D. Wirth, Primary damage formation in bcc iron, Journal of Nuclear Materials, 251 (1997) 49-60.

[14] G.R. Odette, M.J. Alinger, B.D. Wirth, Recent developments in irradiation-resistant steels, Annual Review of Materials Research, 38 (2008) 471-503.

[15] L.K. Mansur, A.F. Rowcliffe, R.K. Nanstad, S.J. Zinkle, W.R. Corwin, R.E. Stoller, Materials needs for fusion, generation iv fission reactors and spallation neutron sources – similarities and differences, Journal of Nuclear Materials, 329-333 (2004) 166-172.

[16] S.J. Zinkle, Fusion materials science: Overview of challenges and recent progress, Physics of Plasmas, 12 (2005) 058101.

[17] R.W. Grimes, R.J.M. Konings, L. Edwards, Greater tolerance for nuclear materials, Nature Materials, 7 (2008) 683-685.

[18] K.Y. Yu, Y. Chen, J. Li, Y. Liu, H. Wang, M.A. Kirk, M. Li, X. Zhang, Measurement of heavy ion irradiation induced in-plane strain in patterned face-centered-cubic metal films: An in situ study, Nano Lett, 16 (2016) 7481-7489.

[19] E. Rutherford, Lxxix. The scattering of α and β particles by matter and the structure of the atom, Philosophical Magazine Series 6, 21 (1911) 669-688.

[20] J.J. Thomson, Xlii. Ionization by moving electrified particles, Philosophical Magazine Series 6, 23 (1912) 449-457.

[21] Iii. On the theory of the decrease of velocity of moving electrified particles on passing through matter, Niels Bohr Collected Works, 8 (1987) 47-71.

[22] D.C. Cox, Ion–solid interactions, in: Introduction to Focused Ion Beam Nanometrology, Morgan & Claypool Publishers, 2015, pp. 3-1-3-15.

[23] Ion-solid interactions fundamentals and applications, Cambridge : Cambridge University Press, Cambridge, 2004.

[24] M.T. Robinson, Basic physics of radiation damage production (general), Journal of Nuclear Materials, 216 (1994) 1-28.

[25] G. Ackland, Materials science. Controlling radiation damage, Science, 327 (2010) 1587-1588.

[26] G. Kinchin, R. Pease, The displacement of atoms in solids by radiation, Reports on Progress in Physics, 18 (1955) 1.

[27] R.S. Averback, Atomic displacement processes in irradiated metals, Journal of Nuclear Materials, 216 (1994) 49-62.

[28] R. Averback, P. Bellon, Fundamental concepts of ion-beam processing materials science with ion beams, in: H. Bernas (Ed.), Springer Berlin / Heidelberg, 2010, pp. 1-28.

[29] R.S. Averback, R. Benedek, K.L. Merkle, J. Sprinkle, L.J. Thompson, Defect production in ion-irradiated aluminum, Journal of Nuclear Materials, 113 (1983) 211-218.

[30] W.E. King, K.L. Merkle, M. Meshii, Threshold energy surface and frenkel pair resistivity for cu, Journal of Nuclear Materials, 117 (1983) 12-25.

[31] D.R. Olander, Fundamental aspects of nuclear reactor fuel elements, in, 1976, pp. Medium: X; Size: Pages: 624.

[32] K. Hauffe, Electron radiation damage in semiconductors and metals, Zeitschrift für Physikalische Chemie, 56 (1967) 117-118.

[33] G.J. Dienes, Radiation effects in solids, New York : Interscience Publishers, New York, 1957.

[34] S. Takaki, J. Fuss, H. Kuglers, U. Dedek, H. Schultz, The resistivity recovery of high purity and carbon doped iron following low temperature electron irradiation, Radiation Effects, 79 (1983) 87-122.

[35] Atomic defects in metals, Landolt-Börnstein - Group III Condensed Matter, Vol. 25, edited by H. Ullmaier, (Springer-Verlag, Berlin, 1991).

[36] S.J. Zinkle, 1.03 - radiation-induced effects on microstructure* a2 - konings, rudy j.M, in: Comprehensive nuclear materials, Elsevier, Oxford, 2012, pp. 65-98.

[37] M. Kiritani, H. Takata, Dynamic studies of defect mobility using high voltage electron microscopy, Journal of Nuclear Materials, 69 (1978) 277-309.

[38] P.R. Thornton, T.E. Mitchell, P.B. Hirsch, The dependence of cross-slip on stacking-fault energy in face-centred cubic metals and alloys, Philosophical Magazine, 7 (1962) 1349-1369.

[39] N. Ichinose, Superfine particle technology, London : Springer London, London, 1992.

[40] P.C.J. Gallagher, The influence of alloying, temperature, and related effects on the stacking fault energy, Metallurgical Transactions, 1 (1970) 2429-2461.

[41] Y.C. Liu, P.C.J. Gallagher, Analytical expressions for the composition dependence of stacking fault energies and probabilities in binary silver systems, Journal of Applied Physics, 42 (1971) 3322-3328.

[42] G.P. Tiwari, R.V. Ramanujan, Review the relation between the electron to atom ratio and some properties of metallic systems, Journal of Materials Science, 36 (2001) 271-283.

[43] J.A. Venables, The electron microscopy of deformation twinning, Journal of Physics and Chemistry of Solids, 25 (1964) 685-692.

[44] Y.N. Osetsky, A. Serra, B.N. Singh, S.I. Golubov, Structure and properties of clusters of self-interstitial atoms in fcc copper and bcc iron, Philosophical Magazine A, 80 (2000) 2131-2157.

[45] D.J. Bacon, A.F. Calder, F. Gao, Defect production due to displacement cascades in metals as revealed by computer simulation, Journal of Nuclear Materials, 251 (1997) 1-12.

[46] D.J. Bacon, F. Gao, Y.N. Osetsky, Computer simulation of displacement cascades and the defects they generate in metals, Nuclear Instruments and Methods in Physics Research Section B: Beam Interactions with Materials and Atoms, 153 (1999) 87-98.

[47] T. Okita, Y. Yang, J. Hirabayashi, M. Itakura, K. Suzuki, Effects of stacking fault energy on defect formation process in face-centered cubic metals, Philosophical Magazine, 96 (2016) 1579-1597.

[48] M. Kiritani, Story of stacking fault tetrahedra, Materials Chemistry and Physics, 50 (1997) 133-138.

[49] M. Hiratani, H.M. Zbib, B.D. Wirth, Interaction of glissile dislocations with perfect and truncated stacking-fault tetrahedra in irradiated metals, Philosophical Magazine A, 82 (2002) 2709-2735.

[50] Y. Matsukawa, S.J. Zinkle, Dynamic observation of the collapse process of a stacking fault tetrahedron by moving dislocations, Journal of Nuclear Materials, 329–333, Part B (2004) 919-923.

[51] M. Niewczas, R.G. Hoagland, Molecular dynamic studies of the interaction of a/6⟨112⟩ shockley dislocations with stacking fault tetrahedra in copper. Part ii: Intersection of stacking fault tetrahedra by moving twin boundaries, Philosophical Magazine, 89 (2009) 727-746.

[52] E.G. Fu, J. Carter, G. Swadener, A. Misra, L. Shao, H. Wang, X. Zhang, Size dependent enhancement of helium ion irradiation tolerance in sputtered cu/v nanolaminates, Journal of Nuclear Materials, 385 (2009) 629-632.

[53] R. Schibli, R. Schäublin, On the formation of stacking fault tetrahedra in irradiated austenitic stainless steels – a literature review, Journal of Nuclear Materials, 442 (2013) S761-S767.

[54] Y.N. Osetsky, R.E. Stoller, D. Rodney, D.J. Bacon, Atomic-scale details of dislocation-stacking fault tetrahedra interaction, Materials Science and Engineering A, 400-401 (2005) 370-373.

[55] E. Martinez, J. Marian, A. Arsenlis, M. Victoria, J.M. Perlado, A dislocation dynamics study of the strength of stacking fault tetrahedra. Part i: Interactions with screw dislocations, Philosophical Magazine, 88 (2008) 809-840.

[56] H.J. Lee, B.D. Wirth, Molecular dynamics simulation of the interaction between a mixed dislocation and a stacking fault tetrahedron, Philosophical Magazine, 89 (2009) 821-841.

[57] S.J. Zinkle, J.T. Busby, Structural materials for fission & fusion energy, Materials Today, 12 (2009) 12-19.

[58] S.J. Zinkle, K. Farrell, Void swelling and defect cluster formation in reactor-irradiated copper, Journal of Nuclear Materials, 168 (1989) 262-267.

[59] S.J. Zinkle, B.N. Singh, Microstructure of neutron-irradiated iron before and after tensile deformation, Journal of nuclear materials, 351 (2006) 269-284.

[60] D.J. Oh, R.A. Johnson, Simple embedded atom method model for fec and hcp metals, Journal of Materials Research, 3 (1988) 471-478.

[61] S.M. Foiles, M.I. Baskes, M.S. Daw, Embedded-atom-method functions for the fcc metals cu, ag, au, ni, pd, pt, and their alloys, Physical Review B, 33 (1986) 7983-7991.

[62] R.W. Balluffi, Vacancy defect mobilities and binding energies obtained from annealing studies, Journal of Nuclear Materials, 69 (1978) 240-263.

[63] B.M. Iskakov, K.B. Baigisova, G.G. Bondarenko, Interatomic interaction and vacancy mobility in fcc metals, Russian Metallurgy (Metally), 2013 (2013) 522-527.

[64] A. Orlov, Y.V. Trushin, Energy of point defects in metals, Energoatomizdat, Moscow, (1983).

[65] T. Korhonen, M.J. Puska, R.M. Nieminen, Vacancy-formation energies for fcc and bcc transition metals, Physical Review B, 51 (1995) 9526-9532.

[66] H.E. Schaefer, Investigation of thermal equilibrium vacancies in metals by positron annihilation, physica status solidi (a), 102 (1987) 47-65.

[67] R. Nazarov, T. Hickel, J. Neugebauer, Vacancy formation energies in fcc metals: Influence of exchange-correlation functionals and correction schemes, Physical Review B, 85 (2012) 144118.

[68] L. Kornblit, Elastic calculation of self-interstitial formation energies in fcc metals, Physical Review B, 22 (1980) 1866-1870.

[69] A.K. Bandyopadhyay, S.K. Sen, Calculation of self-interstitial formation energy (both split and non-split) in noble metals, physica status solidi (b), 157 (1990) 519-530.

[70] N.Q. Lam, L. Dagens, N.V. Doan, Calculations of the properties of self-interstitials and vacancies in the face-centred cubic metals cu, ag and au, Journal of Physics F: Metal Physics, 13 (1983) 2503.

[71] L. Kornblit, Single vacancy formation energies in fcc metals, Physica B+C, 112 (1982) 45-50.

[72] R.W. Siegel, Positron annihilation spectroscopy, Annual Review of Materials Science, 10 (1980) 393-425.

[73] H. Ullmaier, W. Schilling, Radiation damage in metallic reactor materials, IAEA, International Atomic Energy Agency (IAEA), 1980.

[74] R.A. Johnson, Point-defect calculations for an fcc lattice, Physical Review, 145 (1966) 423-433.

[75] W. Wolfer, Fundamental properties of defects in metals, Comprehensive nuclear materials, 1 (2012) 1-45.

[76] Y. Chen, Y. Liu, E.G. Fu, C. Sun, K.Y. Yu, M. Song, J. Li, Y.Q. Wang, H. Wang, X. Zhang, Unusual size-dependent strengthening mechanisms in helium ion-irradiated immiscible coherent cu/co nanolayers, Acta Materialia, 84 (2015) 393-404.

[77] C. Sun, M. Song, K.Y. Yu, Y. Chen, M. Kirk, M. Li, H. Wang, X. Zhang, In situ evidence of defect cluster absorption by grain boundaries in kr ion irradiated nanocrystalline ni, Metallurgical and Materials Transactions A, 44 (2013) 1966-1974.

[78] J. Li, C. Fan, J. Ding, S. Xue, Y. Chen, Q. Li, H. Wang, X. Zhang, In situ heavy ion irradiation studies of nanopore shrinkage and enhanced radiation tolerance of nanoporous au, Sci Rep, 7 (2017) 39484.

[79] S. Zinkle, R. Sindelar, Defect microstructures in neutron-irradiated copper and stainless steel, Journal of Nuclear Materials, 155 (1988) 1196-1200.

[80] A. Kozlov, V. Panchenko, K. Kozlov, I. Russkikh, A.V. Kozlov, Evolution of radiation defects in nickel under low-temperature neutron irradiation, The Physics of Metals and Metallography, 115 (2014) 39-45.

[81] N.H. Packan, Voids in neutron irradiated aluminum, (1970).

[82] M. Kiritani, Similarity and difference between fcc, bcc and hcp metals from the view point of point defect cluster formation, Journal of Nuclear Materials, 276 (2000) 41-49.

[83] Y. Chen, K.Y. Yu, Y. Liu, S. Shao, H. Wang, M.A. Kirk, J. Wang, X. Zhang, Damage-tolerant nanotwinned metals with nanovoids under radiation environments, Nat Commun, 6 (2015) 7036.

[84] Y.N. Osetsky, D.J. Bacon, Defect cluster formation in displacement cascades in copper, Nuclear Instruments and Methods in Physics Research Section B: Beam Interactions with Materials and Atoms, 180 (2001) 85-90.

[85] S.J. Zinkle, Y. Matsukawa, Observation and analysis of defect cluster production and interactions with dislocations, Journal of Nuclear Materials, 329-333 (2004) 88-96.

[86] J. Silcox, P.B. Hirsch, Direct observations of defects in quenched gold, Philosophical Magazine, 4 (1959) 72-89.

[87] Y. Matsukawa, S.J. Zinkle, One-dimensional fast migration of vacancy clusters in metals, Science, 318 (2007) 959-962.

[88] T. Kadoyoshi, H. Kaburaki, F. Shimizu, H. Kimizuka, S. Jitsukawa, J. Li, Molecular dynamics study on the formation of stacking fault tetrahedra and unfaulting of frank loops in fcc metals, Acta Materialia, 55 (2007) 3073-3080.

[89] K.Y. Yu, D. Bufford, C. Sun, Y. Liu, H. Wang, M.A. Kirk, M. Li, X. Zhang, Removal of stacking-fault tetrahedra by twin boundaries in nanotwinned metals, Nature communications, 4 (2013) 1377.

[90] M. Griffiths, Microstructure evolution in h.C.P. Metals during irradiation, Philosophical Magazine A, 63 (1991) 835-847.

[91] M. Griffiths, Evolution of microstructure in hcp metals during irradiation, Journal of Nuclear Materials, 205 (1993) 225-241.

[92] D.J. Bacon, F. Gao, Y.N. Osetsky, The primary damage state in fcc, bcc and hcp metals as seen in molecular dynamics simulations, Journal of Nuclear Materials, 276 (2000) 1-12.

[93] M. Samaras, P.M. Derlet, H.V. Swygenhoven, M. Victoria, Atomic scale modelling of the primary damage state of irradiated fcc and bcc nanocrystalline metals, Journal of Nuclear Materials, 351 (2006) 47-55.

[94] J. Marian, B.D. Wirth, J.M. Perlado, Mechanism of formation and growth of 〈100〉 interstitial loops in ferritic materials, Physical Review Letters, 88 (2002) 255507.

[95] M.L. Jenkins, Z. Yao, M. Hernández-Mayoral, M.A. Kirk, Dynamic observations of heavy-ion damage in fe and fe–cr alloys, Journal of Nuclear Materials, 389 (2009) 197-202.

[96] M. Kirk, X. Yi, M. Jenkins, Characterization of irradiation defect structures and densities by transmission electron microscopy, Journal of Materials Research, 30 (2015) 1195-1201.

[97] X. Yi, M.L. Jenkins, K. Hattar, P.D. Edmondson, S.G. Roberts, Characterisation of radiation damage in w and w-based alloys from 2 mev self-ion near-bulk implantations, Acta Materialia, 92 (2015) 163-177.

[98] M. Downey, B. Eyre, Neutron irradiation damage in molybdenum, Philosophical Magazine, 11 (1965) 53-70.

[99] D. Maher, B. Eyre, Neutron irradiation damage in molybdenum, Philosophical Magazine, 23 (1971) 409-438.

[100] K. Lacefield, J. Moteff, J. Smith, Neutron radiation damage in tungsten single crystals, Philosophical Magazine, 13 (1966) 1079-1081.

[101] M. Kiritani, Y. Maehara, H. Takata, Electron radiation damage and properties of point defects in molybdenum, Journal of the Physical Society of Japan, 41 (1976) 1575-1583.

[102] S. Fukuzumi, T. Yoshiie, Y. Satoh, Q. Xu, H. Mori, M. Kawai, Defect structural evolution in high purity tungsten irradiated with electrons using high voltage electron microscope, Journal of nuclear materials, 343 (2005) 308-312.

[103] A.G. Mikhin, Y.N. Osetsky, V.G. Kapinos, On the anisotropic migration of point defects in h.C.P. Zirconium, Philosophical Magazine A: Physics of Condensed Matter, Structure, Defects and Mechanical Properties, 70 (1994) 25-33.

[104] Y.N. Osetsky, D.J. Bacon, N. De Diego, Anisotropy of point defect diffusion in alpha-zirconium, Metallurgical and Materials Transactions A: Physical Metallurgy and Materials Science, 33 (2002) 777-782.

[105] J. Combronde, G. Brebec, Anisotropy for self diffusion in magnesium, Acta Metallurgica, 19 (1971) 1393-1399.

[106] A.K. Khan, Z. Yao, M.R. Daymond, R.A. Holt, Effect of foil orientation on damage accumulation during irradiation in magnesium and annealing response of dislocation loops, Journal of Nuclear Materials, 423 (2012) 132-141.

[107] D.J. Bacon, A review of computer-models of point-defects in hcp metals, Journal of Nuclear Materials, 159 (1988) 176-189.

[108] H. Foell, M. Wilkens, Transmission electron microscope studies of dislocation loops in heavy-ion irradiated hcp cobalt, Phys Status Solidi A, 39 (1977) 561-571.

[109] V. Levy, Determining the nature of dislocation loops observed in mg, J. Microscopie, 19 (1974) 1-16.

[110] A. Jostsons, R. Blake, J. Napier, P. Kelly, K. Farrell, Faulted loops in neutron-irradiated zirconium, Journal of Nuclear Materials, 68 (1977) 267-276.

[111] M. Griffiths, A review of microstructure evolution in zirconium alloys during irradiation, Journal of Nuclear Materials, 159 (1988) 190-218.

[112] M. Griffiths, D. Faulkner, R. Styles, Neutron damage in α-titanium, Journal of Nuclear Materials, 119 (1983) 189-207.

[113] A.K. Khan, Z. Yao, M.R. Daymond, R.A. Holt, Irradiation damage in commercial purity magnesium, Nuclear Instruments and Methods in Physics Research Section B: Beam Interactions with Materials and Atoms, 272 (2012) 231-235.

[114] M. Griffith, V. Fidleris, R.W. Gilbert, Proceedings of the eighth international symposium on zirconium in the nuclear industry, special technical publication no. 1023, edited by l. F. P. Van swam and c. M. Eucken (philadelphia, pennsylvania: American society for testing and materials), p. 658., 1989.

[115] A. Jostsons, P.M. Kelly, R.G. Blake, K. Farrell, Proceedings of the ninth international symposium on the effects of radiation on structural materials, special technical publications no. 683 (philadelphia, pennsylvania: American society for testing and materials), p. 46., (1979).

[116] M. Griffiths, M.H. Loretto, R.E. Smallman, Anisotropic distribution of dislocation loops in hvem-irradiated zr, Philosophical Magazine A, 49 (1984) 613-624.

[117] S. Yamada, T. Kameyama, Observation of c-component dislocation structures formed in pure zr and zr-base alloy by self-ion accelerator irradiation, Journal of Nuclear Materials, 422 (2012) 167-172.

[118] A. Wolfenden, K. Herschbach, K. Müller, T. Stober, Neutron irradiation damage in magnesium single crystals, Radiation Effects, 39 (1978) 177-180.

[119] O. Anderoglu, T.S. Byun, M. Toloczko, S.A. Maloy, Mechanical performance of ferritic martensitic steels for high dose applications in advanced nuclear reactors, Metallurgical and Materials Transactions a-Physical Metallurgy and Materials Science, 44a (2013) 70-83.

[120] Reduced activation materials for fusion reactors, Philadelphia, PA : ASTM, Philadelphia, PA, 1990.

[121] S.J. Zinkle, P.J. Maziasz, R.E. Stoller, Dose dependence of the microstructural evolution in neutron-irradiated austenitic stainless steel, Journal of Nuclear Materials, 206 (1993) 266-286.

[122] J.J. Kai, R.L. Klueh, Microstructural analysis of neutron-irradiated martensitic steels, Journal of Nuclear Materials, 230 (1996) 116-123.

[123] P.J. Maziasz, Formation and stability of radiation-induced phases in neutron-irradiated austenitic and ferritic steels, Journal of Nuclear Materials, 169 (1989) 95-115.

[124] S.M. Bruemmer, E.P. Simonen, P.M. Scott, P.L. Andresen, G.S. Was, J.L. Nelson, Radiation-induced material changes and susceptibility to intergranular failure of light-water-reactor core internals, Journal of Nuclear Materials, 274 (1999) 299-314.

[125] S.M. Bruemmer, G.S. Was, Microstructural and microchemical mechanisms controlling intergranular stress corrosion cracking in light-water-reactor systems, Journal of Nuclear Materials, 216 (1994) 348-363.

[126] P. Scott, A review of irradiation assisted stress corrosion cracking, Journal of Nuclear Materials, 211 (1994) 101-122.

[127] R.A. Johnson, N.Q. Lam, Solute segregation to voids during irradiation, Physical Review B, 15 (1977) 1794-1800.

[128] N.Q. Lam, P.R. Okamoto, H. Wiedersich, Effects of solute segregation and precipitation on void swelling in irradiated alloys, Journal of Nuclear Materials, 74 (1978) 101-113.

[129] W.Z. Han, E.G. Fu, M.J. Demkowicz, Y.Q. Wang, A. Misra, Irradiation damage of single crystal, coarse-grained, and nanograined copper under helium bombardment at 450 c, Journal of Materials Research, 28 (2013) 2763-2770.

[130] F. Zhang, X. Wang, J.B. Wierschke, L. Wang, Helium bubble evolution in ion irradiated al/b 4 c metal metrix composite, Scripta Materialia, 109 (2015) 28-33.

[131] K.Y. Yu, Y. Liu, C. Sun, H. Wang, L. Shao, E.G. Fu, X. Zhang, Radiation damage in helium ion irradiated nanocrystalline fe, Journal of Nuclear Materials, 425 (2012) 140-146.

[132] H. Iwakiri, K. Yasunaga, K. Morishita, N. Yoshida, Microstructure evolution in tungsten during low-energy helium ion irradiation, Journal of nuclear materials, 283 (2000) 1134-1138.

[133] F.A. Garner, M.B. Toloczko, High dose effects in neutron irradiated face-centered cubic metals, Journal of Nuclear Materials, 206 (1993) 230-248.

[134] L.K. Mansur, Void swelling in metals and alloys under irradiation: An assessment of the theory, Nuclear Technology, 40 (1978) 5-34.

[135] D. Norris, The use of the high voltage electron microscope to simulate fast neutron-induced void swelling in metals, Journal of Nuclear Materials, 40 (1971) 66-76.

[136] E. Little, D. Stow, Void-swelling in irons and ferritic steels: Ii. An experimental survey of materials irradiated in a fast reactor, Journal of Nuclear Materials, 87 (1979) 25-39.

[137] F. Garner, H. Brager, D. Gelles, J. McCarthy, Neutron irradiation of femn, fecrmn and fecrni alloys and an explanation of their differences in swelling behavior, Journal of Nuclear Materials, 148 (1987) 294-301.

[138] N. Packan, K. Farrell, J. Stiegler, Correlation of neutron and heavy-ion damage: I. The influence of dose rate and injected helium on swelling in pure nickel, Journal of Nuclear Materials, 78 (1978) 143-155.

[139] D.I.R. Norris, Voids in irradiated metals (part i), Radiation Effects, 14 (1972) 1-37.

[140] E.A. Little, D.A. Stow, Void-swelling in irons and ferritic steels, Journal of Nuclear Materials, 87 (1979) 25-39.

[141] A.D. Brailsford, R. Bullough, M.R. Hayns, Point defect sink strengths and void-swelling, Journal of Nuclear Materials, 60 (1976) 246-256.

[142] F.A. Garner, M.B. Toloczko, B.H. Sencer, Comparison of swelling and irradiation creep behavior of fcc-austenitic and bcc-ferritic/martensitic alloys at high neutron exposure, Journal of Nuclear Materials, 276 (2000) 123-142.

[143] S. Sharafat, N.M. Ghoniem, M. Anderson, B. Williams, J. Blanchard, L. Snead, Micro-engineered first wall tungsten armor for high average power laser fusion energy systems, Journal of Nuclear Materials, 347 (2005) 217-243.

[144] K. Farrell, J. Houston, Suppression of radiation damage microstructure in aluminum by trace impurities, Journal of Nuclear Materials, 83 (1979) 57-66.

[145] Y.V. Konobeev, A. Dvoriashin, S. Porollo, F.A. Garner, Swelling and microstructure of pure fe and fe–cr alloys after neutron irradiation to∼ 26dpa at 400° c, Journal of nuclear materials, 355 (2006) 124-130.

[146] J.H. Evans, Void swelling and irradiation-induced void shrinkage in neutron irradiated molybdenum and tzm, Journal of Nuclear Materials, 88 (1980) 31-41.

[147] M. Song, Y.D. Wu, D. Chen, X.M. Wang, C. Sun, K.Y. Yu, Y. Chen, L. Shao, Y. Yang, K.T. Hartwig, X. Zhang, Response of equal channel angular extrusion processed ultrafine-grained t91 steel subjected to high temperature heavy ion irradiation, Acta Materialia, 74 (2014) 285-295.

[148] C. Sun, S. Zheng, C. Wei, Y. Wu, L. Shao, Y. Yang, K. Hartwig, S. Maloy, S. Zinkle, T. Allen, Superior radiation-resistant nanoengineered austenitic 304l stainless steel for applications in extreme radiation environments, Scientific reports, 5 (2015).

[149] A. Jostsons, K. Farrell, Structural damage and its annealing response in neutron irradiated magnesium†, Radiation Effects, 15 (1972) 217-225.

[150] D. Faulkner, C.H. Woo, Void swelling in zirconium, Journal of Nuclear Materials, 90 (1980) 307-316.

[151] A. Jostsons, P.M. Kelly, R.G. Blake, K. Farrell, Neutron irradiation-induced defect structures in zirconium, American Society for Testing and Materials, Special Technical Publication, (1978) 46-61.

[152] C.D. Cann, D. Faulkner, K. Nuttall, R.C. Styles, A.J. Shillinglaw, C.K. Chow, A.J. Rogowski, Irradiation growth in zirconium and zirconium alloys irradiated in the dounreay fast reactor, in, Canada, 1986, pp. 77.

[153] J.L. Brimhall, G.L. Kulcinski, H.E. Kissinger, B. Mastel, Microstructural analysis of neutron irradiated titanium and rhenium, Radiation Effects, 9 (1971) 273-278.

[154] N.M. Ghoniem, G.L. Kulcinski, The use of the fully dynamic rate theory to predict void growth in metals, Radiation Effects, 41 (1979) 81-89.

[155] S.K. McLaurin, G.L. Kulcinski, R.A. Dodd, Effects of temperature and helium on void formation in self-ion irradiated aluminum, Journal of Nuclear Materials, 117 (1983) 208-212.

[156] B.N. Singh, J.H. Evans, Significant differences in defect accumulation behaviour between fcc and bcc crystals under cascade damage conditions, Journal of Nuclear Materials, 226 (1995) 277-285.

[157] N.I. Budylkin, E.G. Mironova, V.M. Chernov, V.A. Krasnoselov, S.I. Porollo, F.A. Garner, Neutron-induced swelling and embrittlement of pure iron and pure nickel irradiated in the bn-350 and bor-60 fast reactors, Journal of Nuclear Materials, 375 (2008) 359-364.

[158] T.D. Ryan, A. Taylor, Heavy ion-induced void formation in pure nickel, in: S.T. Picraux, E.P. EerNisse, F.L. Vook (Eds.) Applications of ion beams to metals, Springer US, Boston, MA, 1974, pp. 675-685.

[159] F.A. Garner, J.F. Stubbins, Saturation of swelling in neutron-irradiated molybdenum and its dependence on irradiation temperature and starting microstructural state, Journal of Nuclear Materials, 212 (1994) 1298-1302.

[160] J.D. Elen, G. Hamburg, A. Mastenbroek, Voids in vanadium, niobium and molybdenum by fast neutron irradiation at high temperatures, Journal of Nuclear Materials, 39 (1971) 194-202.

[161] G.L. Kulcinski, J.L. Brimhal, High-temperature heavy ion bombardment of molybdenum, niobium and tzm, in, Belgium, 1972.

[162] B.A. Loomis, A. Taylor, S.B. Gerber, Void swelling of nb and nb-1% zr induced by 58ni+ bombardment, Journal of Nuclear Materials, 56 (1975) 25-37.

[163] F.W. Wiffen, The microstructure and swelling of neutron irradiated tantalum, Journal of Nuclear Materials, 67 (1977) 119-130.

[164] K. Yasunaga, H. Watanabe, N. Yoshida, T. Muroga, N. Noda, Microstructure of tantalum irradiated with heavy ions, Journal of Nuclear Materials, 258–263, Part 1 (1998) 879-882.

[165] W.J. Weber, G.L. Kulcinski, R.G. Lott, P. Wilkes, H.V. Smith, Ion simulation study of void formation in high purity vanadium, in, United States, 1976.

[166] J. Matolich, H. Nahm, J. Moteff, Swelling in neutron irradiated tungsten and tungsten-25 percent rhenium, Scripta Metallurgica, 8 (1974) 837-841.

[167] N.B. Heubeck, Nuclear fuel elements made from nanophase materials. U.S. Patent 5,805,657, 1998.

[168] H. Gleiter, Nanocrystalline materials, Progress in Materials Science, 33 (1989) 223-315.

[169] C. Suryanarayana, C.C. Koch, Nanocrystalline materials – current research and future directions, Hyperfine Interactions, 130 (2000) 5-44.

[170] Q. Guo, P. Landau, P. Hosemann, Y. Wang, J.R. Greer, Helium implantation effects on the compressive response of cu nanopillars, Small, 9 (2013) 691-696.

[171] R. Liontas, X.W. Gu, E. Fu, Y. Wang, N. Li, N. Mara, J.R. Greer, Effects of helium implantation on the tensile properties and microstructure of ni73p27 metallic glass nanostructures, Nano Lett, 14 (2014) 5176-5183.

[172] M. Caro, W.M. Mook, E.G. Fu, Y.Q. Wang, C. Sheehan, E. Martinez, J.K. Baldwin, A. Caro, Radiation induced effects on mechanical properties of nanoporous gold foams, Applied Physics Letters, 104 (2014) 233109.

[173] S.A. Maloy, M.R. James, G. Willcutt, W.F. Sommer, M. Sokolov, L.L. Snead, M.L. Hamilton, F. Garner, The mechanical properties of 316l/304l stainless steels, alloy 718 and mod 9cr–1mo after irradiation in a spallation environment, Journal of Nuclear Materials, 296 (2001) 119-128.

[174] M.J. Demkowicz, A. Misra, A. Caro, The role of interface structure in controlling high helium concentrations, Current Opinion in Solid State and Materials Science, 16 (2012) 101-108.

[175] Q.M. Wei, N. Li, N. Mara, M. Nastasi, A. Misra, Suppression of irradiation hardening in nanoscale v/ag multilayers, Acta Materialia, 59 (2011) 6331-6340.

[176] K.Y. Yu, Z. Fan, Y. Chen, M. Song, Y. Liu, H. Wang, M.A. Kirk, M. Li, X. Zhang, In situobservation of defect annihilation in kr ion-irradiated bulk fe/amorphous-fe2zr nanocomposite alloy, Materials Research Letters, 3 (2014) 35-42.

[177] J. Li, Y. Chen, H. Wang, X. Zhang, In situ studies on twin-thickness-dependent distribution of defect clusters in heavy ion-irradiated nanotwinned ag, Metallurgical and Materials Transactions A, 48 (2017) 1466-1473.

[178] Y. Chen, J. Li, K.Y. Yu, H. Wang, M.A. Kirk, M. Li, X. Zhang, In situ studies on radiation tolerance of nanotwinned cu, Acta Materialia, 111 (2016) 148-156.

[179] J. Li, K.Y. Yu, Y. Chen, M. Song, H. Wang, M.A. Kirk, M. Li, X. Zhang, In situ study of defect migration kinetics and self-healing of twin boundaries in heavy ion irradiated nanotwinned metals, Nano Lett, 15 (2015) 2922-2927.

[180] A. Misra, H. Krug, Deformation behavior of nanostructured metallic multilayers, Advanced Engineering Materials, 3 (2001) 217-222.

[181] A. Misra, J.P. Hirth, R.G. Hoagland, Length-scale-dependent deformation mechanisms in incoherent metallic multilayered composites, Acta Materialia, 53 (2005) 4817-4824.

[182] Z.X. Wu, Y.W. Zhang, D.J. Srolovitz, Dislocation–twin interaction mechanisms for ultrahigh strength and ductility in nanotwinned metals, Acta Materialia, 57 (2009) 4508-4518.

[183] E.M. Bringa, J.D. Monk, A. Caro, A. Misra, L. Zepeda-Ruiz, M. Duchaineau, F. Abraham, M. Nastasi, S.T. Picraux, Y.Q. Wang, D. Farkas, Are nanoporous materials radiation resistant?, Nano Lett, 12 (2012) 3351-3355.

[184] C. Sun, D. Bufford, Y. Chen, M.A. Kirk, Y.Q. Wang, M. Li, H. Wang, S.A. Maloy, X. Zhang, In situ study of defect migration kinetics in nanoporous ag with enhanced radiation tolerance, Sci Rep, 4 (2014) 3737.

[185] O. Anderoglu, A. Misra, H. Wang, X. Zhang, Thermal stability of sputtered cu films with nanoscale growth twins, Journal of Applied Physics, 103 (2008) 094322.

[186] J.Y. Zhang, S. Lei, Y. Liu, J.J. Niu, Y. Chen, G. Liu, X. Zhang, J. Sun, Length scale-dependent deformation behavior of nanolayered cu/zr micropillars, Acta Materialia, 60 (2012) 1610-1622.

[187] C. Sun, K.Y. Yu, J.H. Lee, Y. Liu, H. Wang, L. Shao, S.A. Maloy, K.T. Hartwig, X. Zhang, Enhanced radiation tolerance of ultrafine grained fe–cr–ni alloy, Journal of Nuclear Materials, 420 (2012) 235-240.

[188] E.G. Fu, M. Caro, L.A. Zepeda-Ruiz, Y.Q. Wang, K. Baldwin, E. Bringa, M. Nastasi, A. Caro, Surface effects on the radiation response of nanoporous au foams, Applied Physics Letters, 101 (2012) 191607.

[189] E.G. Fu, N. Li, A. Misra, R.G. Hoagland, H. Wang, X. Zhang, Mechanical properties of sputtered cu/v and al/nb multilayer films, Materials Science and Engineering: A, 493 (2008) 283-287.

[190] X. Zhang, A. Misra, Residual stresses in sputter-deposited copper/330 stainless steel multilayers, Journal of Applied Physics, 96 (2004) 7173.

[191] N. Li, K.Y. Yu, J. Lee, H. Wang, X. Zhang, Size dependent strengthening mechanisms in sputtered fe/w multilayers, Journal of Applied Physics, 107 (2010) 093503.

[192] G. Kurdjumow, G. Sachs, Over the mechanisms of steel hardening, Zeitschrift für Physik, 64 (1930) 325-343.

[193] Z. Nishiyama, X-ray investigation the mechanism of transformation from face-centred to body-centred cubic lattice, Sci. Rep. Res. Insts, 23 (1934) 638.

[194] W. Pitsch, The martensite transformation in thin foils of iron-nitrogen alloys, Philosophical Magazine, 4 (1959) 577-584.

[195] E.C. Bain, The nature of martensite, Trans. AIME, 70 (1924) 25.

[196] A. Misra, M. Verdier, Y.C. Lu, H. Kung, T.E. Mitchell, M. Nastasi, J.D. Embury, Structure and mechanical properties of cu-x (x = nb,cr,ni) nanolayered composites, Scripta Materialia, 39 (1998) 555-560.

[197] G.S. Was, T. Foecke, Deformation and fracture in microlaminates, Thin Solid Films, 286 (1996) 1-31.

[198] N.A. Mara, D. Bhattacharyya, J.P. Hirth, P. Dickerson, A. Misra, Mechanism for shear banding in nanolayered composites, Applied Physics Letters, 97 (2010) 021909.

[199] H. Huang, F. Spaepen, Tensile testing of free-standing cu, ag and al thin films and ag/cu multilayers, Acta Materialia, 48 (2000) 3261-3269.

[200] C. Kim, S.B. Qadri, M.R. Scanlon, R.C. Cammarata, Low-dimension structural properties and microindentation studies of ion-beam-sputtered multilayers of ag/al films, Thin Solid Films, 240 (1994) 52-55.

[201] Q. Li, P.M. Anderson, Dislocation-based modeling of the mechanical behavior of epitaxial metallic multilayer thin films, Acta Materialia, 53 (2005) 1121-1134.

[202] A. Misra, J.P. Hirth, H. Kung, Single-dislocation-based strengthening mechanisms in nanoscale metallic multilayers, Philosophical Magazine A, 82 (2002) 2935-2951.

[203] A. Misra, X. Zhang, D. Hammon, R.G. Hoagland, Work hardening in rolled nanolayered metallic composites, Acta Materialia, 53 (2005) 221-226.

[204] A. Misra, R.G. Hoagland, Plastic flow stability of metallic nanolaminate composites, Journal of Materials Science, 42 (2006) 1765-1771.

[205] E.O. Hall, The deformation and ageing of mild steel: Iii discussion of results, Proceedings of the Physical Society. Section B, 64 (1951) 747.

[206] N.J.J. Petch, The cleavage strength of polycristals, 1953.

[207] Y. Chen, E. Fu, K. Yu, M. Song, Y. Liu, Y. Wang, H. Wang, X. Zhang, Enhanced radiation tolerance in immiscible cu/fe multilayers with coherent and incoherent layer interfaces, Journal of Materials Research, 30 (2015) 1300-1309.

[208] K.Y. Yu, Y. Liu, S. Rios, H. Wang, X. Zhang, Strengthening mechanisms of ag/ni immiscible multilayers with fcc/fcc interface, Surface and Coatings Technology, 237 (2013) 269-275.

[209] X. Zhang, A. Misra, H. Wang, T.D. Shen, M. Nastasi, T.E. Mitchell, J.P. Hirth, R.G. Hoagland, J.D. Embury, Enhanced hardening in cu/330 stainless steel multilayers by nanoscale twinning, Acta Materialia, 52 (2004) 995-1002.

[210] P.M. Anderson, T. Foecke, P.M. Hazzledine, Dislocation-based deformation mechanisms in metallic nanolaminates, Mrs Bulletin, 24 (1999) 27-33.

[211] Y. Liu, Y. Chen, K.Y. Yu, H. Wang, J. Chen, X. Zhang, Stacking fault and partial dislocation dominated strengthening mechanisms in highly textured cu/co multilayers, International Journal of Plasticity, 49 (2013) 152-163.

[212] D. Bufford, Z. Bi, Q.X. Jia, H. Wang, X. Zhang, Nanotwins and stacking faults in high-strength epitaxial ag/al multilayer films, Applied Physics Letters, 101 (2012) 223112.

[213] J.D. Embury, J.P. Hirth, On dislocation storage and the mechanical response of fine scale microstructures, Acta Metallurgica et Materialia, 42 (1994) 2051-2056.

[214] J.S. Koehler, Attempt to design a strong solid, Physical Review B, 2 (1970) 547-551.

[215] S.I. Rao, P.M. Hazzledine, Atomistic simulations of dislocation–interface interactions in the cu-ni multilayer system, Philosophical Magazine A, 80 (2000) 2011-2040.

[216] K.O. Schweitz, J. Chevallier, J. B∅ttiger, W. Matz, N. Schell, Hardness in ag/ni, au/ni and cu/ni multilayers, Philosophical Magazine A, 81 (2001) 2021-2032.

[217] Y. Chen, Y. Liu, C. Sun, K.Y. Yu, M. Song, H. Wang, X. Zhang, Microstructure and strengthening mechanisms in cu/fe multilayers, Acta Materialia, 60 (2012) 6312-6321.

[218] F.C. Frank, J.H. van der Merwe, One-dimensional dislocations. Ii. Misfitting monolayers and oriented overgrowth, Proceedings of the Royal Society of London A: Mathematical, Physical and Engineering Sciences, 198 (1949) 216-225.

[219] B. Ham, A. Junkaew, R. Arroyave, J. Chen, H. Wang, P. Wang, J. Majewski, J. Park, H.C. Zhou, R.K. Arvapally, U. Kaipa, M.A. Omary, X.Y. Zhang, Y. Ren, X. Zhang, Hydrogen sorption in orthorhombic mg hydride at ultra-low temperature, International Journal of Hydrogen Energy, 38 (2013) 8328-8341.

[220] R.G. Hoagland, T.E. Mitchell, J.P. Hirth, H. Kung, On the strengthening effects of interfaces in multilayer fee metallic composites, Philosophical Magazine A, 82 (2002) 643-664.

[221] Y. Liu, D. Bufford, H. Wang, C. Sun, X. Zhang, Mechanical properties of highly textured cu/ni multilayers, Acta Materialia, 59 (2011) 1924-1933.

[222] Y. Liu, D. Bufford, S. Rios, H. Wang, J. Chen, J.Y. Zhang, X. Zhang, A formation mechanism for ultra-thin nanotwins in highly textured cu/ni multilayers, Journal of Applied Physics, 111 (2012) 073526.

[223] J. Wang, R.G. Hoagland, J.P. Hirth, A. Misra, Atomistic simulations of the shear strength and sliding mechanisms of copper–niobium interfaces, Acta Materialia, 56 (2008) 3109-3119.

[224] L. Lu, R. Schwaiger, Z.W. Shan, M. Dao, K. Lu, S. Suresh, Nano-sized twins induce high rate sensitivity of flow stress in pure copper, Acta Materialia, 53 (2005) 2169-2179.

[225] L. Lu, Y. Shen, X. Chen, L. Qian, K. Lu, Ultrahigh strength and high electrical conductivity in copper, Science, 304 (2004) 422-426.

[226] D. Bufford, H. Wang, X. Zhang, High strength, epitaxial nanotwinned ag films, Acta Materialia, 59 (2011) 93-101.

[227] M.A. Meyers, O. Vöhringer, V.A. Lubarda, The onset of twinning in metals: A constitutive description, Acta Materialia, 49 (2001) 4025-4039.

[228] X. Zhang, O. Anderoglu, R.G. Hoagland, A. Misra, Nanoscale growth twins in sputtered metal films, JOM, 60 (2008) 75-78.

[229] J. Wang, O. Anderoglu, J.P. Hirth, A. Misra, X. Zhang, Dislocation structures of σ3 {112} twin boundaries in face centered cubic metals, Applied Physics Letters, 95 (2009) 021908.

[230] J.P. Hirth, J. Lothe, Theory of dislocations, (1982).

[231] K.Y. Yu, D. Bufford, Y. Chen, Y. Liu, H. Wang, X. Zhang, Basic criteria for formation of growth twins in high stacking fault energy metals, Applied Physics Letters, 103 (2013) 181903.

[232] D. Bufford, Y. Liu, Y. Zhu, Z. Bi, Q.X. Jia, H. Wang, X. Zhang, Formation mechanisms of high-density growth twins in aluminum with high stacking-fault energy, Materials Research Letters, 1 (2013) 51-60.

[233] D. Bufford, Y. Liu, J. Wang, H. Wang, X. Zhang, In situ nanoindentation study on plasticity and work hardening in aluminium with incoherent twin boundaries, Nat Commun, 5 (2014) 4864.

[234] O. Anderoglu, A. Misra, H. Wang, F. Ronning, M.F. Hundley, X. Zhang, Epitaxial nanotwinned cu films with high strength and high conductivity, Applied Physics Letters, 93 (2008) 083108.

[235] S. Bonnan, P.-L. Hereil, F. Collombet, Experimental characterization of quasi static and shock wave behavior of porous aluminum, Journal of Applied Physics, 83 (1998) 5741-5749.

[236] Y.F. Zhang, Y.Z. Tang, G. Zhou, J.N. Wei, F.S. Han, Dynamic compression properties of porous aluminum, Materials Letters, 56 (2002) 728-731.

[237] J. Biener, A.M. Hodge, A.V. Hamza, L.M. Hsiung, J.H. Satcher, Nanoporous au: A high yield strength material, Journal of Applied Physics, 97 (2005) 024301.

[238] X.-Y. Sun, G.-K. Xu, X. Li, X.-Q. Feng, H. Gao, Mechanical properties and scaling laws of nanoporous gold, Journal of Applied Physics, 113 (2013) 023505.

[239] H.-J. Jin, L. Kurmanaeva, J. Schmauch, H. Rösner, Y. Ivanisenko, J. Weissmüller, Deforming nanoporous metal: Role of lattice coherency, Acta Materialia, 57 (2009) 2665-2672.

[240] Y. Sun, J. Ye, A.M. Minor, T.J. Balk, In situ indentation of nanoporous gold thin films in the transmission electron microscope, Microscopy Research and Technique, 72 (2009) 232-241.

[241] K.Y. Yu, C. Sun, Y. Chen, Y. Liu, H. Wang, M.A. Kirk, M. Li, X. Zhang, Superior tolerance of ag/ni multilayers against kr ion irradiation: An in situ study, Philosophical Magazine, 93 (2013) 3547-3562.

[242] H. Wang, R. Araujo, J.G. Swadener, Y.Q. Wang, X. Zhang, E.G. Fu, T. Cagin, Ion irradiation effects in nanocrystalline tin coatings, Nuclear Instruments and Methods in Physics Research Section B: Beam Interactions with Materials and Atoms, 261 (2007) 1162-1166.

[243] X.M. Bai, A.F. Voter, R.G. Hoagland, M. Nastasi, B.P. Uberuaga, Efficient annealing of radiation damage near grain boundaries via interstitial emission, Science, 327 (2010) 1631-1634.

[244] Y. Chen, L. Jiao, C. Sun, M. Song, K.Y. Yu, Y. Liu, M. Kirk, M. Li, H. Wang, X. Zhang, In situ studies of radiation induced crystallization in fe/a-y2o3 nanolayers, Journal of Nuclear Materials, 452 (2014) 321-327.

[245] A. Misra, M.J. Demkowicz, X. Zhang, R.G. Hoagland, The radiation damage tolerance of ultra-high strength nanolayered composites, JOM Journal of the Minerals, Metals and Materials Society, 59 (2007) 62-65.

[246] E.G. Fu, A. Misra, H. Wang, L. Shao, X. Zhang, Interface enabled defects reduction in helium ion irradiated cu/v nanolayers, Journal of Nuclear Materials, 407 (2010) 178-188.

[247] Q.M. Wei, Y.Q. Wang, M. Nastasi, A. Misra, Nucleation and growth of bubbles in he ion-implanted v/ag multilayers, Philosophical Magazine, 91 (2010) 553-573.

[248] N. Li, E.G. Fu, H. Wang, J.J. Carter, L. Shao, S.A. Maloy, A. Misra, X. Zhang, He ion irradiation damage in fe/w nanolayer films, Journal of Nuclear Materials, 389 (2009) 233-238.

[249] N. Li, M.S. Martin, O. Anderoglu, A. Misra, L. Shao, H. Wang, X. Zhang, He ion irradiation damage in al/nb multilayers, Journal of Applied Physics, 105 (2009) 123522-123528.

[250] N. Li, J.J. Carter, A. Misra, L. Shao, H. Wang, X. Zhang, The influence of interfaces on the formation of bubbles in he-ion-irradiated cu/mo nanolayers (cumo part), Philosophical Magazine Letters, 91 (2011) 18 - 28.

[251] W. Yuan, Helium effects on the stability of the interface of cu/w nanomultilayers, Acta Phys. Sin., 61 (2012).

[252] M.J. Demkowicz, R.G. Hoagland, J.P. Hirth, Interface structure and radiation damage resistance in cu-nb multilayer nanocomposites, Physical Review Letters, 100 (2008) 136102.

[253] M.J. Demkowicz, P. Bellon, B.D. Wirth, Atomic-scale design of radiation-tolerant nanocomposites, MRS Bulletin, 35 (2010) 992-998.

[254] W.Z. Han, M.J. Demkowicz, E.G. Fu, Y.Q. Wang, A. Misra, Effect of grain boundary character on sink efficiency, Acta Materialia, 60 (2012) 6341-6351.

[255] M.J. Demkowicz, O. Anderoglu, X. Zhang, A. Misra, The influence of ∑3 twin boundaries on the formation of radiation-induced defect clusters in nanotwinned cu, Journal of Materials Research, 26 (2011) 1666-1675.

[256] K.Y. Yu, D. Bufford, F. Khatkhatay, H. Wang, M.A. Kirk, X. Zhang, In situ studies of irradiation-induced twin boundary migration in nanotwinned ag, Scripta Materialia, 69 (2013) 385-388.

[257] C. Sun, B.P. Uberuaga, L. Yin, J. Li, Y. Chen, M.A. Kirk, M. Li, S.A. Maloy, H. Wang, C. Yu, X. Zhang, Resilient zno nanowires in an irradiation environment: An in situ study, Acta Materialia, 95 (2015) 156-163.

[258] S.N. Piramanayagam, Perpendicular recording media for hard disk drives, Journal of Applied Physics, 102 (2007) 011301.

[259] M. Andreas, T. Kentaro, T.M. David, A. Manfred, S. Yoshiaki, I. Yoshihiro, S. Shouheng, E.F. Eric, Magnetic recording: Advancing into the future, Journal of Physics D: Applied Physics, 35 (2002) R157.

[260] P. Chen, M. Zhu, Recent progress in hydrogen storage, Materials Today, 11 (2008) 36-43.

[261] X. Zhang, E.G. Fu, N. Li, A. Misra, Y.Q. Wang, L. Shao, H. Wang, Design of radiation tolerant nanostructured metallic multilayers, Journal of Engineering Materials and Technology, 134 (2012) 041010.

[262] X. Zhang, N. Li, O. Anderoglu, H. Wang, J.G. Swadener, T. Höchbauer, A. Misra, R.G. Hoagland, Nanostructured cu/nb multilayers subjected to helium ion-irradiation, Nuclear Instruments and Methods in Physics Research Section B: Beam Interactions with Materials and Atoms, 261 (2007) 1129-1132.

[263] T. Höchbauer, A. Misra, K. Hattar, R.G. Hoagland, Influence of interfaces on the storage of ion-implanted he in multilayered metallic composites, Journal of Applied Physics, 98 (2005) 123516.

[264] J. Wang, A. Misra, An overview of interface-dominated deformation mechanisms in metallic multilayers, Current Opinion in Solid State and Materials Science, 15 (2011) 20-28.

[265] A. Misra, M. Verdier, H. Kung, J.D. Embury, J.P. Hirth, Deformation mechanism maps for polycrystalline metallic multiplayers, Scripta Materialia, 41 (1999) 973-979.

[266] Y. Kozono, M. Komuro, S. Narishige, M. Hanazono, Y. Sugita, Structures and magnetic properties of fe/ag multilayer films prepared by sputtering and ultrahigh-vacuum depositions, Journal of Applied Physics, 63 (1988) 3470.

[267] X.Y. Zhu, X.J. Liu, F. Zeng, F. Pan, Room temperature nanoindentation creep of nanoscale ag/fe multilayers, Materials Letters, 64 (2010) 53-56.

[268] G. Gladyszewski, K. Temst, K. Mae, R. Schad, F. Beliën, E. Kunnen, G. Verbanck, Y. Bruynseraede, R. Moons, A. Vantomme, S. Blässer, G. Langouche, Structure of ag/fe superlattices probed at different length scales, Thin Solid Films, 366 (2000) 51-62.

[269] Y. Luo, H.-U. Krebs, Structure and solid state reactions of laser-deposited and sputtered fe/nb and fe/ag multilayers, Journal of Applied Physics, 77 (1995) 1482.

[270] B.S. Swartzentruber, Direct measurement of surface diffusion using atom-tracking scanning tunneling microscopy, Physical Review Letters, 76 (1996) 459-462.

[271] D.J. Hepburn, E. MacLeod, G.J. Ackland, Transition metal solute interactions with point defects in fcc iron from first principles, Physical Review B, 92 (2015) 014110.

[272] S. Zhao, G. Velisa, H. Xue, H. Bei, W.J. Weber, Y. Zhang, Suppression of vacancy cluster growth in concentrated solid solution alloys, Acta Materialia, 125 (2017) 231-237.

[273] E.A. Little, Development of radiation resistant materials for advanced nuclear power plant, Materials Science and Technology, 22 (2006) 491-518.

[274] E.A. Little, Neutron-irradiation hardening in irons and ferritic steels, International Metals Reviews, 21 (1976) 25-60.

[275] W. Mansel, G. Vogl, Fast neutron radiation damage in aluminium studied by interstitial trapping at 57 co mossbauer atoms, Journal of Physics F: Metal Physics, 7 (1977) 253.

[276] A.V. Barashev, S.I. Golubov, Unlimited damage accumulation in metallic materials under cascade-damage conditions, Philosophical Magazine, 89 (2009) 2833-2860.

[277] I.J. Beyerlein, X. Zhang, A. Misra, Growth twins and deformation twins in metals, Annual Review of Materials Research, 44 (2014) 329-363.

[278] Y.N. Osetsky, D.J. Bacon, A. Serra, B.N. Singh, S.I. Golubov, One-dimensional atomic transport by clusters of self-interstitial atoms in iron and copper, Philosophical Magazine, 83 (2003) 61-91.

[279] B.D. Wirth, G.R. Odette, D. Maroudas, G.E. Lucas, Energetics of formation and migration of self-interstitials and self-interstitial clusters in α-iron, Journal of Nuclear Materials, 244 (1997) 185-194.

[280] W.C. Oliver, G.M. Pharr, An improved technique for determining hardness and elastic modulus using load and displacement sensing indentation experiments, Journal of Materials Research, 7 (1992) 1564-1583.

[281] M.P. ISO 14577-12002 Metallic materials --- Instrumented Indentation Test for Hardness, International Standard.

[282] D.Williams, C.Carter, Transmission electron microscopy, Springer, 2008.

[283] D.B. Williams, Transmission electron microscopy a textbook for materials science, 2nd ed.. ed., Boston, MA : Springer US, 2009.

[284] J.F. Ziegler, J.P. Biersack, Srim-2008, stopping power and range of ions in matter, Calculation using the Stopping and Range of Ions in Matter (SRIM) Code. <http://www.srim.org/>. (2008).

[285] K.Y. Yu, Y. Liu, E.G. Fu, Y.Q. Wang, M.T. Myers, H. Wang, L. Shao, X. Zhang, Comparisons of radiation damage in he ion and proton irradiated immiscible ag/ni nanolayers, Journal of Nuclear Materials, 440 (2013) 310-318.

[286] Y.T. Zhu, X.L. Wu, X.Z. Liao, J. Narayan, L.J. Kecskés, S.N. Mathaudhu, Dislocation–twin interactions in nanocrystalline fcc metals, Acta Materialia, 59 (2011) 812-821.

[287] K. Lu, L. Lu, S. Suresh, Strengthening materials by engineering coherent internal boundaries at the nanoscale, in, American Association for the Advancement of Science, 2009, pp. 349.

[288] B.J. Daniels, W.D. Nix, B.M. Clemens, Enhanced mechanical hardness in compositionally modulated fe(001)pt(001) and fe(001)cr(001) epitaxial thin films, Thin Solid Films, 253 (1994) 218-222.

[289] A.F. Jankowski, J.P. Hayes, C.K. Saw, Dimensional attributes in enhanced hardness of nanocrystalline ta–v nanolaminates, Philosophical Magazine, 87 (2007) 2323-2334.

[290] Y.Y. Lu, R. Kotoka, J.P. Ligda, B.B. Cao, S.N. Yarmolenko, B.E. Schuster, Q. Wei, The microstructure and mechanical behavior of mg/ti multilayers as a function of individual layer thickness, Acta Materialia, 63 (2014) 216-231.

[291] B. Ham, X. Zhang, High strength mg/nb nanolayer composites, Materials Science and Engineering: A, 528 (2011) 2028-2033.

[292] G.H. Yang, B. Zhao, Y. Gao, F. Pan, Investigation of nanoindentation on co/mo multilayers by the continuous stiffness measurement technique, Surface and Coatings Technology, 191 (2005) 127-133.

[293] J. Xu, M. Kamiko, Y. Zhou, G. Lu, R. Yamamoto, L. Yu, I. Kojima, Structure transformations and superhardness effects in v/ti nanostructured multilayers, Applied Physics Letters, 81 (2002) 1189.

[294] R.G. Hoagland, J.P. Hirth, A. Misra, On the role of weak interfaces in blocking slip in nanoscale layered composites, Philosophical Magazine, 86 (2006) 3537-3558.

[295] J. Wang, R.G. Hoagland, J.P. Hirth, A. Misra, Atomistic modeling of the interaction of glide dislocations with “weak” interfaces, Acta Materialia, 56 (2008) 5685-5693.

[296] X. Zhang, A. Misra, H. Wang, M. Nastasi, J.D. Embury, T.E. Mitchell, R.G. Hoagland, J.P. Hirth, Nanoscale-twinning-induced strengthening in austenitic stainless steel thin films, Applied Physics Letters, 84 (2004) 1096-1098.

[297] Q. Wei, A. Misra, Transmission electron microscopy study of the microstructure and crystallographic orientation relationships in v/ag multilayers, Acta Materialia, 58 (2010) 4871-4882.

[298] J.W. Matthews, A.E. Blakeslee, Defects in epitaxial multilayers: I. Misfit dislocations, Journal of Crystal Growth, 27 (1974) 118-125.

[299] D. Bhattacharyya, X.-Y. Liu, A. Genc, H.L. Fraser, R.G. Hoagland, A. Misra, Heterotwin formation during growth of nanolayered al-tin composites, Applied Physics Letters, 96 (2010) 093113.

[300] P.M. Anderson, C. Li, Hall-petch relations for multilayered materials, Nanostructured Materials, 5 (1995) 349-362.

[301] D. Tabor, A simple theory of static and dynamic hardness, Proceedings of the Royal Society of London A: Mathematical, Physical and Engineering Sciences, 192 (1948) 247-274.

[302] X.F. Zhu, Y.P. Li, G.P. Zhang, J. Tan, Y. Liu, Understanding nanoscale damage at a crack tip of multilayered metallic composites, Applied Physics Letters, 92 (2008) 161905.

[303] X. Zhang, A. Misra, H. Wang, A.L. Lima, M.F. Hundley, R.G. Hoagland, Effects of deposition parameters on residual stresses, hardness and electrical resistivity of nanoscale twinned 330 stainless steel thin films, Journal of Applied Physics, 97 (2005) 094302.

[304] C.G. Rhodes, A.W. Thompson, The composition dependence of stacking fault energy in austenitic stainless steels, Metallurgical Transactions A, 8 (1977) 1901-1906.

[305] B.N. Singh, M. Eldrup, S.J. Zinkle, S.I. Golubov, On grain-size-dependent void swelling in pure copper irradiated with fission neutrons, Philosophical Magazine A, 82 (2002) 1137-1158.

[306] T. Diaz de la Rubia, M. Guinan, New mechanism of defect production in metals: A molecular-dynamics study of interstitial-dislocation-loop formation in high-energy displacement cascades, Physical Review Letters, 66 (1991) 2766-2769.

[307] B.N. Singh, A.J.E. Foreman, Calculated grain size-dependent vacancy supersaturation and its effect on void formation, Philosophical Magazine, 29 (1974) 847-858.

[308] C. Jiang, N. Swaminathan, J. Deng, D. Morgan, I. Szlufarska, Effect of grain boundary stresses on sink strength, Materials Research Letters, 2 (2014) 100-106.

[309] M. Demkowicz, R. Hoagland, J. Hirth, Interface structure and radiation damage resistance in cu-nb multilayer nanocomposites, Physical Review Letters, 100 (2008) 136102.

[310] N. Li, J. Wang, Y.Q. Wang, Y. Serruys, M. Nastasi, A. Misra, Incoherent twin boundary migration induced by ion irradiation in cu, Journal of Applied Physics, 113 (2013) 023508.

[311] K. Arakawa, K. Ono, M. Isshiki, K. Mimura, M. Uchikoshi, H. Mori, Observation of the one-dimensional diffusion of nanometer-sized dislocation loops, Science, 318 (2007) 956-959.

[312] Y.N. Osetsky, D.J. Bacon, A. Serra, B.N. Singh, S.I. Golubov, Stability and mobility of defect clusters and dislocation loops in metals, Journal of Nuclear Materials, 276 (2000) 65-77.

[313] N. Li, J. Wang, J.Y. Huang, A. Misra, X. Zhang, Influence of slip transmission on the migration of incoherent twin boundaries in epitaxial nanotwinned cu, Scripta Materialia, 64 (2011) 149-152.

[314] T.A. Khraishi, J.P. Hirth, H.M. Zbib, T.D. de La Rubia, The stress field of a general circular volterra dislocation loop: Analytical and numerical approaches, Philosophical Magazine Letters, 80 (2000) 95-105.

[315] Y. Liu, J. Jian, Y. Chen, H. Wang, X. Zhang, Plasticity and ultra-low stress induced twin boundary migration in nanotwinned cu by in situ nanoindentation studies, Applied Physics Letters, 104 (2014) 231910.

[316] J. Wang, N. Li, O. Anderoglu, X. Zhang, A. Misra, J.Y. Huang, J.P. Hirth, Detwinning mechanisms for growth twins in face-centered cubic metals, Acta Materialia, 58 (2010) 2262-2270.

[317] Y. Chen, N. Li, D.C. Bufford, J. Li, K. Hattar, H. Wang, X. Zhang, In situ study of heavy ion irradiation response of immiscible cu/fe multilayers, Journal of Nuclear Materials, 475 (2016) 274-279.

[318] R. Sizmann, The effect of radiation upon diffusion in metals, Journal of Nuclear Materials, 69 (1978) 386-412.

[319] T.D. Shen, S. Feng, M. Tang, J.A. Valdez, Y. Wang, K.E. Sickafus, Enhanced radiation tolerance in nanocrystalline mgga2o4, Applied Physics Letters, 90 (2007) 263115.

[320] M.A. Tschopp, K.N. Solanki, F. Gao, X. Sun, M.A. Khaleel, M.F. Horstemeyer, Probing grain boundary sink strength at the nanoscale: Energetics and length scales of vacancy and interstitial absorption by grain boundaries in α-fe, Physical Review B, 85 (2012) 064108.

[321] X. Zhang, A. Misra, Superior thermal stability of coherent twin boundaries in nanotwinned metals, Scripta Materialia, 66 (2012) 860-865.

[322] T.D. Shen, Radiation tolerance in a nanostructure: Is smaller better?, Nuclear Instruments and Methods in Physics Research Section B: Beam Interactions with Materials and Atoms, 266 (2008) 921-925.

[323] B.N. Singh, Effect of grain size on void formation during high-energy electron irradiation of austenitic stainless steel, Philosophical Magazine, 29 (1974) 25-42.

[324] O. El-Atwani, J. Nathaniel II, A. Leff, J. Baldwin, K. Hattar, M. Taheri, Evidence of a temperature transition for denuded zone formation in nanocrystalline fe under he irradiation, Materials Research Letters, (2016) 1-6.

[325] A. Hodge, T. Furnish, C. Shute, Y. Liao, X. Huang, C. Hong, Y. Zhu, T. Barbee Jr, J. Weertman, Twin stability in highly nanotwinned cu under compression, torsion and tension, Scripta Materialia, 66 (2012) 872-877.

[326] X. Wu, Y.T. Zhu, M.W. Chen, E. Ma, Twinning and stacking fault formation during tensile deformation of nanocrystalline ni, Scripta Materialia, 54 (2006) 1685-1690.

[327] H. Idrissi, B. Wang, M.S. Colla, J.P. Raskin, D. Schryvers, T. Pardoen, Ultrahigh strain hardening in thin palladium films with nanoscale twins, Advanced Materials, 23 (2011) 2119-2122.

[328] S. Xue, Z. Fan, Y. Chen, J. Li, H. Wang, X. Zhang, The formation mechanisms of growth twins in polycrystalline al with high stacking fault energy, Acta Materialia, 101 (2015) 62-70.

[329] S.-Z. Lu, A. Hellawell, The mechanism of silicon modification in aluminum-silicon alloys: Impurity induced twinning, Metallurgical Transactions A, 18 (1987) 1721-1733.

[330] M. Timpel, N. Wanderka, R. Schlesiger, T. Yamamoto, N. Lazarev, D. Isheim, G. Schmitz, S. Matsumura, J. Banhart, The role of strontium in modifying aluminium–silicon alloys, Acta Materialia, 60 (2012) 3920-3928.

[331] A.J. Shahani, E.B. Gulsoy, S.O. Poulsen, X. Xiao, P.W. Voorhees, Twin-mediated crystal growth: An enigma resolved, Scientific Reports, 6 (2016) 28651.

[332] J. Li, Y. Chen, S. Xue, H. Wang, X. Zhang, Comparison of size dependent strengthening mechanisms in ag/fe and ag/ni multilayers, Acta Materialia, 114 (2016) 154-163.

[333] Q. Lu, Q. Su, F. Wang, C. Zhang, Y. Lu, M. Nastasi, B. Cui, Influence of laser shock peening on irradiation defects in austenitic stainless steels, Journal of Nuclear Materials, 489 (2017) 203-210.

[334] X.F. Zhu, J.S. Williams, M.J. Conway, M.C. Ridgway, F. Fortuna, M.O. Ruault, H. Bernas, Direct observation of irradiation-induced nanocavity shrinkage in si, Applied Physics Letters, 79 (2001) 3416.

[335] H. Zheng, Y. Liu, F. Cao, S. Wu, S. Jia, A. Cao, D. Zhao, J. Wang, Electron beam-assisted healing of nanopores in magnesium alloys, Sci Rep, 3 (2013) 1920.

[336] K. Krishan, R.V. Nandedkar, Mechanisms for radiation-induced shrinkage of voids, Nature, 280 (1979) 253-253.

[337] R. Bullough, B.L. Eyre, K. Krishan, Cascade damage effects on the swelling of irradiated materials, Proceedings of the Royal Society of London. Series A, Mathematical and Physical Sciences, 346 (1975) 81-102.

[338] B.L. Eyre, Transmission electron microscope studies of point defect clusters in fcc and bcc metals, Journal of Physics F: Metal Physics, 3 (1973) 422.

[339] L.K. Mansur, E.E. Bloom, Radiation effects in reactor structural alloys, JOM, 34 (1982) 23-31.

[340] S. Kashibe, K. Une, K. Nogita, Formation and growth of intragranular fission gas bubbles in uo 2 fuels with burnup of 6–83 gwd/t, Journal of nuclear materials, 206 (1993) 22-34.

[341] J. Turnbull, The distribution of intragranular fission gas bubbles in uo2 during irradiation, Journal of Nuclear Materials, 38 (1971) 203-212.

[342] K. Une, K. Nogita, S. Kashibe, M. Imamura, Microstructural change and its influence on fission gas release in high burnup uo2 fuel, Journal of nuclear materials, 188 (1992) 65-72.

[343] M. Verwerft, Multiple voltage electron probe microanalysis of fission gas bubbles in irradiated nuclear fuel, Journal of nuclear materials, 282 (2000) 97-111.

[344] G.L. Hofman, Y.S. Kim, A classification of uniquely different types of nuclear fission gas behavior, Nuclear Engineering and Technology, 37 (2005) 299-308.

[345] M.P. Surh, J.B. Sturgeon, W.G. Wolfer, Void nucleation, growth, and coalescence in irradiated metals, Journal of Nuclear Materials, 378 (2008) 86-97.

[346] S.F. Pugh, Voids formed by irradiation of reactor materials - report of conference, Journal of the British Nuclear Energy Society, 10 (1971) 159-&.

[347] S.F. Pugh, Radiation induced voids in metals - report on usaec conference, Journal of the British Nuclear Energy Society, 11 (1972) 9-&.

[348] D.I.R. Norris, Voids in irradiated metals (part ii), Radiation Effects, 15 (1972) 1-22.

[349] A.H. King, D.A. Smith, Calculations of sink strength and bias for point-defect absorption by dislocations in arrays, Radiation Effects, 54 (2006) 169-176.

[350] S. Kondo, Y. Katoh, L.L. Snead, Analysis of grain boundary sinks and interstitial diffusion in neutron-irradiated sic, Physical Review B, 83 (2011).

[351] J. Burke, D. Stuckey, Dislocation loop-free zones around grain boundaries in quenched aluminium and aluminium alloys, Philosophical Magazine, 31 (1975) 1063-1080.

[352] Y. Zhang, H. Huang, P.C. Millett, M. Tonks, D. Wolf, S.R. Phillpot, Atomistic study of grain boundary sink strength under prolonged electron irradiation, Journal of Nuclear Materials, 422 (2012) 69-76.

[353] L. Malerba, C.S. Becquart, C. Domain, Object kinetic monte carlo study of sink strengths, Journal of Nuclear Materials, 360 (2007) 159-169.

[354] A.M. Monti, A. Sarce, N. Smetniansky-De Grande, E.J. Savino, C.N. Tomé, Point defects and sink strength in h.C.P. Metals, Philosophical Magazine A, 63 (1991) 925-936.

[355] B.P. Uberuaga, L.J. Vernon, E. Martinez, A.F. Voter, The relationship between grain boundary structure, defect mobility, and grain boundary sink efficiency, Sci Rep, 5 (2015) 9095.

[356] M.J. Demkowicz, R.G. Hoagland, B.P. Uberuaga, A. Misra, Influence of interface sink strength on the reduction of radiation-induced defect concentrations and fluxes in materials with large interface area per unit volume, Physical Review B, 84 (2011) 104102.

[357] M.J. Demkowicz, The influence of sigma 3 twin boundaries on the formation of radiation-induced defect clusters in nanotwinned cu, Journal of Materials Research, 26 (2011) 1666-1675.

[358] J.W. Corbett, Electron radiation damage in semiconductors and metals. [by] james w. Corbett, New York : Academic Press, 1966., 1966.

[359] N. Hashimoto, T.S. Byun, K. Farrell, S.J. Zinkle, Deformation microstructure of neutron-irradiated pure polycrystalline metals, Journal of Nuclear Materials, 329–333, Part B (2004) 947-952.

[360] Y. Dai, M. Victoria, Defect structures in deformed f.C.C. Metals, Acta Materialia, 45 (1997) 3495-3501.

[361] B.N. Singh, D.J. Edwards, A. Horsewell, P. Toft, Dose dependence of microstructural evolution and mechanical properties of neutron irradiated copper and copper alloys, in, Denmark, 1995, pp. 34.

[362] J.W. Muncie, B.L. Eyre, C.A. English, Low-dose neutron irradiation damage in copper. I. Vacancy loop production, Philosophical Magazine A, 52 (1985) 309-331.